AN INVESTIGATION OF THE MECHANICAL PROPERTIES OF SWELLING CLAYS AND CLAY-KEROGEN INTERACTIONS IN OIL SHALE: A MOLECULAR MODELING AND EXPERIMENTAL STUDY

A Dissertation
Submitted to the Graduate Faculty
of the
North Dakota State University
of Agriculture and Applied Science

By

Keshab Bahadur Thapa

In Partial Fulfillment of the Requirements
for the Degree of
DOCTOR OF PHILOSOPHY

Major Department:
Civil and Environmental Engineering

December 2019

Fargo, North Dakota

North Dakota State University
Graduate School

Title

AN INVESTIGATION OF THE MECHANICAL PROPERTIES OF SWELLING CLAYS AND CLAY-KEROGEN INTERACTIONS IN OIL SHALE: A MOLECULAR MODELING AND EXPERIMENTAL STUDY

By

Keshab Bahadur Thapa

The Supervisory Committee certifies that this ***disquisition*** complies with North Dakota State University's regulations and meets the accepted standards for the degree of

DOCTOR OF PHILOSOPHY

SUPERVISORY COMMITTEE:

Dinesh R. Katti
Chair

Kalpana S. Katti

Ying Huang

Alan Denton

Approved:

12/19/2019
Date

David R. Steward
Department Chair

ABSTRACT

This work provides an insight into how the molecular interactions influence macroscale properties of two materials: swelling clay and oil shale. Swelling clays cause enormous damage to infrastructure: buildings, roads, and bridges. Understanding the mechanisms are essential to prevent the detrimental effects and use of these clays for engineering applications. Our group studied the effect of fluid polarity on sodium montmorillonite (Na-MMT) swelling clay mineral using molecular modeling and experiments for bridging the molecular level behavior with the microstructure, swelling pressure, permeability, and compressibility. Various polar fluids (Dielectric Constant 110 to 20) found in landfill leachates are used. Our molecular dynamics (MD) simulations show that the nonbonded interactions of Na-MMT with polar fluids are higher than with low and medium polar fluids. These results are consistent with the results from Fourier transform infrared (FTIR) spectroscopy experiments. The polarity of the fluids and the fluid content influence the interlayer spacing, interlayer modulus, nonbonded interactions, and conformation as well as the shear strength parameters, the angle of internal friction (φ) and cohesion (c). Furthermore, the unconfined compressive strength experiments are used to evaluate the undrained cohesion at various swelling level. The nanomechanical properties, the modulus of elasticity (E) and hardness (H), of the undisturbed dry and saturated Na-MMT at various level of swelling are evaluated using nanoindentation experiments for the first time. The undrained cohesion, modulus of elasticity, and hardness decrease with increase in swelling level. Swelling controls the microstructure of Na-MMT clay, and the clay particles breakdown into smaller sizes with increase in swelling level.

The Green River Formation located in the United States is the richest oil shale deposit in the world. Oil shale contains clay minerals, bitumen, and kerogen—a precursor to crude oil. A

three-dimensional (3D) kerogen model is built from seven fragments, and the interactions of kerogen with Na-MMT is investigated using MD simulations to understand how the kerogen is bound to the clay mineral. The nonbonded interactions between Na-MMT and kerogen as well as among kerogen fragments are found. This work seeks to develop new methods to extract kerogen economically and efficiently.

ACKNOWLEDGEMENTS

I would like to thank my advisor Dr. Dinesh Katti and co-advisor Dr. Kalpana Katti for their guidance and encouragement throughout my doctorate degree. This work would not have been possible without their continuous support and inspiration.

I would like to acknowledge NDSU Center for Computationally Assisted Science and Technology (CCAST) for providing computational resource that was essential for the molecular modeling work. I would like to acknowledge Mountain Plains Consortium (MPC), Civil and Environmental Engineering Department, and ND EPSCoR Doctoral Dissertation Assistantship for supporting my graduate study.

I am thankful to my supervisory committee members: Dr. Ying Huang and Dr. Alan Denton. I would like to thank Dr. Scott Payne for his assistance with electron microscopy experiments. I would also like to thank my group members: Anurag Sharma, Chunju Gu, Him Upadhyay, Md. Molla, Sumanta Kar, Krishna Kundu, Nasrullah Faisal, Haneesh Jasuja, Sharad Jaswandkar, and Preetham Ravi for being helpful. I also thank Jan Lofberg and Milka Singha as well as Civil and Environmental Engineering Department.

Finally, I would like to thank my family members for their unconditional love, encouragement, sacrifices, and patience throughout my degree.

DEDICATION

This dissertation is dedicated to my father (Mr. Punya Bahadur Thapa) and mother (Mrs. Ganga Maya Thapa).

TABLE OF CONTENTS

LIST OF TABLES

LIST OF FIGURES

LIST OF ABBREVIATIONS

MD .....Molecular Dynamics.

SMD.....Steered Molecular Dynamics.

CHARMM .....Chemistry at Harvard Macromolecular Mechanics

3D.....Three Dimensional.

2D.....Two Dimensional.

Na-MMT .....Sodium Montmorillonite.

XRD .....X-Ray Diffraction.

FTIR.....Fourier Transform Infrared.

SEM .....Scanning Electron Microscopy.

ELE .....Electrostatic.

VDW .....van der Waals.

CUS.....Controlled Uniaxial Swelling.

AFM.....Atomic Force Microscopy.

L-D.....Load-Displacement.

E .....Elasticity.

H.....Hardness.

1. INTRODUCTION

1.1. Swelling Clays

Swelling clays are extensively found all over the world. The volume of these clays increases when exposed to water, causing an increase in swelling, swelling pressure, and loss of strength. Sodium-montmorillonite (Na-MMT) is one of the major constituents of swelling clays. The unit cell of Na-MMT consists of one aluminum octahedral (O) sandwiched between two silica tetrahedral (T) sheets [1]. The large stresses due to swelling of clays cause severe damages to the buildings, roads, retaining walls, bridges, and embankments [2, 3]. Figure 1.1 shows the extent of swelling clay deposits in the United States [4]. The red colored regions in the map contain abundant clay having high swelling potential, and the blue colored areas show the regions with less than 50% swelling clays that have high swelling potential. Furthermore, the orange and green regions show abundant and less than 50% swelling clays having slight to moderate swelling potential, respectively.

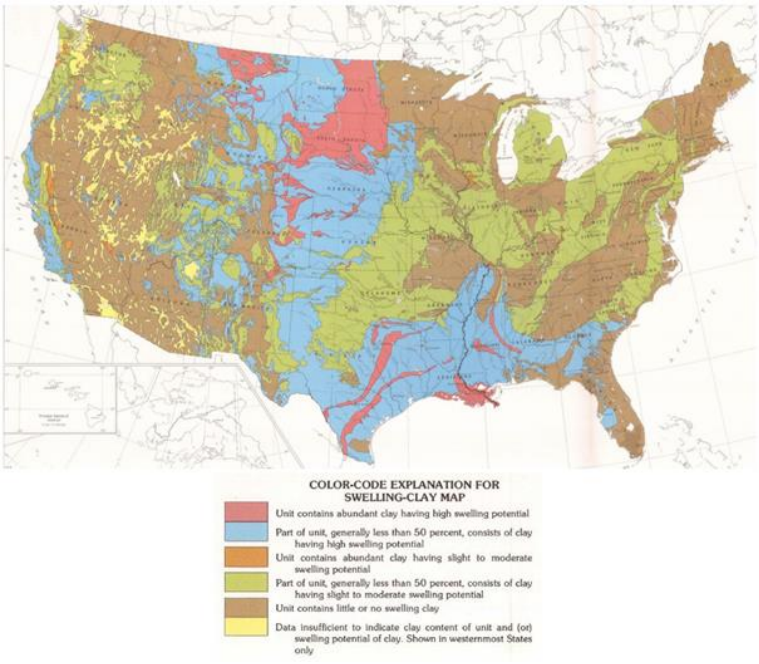

Figure 1.1. Swelling clays deposits in the United States (U.S. Geological Survey publication, 1989; W.W. Olive, 1989).

Some areas in the Midwest United States possess the most abundant clays with high swelling potential. An average annual damage caused by swelling clays is over $9 billion to the infrastructures in the United States [5, 6]. However, these clays also have various useful applications in engineering due to high swelling capacity, small particle size, large surface area to mass ratio [7], and low permeability [8]. Thus, these clays have been used as the barrier liner materials in landfills, as drilling mud and catalyst in petroleum engineering, drug delivery systems in pharmaceutical and biomedical applications, enhancing the mechanical properties of polymer-clay-nanocomposites, and modifiers in pavement construction.

Shear strength is a critical engineering property that controls the bearing capacity of soils. The bearing capacity is ability of soils to carry the load of the structures, which transfers from the foundation to soils, without undergoing a shear failure [9]. The shear failure occurs due to the relative movement of the individual soil particles when the externally applied compressive stresses exceed the internal shear strength of soils. The major civil engineering problems are related to the shear strength. The failure of the building foundations, landslides, and erosions are some examples of failures that are related with shear strength properties of clays.

The term clay indicates the particle size as well as mineral type. The clay mineral crystals consist of sheet like structures that are stacked one upon another and are of colloidal dimension. The lateral dimension of a single clay particle ranges from 10^3 to 10^6 Å and a thickness of about 10 Å. The shape, size, and surface of soil particles and their interactions with various solvents can be evaluated using mineralogy technologies. These characteristics play an important role on various properties of soils such as plasticity, swelling, hydraulic conductivity, compression, and shear strength, and these properties of soils can be further used to mitigate environmental problems like the disposal of hazardous and radioactive wastes [1].

To avoid the detrimental effects of swelling clays on infrastructures and effectively use these clays in geoenvironmental applications and geotechnical engineering, understanding of the swelling mechanisms, evaluating the interactions occurring on the molecular scale, evolution of important engineering properties such as microstructure, swelling pressure, permeability, and consolidation of swelling clay is essential. An attempt has been made to explain the swelling behaviors of clays using the traditional theories, which are based on electric double layer. The diffuse double layer concept, which is also known as Stern and Guy theory [10], has been used to evaluate the clay-water interactions in the interlayer gallery. However, this theory has various limitations such evenly distribution of surface charge, an infinite long clay particle, ions in the solution are considered as point charges, and uniform dielectric permittivity throughout double layer [11]. Furthermore, this theory is unable to precisely describe the expansion of the interlayer as well as swelling behavior [12]. Additionally, the DLVO theory (Derjaguin, Landau, Verwey, and Overbeek) describes the colloidal suspension stability of clay for interlayer spacing of more than 20Å. Thus, the DLVO theory cannot describe the swelling mechanism of the clay interlayer at smaller interlayer spacing.

To overcome these limitations, molecular modeling studies are essential to accurately explain the swelling mechanisms and interactions of swelling clays not only with water but also with various organic fluids at the molecular level. The interactions swelling clays with organic fluids with a wide range of dielectric constants: formamide (110), water (80), methanol (33), acetone (20) are chosen. The values in the parentheses represent the dielectric constant values (DEC) of the fluid molecules. According to the United States Environmental Protection Agency (EPA), these organic fluids are commonly found in landfill leachates, which are also identified as toxic and hazardous to health. Furthermore, the classical theory of bearing capacity does not

account for clay-fluid interactions, thus reducing its predictive capabilities. Globally, the expenditure of the construction-related properties and services in the civil engineering arena is about $10 trillion a year [13], and improving the fundamental theory used in the design and construction of the infrastructures will be an important contribution to the field and the society. A better understanding of shear failure mechanism, accounting for the clay-fluid molecular interactions is crucial not only for economical design and construction but also for public safety. Therefore, this dissertation also provides the development of the multiscale models for the reliable prediction of the shear strength of swelling clays that would improve design capabilities, prevent the failure of civil infrastructures, reduce the cost of the projects, and enhance public safety in swelling clay regions.

1.2. Oil Shale

The world demand for energy continues to increase, and the conventional source of energy is unable to maintain the stability of supply and demand. It is essential to explore and develop alternative unconventional sources of energy to fulfil the future demand. The alternative energy sources such as coal, oil shale, wind energy, solar energy, hydroelectric energy, and oil shale are now becoming popular throughout the world. Thus, oil shale is the most significant and complementary source of energy [14]. Oil shale is a fine-grained sedimentary rock, which is formed by the deposition of the clay minerals and organic matter. The organic matter of oil shale contains bitumen and kerogen. Kerogen is the most abundant form of hydrocarbon, which is a precursor of crude oil and insoluble in common organic solvents [15]. Oil shales are found in 27 countries. Figure 1.2 shows the Green River Formation that is situated in Colorado, Utah, and Wyoming, and this formation has about 70% of the total oil reserves in the world [16]. This is the largest oil shale deposit in the world. It is estimated that there is about 1.8 trillion barrels oils

found in the Green River Formation. An about 800 billion barrels of oil can be recovered, which is three times greater than the oil reserves in Saudi Arabia. Today's oil demand in the United States is over 20 million barrels a day. If 800 billion barrels of recoverable oil can meet a quarter of demand that is 5 million barrels a day, oil shale will supply oil for 400 years in the United States [17].

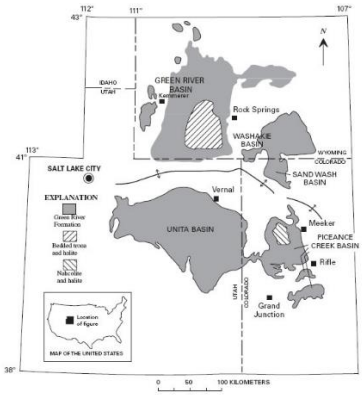

Figure 1.2. The Green River Formation located in the United States parts of Colorado, Utah, and Wyoming.

Green River oil shale has 86.20% mineral matrix, and dolomite, calcite, montmorillonite, feldspar, and quartz are the predominated minerals [18]. Organic matter contains about 13.80% by weight percentage [19]. Kerogen is amorphous organic matter [20] that is finely dispersed on the mineral matrixes with a size in the order of tens of nanometers [21, 22], and there is a significant molecular interactions between kerogen and minerals. Kerogen is in solid form in oil shale, and the extraction of kerogen requires a heat of about 500 ^{o}C in the absence of oxygen [23] to change from solid to liquid state. Thus, this current method of extraction of kerogen requires a tremendous amount of energy.

The major difference between oil shale and shale oil is the size of shale oil that is trapped in mineral matrix. These large pockets of oil in shale oil are commercially extracted using a high-pressure water mixture called fracking method. However, as of now, the commercial

extraction of kerogen from oil shale is not feasible in the United States. It is essential to extract kerogen from the surrounding mineral complexes for the viable production of oil from oil shale in the future. Therefore, the study of kerogen-mineral molecular interactions is crucial to extract the oil efficiently, economically, and environmental friendly from oil shale.

1.3. Significant of the Work

The compressibility and shear strength are the most significant properties for the bearing capacity and slop stability analysis. Current methods for predicting these properties of clays are inadequate, which is also yet to be understood. The clay-fluid molecular interactions play key role in the macroscale properties such as swelling pressure, permeability, compressibility, and shear strength that are not reflected in the current models. Thus, evaluating clay-fluid molecular interactions along with changes to microstructure are key to accurately predicting the macroscale properties. A multiscale approach is needed to relate the molecular interactions and microstructure to the engineering properties. In this study, the role of the molecular scale interaction on the microscale properties such as compressibility and shear strength of clay is investigated using the molecular modeling and experimental techniques.

Furthermore, current practices of excessive oil use increase the oil demand. Overreliance on conventional sources of energy can cause the instability of supply and demand in the future. Therefore, oil shale is an integral and alternative source of energy. Also, the variation of oil price over time has led researchers to develop alternative and unconventional sources of energy. Oil shales are fine-grained sedimentary rocks that contain minerals, bitumen, and kerogen and yield a significant amount of oil by heating in absence of oxygen. Kerogen is the most abundant form of hydrocarbon, and a precursor of crude oil. Kerogen is also finely dispersed on oil shale minerals, and there is a significant molecular interaction between them. Therefore, a better

understanding of the molecular interactions between kerogen and mineral is essential to design new methodologies to extract the oil efficiently, economically, and environmental friendly from oil shale. In this work, the evaluation of how kerogen is locked in oil shale mineral matrix by developing a three-dimensional (3D) kerogen-mineral model is carried out.

1.4. Original Contributions

This research consists of six sections: 1) the role of fluid polarity on the clay-fluid interactions on swelling, swelling pressure, permeability, and evolution of microstructures using molecular modeling and correlated the modeling results with the results from Fourier transform infrared (FTIR) spectroscopy experiments, 2) the influence of fluid polarity on the compressibility of the interlayer of swelling clays using steered molecular dynamics simulations, 3) the investigation of the molecular shear resistance and shear strength parameters—angle of internal friction and cohesion—of swelling clays with various organic fluids using steered molecular dynamics, 4) the relationship between swelling level and the macroscale mechanical properties such as swelling pressure and unconfined compressive strength of undisturbed saturated swelling clays, 5) the investigation of the nanomechanical properties such as the modulus of elasticity and hardness of undisturbed saturated swelling clays at various level of swelling using nanoindentation experiments, and 6) the nonboned kerogen-clay interactions to develop new methodologies for the extraction of kerogen economically and efficiently from the Green River oil shale using molecular dynamics simulations.

In the first part of the research, the nonbonded interactions of Na-Montmorillonite clay with four organic fluids with a wide range of dielectric constant values are quantitatively evaluated using molecular dynamics simulations. Furthermore, the results from the molecular dynamic simulations correlate well with the results from Fourier infrared spectroscopy

experiments. These molecular models are further used in the second part of the research to study the compressibility of clay interlayer spacing using constant-force steered molecular dynamics simulations. Furthermore, the influence of the polarity of fluids in the interlayer spacing, interlayer volume, interlayer strain, interlayer modulus, nonbonded interactions, and conformation of the fluid molecules upon externally applied stresses is studied. The third part of the research includes the shear strength of these clay-fluids molecular models when the clay layer is pulled in the horizontal direction using constant-velocity steered molecular dynamics simulations. Also, the molecular shear strength parameters—cohesion and angle of internal friction angle—are evaluated.

The fourth part of the research explains the experimental study of the measurement of swelling level and swelling pressure using controlled uniaxial swelling (CUS) device. The saturated clay samples are allowed to swell at three level of welling, 0%, 10%, and 20%, with respect to original volume in the CUS devices. The evolution of the microstructures and unconfined compressive strength at three different level of swelling are evaluated. The fifth part of the research comprises the evaluation of nanomechanical properties at three different level of swelling. Furthermore, this is the first study that discloses the variation of the nanomechanical characteristics of swelling clays at various level of swelling of the undisturbed saturated swelling clays.

In the sixth part of the research, molecular dynamics simulations are used to evaluate the nonboned interactions (electrostatic and van der Waals) of kerogen with clay in the Green River oil shale. A three-dimensional (3D) molecular model of kerogen is developed for the first time. This work further provides a comprehensive analysis of the quantitative interactions of the 3D kerogen structure with montmorillonite clay. The nonboned interactions between kerogen and

clay mineral as well as the interactions within kerogen fragments provide insight for future research to develop new methods of extraction of kerogen economically, efficiently, and environmental friendly from oil shale.

1.5. Objectives of the Research

The major objectives of the research are:

- To develop the molecular model of swelling clays with polar, medium polar, and low polar fluids (Dielectric constant from 20 to 110) to investigate the role of clay-fluids molecular interactions to swelling pressure, permeability, compressibility, and shear strength of clays.
- To study the molecular shear strength parameters, cohesion and angle of internal friction, for clay with various organic fluids using molecular dynamics simulations.
- To develop the macroscale relationship between swelling and the mechanical properties such as swelling, swelling pressure, and shear strength of undisturbed saturated swelling clays. The evolution of the microstructures at predetermined level of swelling is also captured using scanning electron microscopy experiments.
- To investigate the nanomechanical properties, modulus of elasticity and hardness and the evolution of microstructural changes of saturated swelling clays at various level of swelling using nanoindentation experiments.
- To understand how the kerogen is “locked” in the mineral matrix by developing a three dimensional kerogen-clay mineral molecular model for the Green River oil shale.

1.6. Dissertation Organization

This dissertation is organized into following manner:

1. Chapter 1: Introduction
2. Chapter 2: This chapter presents review of the literature on clay fluid interactions and mechanical properties such as swelling pressure, permeability, consolidation, and shear strength of swelling clays.
3. Chapter 3: This chapter presents the role of fluid polarity in the swelling of sodium-montmorillonite clay: a molecular dynamics and Fourier transform infrared spectroscopy study.
4. Chapter 4: This chapter describes the compression of Na-montmorillonite swelling clay interlayer is influenced by fluid polarity: a steered molecular dynamics study.
5. Chapter 5: This chapter describes the influence of the molecular interactions on shear strength of Na-MMT with organic fluids: a steered molecular dynamics study.
6. Chapter 6: Experimental evaluation of shear strength of swelling clays for various magnitude of swelling is discussed in this chapter.
7. Chapter 7: This chapter presents the modeling molecular interactions of sodium montmorillonite clay with 3D kerogen models.
8. Chapter 8: This chapter presents summary and major conclusions presented in this dissertation.
9. Chapter 9: This chapter discusses the future directions for the research in this field.

1.7. References

[1] J.K. Mitchell, K. Soga, Fundamentals of soil sehavior, NJ: John Wiley & Sons (2005).

[2] E. Sebastian, G. Cultrone, D. Benavente, L.L. Fernandez, K. Elert, C. Rodriguez-Navarro, Swelling damage in clay-rich sandstones used in the church of San Mateo in Tarifa (Spain), Journal of Cultural Heritage 9(1) (2008) 66-76.

[3] F.H. Chen, Foundations on expansive soils, Elsevier (2012).

[4] W.W. Olive, A.F. Chleborad, C.W. Frahme, J. Schlocker, R.R. Schneider, R.L. Schuster, Swelling clays map of the conterminous United States, Technical Report (1989).

[5] G.S. Dasog, A.R. Mermut, Expansive soils and clays, in: P.T. Bobrowsky (Ed.), Encyclopedia of Natural Hazards, Springer Netherlands, Dordrecht (2013) 297-300.

[6] H.H. Zhao, L. Ge, T.M. Petry, Y.Z. Sun, Effects of chemical stabilizers on an expansive clay, Ksce Journal of Civil Engineering 18(4) (2014) 1009-1017.

[7] H. Van Olphen, An introduction to clay colloid chemistry: for clay technologists, geologists, and soil scientists, 2nd edition, Wiley, New York (1977).

[8] P.M. Amarasinghe, K.S. Katti, D.R. Katti, Insight into Role of Clay-Fluid Molecular Interactions on Permeability and Consolidation Behavior of Na-Montmorillonite Swelling Clay, Journal of Geotechnical and Geoenvironmental Engineering 138(2) (2012) 138-146.

[9] B.M. Das, K. Sobhan, Principles of geotechnical engineering, Cengage Learning (2013).

[10] D. Stigter, Micelle formation by ionic surfactants. II. Specificity of head groups, micelle structure, Journal of Physical Chemistry 78(24) (1974) 2480-2485.

[11] K.H. Tan, Principles of soil chemistry, CRC press (2010).

[12] H.Y. Jo, T. Katsumi, C.H. Benson, T.B. Edil, Hydraulic conductivity and swelling of nonprehydrated GCLs permeated with single-species salt solutions, Journal of Geotechnical and Geoenvironmental Engineering 127(7) (2001) 557-567.

[13] F. Barbosa, J. Woetzel, J. Mischke, M.J. Ribeirinho, M. Sridhar, M. Parsons, N. Bertram, S. Brown, Reinventing construction: A route to higher productivity, McKinsey Global Institute (2017).

[14] S.H. Deng, Z.J. Wang, Q.A. Gu, F.Y. Meng, J.F. Li, H.Y. Wang, Extracting hydrocarbons from Huadian oil shale by sub-critical water, Fuel Processing Technology 92(5) (2011) 1062-1067.

[15] F.P. Miknis, Solid-state 13C NMR in oil shale research: an introduction with selected applications, Composition, Geochemistry and Conversion of Oil Shales, Springer (1995) 69-91.

[16] S. Thompson, Oil shale and tar sands programmatic (EIS), Bureau of Land Management (2009).

[17] A.W. Decora, R.D. Kerr, Processing use, and characterization of shale oil products, Environmental Health Perspectives 30 (1979) 217-223.

[18] E. Fletcher, Development of America's strategic unconventional fuels resources, by task force on strategic unconventional fuels, Resource Specific 2 (2007).

[19] T.F. Yen, G.V. Chilingarian, Oil shale, United States (1976).

[20] M. Vandenbroucke, Kerogen: from types to models of chemical structure, Oil & Gas Science and Technology 58(2) (2003) 243-269.

[21] K.N. Alstadt, K.S. Katti, D.R. Katti, Nanoscale morphology of kerogen and in situ nanomechanical properties of green river oil shale, Journal of Nanomechanics and Micromechanics 6(1) (2015) 1-10.

[22] E. Eseme, J.L. Urai, B.M. Krooss, R. Littke, Review of mechanical properties of oil shales: Implications for exploitation and basin modelling, Oil Shale 24(2) (2007) 159-174.

[23] B. Hascakir, T. Babadagli, S. Akin, Experimental and numerical simulation of oil recovery from oil shales by electrical heating, Energy & Fuels 22(6) (2008) 3976-3985.

2. LITERATURE REVIEW

2.1. Clay Mineralogy

Clay indicates to particle size as well as mineral type. For engineering applications, clays are defined as the fine-grained particles smaller than 0.002 mm (2 μm). The clay mineral possesses specific characteristics such as small in size, negatively charged surface, plasticity upon mixing with water, and resistance to weather [1]. Due to natural weathering of rock forming minerals, clay minerals are formed on the surface of earth. The clay minerals further dominate the mineralogy of soils [2]. Clay minerals consist of complex aluminum phyllosilicates, and the two basic building blocks of phyllosilicates are silica tetrahedral (T) and aluminum octahedral (O). These minerals have a sheet like structure, which has comparatively higher surface area than that of cubic or rectangular shape. Additionally, the ratio of length to thickness of the sheet structure is about twenty, and thus the surface area of a clay particle is three times greater than that of a cube with the same volume [3].

2.1.1. Structure of Clay Minerals

Clay minerals are layered structures that belong to the family of minerals known as phyllosilicates or layer silicates. The unit cell of layer silicate is made of combination of silica tetrahedral and aluminum octahedral sheet. The structure of clay is characterized by stacking of these two sheets. Silica tetrahedral sheet consists of one silicon atom surrounded by four oxygen atoms as shown in Figure 2.1. Also, three out of four oxygen atoms in tetrahedral sheet is shared in order to form a hexagonal net. The chemical composition of the silica tetrahedral sheet is $(Si_4O_{10})^{4-}$, where the negatively charge are balanced by replacing oxygen by hydroxyls [4].

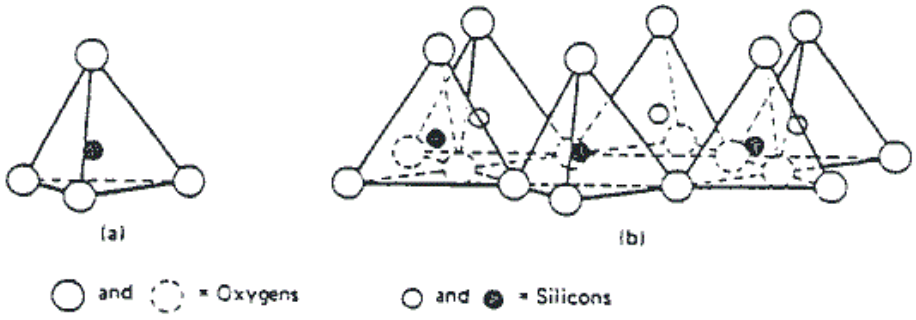

Figure 2.1. Silica tetrahedron cell and silicon tetrahedral sheet (Grim, 1968, as cited by Mitchell, 1993).

On the other hand, the octahedral sheets consist of magnesium or aluminum that are octahedrally connected by oxygen and hydroxyls as shown in Figure 2.2. The chemical composition of octahedral sheet is $Al_2(OH)_6$, and this composition is also known as the gibbsite sheet. When two thirds of the cationic spaces are occupied in the case of trivalent octahedral cations, the structure is known as dioctahedral as shown in Figure 2.3(a). Similarly, when the octahedral coordinated cation is divalent, and all the spaces are filled, and the structure is called trioctahedral sheet as shown in Figure 2.3(b).

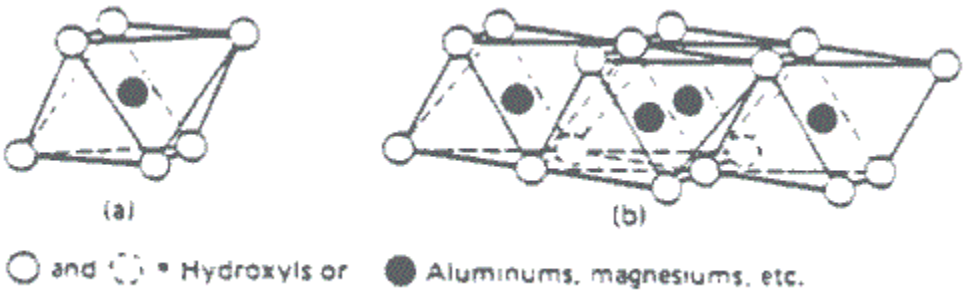

Figure 2.2. The octahedral unit cell and the octahedral sheet (Grim, 1968, as cited by Mitchell, 1993).

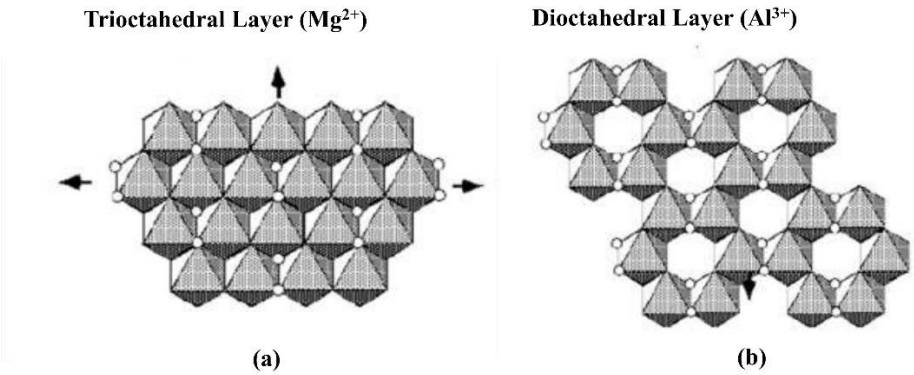

Figure 2.3. (a) Trioctahedral structure and (b) dioctahedral structure (Grim, 1968, as cited by Mitchell, 1993).

The layered structures of clay minerals are formed by stacking one above another, resulting in the formation of the tetrahedral-octahedral sheet. The combination of tetrahedral and octahedral by mutual share of oxygen ions forms the crystal structure of the clay minerals [5]. This crystal structure is termed as a clay layer. Furthermore, the empty space between two consecutive clay layers is called the clay interlayer spacing or simply interlayer. The sum of the layers and interlayer spacing represents a unit structure. When an octahedral sheet is sandwiched between two tetrahedral sheets, the 2:1 structured is formed, which is known as tetrahedral-octahedral-tetrahedral (T-O-T) structure. Furthermore, Si^{+4} atoms in the tetrahedral sheet are replaced by Al^{+3} or Mg^{+2}, and Al^{+3} atoms in the octahedral sheet are replaced by Fe^{+3}. This phenomenon is defined as isomorphs substitution. Thus, negative charges are developed in the clay sheets due to this replacement of an atom of lower valence by higher valance. Additionally, these negative charged ions are balanced by naturally occurring positively charged cations such as sodium, magnesium, and calcium.

2.1.2. Cation Exchange Capacity

The cations, which are present in the interlayer to balance the negatively charge clay surface, can be replaced by other cations. This phenomenon is known as cation exchange

capacity (CEC). These cations are attracted by surface charge or adsorbed onto the internal or external interlayer surfaced. The value of CEC depend on the mineral types, and smectite has the highest CEC followed by illite and kaolinite [6]. Furthermore, the type of cations controls the attraction of the cations on the surfaces [3].

2.1.3. Types of Clay Minerals

Depending up the isomorphic substitution and the combination of octahedral and tetrahedral sheets, clay minerals can be divided into three groups: 1:1 (one tetrahedral and one octahedral sheet), 2:1 (two tetrahedral sheets and an octahedral sheets), and 2:1:1 (additional octahedral sheet in between two 2:1 layers) [5].

2.1.3.1. Kaolinite

The combination of one tetrahedral and one octahedral refers to kaolinite group, which is also termed as a group of 1:1 mineral. Kaolinite has low swelling capacity, low cation exchange capacity, and no interlayer cations [7]. Also, the bonding between the layers is predominated by electrostatic, whereas the attractive nature of van der Waals and hydrogen boding is small.

2.1.3.2. Illite

Illite belongs to 2:1 layers, which is a nonexpanding clay mineral in the presence of water. The separation of clay layers when mixed with solvents does not prevail due to isomorphic substitutions in the tetrahedral sheets. The interlayer spacing contains potassium ions, and these ions have a strong electrostatic interactions to maintain the stability of the clay structure. The deficiency of charge in illite is from 1.3 to 1.5, which is mainly occurred only in the silica tetrahedral sheet. When adding polar fluids, the interlayer spacing remains about 10Å because of the strong bonding in the interlayer.

2.1.3.3. Vermiculate

The 2:1 layer arrangement refers to vermiculite group, which has the combination dioctahedral and trioctahedral sheets. The deficiency of charge in vermiculate is from 1 to 1.4. In vermiculate, isomorphic substitutions occur in tetrahedral sheet, and the CEC is high due to exchange of the interlayer cations. Although there is a strong bonding between the sheets, it also possesses limited swelling [5].

2.1.3.4. Chlorite

Chlorite is a 2:1:1 type clay mineral, which has alternative 2:1 clay layers and octahedral layers. Isomorphic substitutions occur in tetrahedral sheet primarily Al^{+3} for Si^{+4}, resulting in the development of a negative charge. There is a strong interaction between the layers, and there is no welling of the interlayer [5].

2.1.3.5. Sodium-montmorillonite

Smectite minerals are 2:1 clay minerals in which an octahedral sheet is sandwiched between two silica tetrahedral sheets. In smectite clay minerals, isomorphic substitutions occur extensively, and thus these clay minerals exhibit high swelling behavior. The substitutions of Si^{+4} by Al^{+3} and Fe^{+3} occur in the tetrahedral sheet, whereas Al^{+3} can be replaced by Mg^{+2}, Fe^{+3}, Fe^{+2}, Cr^{+2}, Zn^{+2}, and Ni^{+2} [4, 8]. The negative charge in smectite clay minerals vary from 0.5 to 1.2. Furthermore, smectites have both dioctahedral and trioctahedral minerals. Some smectic clay minerals are montmorillonite, beidellite, nontronite, hectotite, sponite, and sauconite.

Sodium-montmorillonite (Na-MMT) is one of the main components of smectite minerals. The mineral consists of a tetrahedral-octahedral-tetrahedral (T-O-T) structure in which the oxygen atoms situated in the tetrahedral sheets share with the octahedral sheet as shown in Figure 2.4.

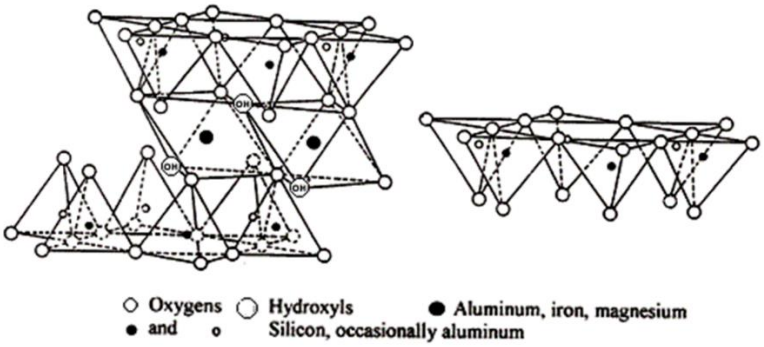

Figure 2.4. Montmorillonite structure (Grim, 1968, as cited by Mitchell, 1993).

The smectite layers are continuous in the horizontal (a-b) axes and stacked one above another in the vertical axis (c). The basal spacing, which is the sum of one clay sheet and interlayer spacing in the vertical direction, varies from 9.60 Å in dry case to complete separation upon saturation [4]. Furthermore, Figure 2.5 shows the dimensions of the unit cell (a=5.15 Å and b=8.90 Å).

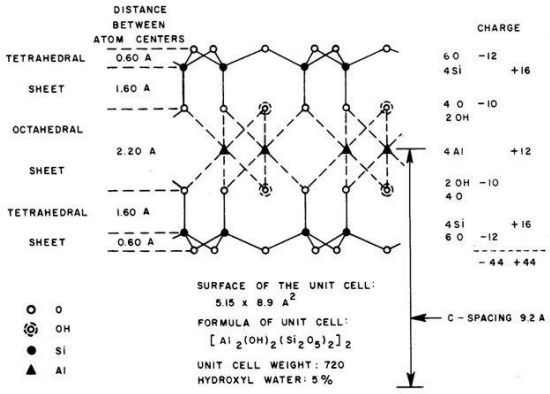

Figure 2.5. Atomic arrangement of the unit cell of 2:1 clay mineral (Van Olphen, 1979).

2.2. Polarity and Dielectric Constant

Dielectric constant has an important role to characterize the various solvents. It is a dimensionless constant and also known as relative permittivity. Dielectric constant is defined as a ratio of the electric field strength in vacuum to that in the material for the same applied potential charge. Dielectric constant can be measured experimentally when the solvent is placed

between two parallel charged plates while monitoring the electric field strength (E). This electric field strength (E) is lower than the electric field in vacuum (E_o). The value of E_o/E provides delectric constant value. When the molecules inserted between parallel plates have a dipole moment, these molecules in the presence of the electric field are forced to an ordered arrangement. This arrangement is known as polarization.

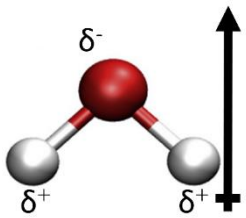

Figure 2.6. Schematic diagram showing dipole moment of water.

The dipole moment is a directional force, which results because of an asymmetrical distribution of charge between atoms within a molecule. In a neutral molecule, the negative charge is balanced by positive charge, but the partial charge is developed in the atom due to difference in electronegativity between two chemically bonded atoms. For example, one oxygen atom is covalently bonded with two hydrogen atoms in a water molecule. The cloud of the shared electrons tend to stay more towards oxygen atom due to high electronegativity, and thus a slightly negative charge is developed in oxygen atom, whereas the positive charge is developed on hydrogen atom. Therefore, a dipole moment in a water molecule is developed as a result of this uneven distribution of charge. Mathematically, a dipole moment is the product of the magnitude of charges and the distance between the centers of the charges. When two charges, q_1 and q_2, are separated by a distance l, then the dipole (μ) = q_1. q_2.l. Also, higher the dipole moment, higher the polarization, which results in reduction of the electric field strength. Therefore, the molecules with high dipole moment have high dielectric constant. Furthermore,

the dipole moment is a measure of the polarity of the molecule. And the dielectric constant of the solvents is a relative measurement of the polarity.

2.3. Kerogen

Oils shale is defined as a fine-grained sedimentary rock that comprises minerals and organic matter. It yields a significant amount of oil when heating at high temperature in the absence of oxygen [9]. The organic matter in oil shale includes kerogen and bitumen. One of the main differences between oil shale and shale oil is that the large pockets of shale oil is locked between rocks. The fracking method is used to extract these large pockets of oil in shale oil. Kerogen, the organic component of oil shale, is the most abundant form of hydrocarbon and precursor of crude oil. Kerogen is finely dispersed in oil shale, and it is a big macromolecule originated from the insoluble organic component such as algae [10].

The Green River Formation was formed about 54 million years ago [11]. This formation has a very rich deposition of oil shale due to the marine lakes. Kerogen in the Green River Formation is originated from cyanobacteria or microalgae that is also referred as blue-green algae [12]. This algae can live in water and use the photosynthesis method to produce its own food. The pigment phycocyanin gives these algae the appearance of blue color.

Oil Shale contains about 86.20% mineral matter and 13.80% organic matter [10]. Furthermore, dolomite and calcite, feldspar, and Montmorillonite are predominated minerals. Organic matter contains 11.04% kerogen and 2.76% bitumen. The overall composition of the Green River oil shale is presented in Table 2.1.

The formation of matured kerogen happens in three stages. The first sage is known as diagenesis, which is the process of sedimentation and consolidation occurred at a depth of 1500 meters. In this stage, a large amount of oxygen from kerogen converts to carbon dioxide and

water [13]. The second stage includes the maturation of organic carbon as the temperature and pressure increases at a depth of 3000 meters [14]. This stage is also knowns as catagenesis. The third stage is called metagenesis in which kerogen matures with a low hydrogen to carbon ratio. In this stage, kerogen becomes amorphous while changing from random molecule to more structure and rings [15].

Table 2.1. The composition of Green River oil shale by weight [Yen, 1975].

Mineral matter 86.20%	Pyrite (FeS_2)			0.86%
	Analcite ($NaAlSi_2O_6*H_2O$)			4.30%
	Quartz (SiO_2)			8.60%
	Montmorillonite $[Na_{0.2}Ca_{0.1}Al_2Si_4O_{10}(OH)_2(H2O)_{10}]$			12.90%
	K-feldspar ($KAlSi_3O_8$)			16.40%
	Dolomite and Calcite ($CaMg(CO3)_2$)	43.10%	O	22.20%
			Ca	9.50%
			Mg	5.80%
			C	5.60%
Organic matter 13.80%	Bitumen	2.76%	S,N,O	1.28%
			H	1.42%
	Kerogen	11.04%	C	11.10%

2.3.1. Composition of Kerogen Structure

Oil shale in the Green River Formation is very young, which is also in the early stage of maturation. Furthermore, oxygen atoms are found either in for form of acid or ester group [16]. Kerogen has hydrogen, oxygen, carbon, nitrogen, and sulphur. Depending up on the on the hydrogen, carbon, and oxygen content, kerogen is classified as Type I, Type II, and Type III [17]. Green River oil shale is a Type I kerogen, as the hydrogen to carbon ratio is greater than 1.25 and oxygen to carbon ratio is less than 0.15 [18].

The predominant structural unit of kerogen is hydrocarbon with straight chains, rings, and heterocyclic structures. Furthermore, the Green River kerogen has 2% alkanes, 2% branched alkanes, 34% cycloalkanes with 1 to 6 rings, 15% aromatic compounds with 1 to 2 rings, and 47% heterocyclic compounds [10]. Figure 2.7 shows the representative two-dimensional (2D) kerogen structure of Green River oil shale developed by Siskin using mass spectroscopy and nuclear magnetic resonance (NMR) spectroscopy analysis [19].

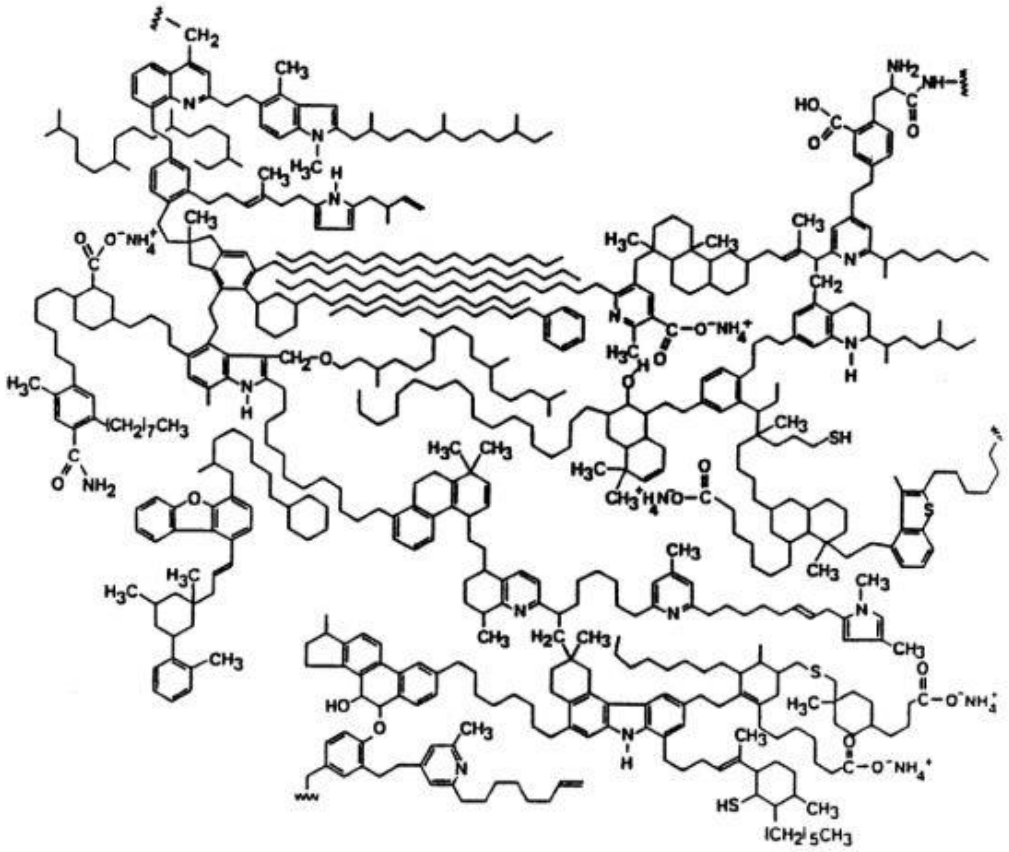

Figure 2.7. Most complete model of the Green River kerogen molecule (Snape, 1995).

2.3.2. Experimental and Molecular Modeling Literature Review

Various characterization techniques are used to evaluate the structure of kerogen. The microstructures captured using scanning electron microscopy of oil shale showed that the organic matter is finely dispersed in thin layers in oil shales from Germany [20]. Furthermore, the SEM

images on in situ oil shale showed that no large pockets of kerogen are observed even at a scale of 200 nm [21]. Thus, the size of kerogen is found in the order of tens of nanometers as shown in Figure 2.8. Two types of oil shale samples, dark and light colored, are used form the Green River oil shale, and it is found that the light samples possess more kerogen than that of dark samples. Since kerogen is finely dispersed with the mineral, there is a significant nonbonded interactions between kerogen and minerals.

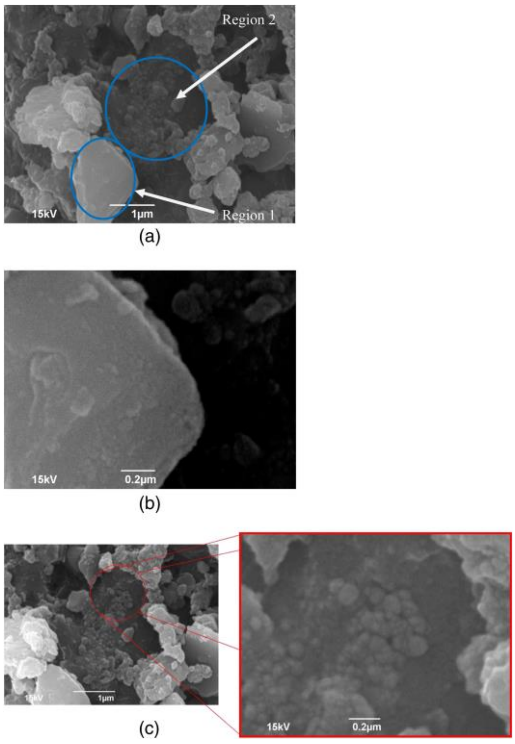

Figure 2.8. Dark-colored oil shale samples (a) at a scale of 1 μm, (b) Region 1, and (c) Region 2 showing the nanoscale kerogen pockets in Green River oil shale (Alstadt et al. 2015).

Furthermore, the spectroscopy study has been carried out to identify structural changes to kerogen because of the kerogen–mineral interactions of in situ oil shale from the Green River Formation. Extensive photoacoustic FTIR experiments on in situ Green River oil shale have been performed [22]. It is found that there are significant kerogen-minerals molecular interactions in oil shale, and these interactions are mainly non-bonded interactions. The band shifts are observed in the spectra between isolated kerogen [23] and kerogen from oil shale. This result also

indicates that the there is a significant molecular interaction between kerogen and mineral matrix. Furthermore, FTIR experiments on light and dark colored oil shale samples, as shown in Figure 2.9, reveal that the light region of shale samples have spectra similar to isolated kerogen form the Green River oil shale found in literature [23].

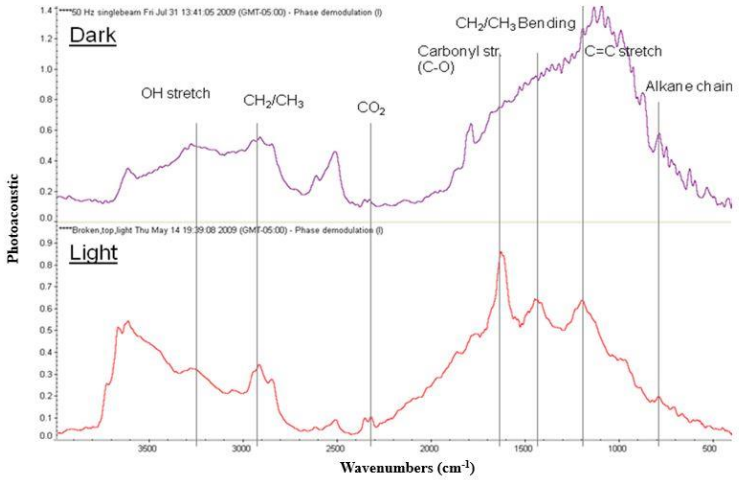

Figure 2.9. The kerogen bands are observed. The spectra of the light and dark colored oil shale samples parallel to the bedding plane (Alstadt et al. 2012).

It has been found that kerogen has isotropic mechanical properties, which means the elastic properties are the same in all directions as well as independent of the directions of compression and bedding plane. The nanomechanical properties—elastic modulus and hardness—of oil shale are very essential. These properties can mimic the pressure experienced by kerogen during the sedimentation process, which would potentially play a significant role in the extraction of oil from oil shale [24]. Kerogen from Bazhenov Formation oil shale has young's modulus value of 10-15 GPa and hardness of 0.57 GPa [25]. Additionally, the modulus of kerogen was found to be in the range of 5– 11 GPa and hardness of 0.9 – 1.3 GPa [21]. Steps of about 5 nm are found on loading plot of load-displacement plot as shown in Figure 2.10. The horizontal nature of these steps suggest that kerogen is finely dispersed on the scale of tens of nanometers in the mineral matrix.

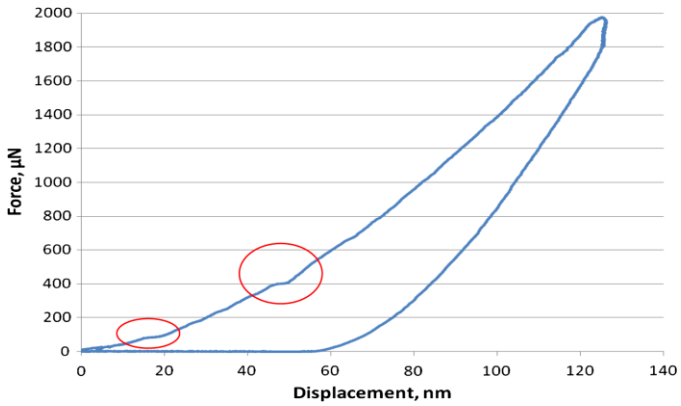

Figure 2.10. Two steps on the loading curve of light-colored oil shale sample showing the soft regions (Alstadt et al. 2015).

The structure of kerogen is complex, and the moieties that small fragment of kerogen molecules have been identified in Green River oil shale [26]. The interactions of these moieties with the minerals have been studied [27]. Molecular dynamics as well as FTIR studies are accomplished to evaluate the molecular interactions of one of the clay minerals, Na-montmorillonite, with three kerogen moieties primarily pyridine, heptylamine, and quinaldine [28]. It has been found that there are significant nonbonded interactions between clay and the kerogen moieties. The extraction and mechanism of these kerogen moieties from the silica surface have also been studied using molecular dynamics simulation [29].

A 3D Green River kerogen model is developed using ab initio and molecular mechanics computations from Siskin's 2D structure [30]. The fundamental 3D kerogen structure is initially obtained [31], but there is no simulations on it. In this dissertation, the molecular model of 3D of Green River kerogen is developed based on 2D Siskin structure and CHARMM compatible force field parameters, mimicking the real kerogen structure in the Green River Formation.

2.4. Molecular Dynamics

Molecular dynamics (MD) is a computational simulation technique, which is used to model atomic scale dynamic of a system. In this method, the trajectory that describes the positions and velocities can be evaluated based on classical mechanics. MD simulations work based on the Newton's second law of motion. A trajectory of atoms that describes the positions, velocities, and accelerations over time can be obtained ("Tutorial-Molecular Dynamics Simulation-CHARMM," 1999).The force on each atom for a simple systems with different atoms can be written as:

$$F_i = m_i a_i = m_i \frac{d^2 r_i}{dt^2} \tag{2.1}$$

where F_i is the force acting on the particle i, m_i is the mass, and a_i is the acceleration of particle over time t. Furthermore, the force on each atom is given by the change in energy, E, of the atom with respect the position vector, r_i. Therefore, the differential equation representing Newton's second law of motion can written as:

$$-\frac{dE}{dr_i} = F_i \tag{2.2}$$

Combining equation 2.1 and 2.2:

$$-\frac{dE}{dr_i} = m_i \frac{d^2 r_i}{dt^2} \tag{2.3}$$

The acceleration and velocity of an atom can be expressed as:

$$a_i = \frac{dv_i}{dt} \tag{2.4}$$

Therefore, integrating equation 2.4 gives the velocity of atom i.

$$v_i = a_i t + v_o \tag{2.5}$$

Here, v_o is the integration constant at t=0

Again, the velocity of each atom is the rate of change of displacement that is expressed as:

$$v_i = \frac{dr_i}{dt} \tag{2.6}$$

Integrating equation 2.6 provides the position of atom over time t.

$$r_i = v_i t + r_o \tag{2.7}$$

Therefore, a trajectory that represents the position and velocity of atom in a molecular system can be calculated using initial position of the atoms. The initial positions of the atoms required for the simulation can be acquired from experimental techniques such as x-ray crystallography ("Tutorial-Molecular Dynamics Simulation-CHARMM," 1999). This means the motion of atoms is deterministic. Furthermore, the trajectory can be used to determine the molecular structure, dynamics and thermodynamic properties of the system.

2.4.1. Force Field

Furthermore, the potential energy function of the system is described by a force field. A molecule has a series of atoms, and atoms are modeled as charged point bonded by a spring. A force field is defined as the time evolution of bond lengths, bond angles, and torsions, van der Waals, and electrostatic interactions among atoms. Force field has two sets of equations, which describe bonded and nonbonded interactions.

$$E = E_{Bond} + E_{Angle} + E_{Dihedral} + E_{van\ der\ Waals} + E_{Electrostatic} \tag{2.8}$$

The bonded interactions include the bond distances, bond angles, and torsion angle; where as nonbonded interactions are van der Waals and electrostatic interactions between atoms. In our simulations, CHARMM (Chemistry at Harvard Macromolecular mechanics) force field parameter have been used [32]. This force field is widely used to predict various properties such as structures, binding and conformation energies, of protein, large macromolecules, and organic molecules. The potential equation of CHARMM force field is given by:

$$E = \sum_{Bond} k_b(r - r_0)^2 + \sum_{Angle} k_\theta(\theta - \theta_0)^2 + \sum_{Dihedral} k_\varphi \quad [1 + \cos(n\varphi + \delta)] + \sum_{van\ der\ Waals} 4\varepsilon_{ij}\left[\left(\frac{\sigma_{ij}}{r_{ij}}\right)^{12} - \left(\frac{\sigma_{ij}}{r_{ij}}\right)^{6}\right] + \sum_{Electrostatic} \frac{q_i q_j}{r_{ij}} \qquad (2.9)$$

where, k_b is force constant of bonds, k_θ is force constant of angles, and k_Φ is dihedral force constant, r_0 is equilibrium bond length, θ_o is equilibrium bond angle. Similarly, n, Φ and δ are the dihedral angles, a multiplicity of dihedral angle or periodicity of the Fourier term, and phase angle of the dihedral cosine function, respectively. The Lennard-Jones or 6-12 potential parameters are represented as σij (distance at which the intermolecular potential between the two particles is zero) and εij (the well depth and a measure of how strongly the two particles attract each other). The distance between nonbonded pairs of atoms i and j separated rij distance, and the partial charges of atoms are denoted by q_i and q_j. For nonbonded interactions, electrostatic and van der Waals, $i \neq j$. Van der walls repulsive force becomes strong when the atoms apart at close range, and the attractive force predominates at long range. In another words, if the distance between a pair atoms is approximately the sum of the van der Waals radii, which are the effective size atoms) then the maximum interaction is obtained. However, the repulsive iteration dominates the attractive interaction as the distance decreases.

2.4.2. Electrostatic Interactions

Electrostatic energy is based on the Coulomb potential energy. The electrostatic energy between two interacting atoms is directly proportional to the partial charges on atoms and inversely proportion to the distance between atoms.

2.4.3. Van der Waals Interactions

The van der Waals (VDW) interaction energy provides one of the major nonbonded interactions between two interacting atoms as presented in equation 2.9. This equation represents that the van der Walls energy depends on the distance between two interacting atoms. A typical

plot of the relationship between the van der Waals energy and distance is shown in Figure 2.11. This plot shows that van der Waals energy between two atoms becomes zero at a particular distance (σ) where the attractive energy is balanced by repulsive energy, and this distance is termed as van der Waals radius, which is represented by σ_{ij} in equation 2.9. If the distance between these two atoms is less than the sum of the contact radii, the repulsive energy predominates. As the distance between two atoms increased beyond this van der Waals radius, van der Waals energy is negative and becomes the smallest in magnitude(indicating two force between atoms). At this point, the pair of interacting atoms achieves the most stable condition. The stable energy is represented by ε_{ij} in equation 2.9. Furthermore, at long-range distances, the negative interaction energy continues to decrease and becomes asymptotic in nature.

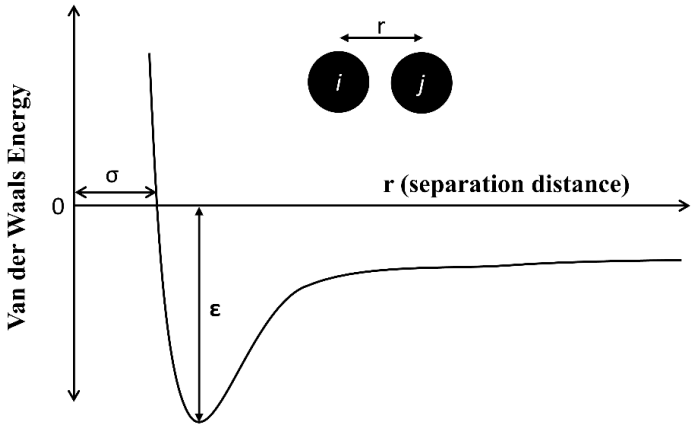

Figure 2.11. Schematic of Lennard-Jones pair potential between two atoms separated by a distance r.

2.5. Steered Molecular Dynamics

Steered molecular dynamics (SMD) simulation technique in which external force is applied to atom or group of atoms to a certain degree of freedom to guide a system from one state to another state [33]. SMD has been extensively used to study the binding/unbinding mechanism and elastic properties of molecules. There are two types of SMD: constant-force

method and constant-velocity method. In constant-force SMD, constant force is applied to selected atoms in a given direction where the typical range of external force would be picoNewtons (pN) [34]. On the other hand, in constant-velocity SMD, one end of the molecule is fixed and other end is pulled with a constant velocity. In constant velocity SMD, the harmonic potential restrains an atom or center of mass of group of atoms to a point in space. This restrained atom is referred as SMD atom or dummy atom, which is connected to the corresponding atom or group of atom using a virtual spring with finite spring constant. The force exerted on the pulling atoms using constant velocity method is as follows:

$$F = K\ (x_o + vt - x) \tag{2.10}$$

Where, K is force constant, v is constant pulling velocity, x_o is the initial position, and x is the position at time t of the end attached to SMD atom.

2.6. Literature Review on Clay-Fluid Interactions using MD and SMD Simulations

MD simulations have been extensively used to evaluate the swelling mechanism of expansive clays [35-37]. Montmorillonite swells when mixed with water, and this behavior where the clay minerals undergo high volume change is known as swelling. There are two types of swelling behaviors: crystalline swelling and osmotic swelling [38]. Crystalline swelling refers to the initial stage or short-range swelling where the water molecules enter the interlayer and trigger swelling. The basal spacing in crystalline swelling ranges from 9-20 Å [39]. Osmotic swelling is the continuous process of crystalline swelling where the basal spacing is over 20 Å, resulting in stacking of layers of water molecules between the clay sheets in the interlayer [40]. The swelling of cesium-montmorillonite with one layer and two layers of hydration where the basal spacing ranged from 12 to 18.5 Å. The influence of water content on swelling was reported [41]. The effect of cations—sodium and calcium—in the Na-MMT clay interlayer has been

studied [42]. The role of different water molecular models and interlayer cations of swelling clay minerals has been studied using MD simulations [43].

The first SMD on dry and hydrated sodium montmorillonite was developed by Katti's research group [44]. The stress-strain behavior of pyrophyllite was studied using constant-force SMD. The interlayer spacing deformed upon externally applied stresses in pyrophyllite, whereas the clay sheet remained fairly rigid [45]. Furthermore, SMD simulations were used to evaluate the mechanical properties of dry Na-MMT clay and Na-MMT with various level of hydration. In this study, the CHARMM force field parameters were derived based on consistent force filed (CFF) force filed parameter of MMT. The results showed that the behavior of interlayer spacing changed from liner to nonlinear with the addition of water content in the interlayer, and the interlayer moduli of the clay interlayer were computed from the stress-strain plot as shown in Figure 2.13 [46]. The major factors that influence the interlayer spacing and interlayer modulus are the level of fluid content in the interlayer, solvation of the interlayer cations, and interactions between the clay and fluids [44, 47, 48]. Also, the density of the interlayer water was found to be higher than the density of water with one monolayer of water molecules in the interlayer. However, the two and three monolayers of water in the interlayer mimicked the density of bulk water.

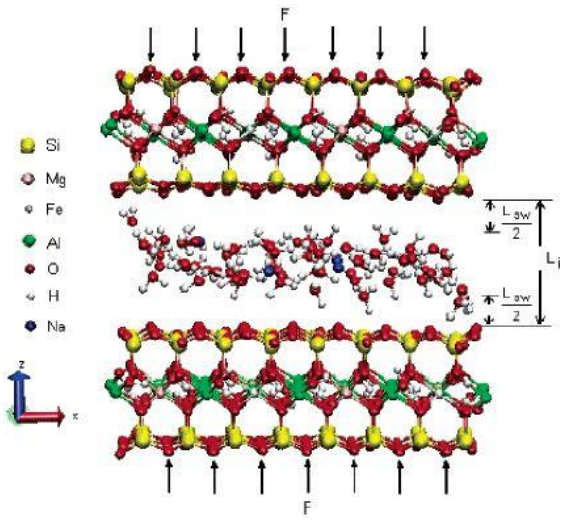

Figure 2.12. Na-MMT model with two layers of water (Katti et al. 2005).

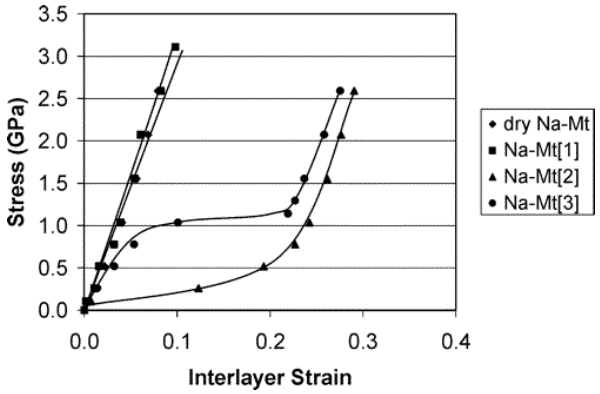

Figure 2.13. Stress-strain plot of Na-MMT with water content in the interlayer (Katti et al. 2005).

Furthermore, the crystalline swelling mechanism has been studied using MD simulation. The interactions sodium cations that attract the water molecules into the clay interlayer, and these interactions are very strong, resulting in the interlayer swelling. The attractive interactions between sodium cations and water molecules resulted in the formation of solvation shell around the sodium cations as shown in Figure 2.14 [49]. This well-organized shell formation reduced the attractive interaction between clay sheets and sodium ions, resulting in crystalline swelling and exfoliation of clay sheets.

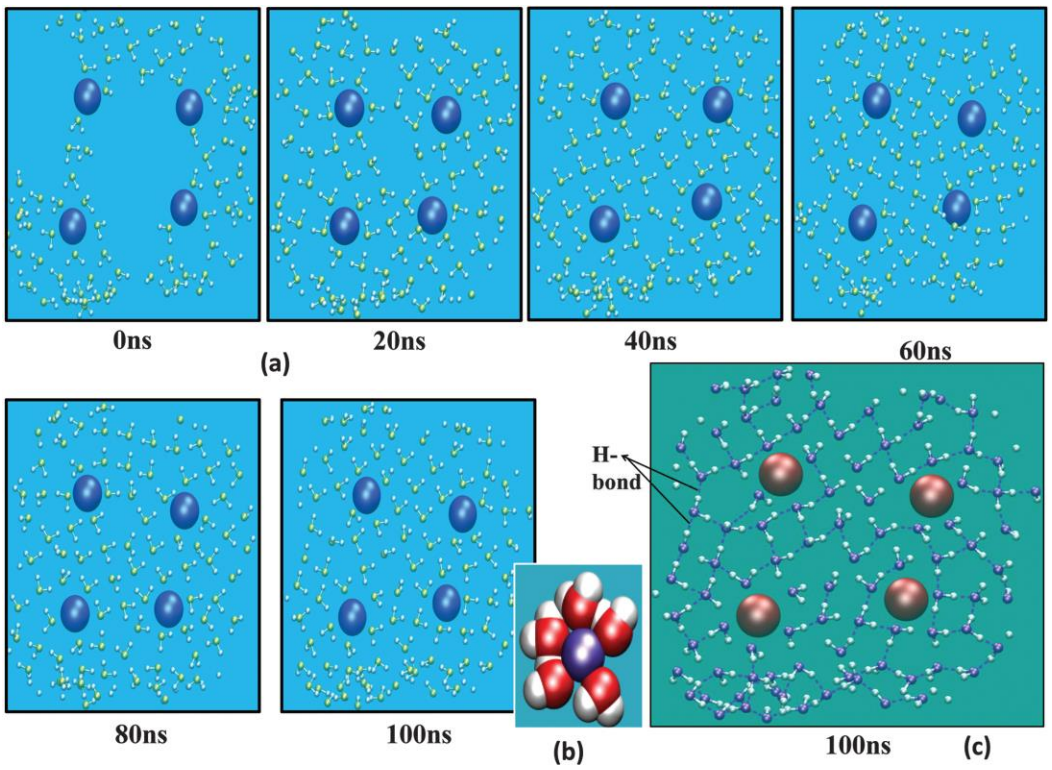

Figure 2.14. (a) Water molecules and sodium at different simulation time, (b) shell formation, and (c) oxygen atoms of water molecules pointing towards sodium ions (Katti et al. 2015).

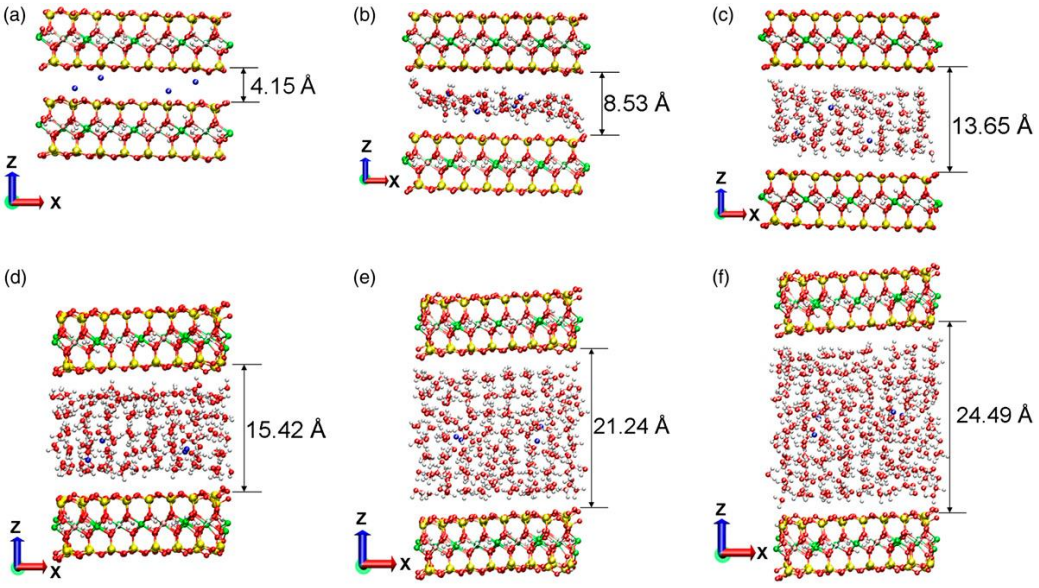

Figure 2.15. Na-MMT clay with different levels of interlayer hydration (Pradhan et al. 2015).

Also, the attractive interactions between clay sheets and sodium interlayer cations maintained the stability of dry clay as well as hydrated clay at various level of hydration as

shown in Figure 2.15, but these interactions decreased significantly upon adding water molecules in the interlayer, causing exfoliation and particle breakdown of swelling clays [50].

Unless the nature of nonbonded interactions of Na-MMT clay with various organics fluids that are commonly found in the landfill leachates and toxic to human health are well understood, the detrimental effects of swelling clays on infrastructures cannot be avoided. Thus, it is essential for the understanding of the swelling mechanisms, evaluating the interactions occurring on the molecular scale, evolution of important engineering properties such as microstructure, swelling pressure, permeability, and consolidation of swelling clay. Therefore, these clays can be effectively used in geoenvironmental applications, geotechnical engineering, and industrial applications.

2.7. Experimental Techniques

2.7.1. Swelling and Swelling Pressure

The correlation between the level of swelling, swelling pressure, and evolution of the microstructure has been carried [51]. A new controlled uniaxial swelling (CUS) is designed in our previous work as shown in Figure 2.16. This CUS device allows the confined sample to saturate in without bulging. Furthermore, this device permits the saturated sample to swells in uniaxial direction, and the device can be easily split vertically to remove the sample. The movable piston, which is also called the connecting rod as shown in Figure 2.16, moves vertically upwards when the swelling pressure is developed upon saturation.

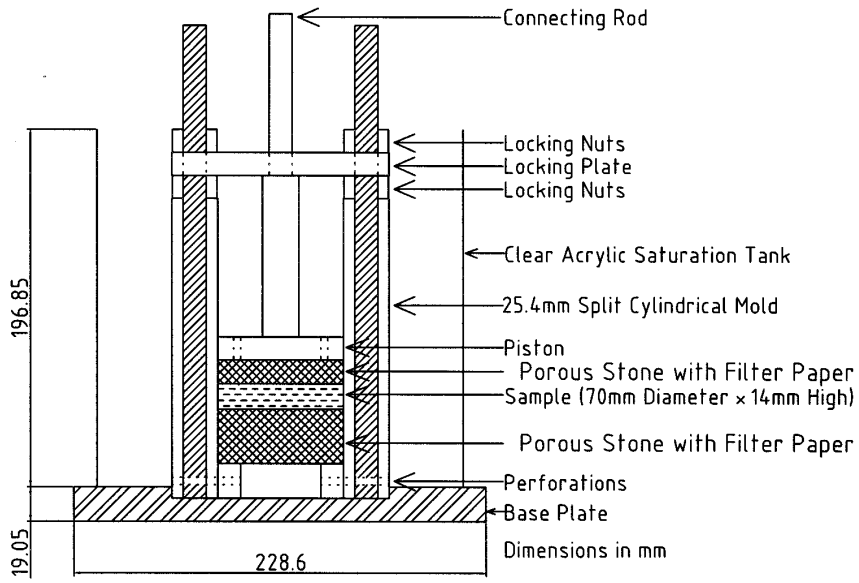

Figure 2.16. A schematic diagram showing the CUS device (Katti and Shanmugasundaram, 2001).

Figure 2.17 shows increase in swelling pressure over time during saturation at no volume change condition, which is known as 0% swelling. It is observed that the swelling pressure rapidly increases to about 120 kPa in one day. The swelling pressure gradually increases within 10 days, and it reached to about 163 kPa and remained constant after 21 days. The sample was removed from the CUS device, and it is found that the degree of saturation is 100%. Therefore, based on this experiments, it is proposed that the minimum time to saturate swelling clay mineral, bentonite this case, is 30 days.

The influence of swelling on swelling pressure, the saturated samples are further allowed to swell to the predermined level of swelling in uniaxial direction. Figure 2.18 shows the decrease in swelling pressure with increased in swelling level. The maximum swelling pressure is observed at 0% swelling.

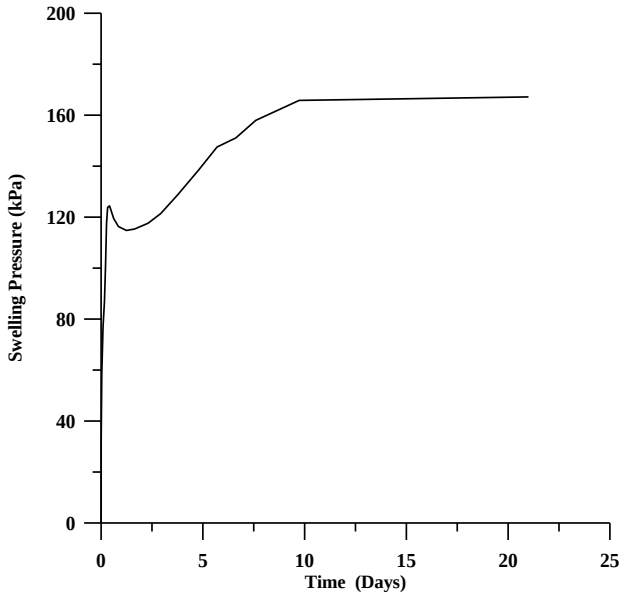

Figure 2.17. Swelling pressure over time from dry state to a complete saturation (Katti and Shanmugasundaram, 2001).

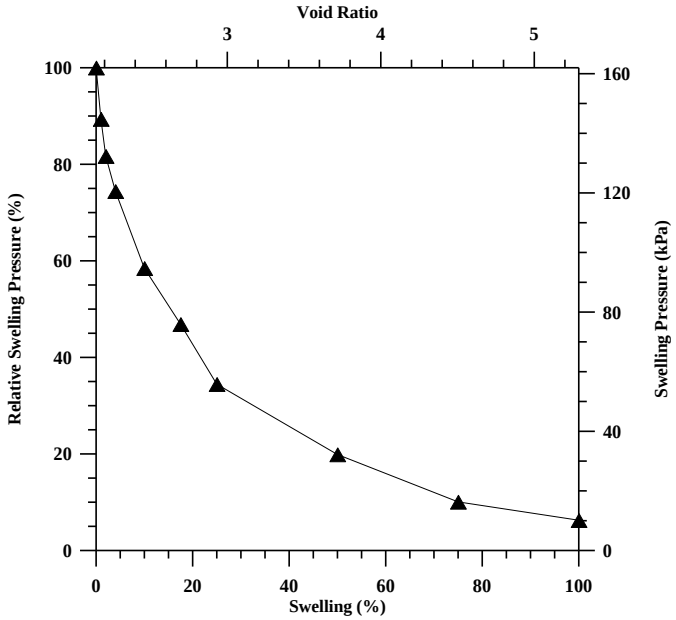

Figure 2.18. Swelling pressure and void ratio at different level of swelling (Katti and Shanmugasundaram, 2001).

2.7.2. Fourier Transform Infrared (FTIR) Spectroscopy

Fourier transform infrared (FTIR) spectroscopy is a powerful nondestructive technique used for determining the structure of the sample, symmetry, functional groups, and hydrogen-

bonding [52]. FTIR provides the distinct infrared absorption spectrum that can be compared as a molecular fingerprint. When the sample material is subjected to infrared radiation, the frequencies and intensities of radiation that is emitted, reflected, or absorbed by the sample can be measured. Furthermore, the interactions of infrared light with the samples are energy absorption process. The total energy of the molecular system exposed to electromagnetic radiation possesses rotational, vibrational, electronic and transitional energy.

$$E = E_{Rotational} + E_{Vibrational} + E_{Electronic} + E_{Translational} \quad (2.11)$$

here, $E_{Rotational}$ is due to the rotation of the molecules, $E_{Vibrational}$ is due to vibration of atoms, $E_{Electronic}$ is due to electrons movements, and $E_{Translational}$ is due to transition of molecules. Among these four energues, IR spectroscopy measures the vibration energy of molecules. A typical range of vibration energy falls from 10^2 cm^{-1} to 10^4 cm^{-1} [53]. For a molecule to absorb electromagnetic radiation, molecule should have the same vibrational energy as that of electromagnetic radiation. Furthermore, the direction of the dipole moment of the molecule should be changed. Hence, these molecules are referred as IR active molecules and further studied using infrared spectroscopy. The intensity of absorption or emission is controlled by the degree of change in dipole moments. The electromagnetic theory states that the intensity of the absorption or emission is proportional to the square root of change of the dipole moment. The intensity of absorption or emission.

$$I_k = A\left(\frac{\partial \mu_d}{\partial x}\right)^2 \quad (2.12)$$

here, μ_d is the dipole moment, and x is the displacement at equilibrium.

The main components of an FTIR spectrometer are: source of electromagnetic radiation, Michelson Interferometer, sample compartment, and the detector. A schematic diagram that represents the Michelson interferometer is shown in Figure 2.19. The interferometer has a beam

splitter, fixed mirror, and a moving mirror. When the IR beam from the IR source strikes the beam splitter, which is made of KBr, the IR beam splits into two beams. One half of the beam transmits through the beam splitter, whereas the other half of the beam reflects off from the beam splitter. Therefore, the reflected beam strikes the fixed mirror, and transmitted beam strikes the movable mirror. As these two beams are reflected by the fixed and movable mirrors, two beams again meet and combine each other at the beam splitter, resulting in the formation of constructive and destructive interference depending upon the position of the movable mirror. Thus, the resulted beam is translated by a mathematical transformation that is known as Fourier transformation and gives intensity-frequency spectrum.

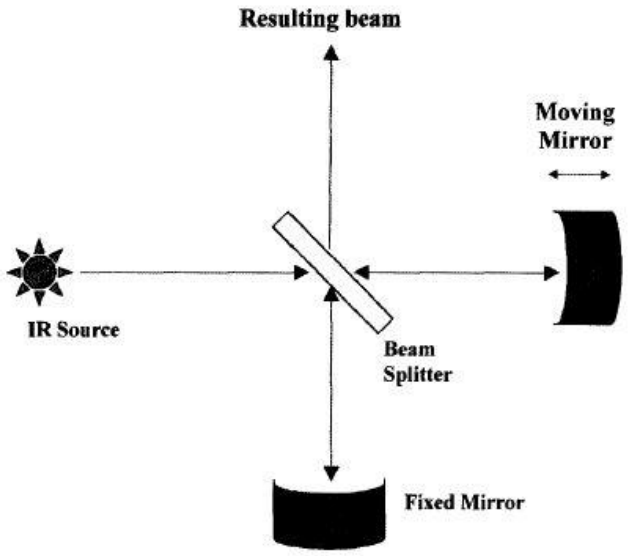

Figure 2.19. Schematic showing Michelson Interferometer (Amarasinghe, 2009).

2.7.3. Nanoindentation

The nanoindentation is an experimental technique to measure the mechanical properties of the materials at the molecular level. The frequently measured two mechanical properties are the elastic modulus (E) and the hardness (H). In nanoindentation, a depth sensing diamond

indenter is allowed to press the sample at a specific load in which the contact area is determined from the measured depth of penetration of the indenter and geometry of the tip indenter [54]. The load-displacement data are recorded from one complete loading and unloading cycle as shown in Figure 2.20. The withdrawn of the indenter results in recovering the elastic deformation, and certain displacement remains as the plastic deformation. The displacement during unloading is typically elastic in nature, and the initial portion of the unloading curve is used for the analysis. The indenter tip is made up of diamond that has high resistance to deformations. Three components of load-displacement curve: maximum load (P_{max}), maximum displacement (h_{max}), and stiffness (S) during unloading.

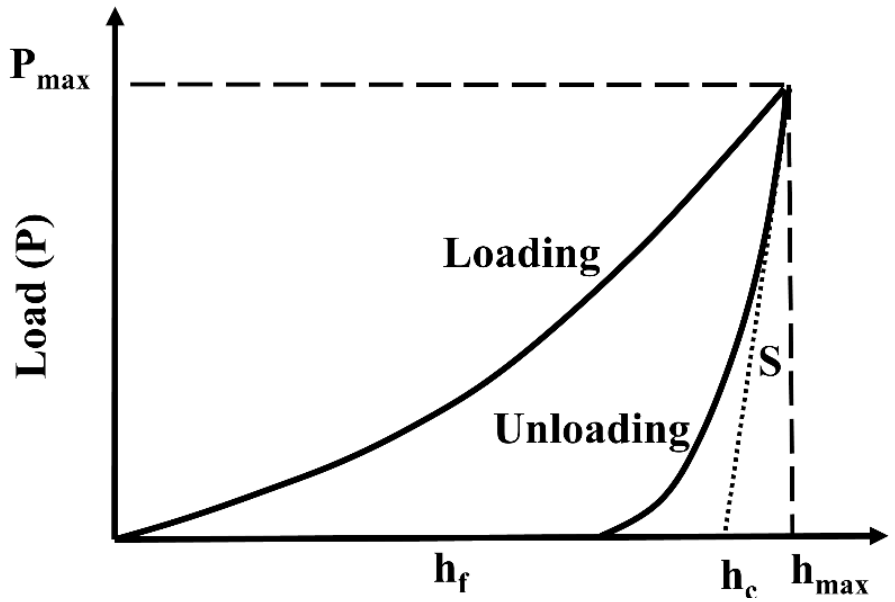

Figure 2.20. A typical load-displacement curve for a completer loading and unloading cycle.

The elastic stiffness is also known as contact stiffness, which is the slope of the beginning portion of unloading curve. The elastic modulus of the specimen is determined by calculating the stiffness and contact area from the load-displacement curve. The unloading curve for the measurement of stiffness is non-liner, and it described by power law relation:

$$P = B(h - h_f)^m \tag{2.13}$$

where the constants B and m are determined by empirically using fitting parameters. The slope of initial unloading curve, which is stiffness, is obtained by differentiating above equation:

$$S = \left(\frac{dP}{dh}\right)_{h=h_{max}} \tag{2.14}$$

$$S = Bm(h_{max} - h_f)^{m-1} \tag{2.15}$$

The reduced modulus and the stiffness are related by

$$\mathrm{S} = \frac{2}{\sqrt{\pi}}\sqrt{A}\,\mathrm{E_r} \tag{2.16}$$

In addition, the tip area function depends on the geometry of the indenter. Indirect measurement of contact area between the tip and the sample is carried out by measuring the penetration depth and known geometry of the indenter. Prior to each indentation test, area function is calculated by indenting on standard sample such as fused quartz. For a Berkovich indenter, a three-sided pyramid with radius on the order of 50-100 nm, the projected area of the tip (A) at the contact depth (h_c) is described by polynomial equation:

$$A(h_c) = C_0{h_c}^2 + C_1h_c + C_2{h_c}^{1/2} + C_3{h_c}^{1/4} + \cdots + C_8{h_c}^{1/128} \tag{2.17}$$

Where C_1 through C_8 are constants and C_0=24.5. The first term, C_0, represents the ideal Berkovich indenter, and the other terms define the deviations from the Berkovich geometry because of tip blunting. The contact depth as shown in Fig. 2 is determined by:

$$h_{max} = h_c + h_s \tag{2.18}$$

$$h_c = h_{max} - h_s \tag{2.19}$$

where h_s is the vertical depth of the contact periphery and given by:

$$h_s = \varepsilon\frac{P_{max}}{S} \tag{2.20}$$

where ε =0.75 for Berkovich indenter.

Furthermore, Hardness (H) is defined as the resistance of the material to plastic deformation. It is also known as the mean pressure that the material supports when load is applied. It is calculated by dividing the peak load (P_{max}) by the projected contact area (A):

$$H = \frac{P_{max}}{A(h_c)} \tag{2.21}$$

The Hardness and the reduced modulus were determined by using Oliver and Pharr method [55]. In this method, unloading segment of the curve was described by a power-law function, and the contact area was obtained. The initial displacement segment of unloading curve was typically elastic, and the contact stiffness was calculated by differentiating the power-law relation. The indenter tip and the sample experienced elastic deformation, and the elastic modulus of each specimen was further calculated considering deformation of both of them. The relationship between the reduced modulus and the elastic modulus is as follows:

$$\frac{1}{E_r} = \frac{1-\nu^2}{E} + \frac{1-\nu_i^2}{E_i} \tag{2.22}$$

Where E_r= reduced elastic modulus, E=elastic modulus of the sample, E_i=elastic modulus of the indenter, ν=Poisson's ratio of the sample, and ν_i=Poisson's ratio of the indenter. For diamond indenter tip, the elastic modulus of 1141 GPa and Poisson's ration of 0.07 were used [55]. Poisson's ratio of 0.255 was used for Na-MMT samples [56].

2.8. References

[1] R.E. Grim, Clay mineralogy, Mcgraw-Hill Book Company, Inc, New York (1953).

[2] W.F. Bleam, Atomic theories of phyllosilicates - quantum-chemistry, statistical-mechanics, electrostatic theory, and crystal-chemistry, Reviews of Geophysics 31(1) (1993) 51-73.

[3] B. Velde, Use of the smectite to illite conversion reaction model - effects of order of magnitude, Bulletin Des Centres De Recherches Exploration-Production Elf Aquitaine 19(1) (1995) 235-242.

[4] J.K. Mitchell, K. Soga, Fundamentals of soil behavior, NJ: John Wiley & Sons (2005).

[5] P.W. Birkeland, Soils and geomorphology, New York Oxford University Press (1999).

[6] K. Cornelis, B. Dutrow, Manual of mineral science, John Wiley & Sons, Inc, (2007).

[7] J.J. Fripiat, H. Van Olphen, S. Clay Minerals, D. Organisation for economic co-operation and, Data handbook for clay materials and other non-metallic minerals : providing those involved in clay research and industrial application with sets of authoriative data describing the physical and chemical properties and mineralogical composition of the available reference materials, Pergamon Press, Oxford, New York, (1979).

[8] H. Van Olphen, An introduction to clay colloid chemistry: for clay technologists, geologists, and soil scientists, 2nd edition, Wiley, New York, (1977).

[9] B. Hascakir, T. Babadagli, S. Akin, Experimental and Numerical Simulation of Oil Recovery from Oil Shales by Electrical Heating, Energy & Fuels 22(6) (2008) 3976-3985.

[10] T.F. Yen, G.V. Chilingarian, Oil shale, (1976).

[11] W.C. Clyde, J. Stamatakos, J.P. Gonneveld, G.F. Gunnell, W.S. Bartels, Timing of the wasatchian-bridgerian (early-middle eocene) faunal transition in the green river basin, Wyoming, Journal of Vertebrate Paleontology 15 (1995) 24A-24A.

[12] U. Lille, Current knowledge on the origin and structure of Estonian kukersite kerogen, Oil Shale 20(3) (2003) 253-263.

[13] B. Durand, Diagenetic modification of kerogens, Philosophical Transactions of the Royal Society a-Mathematical Physical and Engineering Sciences 315(1531) (1985) 77-90.

[14] M. Siskin, A.R. Katritzky, Reactivity of organic-compounds in hot water - geochemical and technological implications, Science 254(5029) (1991) 231-237.

[15] M. Vandenbroucke, C. Largeau, Kerogen origin, evolution and structure, Organic Geochemistry 38(5) (2007) 719-833.

[16] H.I. Petersen, P. Rosenberg, H.P. Nytoft, Oxygen groups in coals and alginite-rich kerogen revisited, International Journal of Coal Geology 74(2) (2008) 93-113.

[17] M. Razvigorova, T. Budinova, B. Tsyntsarski, B. Petrova, E. Ekinci, H. Atakul, The composition of acids in bitumen and in products from saponification of kerogen: Investigation of their role as connecting kerogen and mineral matrix, International Journal of Coal Geology 76(3) (2008) 243-249.

[18] G. Brons, M. Siskin, R.I. Botto, N. Guven, Quantitative mineral distribution in green river and rundle oil shales, Energy & Fuels 3(1) (1989) 85-88.

[19] M. Siskin, C.G. Scouten, K.D. Rose, T. Aczel, S.G. Colgrove, R.E. Pabst Jr, Detailed structural characterization of the organic material in rundle ramsay crossing and green river oil shales, composition, geochemistry and conversion of oil shales, Springer (1995) 143-158.

[20] E. Eseme, J.L. Urai, B.M. Krooss, R. Littke, Review of mechanical properties of oil shales: Implications for exploitation and basin modelling, Oil Shale 24(2) (2007) 159-174.

[21] K.N. Alstadt, K.S. Katti, D.R. Katti, Nanoscale morphology of kerogen and in situ nanomechanical properties of green river oil shale, Journal of Nanomechanics and Micromechanics 6(1) (2015) 1-10.

[22] K.N. Alstadt, D.R. Katti, K.S. Katti, An in situ FTIR step-scan photoacoustic investigation of kerogen and minerals in oil shale, Spectrochimica Acta Part a-Molecular and Biomolecular Spectroscopy 89 (2012) 105-113.

[23] W.E. Robinson, Isolation procedures for kerogens and associated soluble organic materials, Organic Geochemistry, Springer Berlin Heidelberg (1969) 181-195.

[24] J.C. Zeszotarski, R.R. Chromik, R.P. Vinci, M.C. Messmer, R. Michels, J.W. Larsen, Imaging and mechanical property measurements of kerogen via nanoindentation, Geochimica et Cosmochimica Acta 68(20) (2004) 4113-4119.

[25] R. Ahmadov, T. Vanorio, G. Mavko, Confocal laser scanning and atomic-force microscopy in estimation of elastic properties of the organic-rich bazhenov formation, The Leading Edge 28(1) (2009) 18-23.

[26] S. R. Kelemen, M. Afeworki, M. L. Gorbaty, M. Sansone, P. J. Kwiatek, C. C. Walters, H. Freund, M. Siskin, A. E. Bence, D. J. Curry, M. Solum, R. J. Pugmire, M. Vandenbroucke, M. Leblond, F. Behar, Direct characterization of kerogen by X-ray and solid-state 13C nuclear magnetic resonance methods, Energy & Fuels 21(3) (2007) 1548-1561

[27] M. Siskin, G. Brons, J.F. Payack, Disruption of kerogen-mineral interactions in oil shales, Energy & Fuels 1(3) (1987) 248-252.

[28] D.R. Katti, H.B. Upadhyay, K.S. Katti, Molecular interactions of kerogen moieties with Na-montmorillonite: An experimental and modeling study, Fuel 130 (2014) 34-45.

[29] T. Wu, Q. Xue, X. Li, Y. Tao, Y. Jin, C. Ling, S. Lu, Extraction of kerogen from oil shale with supercritical carbon dioxide: Molecular dynamics simulations, The Journal of Supercritical Fluids, 107 (2015) 499-506.

[30] A.M. Orendt, I.S.O. Pimienta, S.R. Badu, M.S. Solum, R.J. Pugmire, J.C. Facelli, D.R. Locke, K.W. Chapman, P.J. Chupas, R.E. Winans, Three-dimensional structure of the siskin green river oil shale kerogen model: A comparison between calculated and observed properties, Energy & Fuels 27(2) (2013) 702-710.

[31] J.L. Faulon, M. Vandenbroucke, J.M. Drappier, F. Behar, M. Romero, 3D Chemical model for geological macromolecules, Organic Geochemistry 16(4-6) (1990) 981-993.

[32] B.R. Brooks, R.E. Bruccoleri, B.D. Olafson, D.J. States, S. Swaminathan, M. Karplus, Charmm - a program for macromolecular energy, minimization, and dynamics calculations, Journal of Computational Chemistry 4(2) (1983) 187-217.

[33] J.C. Phillips, R. Braun, W. Wang, J. Gumbart, E. Tajkhorshid, E. Villa, C. Chipot, R.D. Skeel, L. Kale, K. Schulten, Scalable molecular dynamics with namd, Journal of Computational Chemistry 26(16) (2005) 1781-1802.

[34] H. Lu, K. Schulten, The key event in force-induced unfolding of titin's immunoglobulin domains, Biophysical Journal 79(1) (2000) 51-65.

[35] A. Delville, Modeling the clay water interface, Langmuir 7(3) (1991) 547-555.

[36] F.R.C. Chang, N.T. Skipper, G. Sposito, Computer-simulation of interlayer molecular-structure in sodium montmorillonite hydrates, Langmuir 11(7) (1995) 2734-2741.

[37] E.J.M. Hensen, B. Smit, Why clays swell, Journal of Physical Chemistry B 106(49) (2002) 12664-12667.

[38] F.T. Madsen, M. Muller-Vonmoos, The swelling behaviour of clays, Applied clay science 4(2) (1989) 143-156.

[39] H.Y. Jo, T. Katsumi, C.H. Benson, T.B. Edil, Hydraulic conductivity and swelling of nonprehydrated GCLs permeated with single-species salt solutions, Journal of Geotechnical and Geoenvironmental Engineering 127(7) (2001) 557-567.

[40] M.B. McBride, Trace and toxic elements in soils, Environmental Chemistry of Soils (1994) 308-341.

[41] R.M. Shroll, D.E. Smith, Molecular dynamics simulations in the grand canonical ensemble: Application to clay mineral swelling, Journal of Chemical Physics 111(19) (1999) 9025-9033.

[42] R. Sutton, G. Sposito, Molecular simulation of humic substance-Ca-montmorillonite complexes, Geochimica et Cosmochimica Acta 70(14) (2006) 3566-3581.

[43] T.J. Tambach, E.J.M. Hensen, B. Smit, Molecular simulations of swelling clay minerals, Journal of Physical Chemistry B 108(23) (2004) 7586-7596.

[44] S.R. Schmidt, D.R. Katti, P. Ghosh, K.S. Katti, Evolution of mechanical response of sodium montmorillonite interlayer with increasing hydration by molecular dynamics, Langmuir 21(17) (2005) 8069-8076.

[45] D.R. Katti, S.R. Schmidt, P. Ghosh, K.S. Katti, Modeling the response of pyrophyllite interlayer to applied stress using steered molecular dynamics, Clays and Clay Minerals 53(2) (2005) 171-178.

[46] D.R. Katti, S.R. Schmidt, P. Ghosh, K.S. Katti, Molecular modeling of the mechanical behavior and interactions in dry and slightly hydrated sodium montmorillonite interlayer, Canadian Geotechnical Journal 44(4) (2007) 425-435.

[47] J.A. Greathouse, D.B. Hart, G.M. Bowers, R.J. Kirkpatrick, R.T. Cygan, Molecular simulation of structure and diffusion at smectite-water interfaces: Using expanded clay interlayers as model nanopores, Journal of Physical Chemistry C 119(30) (2015) 17126-17136.

[48] L. Sun, J.T. Tanskanen, J.T. Hirvi, S. Kasa, T. Schatz, T.A. Pakkanen, Molecular dynamics study of montmorillonite crystalline swelling: Roles of interlayer cation species and water content, Chemical Physics 455 (2015) 23-31.

[49] D.R. Katti, L. Srinivasamurthy, K.S. Katti, Molecular modeling of initiation of interlayer swelling in Na-montmorillonite expansive clay, Canadian Geotechnical Journal 52(9) (2015) 1385-1395.

[50] S.M. Pradhan, K.S. Katti, D.R. Katti, Evolution of molecular interactions in the interlayer of Na-montmorillonite swelling clay with increasing hydration, International Journal of Geomechanics 15(5) (2015) 1-9.

[51] D. Katti, V. Shanmugasundaram, Influence of swelling on the microstructure of expansive clays, Canadian Geotechnical Journal 38(1) (2001) 175-182.

[52] A. Maria Gomez-Caravaca, R.M. Maggio, V. Verardo, A. Cichelli, L. Cerretani, Fourier transform infrared spectroscopy-partial least squares (FTIR-PLS) coupled procedure application for the evaluation of fly attack on olive oil quality, Lwt-Food Science and Technology 50(1) (2013) 153-159.

[53] K. Essig, R.D. Urban, H. Birk, H. Jones, Diode-laser spectroscopy of nad, kd, rbd, and csd - determination of the mass-independent parameters and mass scaling coefficients of the alkali-metal hydrides, Zeitschrift Fur Naturforschung Section a-a Journal of Physical Sciences 48(11) (1993) 1111-1114.

[54] A.C. Fischer-Cripps, D.W. Nicholson, Nanoindentation. Mechanical engineering series, Appl. Mech. Rev. 57(2) (2004) B12-B12.

[55] W.C. Oliver, G.M. Pharr, An improved technique for determining hardness and elastic-modulus using load and displacement sensing indentation experiments, Journal of Materials Research 7(6) (1992) 1564-1583.

[56] Z.J. Wang, H. Wang, M.E. Cates, Effective elastic properties of solid clays, Geophysics 66(2) (2001) 428-440.

3. THE ROLE OF FLUID POLARITY IN THE SWELLING OF SODIUM-MONTMORILLONITE CLAY: A MOLECULAR DYNAMICS AND FOURIER TRANSFORM INFRARED SPECTROSCOPY STUDY[1]

3.1. Introduction

Swelling clays are found all over the world. The understanding of the expansive behavior of these clays is of significant importance in geotechnical and geoenvironmental applications, in petroleum and industrial engineering, and for the design of polymer-clay-nanocomposites. The volume of swelling clay increases when it interacts with water, resulting in a significant increase in swelling and swelling pressure. The infrastructure such as buildings, roads, retaining walls, dams, and irrigation canals are prone to damage from swelling pressure [1-3]. However, this type of clay has also been used for landfill liners [4], borehole stabilization when drilling mud [5], enhancing the material properties in clay-nanocomposites [6], biomedical application [7], and modifying asphalt in pavement construction [8].

Sodium-montmorillonite (Na-MMT), in many cases, is the main component of swelling clay mineral found in these clays. The mineral consists of a tetrahedral-octahedral-tetrahedral (T-O-T) structure where octahedral clay sheet is sandwiched between two tetrahedral clay sheets [9]. Na-MMT clay is used extensively as a barrier material in geotechnical and geoenvironmental engineering due to its high surface area and low hydraulic conductivity. Hence, understanding the swelling mechanisms and evaluating the interactions occurring on the molecular scale of Na-

[1] This chapter describes the influence of fluid polarity in swelling of sodium montmorillonite clay. Most of the contents of this chapter has been published in Dinesh R. Katti, Keshab B. Thapa, and Kalpana S. Katti, The role of fluid polarity in the swelling of sodium-montmorillonite clay: a molecular dynamics and Fourier transform infrared spectroscopy study, Journal of Rock Mechanics and Geotechnical Engineering 10(6) (2018) 1133-1144. Keshab B. Thapa had primary responsibility for collecting samples in the field and for interviewing users of the test system. Keshab B. Thapa was the primary developer of the conclusions that are advanced here. Keshab B. Thapa also drafted and revised all versions of this chapter. Dinesh R. Katti and Kalpana S. Katti served as proofreader and checked the math in the statistical analysis conducted by Keshab B. Thapa.

MMT clay with various organic fluids is crucial for predicting swelling clay response, designing landfill clay liners, and avoiding enormous damages caused by swelling clays. Landfill leachate includes a wide range of organic fluids. The United States Environmental Protection Agency (US-EPA) has labeled fluids such as toluene, trichloroethylene (TCE), acetone, methanol, and formamide among other fluids as toxic and dangerous to health. The interactions between Na-MMT clay and organic fluids are very important in determining the appropriate use of clays in the landfill liners. In swelling clays, swelling is categorized as inner crystalline swelling and osmotic swelling [10]. The inner crystalline is due to initial hydration of exchangeable interlayer cations of dry clays when they come in contact with an aqueous phase such as water. The clay-water interactions have been studied using diffuse double layer theory [11]. However, the interlayer hydration of swelling clay was not described accurately by these theories.

In our previous work, swelling pressure of saturated bentonite clay at a predetermined swelling level has been studied experimentally and showed that clay particles break down into a smaller size with increase in swelling level and reduction of swelling pressure Fourier transform infrared (FTIR) spectroscopy is a nondestructive technique [12] and used for the analysis of clay-fluid interactions. Extensive studies on Na-MMT clay with water have been carried out using FTIR technique [13], and the disorientation of clay sheets increases due to clay-water interactions with increasing swelling magnitude. In our prior work, the hydraulic conductivity of the Na-MMT clay interlayer region is studied using polarized FTIR spectroscopy. In addition, the change in Si-O stretching band in tetrahedron clay sheets, O-H stretching of a structural hydroxyl group, and H-O-H bending vibration band of bulk water at the molecular scale showed a significant interaction between clay and water. Extensive experimental studies have been carried out on Na-MMT clay with high polar fluids, formamide and water, medium polar fluids,

methanol, and low polar fluids, acetone, chloroform, trichloroethylene, and toluene [14, 15]. The interactions between Na-MMT and organic fluids are nonbonded in nature: the nonbonded interactions are very high for polar fluids and almost negligible for low polar fluids. Therefore, the clay-fluids molecular interactions control the evolution of the macroscopic structure of Na-MMT clay. The macroscale mechanical properties, such as hydraulic conductivity, consolidation, and swelling pressure, of Na-MMT clay with these fluids, are studied. The hydraulic conductivity decreases dramatically with the increase in polarity of fluids [15]. Furthermore, the initial swelling of montmorillonite clay depends on the type of interlayer cations and hydration energy of interlayer cations [16], and the clay particles breakdown due to a significant cation-fluid hydration energy.

In addition to these experimental studies, the computational techniques have been used to investigate the behavior of swelling clays at the molecular level. Molecular dynamics (MD), Monte Carlo (MC), and discrete element method (DEM) have been carried out to study the interaction between clay and water [17-28]. In our previous work, the mechanical behavior of dry and hydrated Na-MMT clay interlayer and clay-water interactions are studied using steered MD (SMD), and it has been observed that the solvation of interlayer cations and clay sheets play a significant role in the swelling properties of Na-MMT clay [26, 29-31]. DEM studies showed that particle subdivision of Na-MMT clay causes an increase in swelling pressure [32]. The attractive interactions between sodium and clay hold the clay sheets together in dry clay; however, when water is introduced, the attractive interactions between sodium and water result in the formation of solvation shell around the cations, resulting in decreased attractive interactions between clay sheets and sodium ion, in turn increasing the crystalline swelling and with increased interlayer hydration, causing exfoliation and particle breakdown of swelling clay

[27, 33]. The initiation of the crystalline swelling mechanism of Na-MMT clay has been carried out using MD simulations. Interlayer sodium cations attract the water molecules into the interlayer, and there is also a significant attractive nonbonded interaction between them, which initiates interlayer swelling [33]. Furthermore, interactions of Na-MMT with formamide, water, methanol, acetone, and toluene have been quantitatively studied in a previous work. We have observed the significantly higher nonbonded interactions between clay and polar fluids than that between clay and low polar fluids [34]. Previous studies on clay-fluid interactions have been conducted either experimentally or computationally but not concurrently on the same system. In the current work, we attempt to link interaction energies from MD simulations to observed changes in the experimentally obtained FTIR spectroscopy spectra. The molecular models used in the study resemble the clay used in the experiments. Also, by conducting MD studies on the observed d-spacing values of samples used in FTIR studies, the fluid content in the interlayers in MD and FTIR experiments is similar providing an insight into molecular mechanisms. This current study presents our FTIR and MD simulation results on Na-MMT clay with a wide range of organic fluids and provides insight into nonbonded interactions quantitatively at the molecular scale. In addition, the conformations of each organic fluid in close proximity to interlayer sodium cations are presented.

3.2. Materials

Na-MMT (SWy-2, Crook County, Wyoming, USA) clay was acquired from Clay Minerals Repository at the University of Missouri, Columbia, Missouri, USA. The cationic exchange capacity of this clay is about 76.4 meq/100 g. The fluids used were 90%-100% purity formamide and 99.9% purity acetone obtained from Mallinckrodt Baker Inc., New Jersey and 99.9% purity methanol obtained from Alfa Aesar, Massachusetts. The deionized water used was

obtained from our laboratory at North Dakota State University. The fluids used in this study range from high dielectric constant to low dielectric constant reflecting highly polar to low polar fluids. Formamide and water have high dielectric constants of 110 and 80, respectively, methanol has a medium dielectric constant of 33, and acetone has a low dielectric constant of 20.

3.3. Fourier Transform Infrared Technique

A comprehensive infrared spectroscopic study on Na-MMT clay and organic solvents samples was described in our previous work [14]. Briefly, Na-MMT was first ground and passed through a No. 325 sieve (45 μm mesh). The consistent moisture content was acquired by drying clay in an oven at 50 ^{o}C temperature for 24 h prior to each sample preparation. The thin layer of Na-MMT was placed on the gold-coated metal substrate with a glass slide, and fluid was added to the surface of the sample. For transmission FTIR spectroscopy study, the powder samples were gently compressed against a silicon window with a glass side, and then the fluids were added to the surface of the clay. Another silicon window was used to sandwich the sample by gently pressing them together to make a thin layer of sample between silicon windows. The homogeneous samples for formamide and water were prepared by mixing clay with fluids in a porcelain dish to obtain a thin layer of slurry. The sample was smeared on a silicon window, and gold coated a substrate for transmission and reflectance FTIR experiments, respectively. Data acquisition was accomplished immediately after the samples were wetted. The FTIR spectroscopy experiments were performed using a Nicolet 850 FTIR spectrometer with KBr beam splitter in the range of 4000-400 cm^{-1} at a spectral resolution of 4 cm^{-1}. A wire grid polarizer was used to yield a p-polarized IR beam, and angle of incidence was at 45^{o} for the reflectance experiment, and the gold-coated metal substrate was used for obtaining background

spectra. The clean silicon windows and gold-coated metal substrate were used, respectively, for background spectra in transmission and reflectance experiments.

3.4. Model Construction

The chemical formula of the Na-MMT SWy-2 unit cell is $NaSi_{16}(Al_6FeMg)O_{20}(OH)_4$. The initial coordinates were obtained from the model proposed in the literature [35]. Also, the atomic charges were obtained from the literature [23]. The Na-MMT 4×2 model was initially constructed [26] in our previous studies, and the dimensions of unit cell were 5.28 Å × 9.14 Å × 6.56 Å. The structural charges in the molecular models of clay sheets are consistent with the experiments. The reported chemical formula for SWy2 clay used in the experiments [36] is $(Ca_{0.12}Na_{0.32}K_{0.05})[Al_{3.01}Fe(III)_{0.41}Mn_{0.01}Mg_{0.54}Ti_{0.02}][Si_{7.98}Al_{0.02}]O_{20}(OH)_4$. The chemical formula used for the clay models is a simplified version $NaSi_{16}(Al_6FeMg)O_{20}(OH)_4$. Almost all of the unbalanced charge in the clay sheet comes from isomorphous substitution and is reported as 0.53e. In our models, the charge due to isomorphous substitution in the octahedral sheet is 0.5e per unit cell [29]. This model has been extensively used for clay-fluid interactions [24, 26, 27, 29, 33] using CHARMM force field parameters [24, 25, 29]. The Na-MMT clay layers have a T-O-T structure, and each octahedral clay sheet is sandwiched between tetrahedral clay sheets. In our work, the clay model has 6×3 unit cells, and the dimensions of the unit cell are 31.68 Å × 27.44 Å × 24.16 Å. The molecular model consists of 6 unit cells in X-direction and 3 unit cells in Y-direction, as shown in Figure 3.1. A detailed explanation of the model construction is described in our previous work to study polymer clay nanocomposites [37].

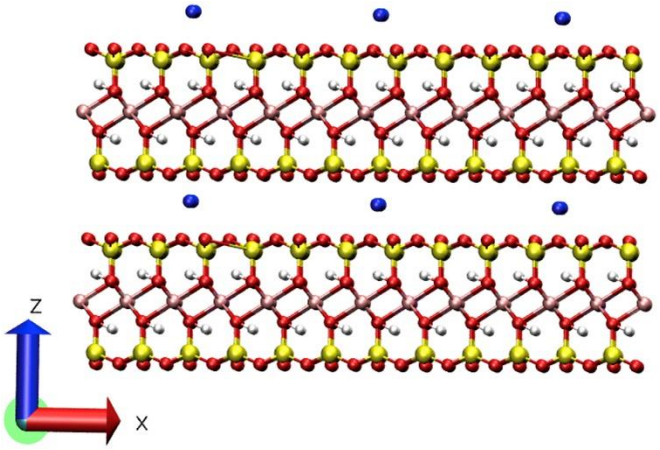

Figure 3.1. Molecular model of Na-MMT showing clay sheets, Na cations, and d-spacing.

The negative charge was developed on the individual clay sheets due to isomorphic substitution in the octahedral sheet. In the 6×3 model, nine aluminum cations (Al^{3+}) are substituted by nine iron cations (Fe^{3+}), and nine aluminum cations (Al^{3+}) are substituted by nine magnesium cations (Mg^{2+}). Thus, nine sodium cations (Na^{+}) were introduced in the interlayer to balance the negative charge (-0.5e per unit cell) of the clay sheets. In this study, the molecular weight of 6×3 unit Na-MMT clay is 13,414 g/mole, and hence 1 mole of clay contains 13,414 g of clay. Figure 3.2(a-d) shows the molecular structures of acetone, methanol, water, and formamide.

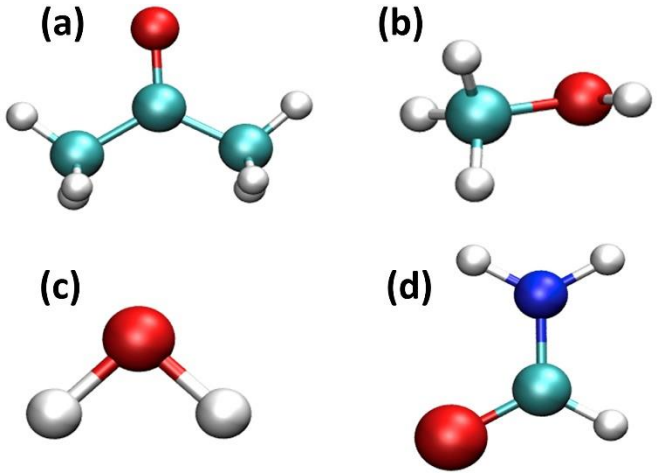

Figure 3.2. The molecular structure of (a) Acetone, (b) Methanol, (c) Water, and (d) Formamide.

The Na-MMT and fluids models were developed using Material Studio™ and PSFGen plug-in of visual MD software (VMD 1.9.2) (Humphrey et al., 1996). The force field parameters for formamide, methanol, and acetone were obtained from CHARMM GUI Archive-CHARMM Small Molecule [38], and the water molecule was Transferable Intermolecular Potential 3 Point (TIP3P) [39]. FTIR spectroscopy experiments were conducted on samples created by clay slurries of clay + acetone and clay + methanol. In addition, samples were prepared with clay mixed with predetermined amount of water and clay mixed with predetermined amount of formamide. Under the same condition, X-ray Diffraction (XRD) experiments were conducted on the samples to evaluate d-spacing. Inverse calculations were conducted to evaluate the amount of fluid in the interlayer by comparing d-spacing obtained from MD simulations with d-spacing values found from XRD experiments. The molecular models with the computed amounts of fluid molecules in the interlayer were used to evaluate the interaction energies. The d-spacing values for the molecular models with 10% acetone, 20% methanol, 30% water, and 30% formamide matched with the d-spacing results from the XRD experiments. In order to compare FTIR spectroscopy results with the MD interaction energy results, the representative clay models consist of 10% acetone, 20% methanol, 30% water, and 30% formamide in the interlayer [14, 15, 40]. The detailed procedure of the model construction is described in our previous work [34]. CHARMM force field parameters have been used for both organic fluids and Na-MMT clay. The CHARMM parameters have been found and validated by the authors. Based on the molecular weight of individual molecules, 10% fluid content is equivalent to 24 molecules of acetone, 40 molecules of methanol, 64 molecules of water, and 48 molecules of formamide. In addition, 20% methanol has 80 methanol molecules, 30% water has 216 water molecules, and 30% formamide has 90 formamide molecules in the clay interlayer.

3.5. Simulation Details

MD simulations and visual MD software (VMD 1.9.1) were used for the molecular modeling of Na-MMT clay with different organic fluids. In MD, nanoscale molecular dynamics software (NAMD 2.9) was used, which was developed by Theoretical and Computational Biophysics Group, Beckman Institute, the University of Illinois at Urbana-Champaign [41]. All interaction energies were computed using VMD, which was compatible with the CHARMM force field [42]. The simulations were run using 2.66 GHz Intel Xenon X5550 processor and 127 nodes, each node consisting of 8 processor cores, at the Center for Computationally Assisted Science and Technology (CCAST) at North Dakota State University.

The conjugate method was carried out for the minimization of all models. The temperature of 0 K and the pressure of 0 atmosphere are used during minimization. All the simulations were run at room temperature and atmospheric pressure, resulting in the isothermal-isobaric ensemble. The temperature was raised in three steps, i.e. 0 K through 300 K, with an increment of 100 K. The pressure was raised in four steps, i.e. 0 kPa through 101 kPa (1 atmosphere), with increment of 25 kPa while keeping the temperature constant at 300 K. The pressure was controlled by the method of Langevin piston Nose-Hoover [43] and temperature by Langevin dynamics.

All the simulations were run for 150,000 steps, which is equivalent to 75 ps (10-12 s), with the time step of 0.5 fs (10-15 s). The infinite number of clay sheets was mimicked by applying the period boundary conditions. Although the clay sheets were restrained in X- and Y-directions, they were allowed to move in the Z-direction. All the organic fluids were free to move in all directions, mimicking experimental conditions. The d-spacing of each model was measured by the distance between the corresponding surface oxygen atoms of clay sheets in the

Z-direction. The interaction energies were computed considering the last 20 ps of the trajectory of simulation. Nonbonded interaction, such as electrostatic energy, was computed using particle mesh Ewald (PME) method. For all models, the van der Waals switch and cut off distances were 16 Å and 17 Å, respectively.

3.6. Results and Discussions

3.6.1. Fourier Transform Infrared Results

In our previous work, a detailed vibrational spectroscopic study on clay-fluid interactions was described using transmission and reflection FTIR experiments [14]. The combined IR spectra for dry Na-MMT and Na-MMT with acetone, methanol, water, and formamide are shown in Figure 3.3a-d.

Table 3.1 shows the band assignments obtained from the literature [13, 44-46]. The band at 1118 cm^{-1} in the IR spectra of dry Na-MMT is attributed to the Si-O stretching. It is observed in Figure 3.3a and b that the Si-O stretching band has a shift of 7 cm^{-1} and 6 cm^{-1} to lower energy for the clay-formamide complex and the clay-water complex, respectively.

The band shift observed in the spectra suggests the alteration in the orientation of silica tetrahedral region due to swelling characteristics, as the polar fluids enter into the clay interlayer galleries. The shift also signifies that there is nonbonded interaction between surface oxygen of clay and interlayer solvents; this phenomenon has been observed in prior work in the literature to study the polymer clay nanocomposites [6], evolution of clay microstructures [13-15], and interaction between clay and organic matter [46].

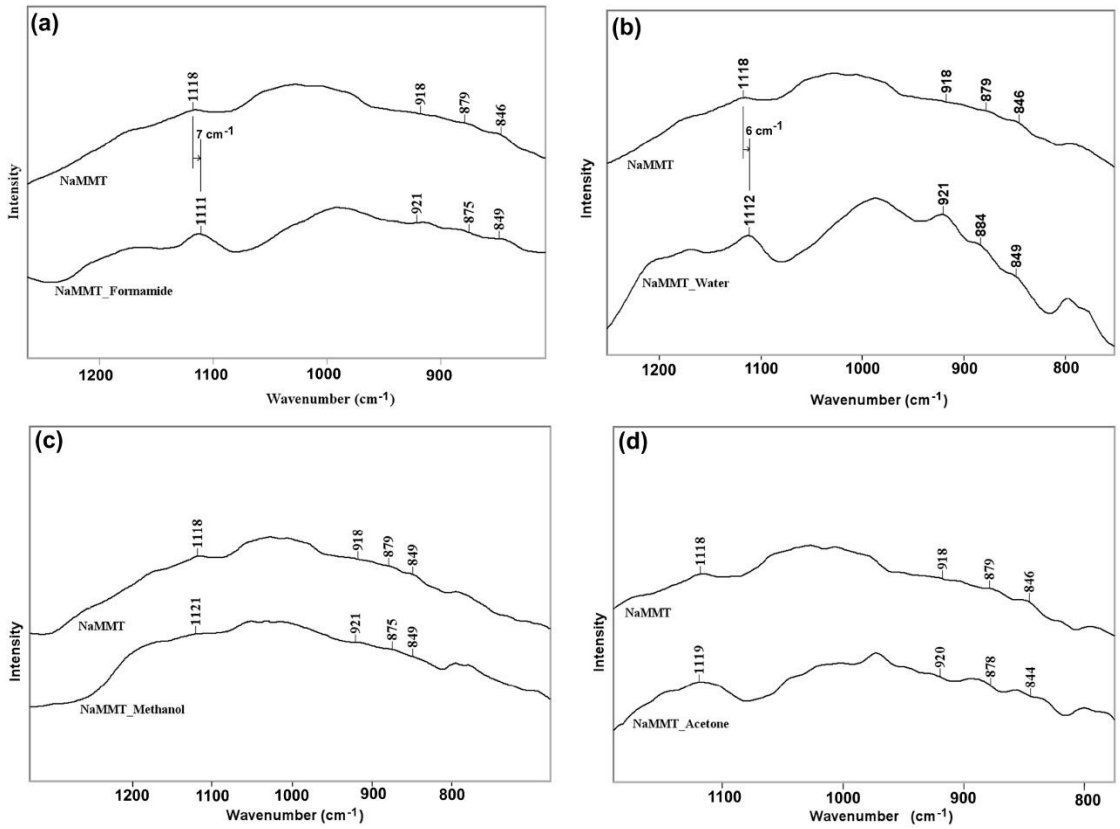

Figure 3.3. IR spectra for (a) Mixture of Na-MMT and formamide in the energy range of 800-1275 cm^{-1}, (b) Mixture of Na-MMT and water in the energy range of 750-1250 cm^{-1}, (c) Mixture of Na-MMT and methanol in the energy range of 675-1325 cm^{-1}, and (d) Mixture of Na-MMT and acetone in the range of 775-1200 cm^{-1}.

Table 3.1. FTIR band assignment for dry Na-MMT clay.

Sample	Band position (cm^{-1})	Band assignment
Dry Na-MMT	688	Si-O deformation [44]
	788	Si-O stretching from quartz and silica [13, 44]
	846	Mg-OH deformation [13, 44]
	879	Fe-OH deformation [44]
	918	Al-OH deformation [44, 45]
	1065	Si-O stretching [13, 44]
	1118	Si-O stretching [44]

The band shifts are not significant in the Si-O region in the case of clay-methanol and clay-acetone complexes, which indicates that intermediate polar and low polar fluids have lower

nonbonded interactions in Si-O region. Furthermore, Mg-OH deformation band at 846 cm^{-1} and Al-OH deformation band at 918 cm^{-1} of dry clay have no significant shifts in any clay-fluids complexes, indicating insignificant nonbonded interactions in the octahedral clay sheets. Fe-OH deformation band of dry Na-MMT at 879 cm^{-1} is shifted towards lower energy by 9 cm^{-1} and 5 cm^{-1} in the spectra of the clay-formamide complex and clay-water complex, respectively. These shifts are significant due to no overlapping bands in IR spectra. From the spectra of clay-methanol and clay-acetone complexes, no significant band shifts are observed in the tetrahedral region, or octahedral region of clay sheets. The shifts towards either lower or higher energy observed in the Si-O stretching band and the Al-OH, Fe-OH, and Mg-OH deformation bands suggest that the molecular interactions between clay and polar fluids are significantly higher than those in clay and medium and low polar fluids.

3.6.2. Molecular Dynamics Simulations

The experimental d-spacing of dry Na-MMT clay is 9.85 Å [14]. The MD simulation showed the average d-spacing of dry Na-MMT to be 10.70 Å, resulting in the representative clay model for this study. The experimental d-spacing values of Na-MMT with acetone, methanol, water, and formamide were found to be 13.07 Å, 17.14 Å, 18.32 Å, and 18.99 Å, respectively [14, 31, 34, 47]. The corresponding d-spacing values of the representative clay-fluid models after simulations are presented in Table 3.2. The d-spacing values of the clay model with 10% acetone, 20% methanol, 30% water, and 40% formamide were 13.38 Å, 17.6 Å, 17.89 Å, and 18.46 Å, respectively, indicating that the interlayer fluid content increased with increase in dielectric constant of fluids.

Table 3.2. d-spacing of the clay-fluid complexes from simulation and experiment results.

Dielectric constant	Fluid	Fluid content (%)	d-spacing (Å)	
			Simulation	Experiment
20	Acetone	10	13.38	13.07
33	Methanol	20	17.6	17.14
80	Water	30	17.89	18.32
110	Formamide	30	18.46	18.99

These results are consistent with experimental results and can be related to the high swelling and swelling pressure, particle breakdown, low permeability, and low compression of the expansive clay in the presence of polar fluids [15]. In this study, the swelling of the interlayer is associated with an increase in the distance between two clay sheets; however, the thickness of clay sheet remains constant. The clay-fluid molecular models consist of clay sheets, sodium ions, and interlayer fluids. The nonbonded interactions among these constituents provide insight into swelling behavior of the expansive clay.

VMD was used to compute the interaction energies quantitatively. Energies were computed by considering the interlayer fluids in the clay interlayer after simulation period of 75 ps. The snapshots of molecular models of Na-MMT with acetone, methanol, water, and formamide after simulation are shown in Figure 3.4(a-d), respectively. The sum of the electrostatic energy and van der Waals energy is the total nonbonded energy. The electrostatic interaction energy is the function of the charge and distance between two sets of atoms, whereas van der Waals interaction energy depends only on the distance between two sets of atoms. The negative interaction energy represents the attractive interaction, and the positive interaction energy represents the repulsive interaction between two atoms.

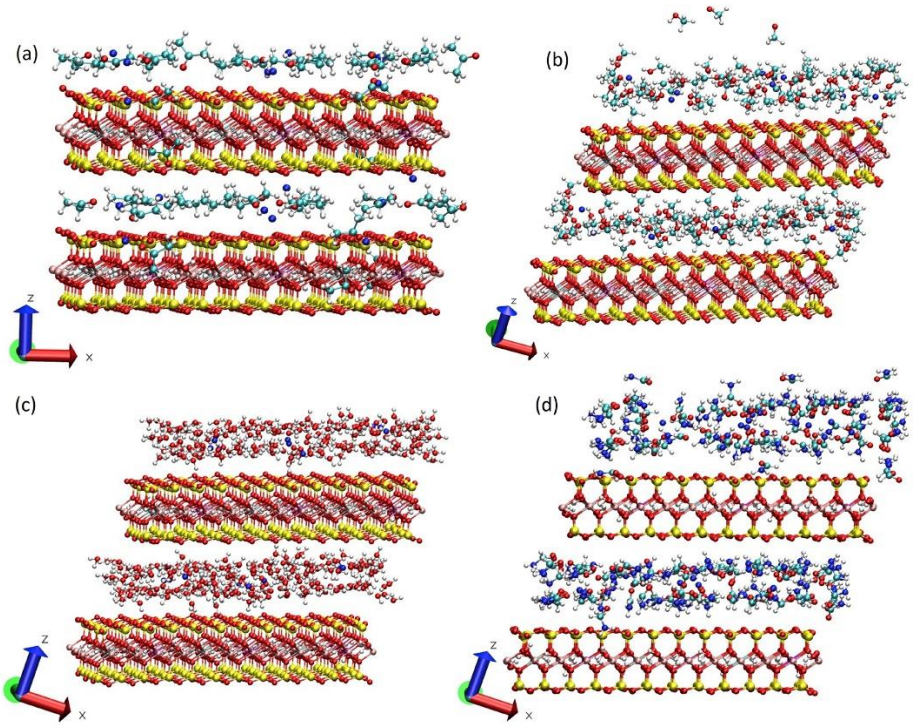

Figure 3.4. Na-MMT models with different interlayer fluids after simulation up to 75 ps: (a) 10% acetone, (b) 20% methanol, (c) 30% water, and (d) 30% formamide.

Figure 3.5 shows the interactions energy between clay sheets in the dry state and various interlayer fluids (polar, medium polar, and low polar fluids). In the case of the dry interlayer, clay-clay interactions are the highest and predominated by van der Waals energy. The repulsive electrostatic interaction was due to negative charge in each clay sheet. When fluids are introduced in the interlayer, the attractive nonbonded interactions are decreased with increasing amount of interlayer fluids and polarity of fluids, and interactions are rapidly diminished almost to zero at 30% of formamide. As shown in Figure 3.6, the attractive nonbonded interactions between sodium and clay layers are the highest in the dry condition, and these attractive interactions are primarily electrostatic and hold the clay sheets together.

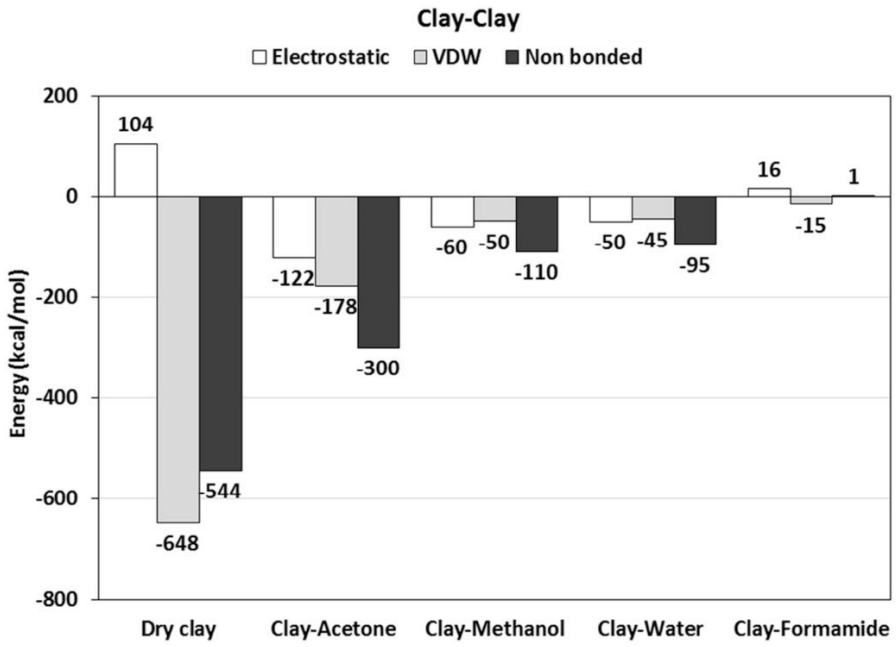

Figure 3.5. Interaction energies between clay sheets for fluids with a wide range of dielectric constants.

This observation has also been studied on Na-MMT swelling clay with increasing water content using MD [27]. At equilibrium, sodium ions are found to be in close proximity to the clay sheets in the molecular model of Na-MMT with acetone and methanol, but sodium ions are located near the center of the interlayer in the molecular model of Na-MMT with water and formamide. The attractive interaction is also decreased with increasing polarity of fluids and fluid content. The electrostatic energy between sodium and clay sheets in dry Na-MMT clay is 1.5 times higher than that in Na-MMT with 10% acetone. It is almost the same for Na-MMT with 20% methanol, 30% water, and 30% formamide, and the van der Waals energy is negligible. Figure 3.7 shows the attractive interactions between sodium ions and interlayer fluid molecules are the highest followed by clay-sodium interactions and then clay-clay interactions.

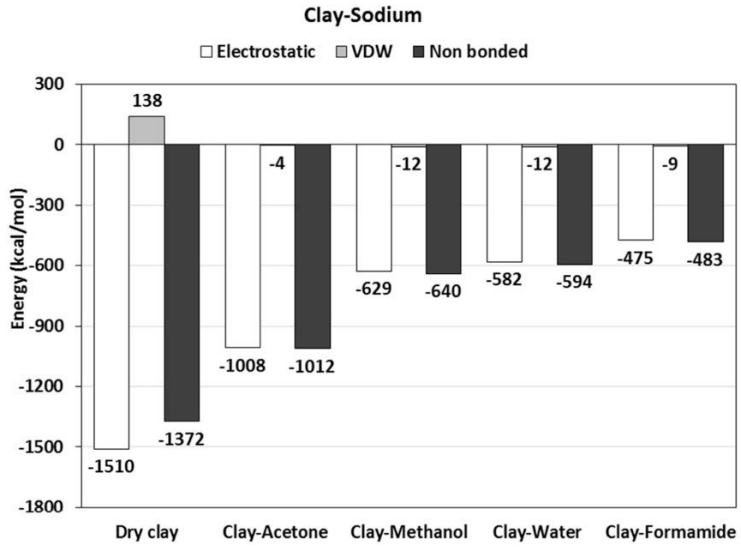

Figure 3.6. Interaction energies between clay sheets and sodium ions for fluids with a wide range of dielectric constants.

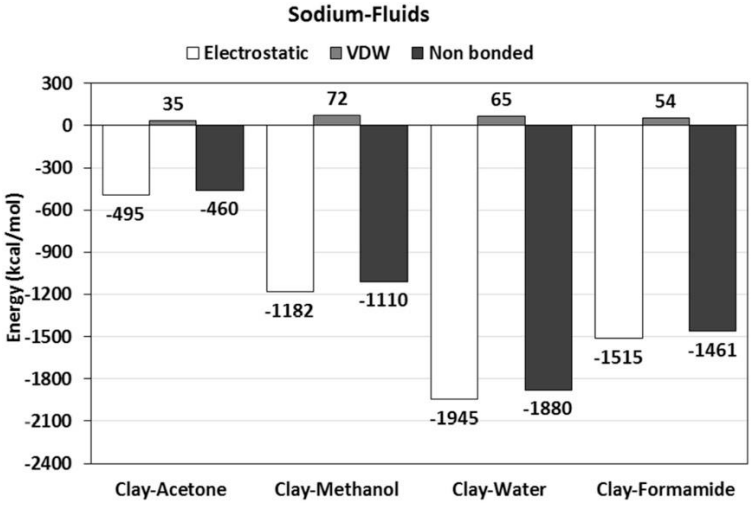

Figure 3.7. Interaction energies between sodium ions and fluid molecules.

The electrostatic energy between sodium ions and 20% methanol was more than 2 times greater than that between sodium ions and 10% acetone. Similarly, the electrostatic energy between Na-MMT and 30% water was 1.5 times greater than that between Na-MMT and 20% methanol. The total nonbonded interaction energy between Na-MMT and 30% water is slightly greater than that between Na-MMT and 30% formamide. The nature of these interactions is predominantly (attractive) electrostatic whereas (repulsive) van der Waals interactions are

negligible. Thus, sodium ions have significant interactions with polar fluids than those with low polar fluids; the solvation of swelling clay was initiated by hydration of interlayer sodium ions, resulting in the initial interlayer swelling.

Figure 3.8 shows the snapshots of the representative models of Na-MMT with 10% acetone, 20% methanol, 30% water, and 30% formamide. This figure shows the planar view of conformation of the interlayer fluids with sodium ions. It was found that the oxygen atoms were attracted and directed to the sodium ions, and hydrogen atoms were attracted to oxygen atoms, resulting in the formation of an organized pattern. It can be seen that two oxygen atoms and four oxygen atoms are in proximity to the sodium ions in case of Na-MMT with 10% acetone and Na-MMT with 20% methanol, respectively. In addition, the clustering and proximity of fluid molecules to the sodium ions increase dramatically as the fluid content and the polarity of fluids increased, and this formation resulted in the well-organized pattern for high polar fluids such as water and formamide. All these fluid molecules laid on the same plane as sodium ions.

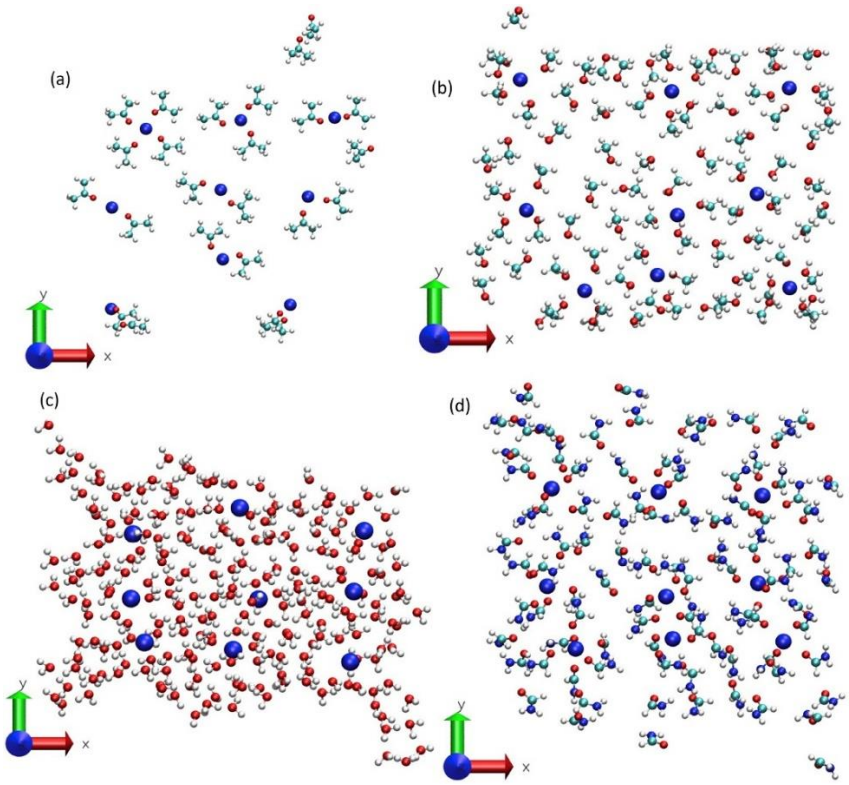

Figure 3.8. Snapshots displaying conformation of molecules of fluids in proximity to sodium ions: (a) Acetone, (b) Methanol, (c) Water, and (d) Formamide. Sodium ions are rendered in VDW format.

The nonbonded interaction energy of Si-O of tetrahedral clay sheets with acetone, methanol, water, and formamide is shown in Figure 3.9. The interaction energy between Si-O and fluids increased as the polarity of fluids increased. The repulsive electrostatic energy between Si-O and water is more than 5.5 times greater than that between Si-O and acetone. Although the total nonbonded interaction energy between Si-O and formamide is slightly greater than that between Si-O and methanol, the corresponding electrostatic energy is similar and attractive in nature. These interaction energies agreed with shifts of Si-O band in our FTIR experimental analysis (Figure 3.3). These shifts suggest strong nonbonded interactions between the surface oxygen of clay sheets and fluid molecules, and strong interactions may change the orientations of silica tetrahedral sheets of clay.

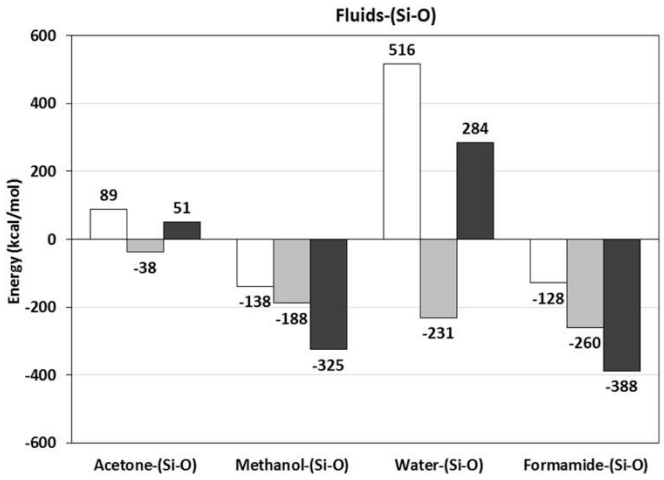

Figure 3.9. Interaction energy of Si-O with (a) Acetone, (b) Methanol, (c) Water, and (d) Formamide.

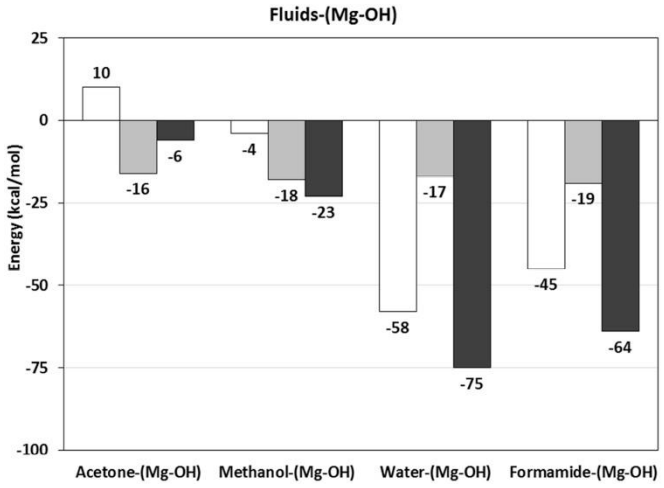

Figure 3.10. Interaction energy of Mg-OH with (a) Acetone, (b) Methanol, (c) Water, and (d) Formamide.

The nonbonded interaction energies of Al-OH and Fe-OH of octahedral clay sheet with fluids are shown in Figures. 11 and 12. Attractive electrostatic interaction energy between Al-OH and water is 2 times greater than that between Al-OH and acetone and almost 1.5 times greater than that between Al-OH and methanol. On the other hand, the electrostatic interaction between Al-OH and formamide is repulsive in nature. The van der Waals energy remains almost the same for all cases. Similarly, the total nonbonded energy between Fe-OH and water is more than 3 times greater than that between Fe-OH and acetone and 1.5 times greater than that

between Fe-OH and methanol, but the (repulsive) electrostatic interaction between Fe-OH and formamide is not significant compared to other fluids. These results were consistent with the FTIR studies, which indicate that the interaction between polar fluids and clay increases with increase in the polarity of fluids. Thus, the FTIR and MD simulations studies showed a significantly higher nonbonded interaction between clay and formamide and water than that between clay and methanol and acetone. In addition, simulation results indicated that clay and formamide interactions were predominant. The results also show that the various entities of the clay sheet interact differently with the fluid molecules even for fluid molecules with similar dielectric constants.

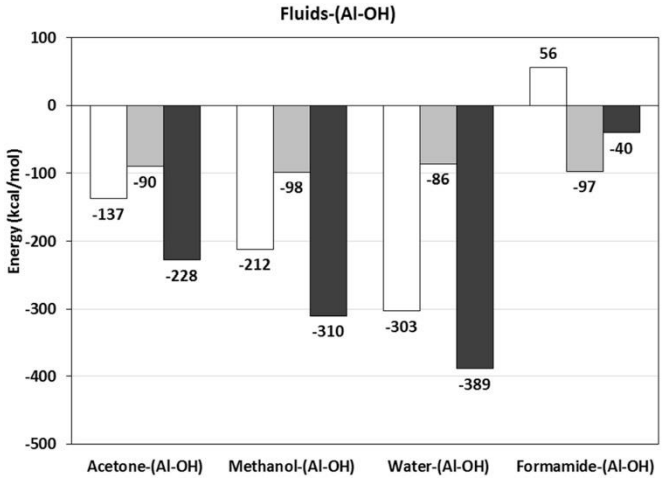

Figure 3.11. Interaction energy of Al-OH with (a) Acetone, (b) Methanol, (c) Water, and (d) Formamide.

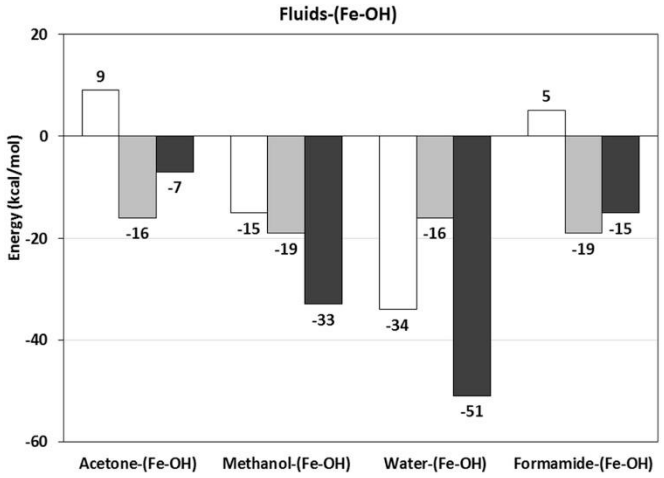

Figure 3.12. Interaction energy of Fe-OH with (a) Acetone, (b) Methanol, (c) Water, and (d) Formamide.

Figure 3.13 shows the evolution of nonbonded interaction energies between the various components of the clay with 10% of fluid content in the interlayer with d-spacing. The d-spacing corresponding to 10% acetone, 10% methanol, 10% water, and 10% formamide were 13.38 Å, 13.88 Å, 13.57 Å, and 13.71 Å, respectively. The figure indicates that although the fluid content is the same, the molecular interactions in the interlayer are significantly different. Although the clay interlayer contained the same fluid content, each of the clay-fluid models had different d-spacing values, and the clay-clay, clay-sodium, sodium-fluids, and clay-fluids interactions were also different, as shown in Figure 3.13. The nonbonded interactions between clay sheets decreased with increase in d-spacing. The 10% of interlayer methanol had the highest d-spacing, resulting in the lowest nonbonded interactions between clay sheets. With the increase in d-spacing, the clay-sodium attractive nonbonded interactions decreased, but the interaction between clay and formamide remained slightly higher than between clay and water, as shown in Figure 3.13. The sodium-fluids attractive nonbonded interactions increased with increase in d-spacing; the sodium-methanol interactions were more than 1.5 times greater than the sodium-acetone interactions; and the sodium-water interactions were slightly greater than the sodium-

methanol and sodium-formamide interactions. The clay-fluids attractive nonbonded interactions increased with increase in d-spacing, but the interactions of water with clay layers had the lowest energy. Also, the interactions of methanol with clay layers were 3 times greater than that of clay layers with acetone and slightly less than that of clay layers with formamide, as shown in Figure 3.13. The clay-clay attractive interactions were predominated by van der Waals energy for dry as well as clay with 10% fluids content, but the attractive clay-sodium, sodium-fluids, and clay-fluids interactions were primarily electrostatic in nature, as shown in Table 3.3.

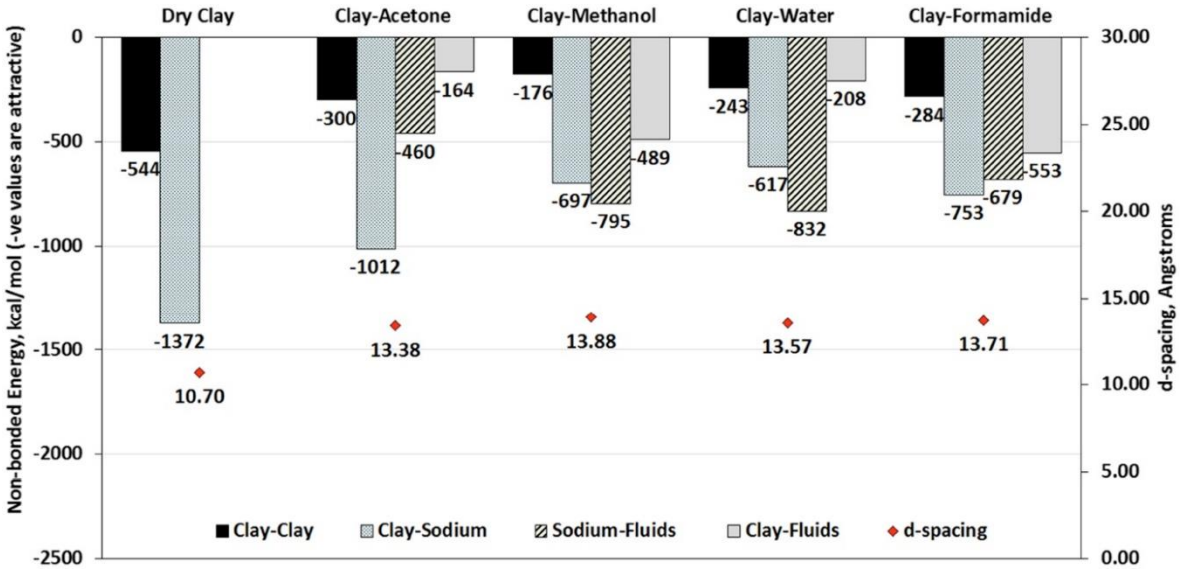

Figure 3.13. Nonbonded interaction energies between clay sheets for 10% acetone, methanol, water, and formamide and corresponding d-spacing. The interaction energies shown are clay-clay, clay-sodium, sodium-fluids, and clay-fluids.

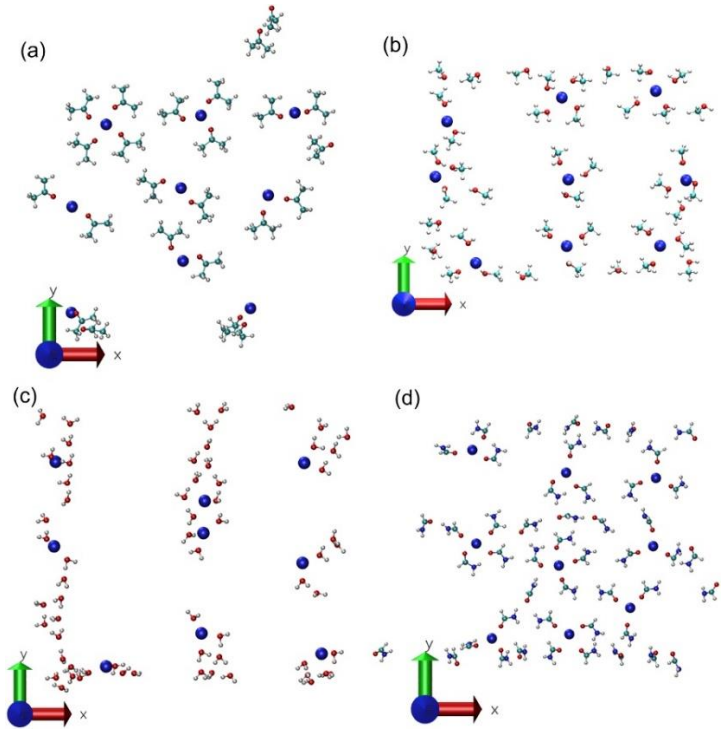

Figure 3.14. Planar view showing the conformation of molecules of fluids in proximity to sodium ions: (a) 10% acetone, (b) 10% methanol, (c) 10% water, and (d) 10% formamide. Fluids molecules and sodium ions are rendered in CPK and VDW formats, respectively.

Table 3.3. Interaction energies of clay-clay, sodium-fluids, clay-sodium, and clay fluids for dry Na-MMT and Na-MMT with 10% acetone, 10% methanol, 10% water, and10% formamide.

Fluid content (%)	Molecular model	Interactions	Energy (kcal/mol)		
			Electrostatic	VDW	Nonbonded
10	Dry clay	Clay-clay	104	-648	-544
	Clay-acetone		-122	-178	-300
	Clay-methanol		-47	-129	-176
	Clay-water		-88	-155	-243
	Clay-formamide		-101	-183	-284
	Clay-acetone	Sodium-fluids	-495	35	-460
	Clay-methanol		-857	62	-795
	Clay-water		-889	57	-832
	Clay-formamide		-734	55	-679
	Dry clay	Clay-sodium	-1510	138	-1372
	Clay-acetone		-1008	-4	-1012
	Clay-methanol		-684	-13	-697
	Clay-water		-604	-13	-617
	Clay-formamide		-751	-2	-753
	Clay-acetone	Clay-fluids	-165	1	-164
	Clay-methanol		-301	-188	-489
	Clay-water		-111	-97	-208
	Clay-formamide		-220	-333	-553

3.7. Conclusions

In this work, FTIR and MD simulations were carried out to investigate the swelling behavior of Na-MMT clay mineral with a wide range of organic fluids: formamide, water, methanol, and acetone. The shifts in the Si-O stretching band and Fe-OH deformation bands were observed on the FTIR spectra of Na-MMT clay with formamide and water showing larger band shifts than clay with methanol and acetone. This result indicates that there are significant nonbonded interactions between clay and polar fluids, resulting in the change in orientation of tetrahedral and octahedral clay sheets. The molecular models of Na-MMT clay with fluids were developed, and the representative clay-fluids models were validated by comparing MD

simulation d-spacing with the experimental results. The MD simulations were used to provide insight into conformation and quantitative nonbonded interactions of clay with formamide, water, methanol, and acetone at the molecular level. The results of our simulations indicate that the attractive nonbonded interactions, which are primarily electrostatic in nature, between clay and formamide and water, are significantly higher than those between clay and methanol and acetone. These results are consistent with the shifts of bands in FTIR studies. Furthermore, the nonbonded interactions play a significant role in the conformations of fluid molecules in proximity to sodium ions in the interlayer. A planar view of the conformations shows a well-organized pattern as the amount and polarity of interlayer fluids increase. The modeling study with ten weight percent of the four fluids in the interlayer gallery showed that the molecular interactions between clay sheets, sodium ions and fluid molecules are significantly different. The d-spacings in all four cases were different and ranged from 13.38 Å to 13.88 Å. The clay-clay interactions decreased with increasing d-spacing. The sodium-fluid and clay-fluid interactions appear to relate to the size, number of fluid molecules and the physical distribution of the molecules in the interlayer. These studies provide an insight into the molecular mechanism and indicate that the polarity of fluids plays a significant role in the interlayer swelling, alternation in the orientations, and evolution of microstructure of swelling clays at the molecular scale.

3.8. Conflict of Interest

The authors wish to confirm that there are no known conflicts of interest associated with this publication and there has been no significant support for this work that could have influenced its outcome.

3.9. Acknowledgements

The authors acknowledge the support of USDoT/Mountain Plains Consortium/UGPTI under grant No. #69A3551747108. The authors also acknowledge Computationally Assisted Science and Technology (CCAST) for providing computational resources at North Dakota State University.

3.10. References

[1] F.H. Chen, Foundations on expansive soils, Elsevier (2012).

[2] R.R. Rao, H. Rahardjo, D.G. Fredlund, Closed-form heave solutions for expansive soils, Journal of Geotechnical Engineering-Asce 114(5) (1988) 573-588.

[3] R.K. Katti, A.R. Katti, Behaviour of saturated expansive soil and control methods, AA Balkema (1994).

[4] K. Kayabali, Engineering aspects of a novel landfill liner material: Bentonite-amended natural zeolite, Engineering Geology 46(2) (1997) 105-114.

[5] H.H. Murray, Applied clay mineralogy today and tomorrow, Clay Minerals 34(1) (1999) 39-49.

[6] D. Sikdar, S.M. Pradhan, D.R. Katti, K.S. Katti, B. Mohanty, Altered phase model for polymer clay nanocomposites, Langmuir 24(10) (2008) 5599-5607.

[7] A.H. Ambre, D.R. Katti, K.S. Katti, Nanoclays mediate stem cell differentiation and mineralized ECM formation on biopolymer scaffolds, Journal of Biomedical Materials Research Part A 101(9) (2013) 2644-2660.

[8] M. Abdelrahman, D.R. Katti, A. Ghavibazoo, H.B. Upadhyay, K.S. Katti, Engineering physical properties of asphalt binders through nanoclay-asphalt interactions, Journal of Materials in Civil Engineering 26(12) (2014).

[9] J.K. Mitchell, K. Soga, Fundamentals of soil behavior, (2005).

[10] F.T. Madsen, M. Muller-Vonmoos, The swelling behaviour of clays, Applied clay science 4(2) (1989) 143-156.

[11] H.Y. Jo, T. Katsumi, C.H. Benson, T.B. Edil, Hydraulic conductivity and swelling of nonprehydrated GCLs permeated with single-species salt solutions, Journal of Geotechnical and Geoenvironmental Engineering 127(7) (2001) 557-567.

[12] A. Maria Gomez-Caravaca, R.M. Maggio, V. Verardo, A. Cichelli, L. Cerretani, Fourier transform infrared spectroscopy-Partial Least Squares (FTIR-PLS) coupled procedure application for the evaluation of fly attack on olive oil quality, Lwt-Food Science and Technology 50(1) (2013) 153-159.

[13] K.S. Katti, D.R. Katti, Relationship of swelling and swelling pressure on silica-water interactions in montmorillonite, Langmuir 22(2) (2006) 532-537.

[14] P.M. Amarasinghe, K.S. Katti, D.R. Katti, Nature of organic fluid-montmorillonite interactions: An FTIR spectroscopic study, Journal of Colloid and Interface Science 337(1) (2009) 97-105.

[15] P.M. Amarasinghe, K.S. Katti, D.R. Katti, Insight into role of clay-fluid molecular interactions on permeability and consolidation behavior of na-montmorillonite swelling clay, Journal of Geotechnical and Geoenvironmental Engineering 138(2) (2012) 138-146.

[16] K. Norrish, The swelling of montmorillonite, Discussions of the Faraday Society (18) (1954) 120-134.

[17] A. Delville, Modeling the clay water interface, Langmuir 7(3) (1991) 547-555.

[18] E.S. Boek, P.V. Coveney, N.T. Skipper, Monte Carlo molecular modeling studies of hydrated Li-, Na-, and K-smectites: Understanding the role of potassium as a clay

swelling inhibitor, Journal of the American Chemical Society 117(50) (1995) 12608-12617.

[19] F.R.C. Chang, N.T. Skipper, G. Sposito, Computer-simulation of interlayer molecular-structure in sodium montmorillonite hydrates, Langmuir 11(7) (1995) 2734-2741.

[20] S. Karaborni, B. Smit, W. Heidug, J. Urai, E. Van Oort, E. van Oort, The swelling of clays: Molecular simulations of the hydration of montmorillonite, Science 271(5252) (1996) 1102-1104.

[21] A. Anandarajah, Influence of particle orientation on one-dimensional compression of montmorillonite, Journal of Colloid and Interface Science 194(1) (1997) 44-52.

[22] R.M. Shroll, D.E. Smith, Molecular dynamics simulations in the grand canonical ensemble: Application to clay mineral swelling, Journal of Chemical Physics 111(19) (1999) 9025-9033.

[23] B.J. Teppen, K. Rasmussen, P.M. Bertsch, D.M. Miller, L. Schafer, Molecular dynamics modeling of clay minerals .1. Gibbsite, kaolinite, pyrophyllite, and beidellite, Journal of Physical Chemistry B 101(9) (1997) 1579-1587.

[24] D.R. Katti, P. Ghosh, S. Schmidt, K.S. Katti, Mechanical properties of the sodium montmorillonite interlayer intercalated with amino acids, Biomacromolecules 6(6) (2005) 3276-3282.

[25] D.R. Katti, S.R. Schmidt, P. Ghosh, K.S. Katti, Modeling the response of pyrophyllite interlayer to applied stress using steered molecular dynamics, Clays and Clay Minerals 53(2) (2005) 171-178.

[26] S.R. Schmidt, D.R. Katti, P. Ghosh, K.S. Katti, Evolution of mechanical response of sodium montmorillonite interlayer with increasing hydration by molecular dynamics, Langmuir 21(17) (2005) 8069-8076.

[27] S.M. Pradhan, K.S. Katti, D.R. Katti, Evolution of molecular interactions in the interlayer of na-montmorillonite swelling clay with increasing hydration, International Journal of Geomechanics 15(5) (2015) 1-9.

[28] A. Kadoura, A.K.N. Nair, S.Y. Sun, Molecular simulation study of montmorillonite in contact with variably wet supercritical carbon dioxide, Journal of Physical Chemistry C 121(11) (2017) 6199-6208.

[29] D.R. Katti, S.R. Schmidt, P. Ghosh, K.S. Katti, Molecular modeling of the mechanical behavior and interactions in dry and slightly hydrated sodium montmorillonite interlayer, Canadian Geotechnical Journal 44(4) (2007) 425-435.

[30] J.A. Greathouse, D.B. Hart, G.M. Bowers, R.J. Kirkpatrick, R.T. Cygan, Molecular simulation of structure and diffusion at smectite-water interfaces: Using expanded clay interlayers as model nanopores, Journal of Physical Chemistry C 119(30) (2015) 17126-17136.

[31] L. Sun, J.T. Tanskanen, J.T. Hirvi, S. Kasa, T. Schatz, T.A. Pakkanen, Molecular dynamics study of montmorillonite crystalline swelling: Roles of interlayer cation species and water content, Chemical Physics 455 (2015) 23-31.

[32] D.R. Katti, M.I. Matar, K.S. Katti, P.M. Amarasinghe, Multiscale modeling of swelling clays: A computational and experimental approach, KSCE Journal of Civil Engineering 13(4) (2009) 243-255.

[33] D.R. Katti, L. Srinivasamurthy, K.S. Katti, Molecular modeling of initiation of interlayer swelling in Na-montmorillonite expansive clay, Canadian Geotechnical Journal 52(9) (2015) 1385-1395.

[34] D.R. Katti, K.B. Thapa, K.S. Katti, Modeling molecular interactions of sodium montmorillonite clay with 3D kerogen models, Fuel 199 (2017) 641-652.

[35] N.T. Skipper, G. Sposito, F.R.C. Chang, Monte-carlo simulation of interlayer molecular-structure in swelling clay-minerals .2. monolayer hydrates, Clays and Clay Minerals 43(3) (1995) 294-303.

[36] J.J. Fripiat, H. Van Olphen, S. Clay Minerals, D. Organisation for economic co-operation and, data handbook for clay materials and other non-metallic minerals : providing those involved in clay research and industrial application with sets of authoriative data describing the physical and chemical properties and mineralogical composition of the available reference materials, Pergamon Press, Oxford ; New York, (1979).

[37] D. Sikdar, D.R. Katti, K.S. Katti, A molecular model for epsilon-caprolactam-based intercalated polymer clay nanocomposite: Integrating modeling and experiments, Langmuir 22(18) (2006) 7738-7747.

[38] A.D. MacKerell, D. Bashford, M. Bellott, R.L. Dunbrack, J.D. Evanseck, M.J. Field, S. Fischer, J. Gao, H. Guo, S. Ha, D. Joseph-McCarthy, L. Kuchnir, K. Kuczera, F.T.K. Lau, C. Mattos, S. Michnick, T. Ngo, D.T. Nguyen, B. Prodhom, W.E. Reiher, B. Roux, M. Schlenkrich, J.C. Smith, R. Stote, J. Straub, M. Watanabe, J. Wiorkiewicz-Kuczera, D. Yin, M. Karplus, All-atom empirical potential for molecular modeling and dynamics studies of proteins, Journal of Physical Chemistry B 102(18) (1998) 3586-3616.

[39] W.L. Jorgensen, J. Chandrasekhar, J.D. Madura, R.W. Impey, M.L. Klein, Comparison of simple potential functions for simulating liquid water, Journal of Chemical Physics 79(2) (1983) 926-935.

[40] D.R. Katti, Z.R. Patwary, K.S. Katti, Modelling clay-fluid interactions in montmorillonite clays, Environmental Geotechnics 4(5) (2016) 322-338.

[41] J.C. Phillips, R. Braun, W. Wang, J. Gumbart, E. Tajkhorshid, E. Villa, C. Chipot, R.D. Skeel, L. Kale, K. Schulten, Scalable molecular dynamics with NAMD, Journal of Computational Chemistry 26(16) (2005) 1781-1802.

[42] B.R. Brooks, R.E. Bruccoleri, B.D. Olafson, D.J. States, S. Swaminathan, M. Karplus, CHARMM - a program for macromolecular energy, minimization, and dynamics calculations, Journal of Computational Chemistry 4(2) (1983) 187-217.

[43] S.E. Feller, Y.H. Zhang, R.W. Pastor, B.R. Brooks, Constant-pressure molecular-dynamics simulation - the langevin piston method, Journal of Chemical Physics 103(11) (1995) 4613-4621.

[44] P.M. Amarasinghe, K.S. Katti, D.R. Katti, Molecular hydraulic properties of montmorillonite: A polarized fourier transform infrared spectroscopic study, Applied Spectroscopy 62(12) (2008) 1303-1313.

[45] A. Ambre, K.S. Katti, D.R. Katti, In situ mineralized hydroxyapatite on amino acid modified nanoclays as novel bone biomaterials, Materials Science & Engineering C-Materials for Biological Applications 31(5) (2011) 1017-1029.

[46] D.R. Katti, H.B. Upadhyay, K.S. Katti, Molecular interactions of kerogen moieties with Na-montmorillonite: An experimental and modeling study, Fuel 130 (2014) 34-45.

[47] M.H. Fu, Z.Z. Zhang, P.F. Low, Changes in the properties of a montmorillonite-water system during the adsorption and desorption of water - hysteresis, Clays and Clay Minerals 38(5) (1990) 485-492.

4. COMPRESSION OF NA-MONTMORILLONITE SWELLING CLAY INTERLAYER IS INFLUENCED BY FLUID POLARITY: A STEERED MOLECULAR DYNAMICS STUDY[2]

4.1. Introduction

Swelling clays are found all over the world. These clays are of significant importance in engineering due to properties exhibited such as high swelling capacity [1], high specific area [2], and low hydraulic conductivity [3]. These clays are used as the barrier liner materials in landfills [4] and high-level radioactive waste disposal [5], drug delivery systems in biomedical applications [6], as biomaterials in tissue engineering [7] and modifiers in pavement construction [8]. However, civil infrastructures are susceptible to damage due to high volume change exhibited by these clays, resulting in enormous damage to the buildings, roads, bridges, and embankments [9, 10].

Sodium-montmorillonite (Na-MMT), a smectite clay mineral is one of the major constituents of swelling clays [11]. This mineral comprises of a tetrahedral-octahedral-tetrahedral (T-O-T) structure where an octahedral clay sheet is sandwiched between tetrahedral clay sheets [12]. A negative charge on the individual clay sheets is developed due to isomorphous substitution by metal ions in the tetrahedral or octahedral clay sheets [13]. These charges are balanced by cations in the interlayer. In Na-MMT, the interlayer cations are sodium ions. In this study, in order to vary the clay-fluid interactions, fluids with a wide range of dielectric constants — formamide (110), water (80), methanol (33), acetone (20) are chosen. The

[2] This chapter describes the role of fluid polarity in the compressibility of swelling clay interlayer using molecular dynamic simulations. The content of this chapter is submitted for publication and is currently under review. The submitted article is coauthored by Keshab B. Thapa, and Kalpana S. Katti, and Dinesh R. Katti. Keshab B. Thapa had primary responsibility for collecting samples in the field and for interviewing users of the test system. Keshab B. Thapa was the primary developer of the conclusions that are advanced here. Keshab B. Thapa also drafted and revised all versions of this chapter. Dinesh R. Katti and Kalpana S. Katti served as proofreader and checked the math in the statistical analysis conducted by Keshab B. Thapa.

values in the parentheses are the dielectric constant values (DEC) of the fluid. These fluids are commonly found in landfill leachates and are identified as toxic and hazardous to health by the United States Environmental Protection Agency (EPA). Our previous experimental studies have shown that clay-fluid interactions significantly affect the macroscale properties of clays, including compressibility, consolidation, permeability, and swelling pressure [14]. Development of multiscale models that bridge molecular-scale interactions to macroscale properties are essential for accurate prediction of the clay response and also to tailor responses for avoiding detrimental effects and improve beneficial uses. In swelling clays, the hydration of the interlayer cations triggers the interlayer crystalline swelling [15-17]. The earlier double-layer models [18-20] attempt to evaluate the clay-water interactions in the clay interlayer [21]; however, these theories are not able to predict the interlayer swelling at smaller layer spacing.

Our previous experimental study shows that the particles of the saturated swelling clays successively breakdown into smaller sizes resulting in increased swelling and reduction of swelling pressure [22]. This phenomenon is further incorporated into a computational model to capture the role of the particle subdivision on swelling and swelling pressure [23]. The evolution of microstructure, mechanical properties, and fluid flow behavior of Na-MMT clay with various organic fluids are also studied experimentally [14]. The molecular interactions of Na-MMT clay with these fluids are primarily nonbonded, and the nonbonded interactions for polar fluids with the clay are significantly higher than with low and medium polar fluids [24]. With an increase in the polarity of the fluids, the swelling pressure increases; however, the hydraulic conductivity decreases dramatically [14]. Thus, the clay-fluid interactions at the molecular level control the macroscopic properties of Na-MMT clay.

Many computational studies—molecular dynamics (MD), Monte Carlo (MC) method, and Discrete Element Method (DEM)—have been conducted to evaluate the nature of interactions of swelling clays with a various interlayer cations[25-28], at different levels of hydration [29-32], and with organic fluids [33, 34]. Molecular dynamics studies are also conducted to study the swelling mechanism and hysteresis of expansive clay [35]. Steered molecular dynamics (SMD) simulation is a computational technique in which the external forces are applied to the molecules to guide a system from one state to another at an atomic scale [36]. In our prior work, the evolution of the mechanical response of the dry and hydrated Na-MMT clay with multiple layers of water is evaluated using SMD simulations [37, 38]. The stress-deformation response of the clay interlayer is linear for dry clay and clay with one monolayer of water and nonlinear for clay with two and three monolayers of water in the interlayer [30]. The level of hydration, solvation of interlayer cations, and clay-fluid interactions control the interlayer spacing and modulus of swelling of Na-MMT clay upon compression. The elastic properties of swelling clays have been studied using MD simulations, and it has been reported that the water content, nature of interlayer cation, and temperature influence the stiffness tensor of montmorillonite clays [39]. The stiffness of the layer silicates in the presence of the surface charges is calculated using density functional theory (DFT) and MD simulations [40]. The elastic tensors of Na-MMT clays over a wide range of hydrations are computed using MD simulations[41]. The nanoscale hardness of tobermorite and montmorillonite clay has been computed using local structure optimization (LSO) approach by applying a biaxial deformation or stress [42].

For the dry case, the stability of the stacked structure is maintained by the nonbonded interactions between sodium ions and clay sheets [43, 44]. However, these attractive interactions

decrease as soon as the water molecules are introduced in the swelling clay interlayer [44]. The sodium ions also attract the water molecules in the interlayer, and the sodium-water interactions appear to reduce the sodium-clay interactions, resulting in the initiation of interlayer swelling of Na-MMT clay [34]. The nonbonded interactions of Na-MMT clay with toluene, acetone, methanol, water, and formamide are studied experimentally and computationally, and results show that the polar fluids have higher interactions with clay than low and medium polar fluids [34, 45]. However, the compressive behavior of Na-MMT clay with these fluids have not been investigated at the molecular level. These clay-fluid interactions and the interlayer response of swelling clays upon compression are essential for reliable prediction of the macroscale compression that is crucial for the effective and economical design of infrastructure and for public safety. In this study, we present our results from SMD simulations on Na-MMT clay with a wide range of organic fluids. This work also provides an insight into the role of the fluid content, and the polarity of the fluids on the interlayer spacing, interlayer volume, interlayer strain, interlayer modulus, nonbonded interactions and fluid conformations upon externally applied stresses at the molecular level.

4.2. Model Construction

The chemical formula for Na-MMT clay that is used in the experiments [46] is (Ca0.12Na0.32K0.05)[Al3.01Fe(III)0.41Mn0.01Mg0.54Ti0.02][Si7.98Al0.02]O20(OH)4, which has both octahedral and tetrahedral isomorphic substitutions. The chemical formula of the clay model is simplified to $NaSi_{16}(Al_6FeMg)O_{20}(OH)_4$. The coordinates of the unit cell are obtained from Skipper et al., [47] and the atomic charges are obtained from Teppen et al. [48]. The dimensions of the unit cell of this model are 5.28 Å x 9.14 Å x 6.56 Å. In this work, a 6x3 Na-

MMT model is used, which is comprised of 6 unit cells in X-direction and 3 unit cells in Y-direction, as shown in Figure 4.1 (a).

The isomorphic substitution by metal atoms in the octahedral sheet results in a negative charge on the individual clay sheets. In order to account for isomorphic substitution, nine Aluminum ($Al3^{+}$) cations were replaced by nine Iron ($Fe3^{+}$) cations and another nine Aluminum ($Al3^{+}$) cations by Magnesium ($Mg2^{+}$) cations in 6x3 Na-MMT model. These negative charges of the clay sheets are balanced by inserting nine sodium (Na^{+}) cations. The detailed construction of 6x3 model is described in our previous work. The overall dimensions of the model are 31.68 Å x 27.44 Å x 24.16 Å. The Na-MMT and fluids models are developed using Material Studio™ and PSFGen plug-in of Visual Molecular Dynamics (VMD 1.9.3) software [36, 49]. The CHARMM force field parameters for formamide, methanol, and acetone are obtained from the Chemistry at Harvard Macromolecular Mechanics (CHARMM) force field parameters GUI Archive-CHARMM Small Molecule [50], and the water molecule was Transferable Intermolecular Potential 3 Point (TIP3P) [51].

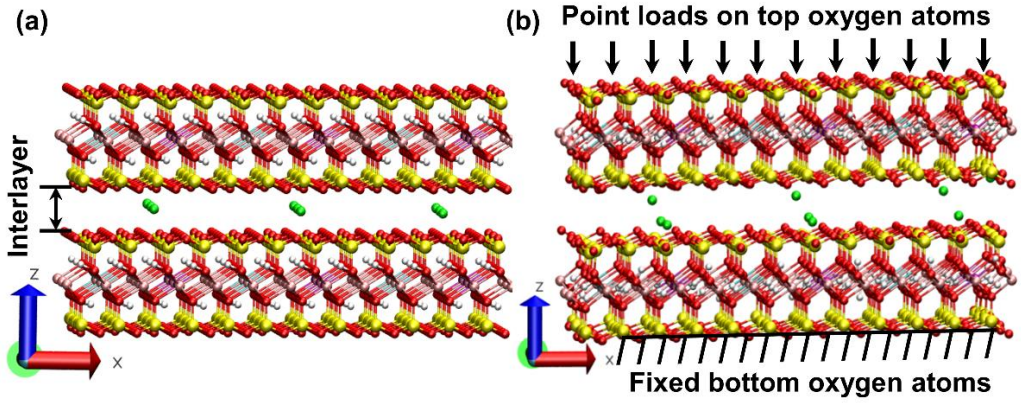

Figure 4.1. (a) Initial molecular model of dry Na-MMT and (b) equilibrium Na-MMT clay at 300 K temperature and one atmospheric pressure.

In this study, the representative clay models consist of 10% acetone, methanol, water, and formamide as well as 30% methanol, water, and formamide in the interlayer. Based on the

molecular weight of individual atoms, 10% fluid content has 24 acetone molecules, 40 methanol molecules, 64 water molecules, and 48 formamide molecules. Similarly, 30% fluid content is equivalent to 120 molecules of methanol, 216 molecules of water, and 120 molecules of formamide. Initially, we placed the interlayer fluid molecules in a single layer for 10% fluid and three layers for 30% fluid.

4.3. Simulation Details

In this study, MD and SMD simulations of dry and hydrated 6x3 unit Na-MMT clay models were carried out by using NAMD 2.12 that is developed by Theoretical and Computational Biophysics Group, Beckman Institute at the University of Illinois at Urbana-Champaign [52]. The CHARMM force field parameters reported in our previous studies [30, 38] were used. Visual molecular dynamics (VMD 1.9.3) was used for visualization and interaction energy computation. An isothermal-isobaric (NPT) ensemble was used for running the MD simulations. Further, we minimized the model by using a conjugate gradient method followed by increasing the temperature from 0 K to 300 K in three steps with an increment of 100 K using the Langevin dynamics control method [53]. Following this, we increased the pressure from 0 bar to 1.01 bar in four steps with 0.25 bar increments using the Nose-Hoover Langevin piston control method [54] while maintaining a constant temperature at 300 K. The simulation was run for an additional 400 ps. The total simulation time up to this point was one ns.

We conducted constant-force SMD simulations to evaluate the compression of clay interlayer spacing for dry and hydrated 6x3 unit Na-MMT clay molecular models. The interlayer spacing refers to the void space between adjacent clay layers, and the sum of the interlayer spacing and the thickness of the clay sheet is the d-spacing. The interlayer strain is measured by a change in interlayer spacing upon the application of a load relative to the original position. We

applied a uniform compressive point load in the z-direction on each of the oxygen atoms lying on the top surface of the clay sheet. A total of 108 oxygen atoms on the top surface of the clay sheet were selected, and the average projected load-bearing area was 729.63 Å2 in the x-y plane. Also, we fixed the 108 oxygen atoms of the bottom surface of the clay sheet in x, y, and z directions, mimicking axial compression, as shown in Figure 4.1(b). In this model, the fluid molecules are free to move in all directions. Further, we applied a wide range of compressive loads on each oxygen atom of the top clay sheet. The applied loads were, 0, 25, 50, 75, 100, 150, 200, 300, 400, and 600 pN (10-12 N) per atom for dry and hydrated Na-MMT clay model, and the equivalent stresses were 0, 0.37, 0.74, 1.11, 1.48, 2.22, 2.96, 4.44, 5.92, and 8.88 GPa.

SMD simulations were run for a total simulation time of 1.2 ns at a time step of 0.5 fs (10-15 s). We averaged the last 20 ps of constant-force SMD simulation trajectory to compute the nonbonded interaction energies. The switch and cut-off distances for Van der Waals and electrostatic energy computations were 16 Å and 17 Å, respectively. All the simulations were run with ten nodes and 20 CPUs (total of 200 CPUs) using 2.66 GHz Intel Xenon X5550 processor at the Center for Computationally Assisted Science and Technology (CCAST) at North Dakota State University.

4.4. Results and Discussions

We measured the interlayer spacings after MD simulations for the dry clay model and the clay intercalated with acetone, methanol, water, and formamide, models, by computing the vertical distance between the corresponding surface oxygen atoms of the top and bottom clay sheets. For the dry Na-MMT clay, the average interlayer spacing and d-spacing are 3.96 Å and 10.52 Å, respectively. These values are obtained from equilibrated MD simulation and consistent with the experimentally obtained values from a previous study [24] (Priyanthi M. Amarasinghe

et al., 2009). The interlayer spacing for Na-MMT clay with 10% acetone, methanol, water, and formamide is 6.29 Å, 6.42 Å, 6.51 Å, and 6.72 Å, respectively, as shown in Figure 4.2 (a-d).

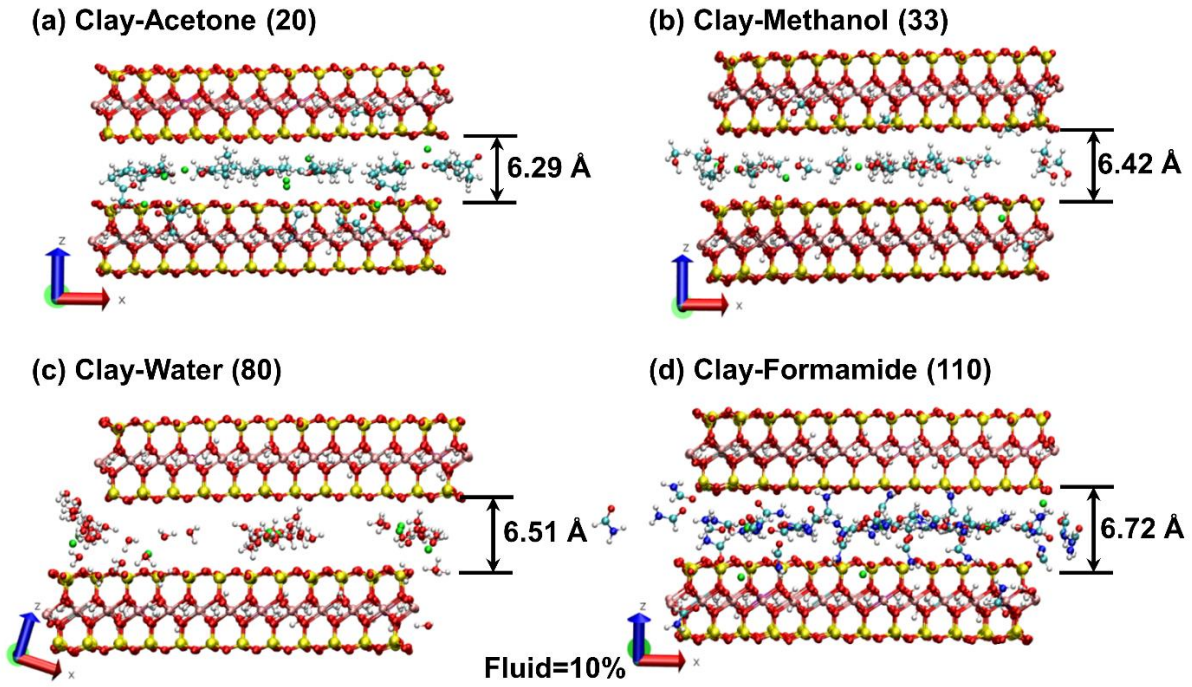

Figure 4.2. Na-MMT clay models with 10% interlayer fluids showing the interlayer spacing for: (a) clay-acetone (20), (b) clay-methanol (33), (c) clay-water (80), and (d) clay-formamide (110). The values in the parentheses are the dielectric constant of the fluid.

Our previous work has shown that the maximum acetone content in the clay interlayer based on experiments and modeling is 10% [24, 45]. As shown in Figure 4.3 (a-c), the interlayer spacing for Na-MMT clay with 30% methanol, water, and formamide is 9.94 Å, 10.85 Å, and 6.72 Å, respectively. These results are also consistent with our previous study [45]. We observed that the interlayer spacing increases with an increase in the polarity of fluids as well as with an increase in fluid content. Subsequently, the dry clay and hydrated clay-fluid molecular models are used for the constant-force SMD simulations to evaluate the compressive response of the interlayer with fluids of varying polarities and three fluid contents (0%,10%, and 30%).

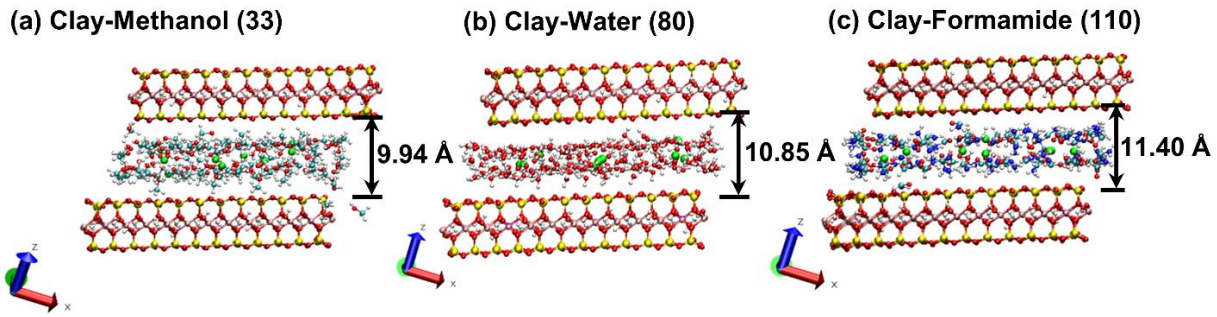

Figure 4.3. Na-MMT clay models with 30% interlayer fluids at NPT showing the interlayer spacing: (a) clay-methanol (33), (b) clay-water (80), and (c) clay-formamide (110). The values in the parentheses are the dielectric constant of the fluid.

A comparison of interlayer spacing values upon compression for dry clay, clay-acetone, clay-methanol, clay-water, and clay-formamide molecular models for 10% and 30% fluid content are presented in Table 4.1. For dry clay, a relatively significant drop in the interlayer spacing is observed at 0 to 1.48 GPa stress, and a more gradual drop in the interlayer spacing is observed from 2.22 to 8.88 GPa stress as shown in Figure 4.4(a). For 10% clay-fluid models, we observe an approximately linear decrease in interlayer spacing from 0 to 1.48 GPa stress. The decrease is 0.53 Å for clay-acetone, 0.52 Å for clay-methanol, 0.54 Å for clay-water, and 0.49 Å for clay-formamide. This is followed by a nonlinear drop in the interlayer spacing for 2.22 to 8.88 GPa stress, of 1.57 Å for clay-acetone, 1.11 Å for clay-methanol, 0.86 Å for clay-water, and 0.82 Å for clay-formamide. It is also observed that a significant reduction in the interlayer spacing upon compression takes place for 0 to 1.48 GPa stress for Na-MMT with 30% clay-fluid models. The reduction in interlayer spacing is 2.21 Å for clay-methanol, 1.54 Å for clay-water, and 1.28 Å for clay-formamide, as shown in Figure 4.4(b). Further significant nonlinear drop is observed in the interlayer spacing for 2.22 to 8.88 GPa stress of 2.01 Å for clay-methanol, 1.89 Å for clay-water, and 1.25 Å for clay-formamide.

Table 4.1. The decrease in the interlayer spacing at various normal stresses of the SMD simulations of Na-MMT dry clay as well as clay with 10% and 30% fluid content in the interlayer.

Normal Stress (GPa)	Interlayer Spacing (Å)							
	Dry Clay	Clay-Acetone	Clay-Methanol		Clay-Water		Clay-Formamide	
	-	FC=10	FC=10	FC=30	FC=10	FC=30	FC=10	FC=30
0.00	3.83	6.29	6.42	9.94	6.51	10.85	6.72	11.40
0.37	3.74	6.20	6.27	9.29	6.39	9.90	6.55	10.78
0.74	3.68	6.07	6.16	8.76	6.23	9.65	6.44	10.47
1.11	3.63	5.89	6.02	8.27	6.14	9.45	6.31	10.30
1.48	3.59	5.76	5.90	7.73	5.97	9.31	6.23	10.12
2.22	3.58	5.51	5.71	7.20	5.72	9.05	6.08	9.84
2.96	3.57	5.31	5.47	6.74	5.55	8.69	5.84	9.56
4.44	3.55	4.89	5.18	5.91	5.27	7.91	5.63	9.20
5.92	3.54	4.51	4.92	5.39	5.12	7.55	5.48	8.90
8.88	3.52	3.94	4.60	5.19	4.86	7.16	5.26	8.59

FC=Fluid content (%) in the clay interlayer

Given the surface area of the clay sheet (729. 63 $Å^2$) and interlayer spacing of the clay-fluid models, the interlayer volume upon compression from 0 to 8.88 GPa stress for clay with 10% and 30% fluid content is presented in Table 4.2. For 10% fluid content, the interlayer volume at 0 GPa stress is 4589 $Å^3$ for clay-acetone, 4684 $Å^3$ for clay-methanol, 4750 $Å^3$ for clay-water, and 4903 $Å^3$ for clay-formamide. This interlayer volume upon compression at 1.48 GPa is decreased by about 8% for clay-acetone, clay-methanol, clay-water, and 6% for clay-formamide. Furthermore, the interlayer volume under externally applied stress of 8.88 GPa with relative to that of 0 GPa decreases by 37% for clay-acetone, 28% for clay-methanol, 25% for clay-water, and 22% for clay-formamide. Similarly, the interlayer volume at 0 GPa stress for 30% fluid content is 7253 $Å^3$ for clay-methanol, 7916 $Å^3$ for clay-water, and 8318 $Å^3$ for clay-formamide. Relative to this interlayer volume, the interlayer volume at a compressive stress of 1.48 GPa decreases by 22% for clay-methanol, 14% for clay-water, and 11% for clay-

formamide. Furthermore, the interlayer volume at 8.88 GPa with relative to that of 0 GPa is dramatically decreased by 48% for clay-methanol, 34% for clay-water, and 25% for clay-formamide. Thus, for Na-MMT clay with 10% and 30% fluid, the compression of the interlayer volume for polar fluids at 8.88 GPa stress with respect to a stress of 0 GPa is significantly lower than that for medium and low polar fluids as shown in Figure 4.5. It appears that the swelling pressure which increases with increase in fluid polarity opposes the compression of the clay sheets.

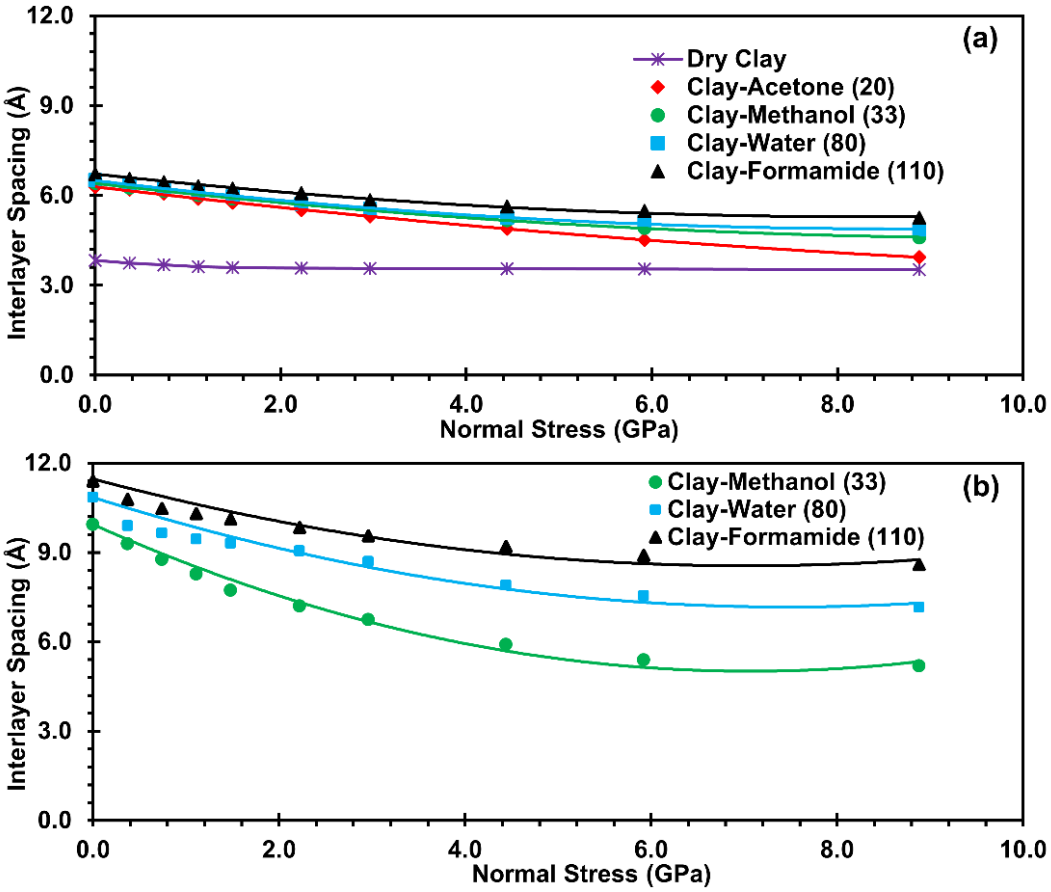

Figure 4.4. Change in interlayer spacing of clay containing fluids of different polarities for identically applied normal stress for (a) Na-MMT dry clay and clay with 10% fluid and (b) Na-MMT clay with 30% fluid. Dielectric constant values of fluids are shown in parenthesis.

Table 4.2. Interlayer volume when the normal stresses are applied on dry clay as well as clay with 10% and 30% fluid content in the interlayer.

Normal Stress (GPa)	Interlayer Volume (Å^3)							
	Dry Clay	Clay-Acetone	Clay-Methanol		Clay-Water		Clay-Formamide	
	-	FC=10	FC=10	FC=30	FC=10	FC=30	FC=10	FC=30
0.00	2794	4589	4684	7253	4750	7916	4903	8318
0.37	2729	4524	4575	6778	4662	7223	4779	7865
0.74	2685	4429	4495	6392	4546	7041	4699	7639
1.11	2645	4298	4392	6034	4480	6895	4604	7515
1.48	2619	4203	4305	5640	4356	6793	4546	7384
2.22	2608	4020	4166	5253	4173	6603	4436	7180
2.96	2603	3874	3991	4918	4049	6340	4261	6975
4.44	2590	3568	3779	4312	3845	5771	4108	6713
5.92	2584	3291	3590	3933	3736	5509	3998	6494
8.88	2570	2875	3356	3787	3546	5224	3838	6268

FC=Fluid content (%) in the interlayer

4.4.1. Evaluation of Mechanical Properties of the Clay Interlayer

As the external stress is applied on the clay sheet, the interlayer spacing for dry clay decreases, accompanied by minimal deformation of the clay sheet. We observe a linear reduction in interlayer spacing of the dry clay reduced from 3.83 Å to 3.59 Å for a stress range of 0-1.48 GPa in region-I, resulting in a strain of 0.06, as shown in Figure 4.6(a). We also observe a linear decrease in interlayer spacing from 3.58 Å to 3.45 Å for applied stress from 2.22 GP to 8.88 GPa with a simultaneous increase in interlayer strain to 0.08 at the end of 8.88 GPa stress in region-II. Thus, two distinct stress-interlayer spacing responses are observed for regions I and II. An attempt is made to evaluate the interlayer modulus by using the least-square method. The interlayer moduli for dry clay in region-I and region-II are found to be 21.39 GPa and 476.16

GPa, respectively. These values are the same order of magnitude with our previous experimental and computational studies [38, 55].

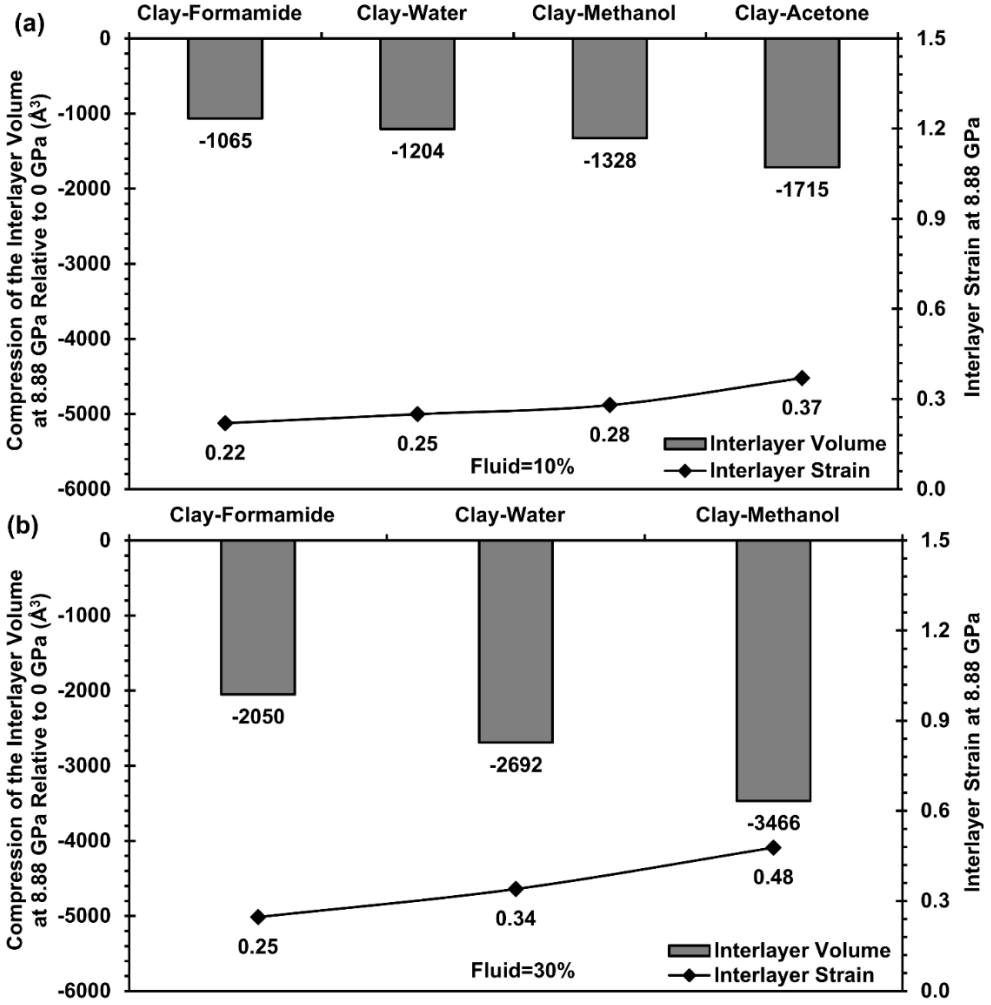

Figure 4.5. Decrease in the interlayer volume at 8.88 GP with respect to 0 GPa for Na-MMT with (a) 10% acetone, methanol, water, and formamide and (b) 30% methanol, water, and formamide. The interlayer strain at 8.88 GPa increased with decrease in the polarity of the fluid.

Figure 4.6(a) also shows the stress-strain characteristics along the c-axis for clay with 10% fluid. For all models, the strain in region-I increases linearly to about 0.08, which is consistent with the previous SMD simulations of hydrated Na-MMT clay [30] and organically modified clay where the interlayer deformation is very small in the level of stresses from 0-1.48 GPa. However, the strain in region-II increased from 0.12 to 0.37 for clay-acetone, 0.11 to 0.28

for clay-methanol, 0.12 to 0.25 for clay-water, and 0.10 to 0.22 for clay-formamide. Figure 4.6(b) shows the stress-strain behavior of clay with 30% fluid. In region-I from 0-1.48 GPa, the interlayer spacing results in a strain of to 0.22 for clay-methanol, 0.14 for clay-water, 0.11 for clay-formamide. At 8.88 GPa of stress, the interlayer undergoes a maximum strain of 0.48 for clay-methanol, 0.34 for clay-water, and 0.25 for clay-formamide. The interlayer strain at a normal stress of 8.88 GPa increases with an increase in the amount of the fluid content and with the decrease in the polarity of fluid.

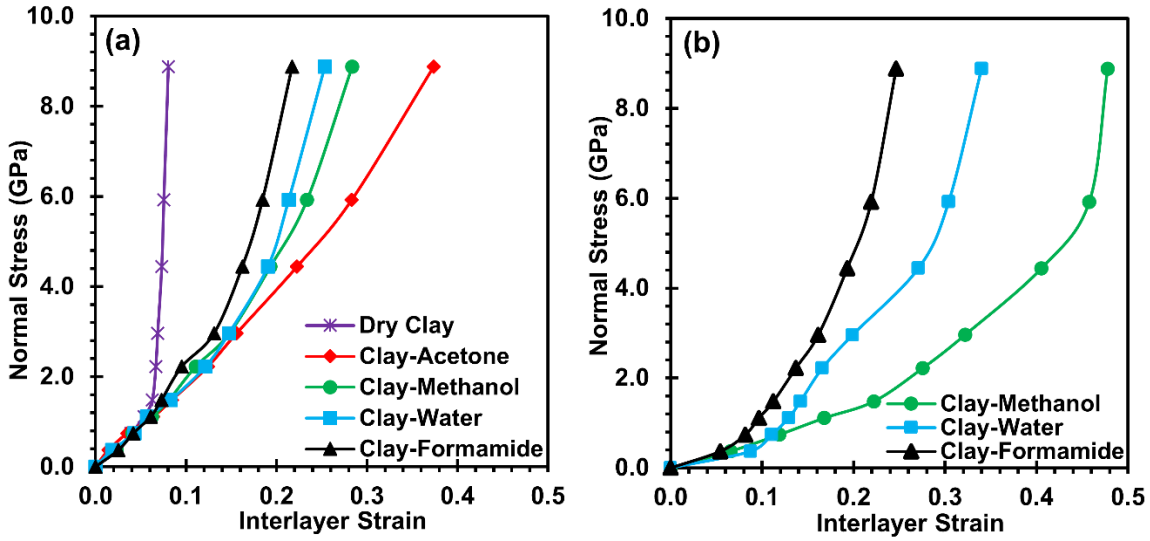

Figure 4.6. Stress versus interlayer strain for (a) dry clay and clay with 10% fluid (b) clay with 30% fluid. Numbers in parentheses represent values of dielectric constants for the fluids.

Thus, the clay interlayers are more compressible when they contain fluids of lower polarity compared to high polarity fluids. Also, the stress-strain plot of the medium polar fluid methanol falls between the low polar fluid acetone and high polar fluids formamide as shown in Figure 4.6(b). Our previous consolidation experiments have also shown that the void ratio versus effective stress curve for medium polar fluid lies between the low and high polar fluids, and void ratio of Na-MMT clay with polar fluid is significantly higher than that for low polar fluid for a given effective stress [14]. The effect of the polarity of fluid under compression of swelling clay

is observed not only at the micro-scale but also at the molecular level. The macroscale responses are influenced by both the microstructure and the molecular-scale interactions; thus an attempt to directly correlating the molecular scale observations to the macroscale responses would be a stretch. However, the similarities of the responses do point to the possible relationship between the molecular scale responses and macroscale compressive behavior of swelling clays.

We calculated the interlayer modulus for all 10% clay-fluid models from the slope of the least square fit line of the stress-strain plot. The stress-strain plot for clay with all four fluids is linear with a relatively shallow slope from 0-1.48 GPa in the region-I. The interlayer moduli in this level of stress are found to be 21.39 GPa for dry clay, 18.46 GPa for clay-formamide, 18.25 GPa for clay-water, 18.03 GPa for clay-methanol, and 18.02 GPa for clay-acetone. The interlayer modulus in the region-I is lower relative to the interlayer modulus of dry clay, indicating that a softer interlayer response results for clay-fluid models under compression, as the clay layers separate more by the introduction of the fluids in the clay interlayer. In region-II, the slope of the stress-strain plot is steeper for clay with polar fluid than for low polar fluid. The interlayer moduli in the region-II are 26.30 GPa, 38.05 GPa, 49.37 GPa, and 52.61 GPa for clay-acetone, clay-methanol, clay-water, and clay-formamide, respectively. Similarly, we also computed the interlayer moduli in the region I and region II for Na-MMT with 30% methanol, water, and formamide. The interlayer modulus in region-I is 7.07 GPa for clay-methanol, 20.42 GPa for clay-water, and 19.18 GPa for clay-formamide. Additionally, the interlayer moduli in region-II are 37.96 GPa for clay-methanol, 41.98 GPa for clay-water, and 69.57 GPa clay-formamide, resulting in an increase in the interlayer modulus with an increase in the fluid polarity.

4.4.2. Volumetric Analysis of the Compression of the Clay Interlayer

We conducted a volumetric analysis of the various components of the interlayer to attempt to identify the key mechanisms responsible for the observed differences in the compressibility of the clay interlayer for fluids with different dielectric constants. The results of the analysis at 8.88 GPa compressive stress relative to the 0GPa compressive stress are presented in Table 4.2. As indicated earlier, for a given fluid content, the change in the volume of the interlayer decreases with an increase in the dielectric constant of the fluid. In addition, for a given fluid, the volume change increases with an increase in the initial fluid content. Upon the application of the compressive stress of 8.88GPa, the compression of methanol, water and formamide filled interlayers at 30 percent initial fluid content when compared to compression of 10% initial fluid content interlayers showed additional compression of 161%, 124%, and 92.5% respectively. The change in the interlayer volume or the compression of the interlayer under the applied stress is the sum of the volume of the fluid molecules exiting the interlayer, the change in the volume of the clay-fluid interaction zone and the compression of the fluid layer in the interlayer. At a fluid content of 10%, the compression of the fluid ranges from about 1% to 14% of the change in the interlayer volume, while for fluid content of 30%, the contribution to the compression of the fluid layer increases to 29% to 57%. The contribution of fluid exiting the interlayer under the applied compression ranges from 5% to 16% at fluid content of 10% and from 15% to 25% at fluid content of 30%, indicating increased expulsion of fluid under compression at higher fluid content. The largest contribution to the compression of the interlayer arises from the compression of the clay-fluid interaction zone, defined as the region between the clay sheets and the fluid molecules and ranges from 79% to 87% of the interlayer volume change for 10% fluid content and 27% to 47% for the interlayer volume change for 30% fluid content.

The reduced contribution of the clay-fluid interaction zone contribution to the interlayer volume change at higher fluid content results from increased contribution from the change in volume of the fluid layer and the volume of the expelled fluid molecules from the interlayer. Also, the volume change of the clay-fluid interaction zone for low dielectric constant fluids (acetone and methanol) is larger than the volume change of the interaction zone for high dielectric constant fluids (water and formamide).

4.4.3. Conformation of the Fluid Molecules in the Interlayer

A planar view of the equilibrated model of Na-MMT with 10% acetone, methanol, water, and formamide is shown in Figure 4.7. This snapshot shows the hydration of sodium ions by four fluids at equilibrium condition (NPT) and 0 GPa stress in XY-plane. Similarly, Figure 4.8 shows the planar view at the end of 8.88 GPa stress. Upon compression, the proximity of the fluid molecules around the sodium ions increases with an increase in the polarity of the fluids, resulting in the formation of a well-organized configuration for high polar fluids. At 8.88 GPa, the oxygen atoms are attracted and oriented towards the sodium ions, suggesting a shell formation around the fluid molecules. At of the end of 8.88 GPa stress loading, 11 out of 24 acetone molecules, 18 out of 40 methanol molecules, 31 out of 64 water molecules, and 21 out of 48 formamide molecules exited the interlayer. The volume of the fluid molecules that have exited from the interlayer is 210 $Å^3$ for acetone, 234 $Å^3$ for methanol, 63 $Å^3$ for water, and 200 $Å^3$ for formamide.

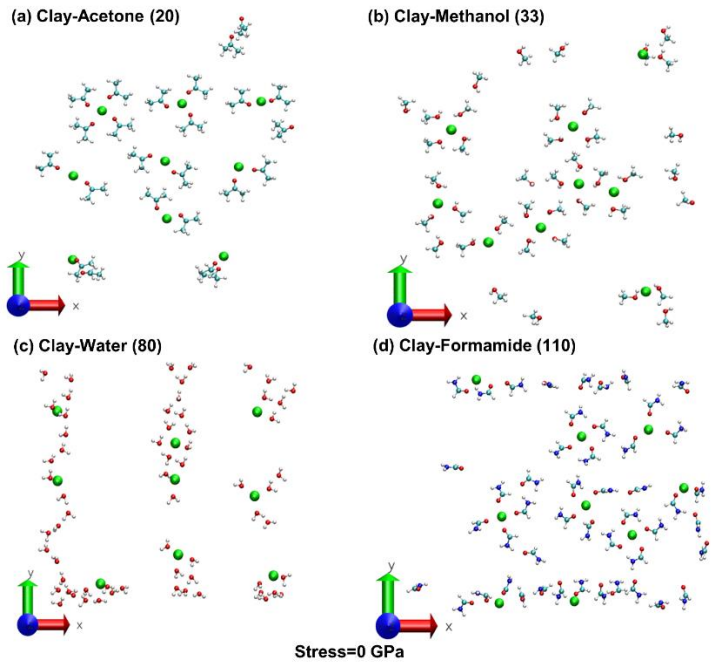

Figure 4.7. Planar view displaying conformation of 10% interlayer fluids in close proximity to sodium cations upon compression at NTP and 0 GPa: (a) clay-acetone (20), (b) clay-methanol (33), (c) clay-water (80), and (d) clay-formamide (110). The values in the parenthesis are dielectric constant.

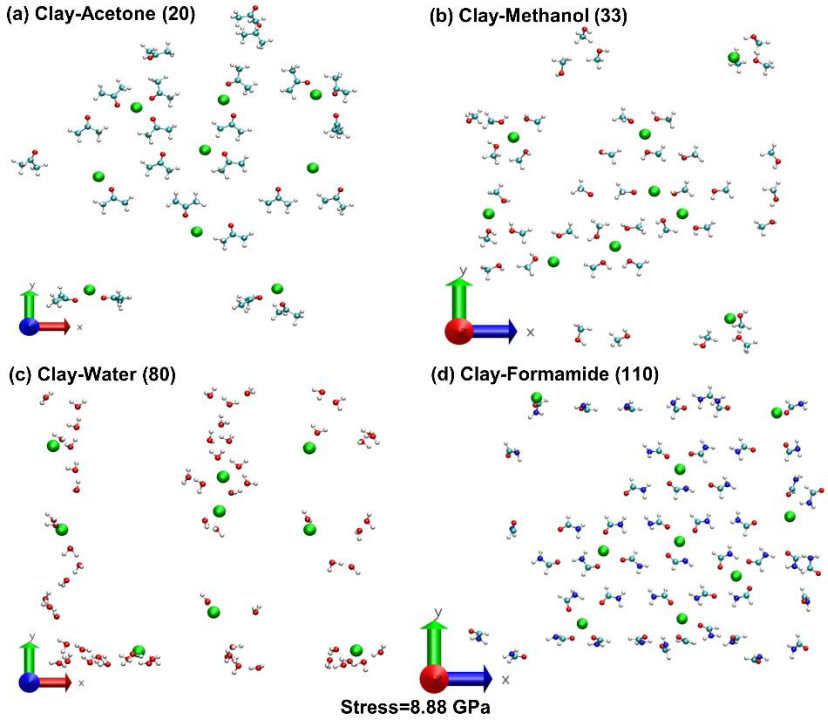

Figure 4.8. Planar view displaying the conformation of 10% fluid in proximity to sodium cations at 8.88 GPa: (a) clay-acetone, (b) clay-methanol, (c) clay-water, and (d) clay-formamide.

Figure 4.9 (a-c) shows the hydration of the sodium ions for Na-MMT with 30% fluid at 0 GPa in XY-plane. Similarly, Figure 4.9 (d-f) shows the change in conformation of the fluid molecules around sodium ions at 8.88 GPa. At the end of 8.88 GPa stress loading, 48 out of 120 formamide molecules, 64 out of 216 water, and 94 out of 120 methanol have exited the interlayer. The volume of the fluid molecules that have exited from the interlayer is 1248 $Å^3$ for methanol, 479 $Å^3$ for water, and 649 $Å^3$ for formamide. It is observed that three oxygen atoms of interlayer methanol and five oxygen atoms of water and formamide molecules are attracted and oriented towards each of the sodium ions, resulting in the well-organized formation.

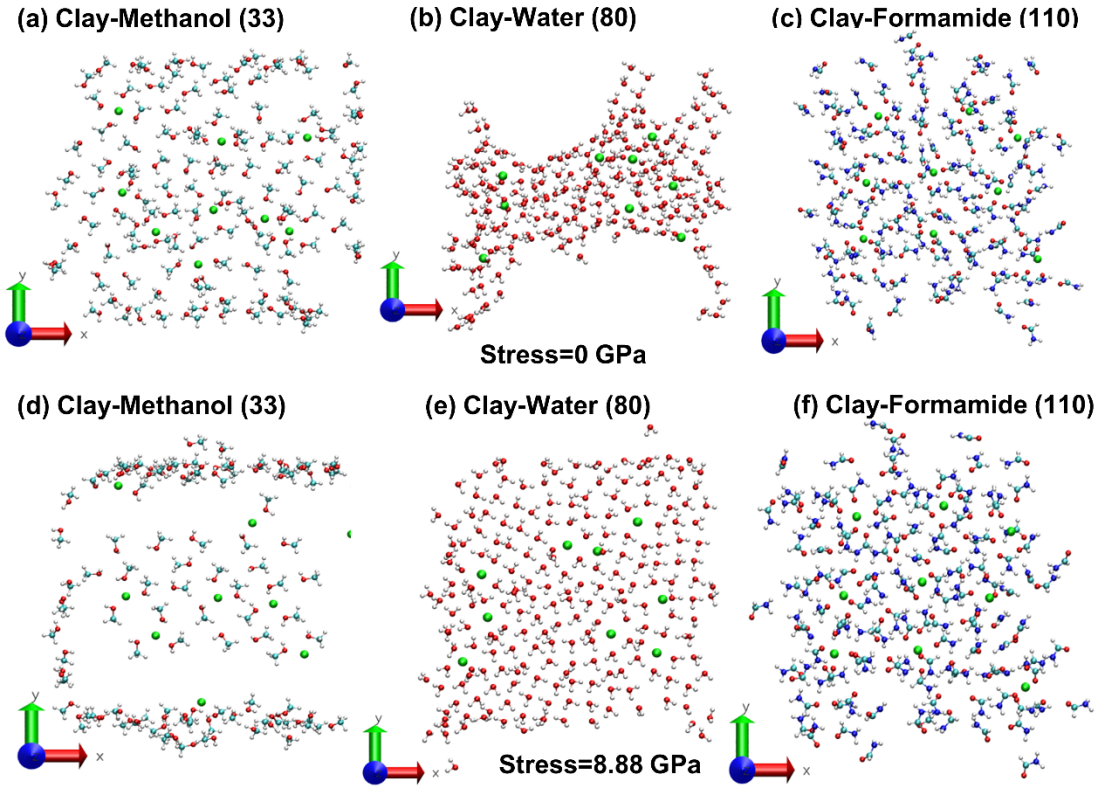

Figure 4.9. Planar view of 30% fluid around sodium cations for Na-MMT with methanol, water, and formamide at 0 GPa (a-c) and at 8.88 GPa (d-f).

The conformation of the 10% fluid molecules in the vertical XZ-plane at 0 GPa and 8.88 GPa is shown in Figure 4.10. Although the fluid molecules in the interlayer remained in the single-layer before and after compression, the polar fluids formamide and water behave more

like a relatively rigid layer of constant thickness relative to the low, medium polar fluids which were more deformable.

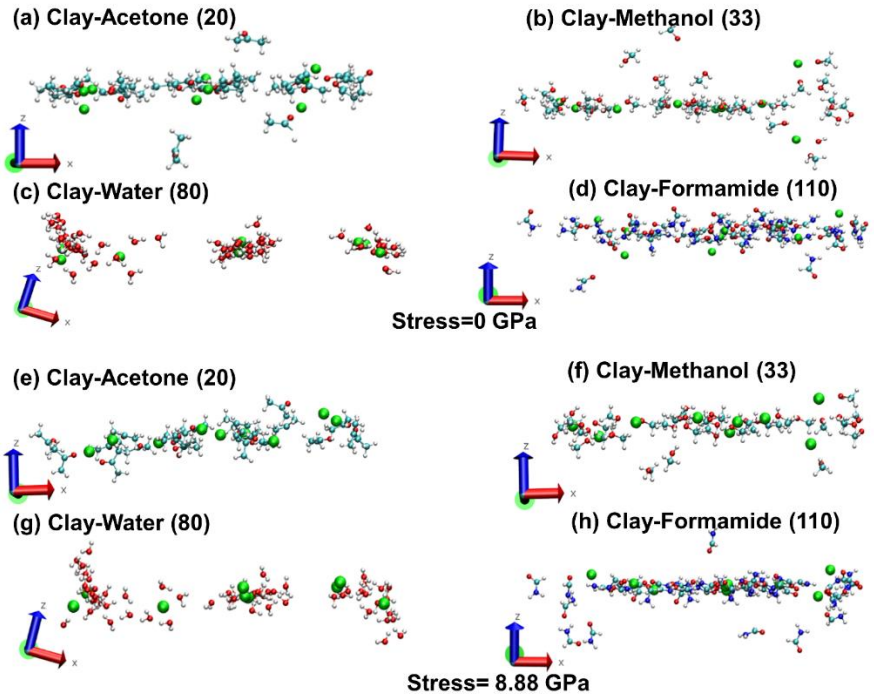

Figure 4.10. Planar view showing the thickness of 10% interlayer fluids in close proximity to the sodium cations: (a-d) at 0 GPa and (e-f) at 8.88 GPa. The values in the parenthesis are dielectric constant.

Figure 4.11 shows the conformation of 30% fluid in XZ-plane at 0 GPA and 8.88 GPa. It is observed that the two monolayers of the methanol and water at 0 GPa have been noticeably compressed to one distinct monolayer at 8.88 GPa, resulting in a significant decrease in the thickness of the fluid molecules from 3.67 Å to 1.43 Å for methanol and from 5.25 Å to 2.74 Å for water. However, the two monolayers of the interlayer formamide molecules are compressed from 5.83 Å to 4.76 Å, which indicates that the two formamide layers have remained relatively intact as compared to methanol and water**.** Therefore, the total interlayer deformation upon compression results not only due to the compression of the void space between the clay sheets and fluids but also from the compression of the fluid molecules in the interlayer, in addition to the volume of the fluids exiting the interlayer.

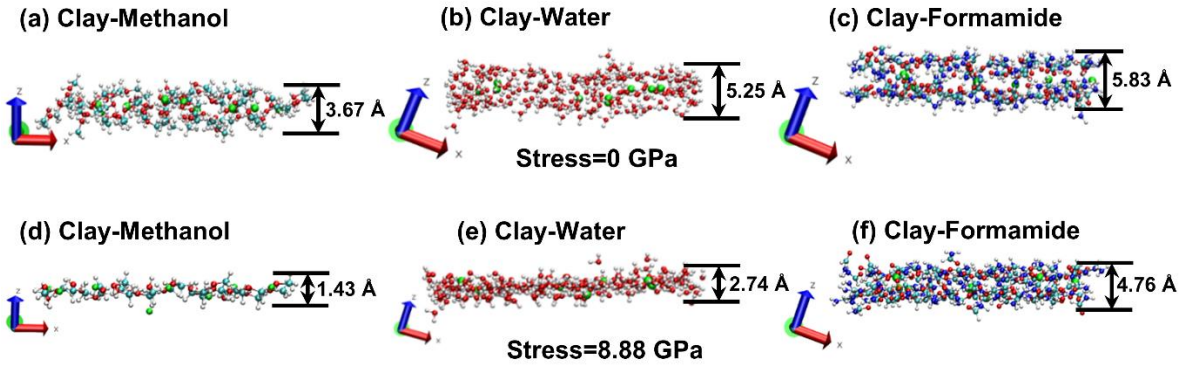

Figure 4.11. The conformation showing the thickness of 30% fluid in proximity to sodium cations for Na-MMT with methanol, water, and formamide at 0 GPa (a-c) and at 8.88 GPa (d-f).

4.4.4. Quantitative Interactions of Clay with the Interlayer Fluids

The role of fluid polarity and the nature of the total nonbonded interactions—both electrostatic and van der Waals—could provide an insight into the molecular mechanisms that influence the compressive response of the clay interlayer. The nonbonded interaction energies between clay-clay, clay-sodium, sodium-fluid, and clay-fluid for dry Na-MMT clay and clay with 10% and 30% fluids before and after compression are presented in Table 4.3. The magnitude of the nonbonded interactions between clay sheets are approximately the same for Na-MMT clay with 10% acetone, methanol, water, and formamide at 8.88 GPa, however, these interaction energies as compared to 0 GPa increased by 46%, 89%, 112%, and 85% for clay-acetone, clay-methanol, clay-water, and clay-formamide, respectively. The repulsive electrostatic energy for dry clay is due to negatively charged clay sheets, and the total clay-clay interactions at 8.88 GPa is 16% less than at 0 GPa. The nature of clay-clay interactions before and after compression is predominantly attractive van der Waals energies, and the attractive electrostatic interactions are very small.

Table 4.3. Non-bonded interaction energies of clay-clay, clay-sodium, sodium-fluid, and clay-fluid for dry clay and clay with 10% and 30% fluid content upon compression at 0 GPa and 8.88 GPa.

Fluid	Interactions	Molecular Models	Energy (kJ/mol)					
			At 0 GPa			At 8.88 GPa		
			ELE	VDW	Total	ELE	VDW	Total
10%	Clay-Clay	Dry Clay	+372	-2766	-2389	+259	-2268	-2013
		Clay-Acetone	-510	-761	-1272	-393	-1469	-1862
		Clay-Methanol	-280	-644	-925	-88	-1657	-1745
		Clay-Water	-397	-686	-1088	-8	-2301	-2310
		Clay-Formamide	-347	-707	-1050	-238	-1703	-1941
	Clay-Sodium	Dry Clay	-6456	+644	-5816	-6385	+879	-5506
		Clay-Acetone	-4188	-17	-4205	-4531	+92	-4439
		Clay-Methanol	-3305	-46	-3351	-3623	+243	-3381
		Clay-Water	-2548	-50	-2598	-3640	+343	-3293
		Clay-Formamide	-3937	-21	-3958	-4113	+310	-3803
	Sodium-Fluid	Clay-Acetone	-2084	+151	-1933	-887	+54	-833
		Clay-Methanol	-3582	+264	-3322	-2598	+184	-2414
		Clay-Water	-3724	+238	-3485	-1724	+230	-1498
		Clay-Formamide	-2519	+176	-2343	-1820	+159	-1665
	Clay-Fluid	Clay-Acetone	+54	-678	-628	+4	+1322	+1326
		Clay-Methanol	-1008	-870	-1879	-222	+1234	+1013
		Clay-Water	-431	-423	-854	-163	+920	+761
		Clay-Formamide	-736	-1251	-1992	-372	+736	+377
30%	Clay-Clay	Clay-Methanol	+29	-146	-117	-25	-1435	-1460
		Clay-Water	-222	-38	-259	-247	-745	-992
		Clay-Formamide	-155	-29	-184	-439	-209	-649
	Clay-Sodium	Clay-Methanol	-3180	-50	-3230	-4540	+197	-4343
		Clay-Water	-2297	-33	-2330	-3151	-59	-3209
		Clay-Formamide	-1761	-25	-1787	-2464	-50	-2515
	Sodium-Fluid	Clay-Methanol	-6895	+318	-6577	-2243	+255	-1987
		Clay-Water	-9586	+259	-9330	-6757	+402	-6355
		Clay-Formamide	-5983	+218	-5766	-3795	+297	-3498
	Clay-Fluids	Clay-Methanol	-4289	-2067	-6351	-113	+1100	+987
		Clay-Water	-1042	-1084	-2125	-63	-1029	-1092
		Clay-Formamide	-1234	-1849	-3084	-301	-808	-1109

ELE=Electrostatic; VDW=van der Waals; and Total=ELE+VDW=Nonbonded

The total attractive clay-sodium interactions at 8.88 GPa are the highest and decrease with an increase in the fluid polarity, as shown in Figure 4.12(a). The predominantly attractive

electrostatic interactions are due to negatively charged clay sheets and positively charged sodium ions. However, the attractive Van der Waals energy at 0 GPa switched to repulsive energy at 8.88 GPa for all cases with fluid in the interlayer. This is due to a decrease in the distance between clay sheets and sodium ions at high stresses, and the repulsive nature of short-range van der Waals energy dominates.

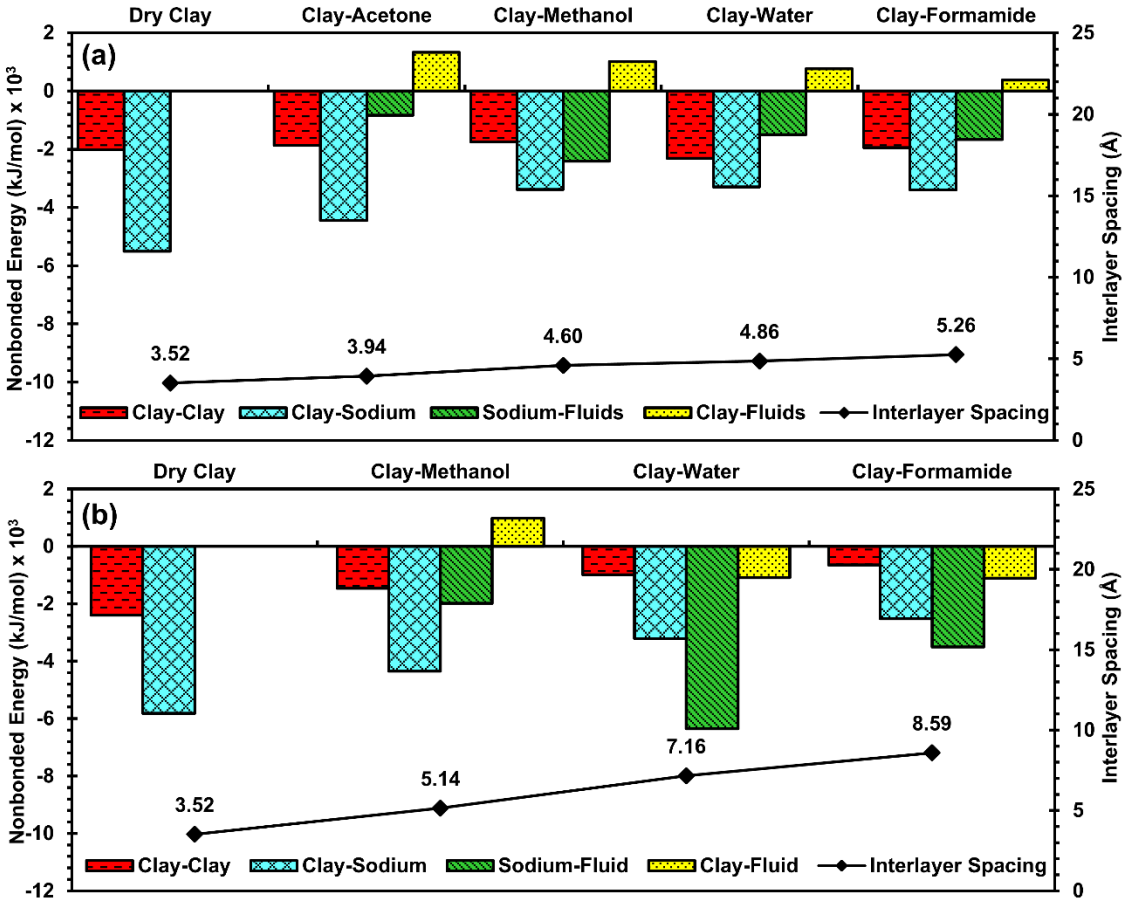

Figure 4.12. Interlayer spacing increased with the increase in the fluid polarity and the corresponding non-bonded interaction energies at 8.88 GPa of clay with (a) 10% and (b) 30% fluid.

Although the total sodium-fluid interactions at 8.88 GPa are lower than at 0 GPa as shown in Table 4.3, potentially as a result of fluid molecules exiting the interlayer due to compression, the attractive interactions of the sodium ions with the fluid molecules indicate that these fluid molecules are hydrated and strongly bound to sodium ions at 8.88 GPa. These

attractive interactions are predominantly electrostatic in nature. However, the repulsive Van der Waals interactions in both cases are small. Generally, the total sodium-fluid interactions increased with increase in the polarity of the fluids, with the exception of medium polar fluid methanol, which showed highest attractive interactions with the sodium ions among all fluids. Another significant observation is that the attractive van der Waals interactions of clay sheets with these four fluids at 0 GPa changed to repulsive interactions at 8.88 GPa. The short-range repulsive van der Waals interactions become strong. The applied external stresses push the top clay sheet in close proximity to the fluid molecules by reducing the interlayer spacing, and thus the clay sheets and fluid molecules repel each other.

The nonbonded interaction energies at 0 GPa and 8.88 GPa for Na-MMT with 30% methanol, water, and formamide are also presented in Table 4.3. The attractive clay-clay interactions, which are dominated by van der Waals energy, at 8.88 GPa decreased with an increase in the polarity of fluids, as shown in Figure 4.12(b). Moreover, these interaction energies as compared to 0 GPa are significantly increased by 1146%, 282%, and 252% for clay-methanol, clay-water, and clay-formamide, respectively. Similarly, the nonbonded clay-sodium interactions at 8.88 GPa are increased with an increase in the fluid polarity, and the nature of the interactions are electrostatic. These interactions relative to 0 GP increased by 34%, 38%, and 41% for clay-methanol, clay-water, and clay-formamide, respectively. The sodium-fluid interactions upon compression at 8.88 GPa for clay-formamide and clay-water are higher than clay-methanol. These interactions with respect to 0 GPa decreased by 70%, 32%, and 39% for clay-methanol, clay-water, and clay-formamide, respectively. The attractive nonbonded clay-fluid interaction for clay with 30% methanol at 0 GPa changed to the repulsive interactions, as shown in Table 4.3. The interaction is dominated by repulsive Van der Waals energy. However,

these attractive nonbonded clay-fluid interactions at 8.88 GPa as compared to 0 GPa decrease by 49% for clay-water and 64% for clay-formamide.

4.4.5. Comparison of Na-MMT Clay with 10% and 30% Fluid Content in the Interlayer

Although the clay interlayer has the same fluid content for all fluids, the interlayer spacing values are significantly different before and after the application of normal stress on the top of the clay sheet. On comparing the clay interlayer spacing of dry clay with that of the clay with the four fluids, we observed that the interlayer spacing increases with increase in the fluid polarity as well as with an increase in the fluid content in the interlayer. We also observe that the presence of the fluids in the interlayer lead to the interlayer being more compressible than dry clay. The clay-formamide model has the highest interlayer spacing. For a given normal stress, interlayer strain is significantly lower for clay with polar fluids than that of low polar fluids for both 10% and 30% fluid content, which indicates that the externally applied normal stress faces more resistance by the swelling pressure in the interlayer for clay with polar fluids than the lower polarity fluids.

Although the fluid molecules maintain a well-organized configuration around the sodium ions, the tendency of the fluid molecules to exit the interlayer for 30% fluid is higher than 10% fluid, and these fluid molecules are much more randomly oriented upon compression. For Na-MMT with 10% fluid, the compression of the fluid molecules with increasing stress is very small, whereas significant compression of the fluid layers occurs for 30% fluid. Thus the compression of the space between the clay sheets and fluid molecules (clay-fluid interaction zone) and exiting of fluid molecules from the interlayer contribute to the overall interlayer strain for Na-MMT with 10% fluid in the interlayer. However, the overall strain upon compression for Na-MMT with 30% fluid is not only due to the compression of the clay-fluid interaction zone

and exiting of the fluid molecules from the interlayer, but also the compression of the fluid molecules in the interlayer.

When the fluid molecules are introduced into the clay interlayer, the clay-clay and clay-sodium interactions decrease; however, the sodium-fluid and clay-fluid interactions increase both for 10% and 30% fluid content. Relative to dry clay, the clay-clay interactions at 0 GPa for 10% fluid are slightly decreased, and these interactions are small for 30% fluid.

As the number of fluid molecules in the interlayer increase, the clay-sodium interactions reduce, and these interaction energies increase upon compression. The nature of the clay-sodium interactions before and after compression is primarily attractive electrostatic energy. The clay-sodium and clay-clay interactions reduce more with the increase in fluid polarity. However, the sodium-fluid interactions increase with an increase in the fluid content, as a result of more fluid molecules in the interlayer. These interactions, however, decrease significantly upon compression.

The attractive clay-fluid interactions further increased with an increase in fluid content, again due to the increased number of fluid molecules. Under the stress of 8.88 GPa, the clay-fluid interactions changed from attractive to repulsive energy for Na-MMT with 10% acetone, methanol, water, and formamide. The attractive clay-fluid interaction before compression changes to repulsive energy upon compression, only for clay with 30% methanol but decreases significantly for clay with 30% water and formamide. This suggests that the hydration of the clay sheets also persists in the presence of the greater amount of polar fluids even upon compression. The sodium ion-fluid interactions also decrease upon compression, likely as the result of fluid molecules existing the interlayer and changes to the conformation of the fluid molecules in the interlayer. At higher fluid content (30%), it is apparent that the change in the interactions

between fluid molecules and both clay and sodium ions upon compression is significantly higher for lower polarity fluid methanol (92%) versus that for higher polarity fluids water (35%) and formamide (48%), and correlate well with the volume of the expulsion of the fluid molecules which is the highest for methanol followed by water and formamide.

4.5. Conclusions

- SMD simulations are used to evaluate the mechanical response of the interlayer of dry Na-MMT clay and clay with 10% and 30% fluid content with fluids with a range of polarities reflected by their dielectric constants: low polar fluids acetone(20), methanol(33), and high polar fluids water(80), and formamide(110). The interlayer spacing for dry Na-MMT clay decreased rapidly and linearly upon externally applied stress from 0-1.48 GPa and increased more slowly from 2.22-8.88 GPa. While the stress-deformation response of the clay interlayer is linear from 0-1.48 GPa, it is nonlinear from 2.22 to 8.88 GPa for all clay-fluid models.
- Upon compression, a softer clay interlayer response is observed for clay with fluids than that of dry clay interlayer. Additionally, clay interlayer with polar fluids is less compressible but much stiffer than that of low and medium polar fluids. Thus, the compressibility of clay interlayer is influenced by the polarity of the fluid in the interlayer.
- The compressibility of the clay interlayer is the result of compression of the clay-fluid interaction zone, exiting of the fluid molecules from the interlayer and the compression of the fluid in the interlayer. The compression of the clay-fluid interaction zone has a substantial contribution to the overall compression of the interlayer. Significant compression of the thickness of the fluid layers is observed

for clay with 30% fluid content as opposed to the interlayer with 10% fluid content. The number and volume of the fluid molecules that exited from the interlayer upon compression for clay with 30% fluid are greater than that of 10% fluid.

- The nonbonded interaction energies between clay-clay, clay-sodium, sodium-fluid, and clay-fluid molecules for 10% and 30% fluid content as well as before and after compression is computed. For Na-MMT clay with 10% acetone (20), methanol (33), water (80), and formamide (110), the attractive clay-fluid interactions changed to the repulsive interactions upon compression. The attractive clay-fluid interactions for Na-MMT with 30% methanol (33) changed to repulsive interactions upon compression, whereas the clay-fluid interactions for Na-MMT clay with 30% water (80) and formamide (110) remain attractive, indicating that the hydration of the clay sheets upon compression continues when polar fluid molecules are present in the interlayer than lower polarity fluids. Sodium ion-fluid interactions also decreased significantly upon compression. At higher fluid content, it is apparent that the change in the interaction energy between fluid molecules and both clay and sodium ions upon compression is significantly higher for lower polarity fluid methanol compared to high polar fluids water and formamide and correlates well with the volume of the expulsion of fluid molecules from the interlayer.
- This study demonstrates that the compressibility of the Na-montmorillonite clay interlayer is influenced by fluid polarity and would be an important factor to consider for the development of robust multiscale models of clays.

4.6. Acknowledgments

The authors would like to acknowledge the support of USDoT, Mountain Plains Consortium (MPC) grants MPC-506 (agreement # DTRT13-G-UTC38) and MPC-548(agreement# 69A3551747108). We also acknowledge Computationally Assisted Science and Technology (CCAST) (NSF# 1229316) for providing computational resources at North Dakota State University. Author K. B. T. acknowledges support from ND EPSCoR through a doctoral dissertation fellowship.

4.7. References

[1] J.M. Cases, I. Berend, G. Besson, M. Francois, J.P. Uriot, F. Thomas, J.E. Poirier, Mechanism of adsorption and desorption of water-vapor by homoionic montmorillonite .1. the sodium-exchanged form, Langmuir 8(11) (1992) 2730-2739.

[2] I. Berend, J.M. Cases, M. Francois, J.P. Uriot, L. Michot, A. Masion, F. Thomas, Mechanism of adsorption and desorption of water-vapor by homoionic montmorillonites. 2. the $Li^{+,}$ Na^{+}, K^{+}, Rb^{+} and Cs^{+}-exchanged forms, Clays and Clay Minerals 43(3) (1995) 324-336.

[3] R.P. Chapuis, Sand-bentonite liners - predicting permeability from laboratory tests, Canadian Geotechnical Journal 27(1) (1990) 47-57.

[4] K. Kayabali, Engineering aspects of a novel landfill liner material: Bentonite-amended natural zeolite, Engineering Geology 46(2) (1997) 105-114.

[5] A.M. Tang, Y.J. Cui, N. Barnel, Thermo-mechanical behaviour of a compacted swelling clay, Geotechnique 58(1) (2008) 45-54.

[6] J.H. Choy, S.J. Choi, J.M. Oh, T. Park, Clay minerals and layered double hydroxides for novel biological applications, Applied Clay Science 36(1-3) (2007) 122-132.

[7] A. Ambre, K.S. Katti, D.R. Katti, In situ mineralized hydroxyapatite on amino acid modified nanoclays as novel bone biomaterials, Materials Science & Engineering C-Materials for Biological Applications 31(5) (2011) 1017-1029.

[8] J.Y. Yu, P.C. Feng, H.L. Zhang, S.P. Wu, Effect of organo-montmorillonite on aging properties of asphalt, Construction and Building Materials 23(7) (2009) 2636-2640.

[9] R.R. Rao, H. Rahardjo, D.G. Fredlund, Closed-form heave solutions for expansive soils, Journal of Geotechnical Engineering 114(5) (1988) 573-588.

[10] E. Sebastian, G. Cultrone, D. Benavente, L.L. Fernandez, K. Elert, C. Rodriguez-Navarro, Swelling damage in clay-rich sandstones used in the church of San Mateo in Tarifa (Spain), Journal of Cultural Heritage 9(1) (2008) 66-76.

[11] R.E. Grim, Clay mineralogy, Mcgraw-Hill Book Company, Inc; New York (1953).

[12] J.K. Mitchell, K. Soga, Fundamentals of soil behavior, (2005).

[13] R.W.G. Wyckoff, Crystal structures, Krieger (1964).

[14] P.M. Amarasinghe, K.S. Katti, D.R. Katti, Insight into role of clay-fluid molecular interactions on permeability and consolidation behavior of Na-montmorillonite swelling clay, Journal of Geotechnical and Geoenvironmental Engineering 138(2) (2012) 138-146.

[15] A. Delville, Modeling the clay water interface, Langmuir 7(3) (1991) 547-555.

[16] D.R. Katti, L. Srinivasamurthy, K.S. Katti, Molecular modeling of initiation of interlayer swelling in Na-montmorillonite expansive clay, Canadian Geotechnical Journal 52(9) (2015) 1385-1395.

[17] F.T. Madsen, M. Muller-Vonmoos, The swelling behaviour of clays, Applied clay science 4(2) (1989) 143-156.

[18] D.C. Grahame, Diffuse double layer theory for electrolytes of unsymmetrical valence types, Journal of Chemical Physics 21(6) (1953) 1054-1060.

[19] H. Van Olphen, An introduction to clay colloid chemistry: for clay technologists, geologists, and soil scientists, 2nd Edition, Wiley, New York, (1977).

[20] E.J.W. Verwey, Theory of the stability of lyophobic colloids, Journal of Physical and Colloid Chemistry 51(3) (1947) 631-636.

[21] H.Y. Jo, T. Katsumi, C.H. Benson, T.B. Edil, Hydraulic conductivity and swelling of nonprehydrated GCLs permeated with single-species salt solutions, Journal of Geotechnical and Geoenvironmental Engineering 127(7) (2001) 557-567.

[22] D. R. Katti, V. Shanmugasundaram, Influence of swelling on the microstructure of expansive clays, Canadian Geotechnical Journal 38(1) (2001) 175-182.

[23] D. R. Katti, M.I. Matar, K.S. Katti, P.M. Amarasinghe, Multiscale modeling of swelling clays: A computational and experimental approach. KSCE Journal of Civil Engineering, 13(4) (2009) 243-255

[24] P.M. Amarasinghe, K.S. Katti, D.R. Katti, Nature of organic fluid-montmorillonite interactions: An FTIR spectroscopic study, Journal of Colloid and Interface Science 337(1) (2009) 97-105.

[25] R.T. Cygan, J.J. Liang, A.G. Kalinichev, Molecular models of hydroxide, oxyhydroxide, and clay phases and the development of a general force field, Journal of Physical Chemistry B 108(4) (2004) 1255-1266.

[26] P. Mignon, P. Ugliengo, M. Sodupe, E.R. Hernandez, Ab initio molecular dynamics study of the hydration of Li^+, Na^+ and K^+ in a montmorillonite model. Influence of isomorphic substitution, Physical Chemistry Chemical Physics 12(3) (2010) 688-697.

[27] M. Segad, B. Jonsson, T. Akesson, B. Cabane, Ca/Na montmorillonite: Structure, forces and swelling properties, Langmuir 26(8) (2010) 5782-5790.

[28] D.E. Smith, Molecular computer simulations of the swelling properties and interlayer structure of cesium montmorillonite, Langmuir 14(20) (1998) 5959-5967.

[29] V. Marry, B. Rotenberg, P. Turq, Structure and dynamics of water at a clay surface from molecular dynamics simulation, Physical Chemistry Chemical Physics 10(32) (2008) 4802-4813.

[30] S.R. Schmidt, D.R. Katti, P. Ghosh, K.S. Katti, Evolution of mechanical response of sodium montmorillonite interlayer with increasing hydration by molecular dynamics, Langmuir 21(17) (2005) 8069-8076.

[31] R.M. Shroll, D.E. Smith, Molecular dynamics simulations in the grand canonical ensemble: Application to clay mineral swelling, Journal of Chemical Physics 111(19) (1999) 9025-9033.

[32] T.J. Tambach, E.J.M. Hensen, B. Smit, Molecular simulations of swelling clay minerals, Journal of Physical Chemistry B 108(23) (2004) 7586-7596.

[33] E.J.M. Hensen, B. Smit, Why clays swell, Journal of Physical Chemistry B 106(49) (2002) 12664-12667.

[34] D.R. Katti, K.B. Thapa, K.S. Katti, The role of fluid polarity in the swelling of sodium-montmorillonite clay: A molecular dynamics and Fourier transform infrared spectroscopy study, Journal of Rock Mechanics and Geotechnical Engineering 10(6) (2018) 1133-1144.

[35] S. Karaborni, B. Smit, W. Heidug, J. Urai, E. Van Oort, E. van Oort, The Swelling of Clays: Molecular simulations of the hydration of montmorillonite, Science 271(5252) (1996) 1102-1104.

[36] J.C. Phillips, R. Braun, W. Wang, J. Gumbart, E. Tajkhorshid, E. Villa, C. Chipot, R.D. Skeel, L. Kale, K. Schulten, Scalable molecular dynamics with NAMD, Journal of Computational Chemistry 26(16) (2005) 1781-1802.

[37] D.R. Katti, S.R. Schmidt, P. Ghosh, K.S. Katti, Modeling the response of pyrophyllite interlayer to applied stress using steered molecular dynamics, Clays and Clay Minerals 53(2) (2005) 171-178.

[38] D.R. Katti, S.R. Schmidt, P. Ghosh, K.S. Katti, Molecular modeling of the mechanical behavior and interactions in dry and slightly hydrated sodium montmorillonite interlayer, Canadian Geotechnical Journal 44(4) (2007) 425-435.

[39] B. Carrier, M. Vandamme, R.J.M. Pellenq, H. Van Damme, Elastic properties of swelling clay particles at finite temperature upon hydration, Journal of Physical Chemistry C 118(17) (2014) 8933-8943.

[40] G.D. Zartman, H. Liu, B. Akdim, R. Pachter, H. Heinz, Nanoscale tensile, shear, and failure properties of layered silicates as a function of cation density and stress, Journal of Physical Chemistry C 114(4) (2010) 1763-1772.

[41] D. Ebrahimi, R.J.M. Pellenq, A.J. Whittle, Nanoscale elastic properties of montmorillonite upon water adsorption, Langmuir 28(49) (2012) 16855-16863.

[42] M.J.A. Qomi, D. Ebrahimi, M. Bauchy, R. Pellenq, F.J. Ulm, Methodology for estimation of nanoscale hardness via atomistic simulations, Journal of Nanomechanics and Micromechanics 7(4) (2017) 1-7.

[43] K. Cornelis, B. Dutrow, Manual of mineral science, John Wiley & Sons, Inc, (2007).

[44] S.M. Pradhan, K.S. Katti, D.R. Katti, Evolution of molecular interactions in the interlayer of na-montmorillonite swelling clay with increasing hydration, International Journal of Geomechanics 15(5) (2015) 1-9.

[45] D.R. Katti, Z.R. Patwary, K.S. Katti, Modelling clay-fluid interactions in montmorillonite clays, Environmental Geotechnics 4(5) (2016) 322-338.

[46] J.J. Fripiat, H. Van Olphen, S. Clay Minerals, D. Organisation for economic co-operation and, data handbook for clay materials and other non-metallic minerals : providing those involved in clay research and industrial application with sets of authoriative data describing the physical and chemical properties and mineralogical composition of the available reference materials, Pergamon Press, Oxford ; New York (1979).

[47] E.S. Boek, P.V. Coveney, N.T. Skipper, Monte Carlo molecular modeling studies of hydrated Li-, Na-, and K-smectites: Understanding the role of potassium as a clay swelling inhibitor, Journal of the American Chemical Society 117(50) (1995) 12608-12617.

[48] B.J. Teppen, K. Rasmussen, P.M. Bertsch, D.M. Miller, L. Schafer, Molecular dynamics modeling of clay minerals .1. Gibbsite, kaolinite, pyrophyllite, and beidellite, Journal of Physical Chemistry B 101(9) (1997) 1579-1587.

[49] W. Humphrey, A. Dalke, K. Schulten, VMD: Visual molecular dynamics, Journal of Molecular Graphics 14(1) (1996) 33-38.

[50] A.D. MacKerell, D. Bashford, M. Bellott, R.L. Dunbrack, J.D. Evanseck, M.J. Field, S. Fischer, J. Gao, H. Guo, S. Ha, D. Joseph-McCarthy, L. Kuchnir, K. Kuczera, F.T.K. Lau, C. Mattos, S. Michnick, T. Ngo, D.T. Nguyen, B. Prodhom, W.E. Reiher, B. Roux,

M. Schlenkrich, J.C. Smith, R. Stote, J. Straub, M. Watanabe, J. Wiorkiewicz-Kuczera, D. Yin, M. Karplus, All-atom empirical potential for molecular modeling and dynamics studies of proteins, Journal of Physical Chemistry B 102(18) (1998) 3586-3616.

[51] W.L. Jorgensen, J. Chandrasekhar, J.D. Madura, R.W. Impey, M.L. Klein, COmparison of simple potential functions for simulating liquid water, Journal of Chemical Physics 79(2) (1983) 926-935.

[52] L. Kale, R. Skeel, M. Bhandarkar, R. Brunner, A. Gursoy, N. Krawetz, J. Phillips, A. Shinozaki, K. Varadarajan, K. Schulten, NAMD2: Greater scalability for parallel molecular dynamics, Journal of Computational Physics 151(1) (1999) 283-312.

[53] S.E. Feller, Y.H. Zhang, R.W. Pastor, B.R. Brooks, Constant-pressure molecular-dynamics simulation - the langevin piston method, Journal of Chemical Physics 103(11) (1995) 4613-4621.

[54] G.J. Martyna, D.J. Tobias, M.L. Klein, Constant-pressure molecular-dynamics algorithms, Journal of Chemical Physics 101(5) (1994) 4177-4189.

[55] D. Sikdar, S.M. Pradhan, D.R. Katti, K.S. Katti, B. Mohanty, Altered phase model for polymer clay nanocomposites, Langmuir 24(10) (2008) 5599-5607.

5. INFLUENCE OF THE MOLECULAR INTERACTIONS ON SHEAR STRENGTH OF NA-MMT WITH ORGANIC FLUIDS: A STEERED MOLECULAR DYNAMICS STUDY[3]

5.1. Introduction

Swelling clays are encountered all over the world. These clays can undergo a significant amount of volume change with respect to the original volume when mixed with water. Sodium montmorillonite is one of the major reactive clay minerals that has some unique properties such as low permeability and high specific surface area. Thus, the volumetric fluctuations of swelling clays result in developing high uplift pressures; the civil infrastructures such as roads, buildings, pavements, and canals are susceptible to fail upon swelling. However, these swelling clays have been extensively used in various applications such as barrier materials in landfill liners [1], borehole stabilization during drilling [2], to enhance the mechanical properties of clay-polymer-nanocomposities [3], and as modifiers in pavement construction [4]. Therefore, understanding of swelling behavior and shear failure mechanism of swelling clays is crucial to avoid damages and use these clays in in geotechnical engineering, geoenvironmental applications, and industrial engineering.

The swelling pressure at various level of swelling has been evaluated using controlled uniaxial device in our previous experimental work [5]. The swelling pressure is decreased with an increase in the swelling level. The microstructure of the swelling clays upon swelling is also altered with increase in the leverl of swelling, causing breakdown of clay particles into small

[3] This chapter describes the evaluation of the shear strength properties of swelling clays with various organic fluids at the molecular level using steered molecular dynamics simulations. The content of this chapter will be submitted for the publication. Keshab B. Thapa had primary responsibility for collecting samples in the field and for interviewing users of the test system. Keshab B. Thapa was the primary developer of the conclusions that are advanced here. Keshab B. Thapa also drafted and revised all versions of this chapter. Dinesh R. Katti and Kalpana S. Katti served as proofreader and checked the math in the statistical analysis conducted by Keshab B. Thapa.

particles. Furthermore, the hydraulic flow property and mechanical properties such as swelling pressure, compressibility, and consolidation of sodium montmorillonite (Na-MMT) clay with low, medium, and high polar fluids have been investigated [6]. The nature of the interactions between Na-MMT with these organic fluids is primarily nonbonded. Also, the polarity of the fluid altered the microstructure of swelling clays, resulting in more particle breakdown with increased in the polarity of fluids.

In addition to above experimental work, the clay-fluid interactions have been studied using Molecular Dynamics (MD) simulations and Steered Molecular Dynamics (SMD). SMD simulation is an excellent computational tool where the externally applied forces to the molecules guide a system from one state to another at the molecular level [4]. SMD is divided into two groups: constant-force SMD and constant-velocity SMD. In constant-force SMD, the small magnitude of force is applied to the selected atom in a given direction; whereas one end of the molecule is fixed while the other end is pulled by applying a constant velocity in constant-velocity SMD. In our previous study, the mechanical response of dry and hydrated Na-MMT and pyrophyllite with various water content in the clay interlayer has been carried out using constant-force SMD [5, 6]. Upon compression, the interlayer spacing is decreased linearly not only for dry clay but also for one monolayer of water. However, the stress-displacement response with increasing number of monolayers—two and three monolayers of water in the clay interlayer—is nonlinear. Furthermore, the major factors that control the interlayer response compression, stress-strain characteristics, and interlayer modulus are the level of hydration, hydration of interlayer cations, and interactions between clay sheets, cations, and water molecules [7]. Furthermore, the interactions between Na-MMT clay and fluids at various level of hydrations have been studied using MD simulations [7]. The attractive clay-sodium interactions

are responsible to hold the dry clay sheets together, but these interactions significantly decreased with increased hydration level, resulting in exfoliation and particle breakdown. Due to high clay-sodium interactions, a well-organized solvation shell is formed around sodium cations, causing the initiation of swelling in the clay interlayer [8]. The role of the polarity of the fluid at the molecular level has been conducted using MD simulations [9]. The nonboned interactions increased with increased polarity of fluids, and these results are consistent and correlated well with the results from the Infrared (IR) spectroscopy experiments [10].

The shear strength of a soil mass is referred as the internal ability that the soil mass can resist failure against sliding any plane [11]. A measure of the shear strength of soils comes from two parameters, which are angle of internal friction and cohesion. These two parameters of clay minerals provide the maximum ability to resist shear stress under externally applied normal. Cohesion holds the soil particles together in a soil mass and is independent of externally applied normal stresses. On the other hand, the angle of internal friction is referred as the resistance between the particles and is proportional to the normal stresses. The internal friction increases with increase in the external stresses, as the clay particles consolidate upon compression. Furthermore, the classical bearing capacity theory is unable to account for clay-fluid interactions, resulting in reducing its predictive capabilities. The expenditure of the construction-related projects throughout the world is about $10 trillion a year [12]. Therefore, the improvement of the fundamental theory, which has been used in the design and construction of the infrastructures for years will be a significant contribution to the society. It is essential to understand the shear failure mechanisms by incorporating the clay-fluid molecular interactions for effective design and economical construction.

When the moisture content varies from high to low in clays, the friction angle decreases because the clay particles aggregates to form group that results in larger effective particle size [13]. The results from direct shear experiments showed that the shear strength parameters, angle of friction and cohesion, of the compacted bentonite clay decrease with increase in the moisture content [14]. The direct shear experiments have been extensively conducted to evaluate the angle of internal friction for saturated smectite clay minerals. The angle of internal friction reported is 3.43º for bentonite [15] and 5.14º for sodium montmorillonite [16]. The nanoscale friction angle and cohesion of tobermorite and montmorillonite clay has been computed by applying a biaxial deformation or stress. The angle of internal friction for 2x2x1 unit Na-MMT with one monolayer is 3.2º, and cohesion is about 270 MPa. On the other hand, the internal friction for tobermotite is 10.2º, and cohesion is about 1010 MPa. The tensile strength and shear failure mechanics of laponite, which is one of the smectite clay minerals, with various organic dye such as pyronin presented in the clay interlayer have been studied using molecular modeling. They reported that the interactions between the negatively charged clay sheets and interlayer cations provides cohesion [17]. The elastic and failure properties of the illite clay mineral have been using MD simulation. The authors proposed the nanoscale failure mechanism under shear loading between clay sheets by a stick-slip behavior, which results from the successive stable and unstable regimes with an increase in shear strain [18].

The limited research that has been carried out on evaluating the shear strength parameters of the layer silicates, specifically montomorillonite clay mineral, with various organic fluids at the molecular. This current work provides the results from constant-velocity SMD on Na-MMT clay with various organic fluids. Furthermore, this study seeks to insight into the role of fluid content and effect of polarity on the shear stress, shear strain, molecular shear strength

parameters including angle of internal friction and cohesion, nonbonded interactions, and the conformation of the fluid molecules when shearing the clay sheet at the molecular level.

5.2. Model Construction

For Na-MMT, the chemical formula of the unit cell is $NaSi_{16}(Al_6FeMg)O_{20}(OH)_4$.. The coordinates of the unit cell are acquired from Skipper et al. [19], and the values of the atomic charges are obtained from Tappen et al. [20]. Initially, the 4x2 Na-MMT model is developed to investigate the mechanical response of dry and hydrated Na-MMT clay [40]. Furthermore, this 4x2 Na-MMT model has been used to study the interactions between clay and water using CHARMM force field parameters [21, 22], which are developed in our group, are used. The Na-MMT clay sheet has a tetrahedral-octahedral-tetrahedral (T-O-T) structure in which an octahedral clay sheet is sandwiched between tetrahedral clay sheets. Additionally, the dimensions of unit cell are 5.28Å x 9.14Å x 6.56Å. In this study, the clay model has 6x3 unit cells in which 6 unit cells are in X-direction and 3 unit cells are in Y-direction, resulting in overall dimensions of 31.68 Å x 27.44 Å x 24.16 Å as shown in Figure 5.1. The isomer substitution by metal atoms in the octahedral sheet results in the negative charge on the individual clay sheets. The negative charges developed during isomer substitution can be explained by the fact that nine Aluminum (Al^{+3}) cations are replaced by nine Iron (Fe^{+3}) cations and another nine Aluminum (Al^{+3}) cations by Magnesium (Mg^{+2}) cations. These negative charges are balanced by adding nine sodium (Na^{+}) cations in the clay interlayer. A detailed construction of the 6x3 Na-MMT model is described in our previous work [23]. In brief, the Na-MMT and fluids models are developed with the help of the Material Studio™ and PSFGen of Visual Molecular Dynamics (VMD 1.9.3) software [24, 25].

For organic fluids such as formamide, methanol, and acetone used in this study, the CHARMM force field parameters are acquired from the Chemistry at Harvard Macromolecular Mechanics (CHARMM) force field parameters GUI Archive-CHARMM Small Molecule [26]. Also, Transferable Intermolecular Potential 3 Point (TIP3P) water molecule is used [27]. In this work, the interlayer of the Na-MMT molecular model has 10% acetone (24 acetone molecules), 10% methanol (40 methanol molecules), 10% water (64 water molecules), and 10% formamide (48 formamide molecules), as well as 30% methanol, (120 methanol molecules) 30% water (216 water molecules), and 30% formamide (120 formamide molecules). The number of molecules for each fluid content is calculated based on the molecular weight of the individual atoms.

5.3. Simulation Details

Molecular dynamics (MD) and steered molecular dynamics (SMD) of dry and hydrated 6x3 unit Na-MMT clay models are carried out by using NAMD 2.12 developed by Theoretical and Computational Biophysics Group, Beckman Institute, the University of Illinois at Urbana-Champaign [28]. CHARMM force field parameters for the clay and fluids are used. Visual molecular dynamics (VMD) 1.9.3 is used for visualization and interaction energy computations. An isothermal-isobaric (NTP) ensemble is used for running the MD simulation.

In the first step of MD simulation, the model is minimized by using a conjugate gradient method to find the geometric conformation with minimum energy. After minimization, the temperature is increased from 0 K to 300 K in three steps with an increment of 100 K using the Langevin dynamics control method. The pressure is increased from 0 bar to 1.01 bar in four steeps with 0.25 bar increments using the Nose-Hoover Langevin piston control method, while keeping the temperature constant at 300 K. After bringing all the molecular models at NTP

condition, the simulations are run for additional 400 ps. The total simulation time up to this point is 1 ns.

The mechanical properties—the displacement of clay interlayer and stress-strain response—of dry 6x3 unit dry as well as hydrated Na-MMT clay molecular model are carried out using constant-force SMD simulations. In the constant-force SMD, constant point force is applied to the individual atoms in the specified direction during the entire simulation. A uniform compressive point load is applied in z-direction on each of the oxygen atoms lying on the top surface of the clay sheet. A total of 108 oxygen atoms on the top surface of the clay sheet are identified, and the average projected load-bearing area is 729.63 $Å^2$ in the x-y plane. The 108 oxygen atoms of the bottom surface of the clay sheet are fixed in all x, y, and z directions. During the application of constant force, the displacement of all the atoms on the top surface of the clay sheet is unrestrained in the z-direction but restrained in x and y directions. All the fluid molecules are kept free in all directions, mimicking standard experimental conditions. A wide range of compressive loads that are applied on each atom of the top clay sheet were 0, 25, 50, 75, 100, 150, 175, 200, 300, 400, and 600 pN per atom for dry and hydrated Na-MMT clay model, and the equivalent stresses are 0, 0.37, 0.74, 1.11, 1.48, 2.96, 4.44, 5.92, and 8.88 GPa.

The constant-force SMD simulations are run for 400000 steps with a time step of 0.5 fs, which is equivalent to 200 ps. The mechanical properties are evaluated by measuring the average change in thickness of the clay sheet and clay interlayer of the model before and after the application of point loads (upon the application load with respect to the original state). After constant-force SMD simulations, constant-velocity SMD simulations are carried out by pulling the center of mass of 6x3 unit Na-MMT clay models by using a harmonic spring to evaluate the shear strength at dry as well as hydrated clay conditions. The 108 oxygen atoms of the bottom

surface of the clay sheet are fixed in all y and z directions, resulting in not allowing them to move in vertical direction so that the normal stresses keep acting on top clay sheet. But those 108 atoms are allowed to move in x-direction. The top clay sheet is pulled using spring constant of 9 kcal/mol/Å^2 and velocity of 0.1 Å/ps for 400 ps. The total simulation time after constant-velocity SMD is 1.6 ns. A schematic diagram that shows imposing a normal stress and then shear flow is shown in Figure 5.1 (b-c). All simulations are run with ten nodes and 20 CPUs with total of 200 CPUS using 2.66 GHz 40 processors using Xenon X5550 processor using Thunder Cluster at the Center for Computationally Assisted Science and Technology (CCAST) at North Dakota State University.

5.4. Results and Discussions

For the representative molecular models of dry and hydrated Na-MMT with 10% and 30% fluid content, the average interlayer spacing is measured by computing the vertical between the corresponding surface oxygen atoms of the top and bottom clay sheets. The interlayer spacing for dry clay is about 3.94 Å; the interlayer spacing for Na-MMT with 10% acetone, methanol, water, and formamide is 6.28 Å, 6.44 Å, 6.52Å, and 6.71Å, respectively. Similarly, the interlayer spacing for 30% methanol, water, and formamide is 9.94 Å, 10.85 Å, and 11.40 Å, respectively. The values of the interlayer spacing for dry clay and clay with 10% and 20% are well agreed and consistent with the experimental [29] and molecular modeling studies [9, 10]. It has been found that the interlayer spacing for polar fluids is significantly higher than medium and low polar fluids; interlayer spacing is increased with an increase in the fluid polarity. Furthermore, these models at equilibrium are compressed and then sheared in the horizontal direction as shown in Figure 5.1(b-c).

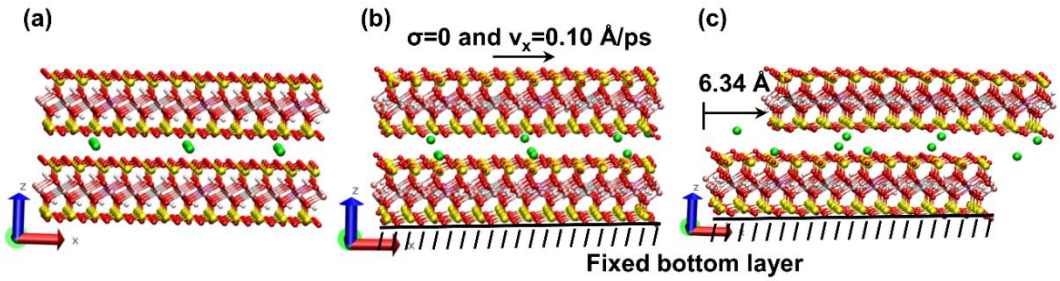

Figure 5.1. (a) Molecular model of dry Na-MMT showing interlayer sodium cations and (b) pulling of equilibrated top layer at 0.1 A˚/ps, and (c) top layer with displacement of 6.34 Å.

5.4.1. The Shear Stress and Displacement Behavior of Dry and Hydrated Na-MMT

The pulling of the top layer of Na-MMT was carried out for dry Na-MMT and hydrated Na-MMT with 10% and 30% interlayer fluids to evaluate the molecular shear strength parameter of Na-MMT. The snapshot of pulling of dry Na-MMT at a velocity of v_x= 0.1 Å/ps in the absence of normal stress (σ=0 GPa) was shown in Figure 5.1 (c). The maximum displacement of the top layer was 6.34 Å, which was equivalent to a strain of 20%. This displacement also corresponded to the point at which shear stress decreased without any peaks. When the top layer was pulled, the sodium cations were moved along with the top layer, resulted in a significant change in the conformation of the sodium cations in the interlayer space.

Figure 5.2 showed the conformation of Na-MMT with 10% acetone, methanol, water, and formamide when the top layer of Na-MMT was pulled. The fluid molecules and the interlayer cations remained in proximity to the layers of Na-MMT throughout the simulation, which indicated a strong binding between the layers, fluid molecules, and sodium cations. A wide range of normal stresses were externally applied on the top layer and then sheared by applying constant velocity for dry as well as hydrated Na-MMT molecular models. The snapshot of shearing of Na-MMT with 10% acetone, methanol, water, and formamide at high normal stress (σ=8.88 GPa) was shown in Figure 5.3. The sodium cations and fluid molecules continued to be in proximity to the layers, indicating strong binding between the sodium cations and layers.

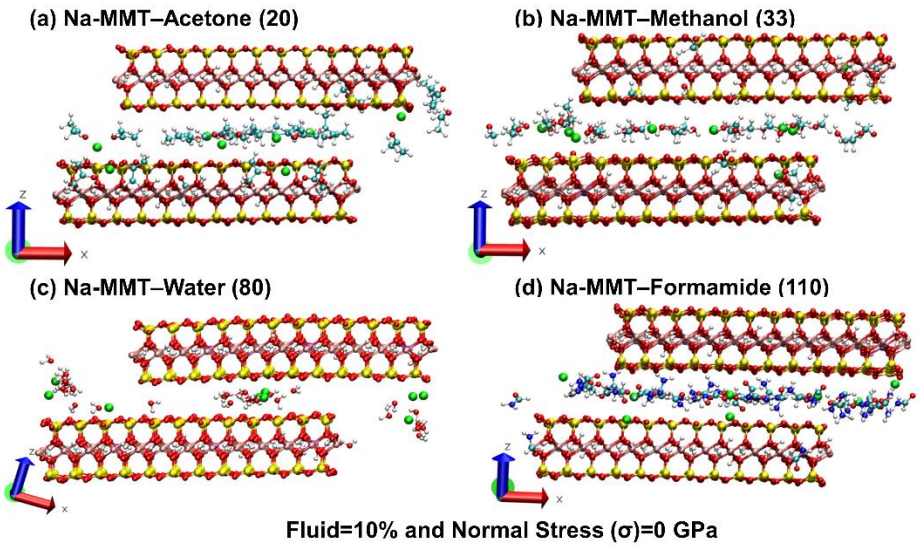

Figure 5.2. Na-MMT models with 10% fluid showing the shearing of top layer at no normal stress (σ=0 GPa) (a) Na-MMT–Acetone (20), (b) Na-MMT–Methanol (33), (c) Na-MMT–Water (80), and (d) Na-MMT–Formamide (110). Dielectric constant is presented in the parenthesis.

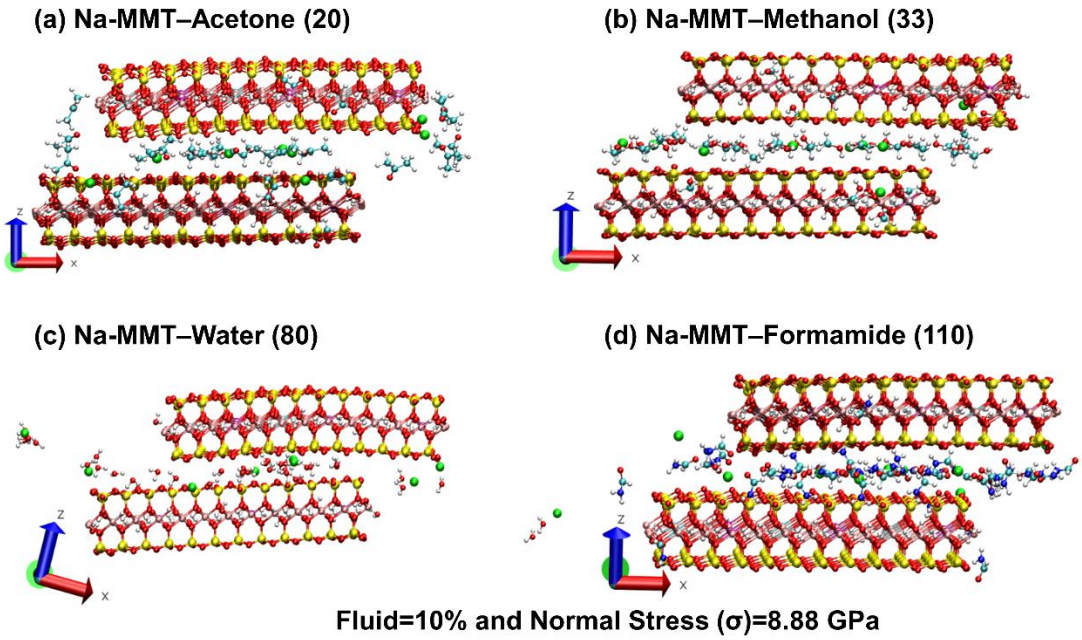

Figure 5.3. Na-MMT models with 10% fluid showing the shearing of top layer at no normal stress (σ=8.88 GPa) (a) Na-MMT–Acetone (20), (b) Na-MMT–Methanol (33), (c) Na-MMT–Water (80), and (d) Na-MMT–Formamide (110). Dielectric constant is presented in the parenthesis.

The deformation responses of the top layer of dry Na-MMT model sheared at a velocity of v_x=0.1 Å/ps to the maximum strain of 20% were shown in Figure 5.4(a). The red, black, gray,

yellow, blue, and green plots in Figure 5.4(a) indicated the shear stress-displacement characteristics of dry Na-MMT at σ=0 GPa, σ=1.48 GPa, σ=2.96 GPa, σ=4.44 GPa, σ=5.92 GPa, and σ=8.88 GPa, respectively. These plots showed different mechanisms responsible to shear dry Na-MMT at various normal stresses conditions. The previous studies showed that the structural stability of stacking of dry Na-MMT was maintained by the interactions between layers and sodium cations [7, 10]. When the top layer was pulled, it had to overcome the attractive interaction of sodium cations with the layers. This behavior of shearing at no normal stress (σ=0 GPa) was captured by the initial portion, path OM_1, of the shear stress-displacement plot when the top layer moved opposite to the pulling direction as shown in Figure 5.5(a). In addition, a sawtooth-like feature of the curve was observed, which indicated that the sodium cations were holding the layer and prevented to move forward.

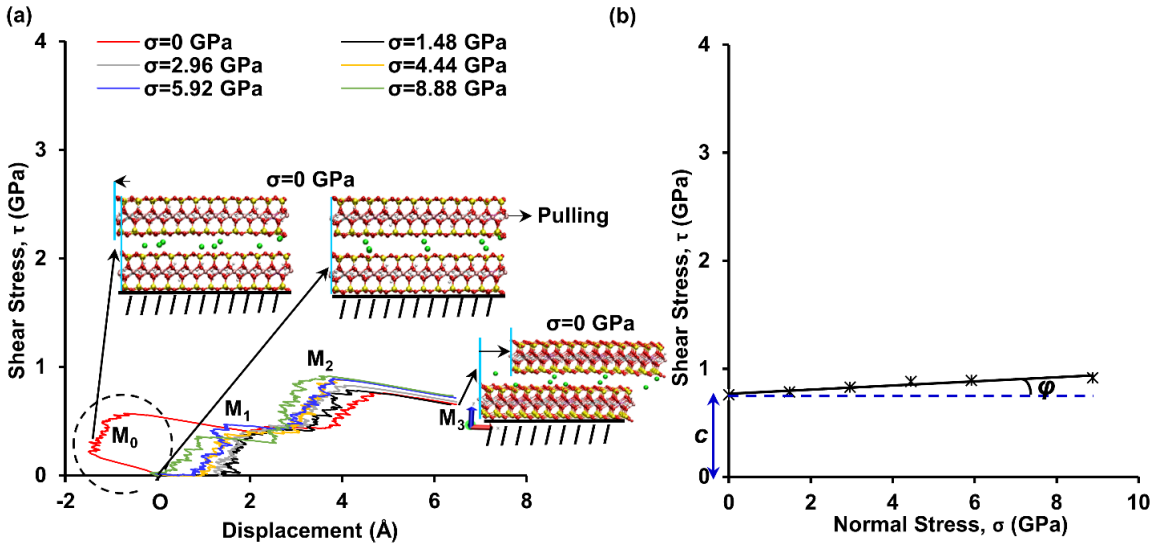

Figure 5.4. (a) Typical shear stress-displacement behavior and (b) the σ-τ characteristics of dry Na-MMT.

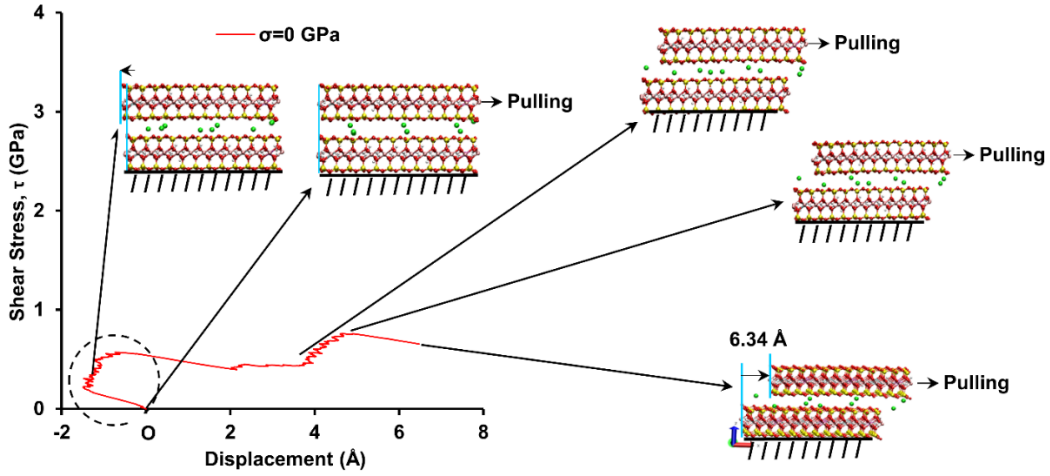

Figure 5.5. Typical shear stress-displacement behavior at σ=0 GPa and conformation clay sheets and sodium ions at various portion of the plot.

Figure 5.4(a) also showed two peaks (M_0 and M_2 for σ =0 GPa and M_1 and M_2 for σ =1.48-8.88 GPa) during the shearing of layer. The first peak for no normal stress case was observed at opposite of the pulling direction at the initial stage of pulling, whereas the first peak for normal stress from 1.48 to 8.88 GPa was observed approximately at displacement of 1.50 Å. Furthermore, the maximum shear stress was observed at the later stage indicated by path M_2M_3: 0.759 GPa at 4.64 Å for σ=0 GPa, 0.785 GPa at 4.09 Å for σ=1.48 GPa, 0.830 GPaat 4.04 Å for σ=2.96 GPa, 0.882 GPa at 3.83 Å for σ=4.44 GPa, and 0.892 GPa at 3.81 Å for σ=5.92 GPa, and 0.917 GPa at 5.65 Å for σ=8.88 GPa. Shear stress increased with increased in normal stress. Additionally, the shear stress values decreased after the maximum peak values, and thus the top clay layer was sheared up to maximum strain of 20%.

The shear stress-displacement responses of Na-MMT with 10% acetone, methanol, water, and formamide pulled at a velocity of vx=0.1 Å/ps under different normal stresses were showed in Figure 5.6. The initial shear stress-displacement characteristics of Na-MMT with 10% fluids before and after normal stresses were significantly different than that of dry Na-MMT. For Na-MMT-acetone, there was only one peak (A_1) observed as showed in Figure 5.6 (a). The

maximum shear stress was found to be 0.289GPa at 6.07 Å for σ=0 GPa, 0.369 GPa at 3.96 Å for σ=1.48 GPa, 0.502 GPa at 2.53 Å for σ=2.96 GPa, 0.580 GPa at 3.69 Å for σ=4.44 GPa, and 0.711 GPa at 2.61 Å for σ=5.92 GPa, and 0.991 GPa at 2.79 Å for σ=8.88 GPa. The shear stress-displacement responses in the O-A_1 region showed a significant increase in shear stress for a small displacement. Furthermore, shear stress increased linearly with increased in normal stress.

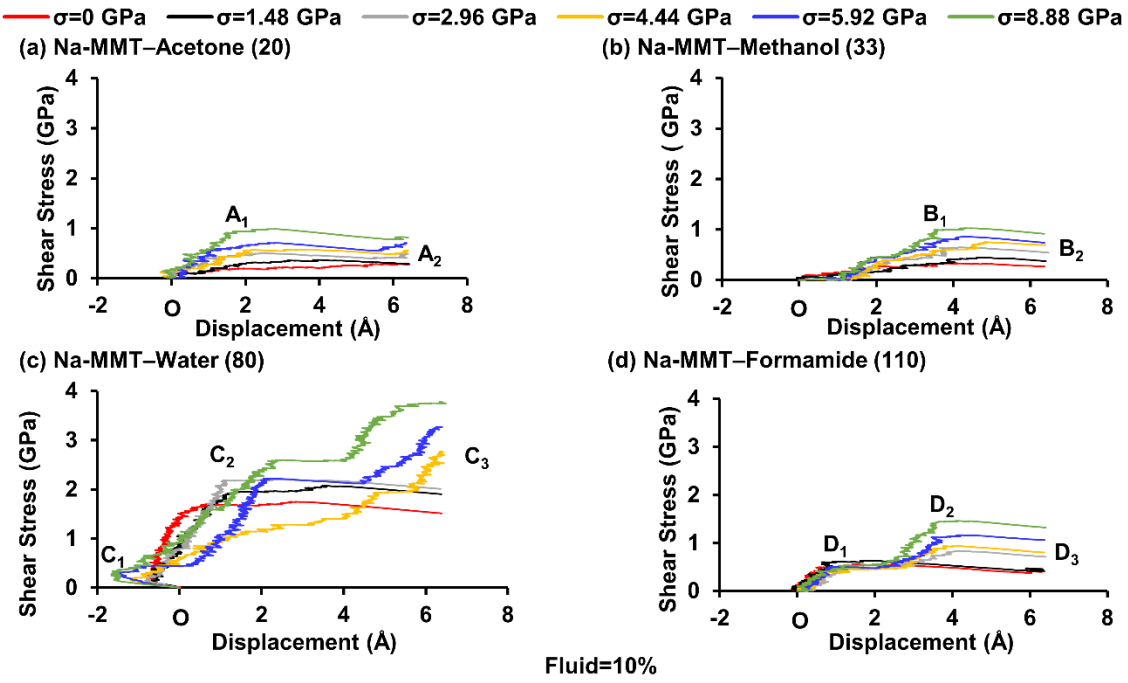

Figure 5.6. Typical shear stress-displacement behavior of Na-MMT with 10% fluid: (a) Na-MMT-Acetone (20), (b) Na-MMT-Methanol (33), (c) Na-MMT-Water (80), and (d) Na-MMT-Formamide (110).

Figure 5.6(b) showed the shear stress-displacement response of Na-MMT with 10% methanol, and only one peak (B_1) was observed. As showed in Figure 5.6(b), the displacement increased abruptly to about 1.30 Å in the initial stage of the curve, which resulted in requiring relatively small shear stress to shearthe top layer. Afterwards, greater shear stress is required to shear the top layer. The maximum shear stress was found 0.333 GPa at 3.83 Å for σ=0 GPa, 0.448 GPa at 4.61 Å for σ=1.48 GPa, 0.650 GPa at 4.20 Å for σ=2.96 GPa, 0.750 GPa at 34.80 Å for σ=4.44 GPa, and 0.862 GPa at 4.34 Å for σ=5.92 GPa, and 1.027 GPa at 4.28 Å for σ=8.88

GPa. In Figure 5.6(b), no peaks were observed beyond a displacement of 4 Å, and the shear stress-displacement plot furthermore became smooth and decreased gradually for up to 20% strain, as indicated by the path B_1-B_2.

The shear stress-displacement behavior of Na-MMT with 10% water was shown in Figure 5.6(c). The initial stage of the curve for Na-MMT-water was significantly different than that of the Na-MMT-acetone and Na-MMT-methanol curves. It was observed that there is only one peak for normal stress of 0, 1.48, and 2.96 GPa; whereas three peaks were observed for normal stress of 4.44, 5.92, and 8.88 GPa. The initial portion of the shear stress-displacement showed the top layer moved opposite to the pulling direction, which indicated the strong attractive interactions between the interlayer cations and water molecules. The shear stress-deformation curve in the C_1-C_2 showed a large increase in shear stress for small displacement. The slope of the shear stress-displacement for Na-MMT with water was stiffer than that of Na-MMT with acetone and Na-MMT with methanol. In addition, the maximum shear stress was found to be 1.751 GPa at 2.82 Å for σ=0 GPa, 2.076 GPa at 3.48 Å for σ=1.48 GPa, 2.209 GPa at 2.28 Å for σ=2.96 GPa, 2.771 GPa at 6.40 Å for σ=4.44 GPa, and 3.450 GPa at 6.27 Å for σ=5.92 GPa, 4.198 GPa at 4.33 Å for σ=8.88 GPa. The maximum shear stress for normal stress of 0, 1.48, and 2.96 GPa was observed at the initial stage of the curve in the region C_1-C_2 as showed in Figure 5.6(c). However, with increased in normal stress from 4.44 to 8.88 GPa on top of the layer offered more resistance against shearing, which caused the magnitude of shear stress to rise distinctly.

Furthermore, the shear stress-displacement response of Na-MMT with 10% formamide was shown in Figure 5.6(d), and two peaks (D_1 and D_2) were observed. The slope at the initial stage in the O-D_1 region was about the same for all normal stresses. The peaks for normal

stresses from 0 to 1.48 GPa were observed at the initial stage of the plot (region 0-D_1), whereas the peaks for normal stress from 2.96 to 8.88 GPa were observed in the later stage of the curve in the region D_1-D_2 as showed in Figure 5.6(d). The maximum shear stress was 0.562 GPa at 1.47 Å for σ=0 GPa, 0.636 GPa at 3.01 Å for σ=1.48 GPa, 0.833 GPa at 4.25 Å for σ=2.96 GPa, 0.940 GPa at 4.19 Å for σ=4.44 GPa, 1.116 GPa at 3.78 Å for σ=5.92 GPa, and 1.460 GPa at 4.14 Å for σ=8.88 GPa. The shear stress-displacement curve became smooth and decreased beyond a displacement of 4.30 Å, which was equivalent to 20% strain.

Similarly, the shear stress-displacement responses of Na-MMT with 30% methanol, water, and formamide pulled at a velocity of v_x=0.1 Å/ps at various external normal stresses were showed in Figure 5.7. The initial shear stress-displacement characteristics of Na-MMT with 30% fluids before and after normal stresses were different than that of dry Na-MMT and 10% fluid content. For Na-MMT with 30% methanol, only one peak (E_1) was observed as showed in Figure 5.7 (a). The maximum shear stress was found to be 0.406 GPa at 2.44 Å for σ=0 GPa, 0.423 GPa at 3.05 Å for σ=1.48 GPa, 0.521 GPa at 2.49 Å for σ=2.96 GPa, 0.545 GPa at 2.88 Å for σ=4.44 GPa, and 0.595 GPa at 4.51 Å for σ=5.92 GPa, and 0.648 GPa at 1.39 Å for σ=8.88 GPa. The shear stress-displacement responses in the after the maximum shear value gradually decreased up to 20% strain. Furthermore, shear stress increased linearly with increased in normal stress.

Similarly, only one peak (F_1) observed Na-MMT with 30% water as shown in Figure 5.7 (b). The maximum shear stress was found to be 0.401GPa at 1.39 Å for σ=0 GPa, 0.512 GPa at 2.08 Å for σ=1.48 GPa, 0.578 GPa at 6.29 Å for σ=2.96 GPa, 0.616 GPa at 6.03 Å for σ=4.44 GPa, and 0.665 GPa at 4.04 Å for σ=5.92 GPa, and 0.712 GPa at 3.66 Å for σ=8.88 GPa. After maximum peak shear stress, the shear stress-displacement responses gradually decreased up to

20% strain. Lastly, the shear stress and strain curves for Na-MMT with 30% formamide were very similar for all level of normal stresses as shown in Figure 5.7 (c). The maximum shear stress was found to be 0.231 GPa for σ=0 GPa, 0.252 GPa for σ=1.48 GPa, 0.278 GPa for σ=2.96 GPa, 0.287 GPa for σ=4.44 GPa, and 0.310 GPa for σ=5.92 GPa, and 0.0.332 GPa for σ=8.88 GPa. These maximum shear stress values were found at about 6.38 Å at peak G_1, which is about 20% strain. Furthermore, shear stress increased linearly with increased in normal stress.

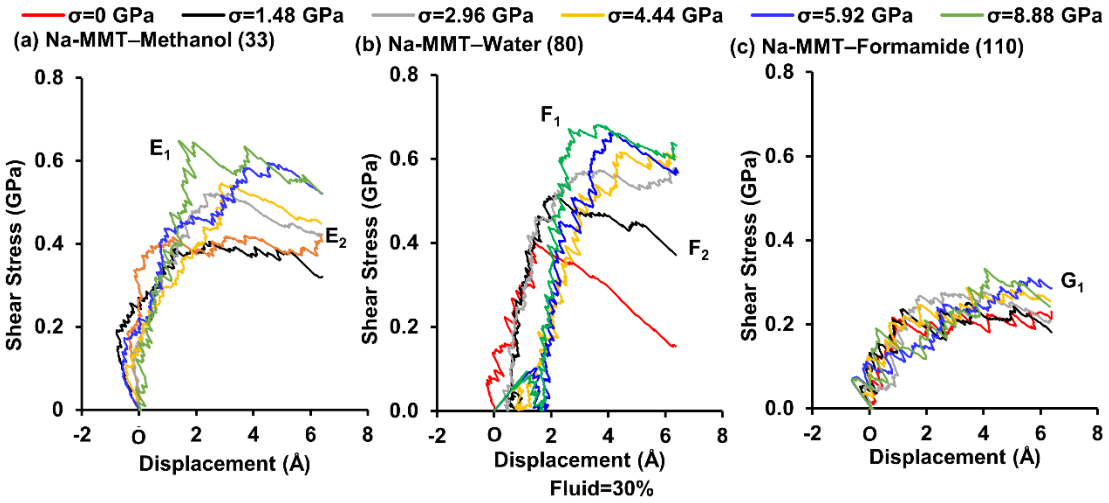

Figure 5.7. Typical shear stress-displacement behavior of Na-MMT with 30% fluid: (a) Na-MMT-Methanol (33), (b) Na-MMT-Water (80), and (c) Na-MMT-Formamide (110).

5.4.2. Molecular Shear Strength Parameters: Cohesion and Angle of Friction

An attempt was carried out to evaluate the molecular shear strength parameters, angle of internal friction (φ) and cohesion, using least-square method of dry Na-MMT as well Na-MMT hydrated with 10% and 30% fluid. The maximum shear strength failure envelopes fitted linearly and described by the Mohr-Coulomb failure criteria where shear stress (τ) was plotted as a function of normal stress (σ). The intercept on a Mohr-Coulomb plot provided the cohesion, which was also defined as an intrinsic strength that existed even at no externally applied stress. Figure 5.4(b) showed the shear stress-normal stress plot for dry Na-MMT; the y-intercept of this plot represented cohesion, and the slope of the trend line was the angle of internal friction. The

Mohr-Coulomb failure criterion was applied to evaluate the friction angle and cohesion, and the value of cohesion was found 769.60 MPa, and the angle of friction was 1.10^{o} for dry Na-MMT.

Furthermore, Figure 5.8 (a) showed the shear stress-normal stress characteristics for Na-MMT with 10% acetone, methanol, water, and formamide. Shear stress increased with increased in the normal stress for all models. Also, the shear stress-normal stress plot for Na-MMT with medium polar fluid fell between Na-MMT with low polar fluid and high polar fluid as showed in Figure 5. 6a. The slope of the Morh-Coulomb failure envelop and cohesion intercept increased with increase in the polarity of the fluids. The angle of internal friction was 4.51^{o} for Na-MMT-acetone, 4.56^{o} for Na-MMT-methanol, 13.50^{o} for Na-MMT-water, and 5.89^{o} for Na-MMT-formamide, which indicated the ability to withstand a shear stress as well as interlocking between the clay particles increased with increase the polarity of the fluids. The angle of friction for Na-MMT with water in this study was on the order of the same magnitude with the results from undrained triaxial experiments from the literature [30] where the angle of friction for natural sodium bentonite (φ=9.90^{o}) and calcium bentonite (φ=13.50^{o}). Although the molecular angle of friction for Na-MMT with acetone and methanol was about the same, Na-MMT with water had the highest angle of friction followed by Na-MMT formamide. Furthermore, the molecular cohesion was 262.30 MPa for Na-MMT-acetone, 363.50 MPa for Na-MMT methanol, 1696.70 MPa for Na-MMT-water, and 430.90 for Na-MMT-formamide, which indicated that the cohesive strength of Na-MMT developed rapidly and increased with increase in the polarity of the fluids.

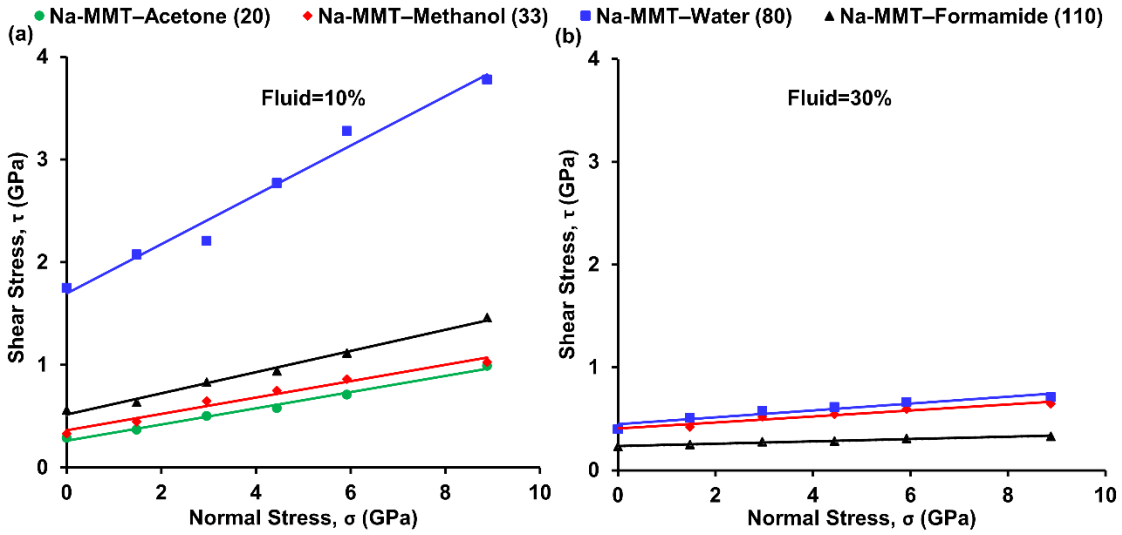

Figure 5.8. Typical σ-τ characteristics of Na-MMT with (a) 10% fluid and (b) 30% fluid in the interlayer space.

Similarly, Figure 5.8 (b) showed the shear stress-normal stress characteristics for Na-MMT with 30% methanol, water, and formamide. Here, shear stress increased with increase in the normal stress for all models. However, shear stress-normal stress plot for Na-MMT with medium polar fluid fell between Na-MMT water and formamide as showed in Figure 5.8 (b). The angle of internal friction was 1.66^{o} for Na-MMT with methanol, 1.92^{o} for Na-MMT with water, and 0.65^{o} for Na-MMT with formamide as showed in Figure 5.9 (a), which indicated that the angle of internal friction for 30% fluid content was in the order of same magnitude. The shear behaviors of Na-MMT observed in this work agreed with the results from the literatures where the friction angle decreased significantly with increased in water content [31, 32]. As a result, the failure of Na-MMT with the low and medium polar fluids was most like to happen earlier than that of Na-MMT with the high polar fluids. Neglecting the angle of friction of clays leaded to the overestimation of the reliable prediction of shear strength of swelling clays. Additionally, the molecular cohesion was 408.50 MPa for Na-MMT with methanol, 448.20 MPa for Na-MMT with water, and 236.50 for Na-MMT with formamide as showed in Figure 5.9(a).

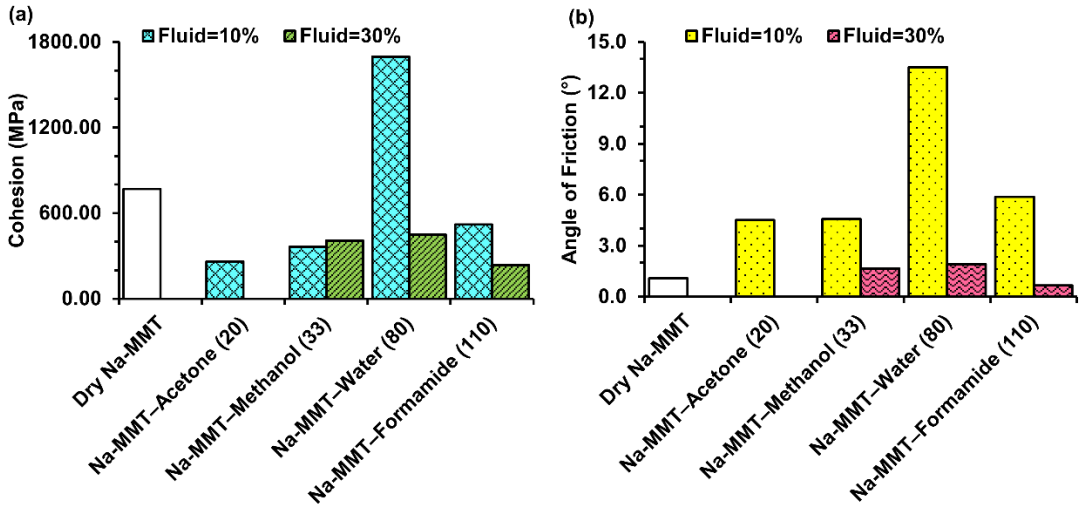

Figure 5.9. The molecular shear strength parameters for dry and 10% and 30% fluid content for Na-MMT with various organic fluids: (a) cohesion and (b) angle of internal friction.

5.4.3. Conformation of the Fluid Molecules upon Shearing

Figure 5.10 showed a planar view of the equilibrated model of Na-MMT with 10% acetone, methanol, water, and formamide when shearing at 0 GPa in XY-plane. The snapshot showed the conformation of the sodium cations and fluids in the interlayer where the proximity of the sodium cations increased with increase in the polarity of the fluids. This planer view also showed the formation of a well-organized pattern, resulted in the hydration of sodium ions even up on shearing at no externally applied normal stress.

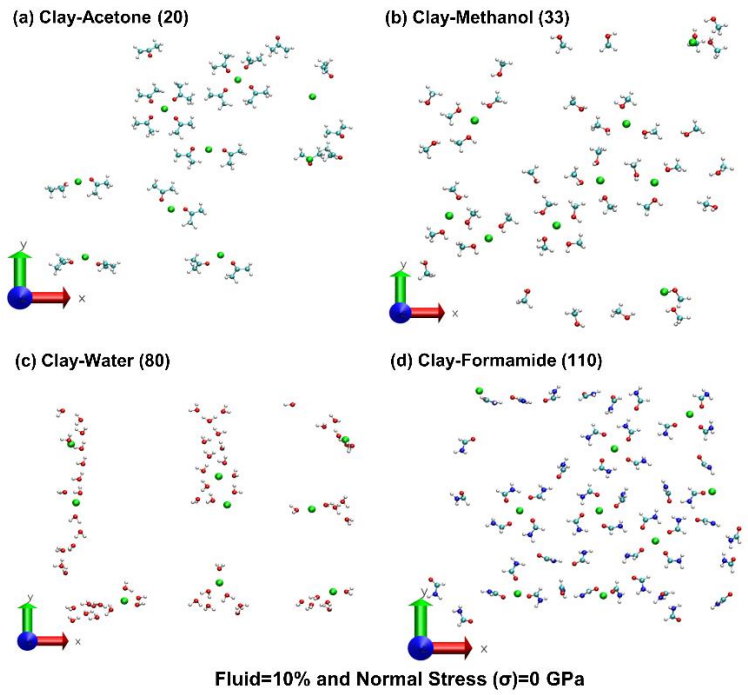

Figure 5.10. Planar view showing the hydration of sodium cations in the interlayer for Na-MMT with 10% acetone, methanol, water, and formamide when shearing (a-d) σ=0 GPa.

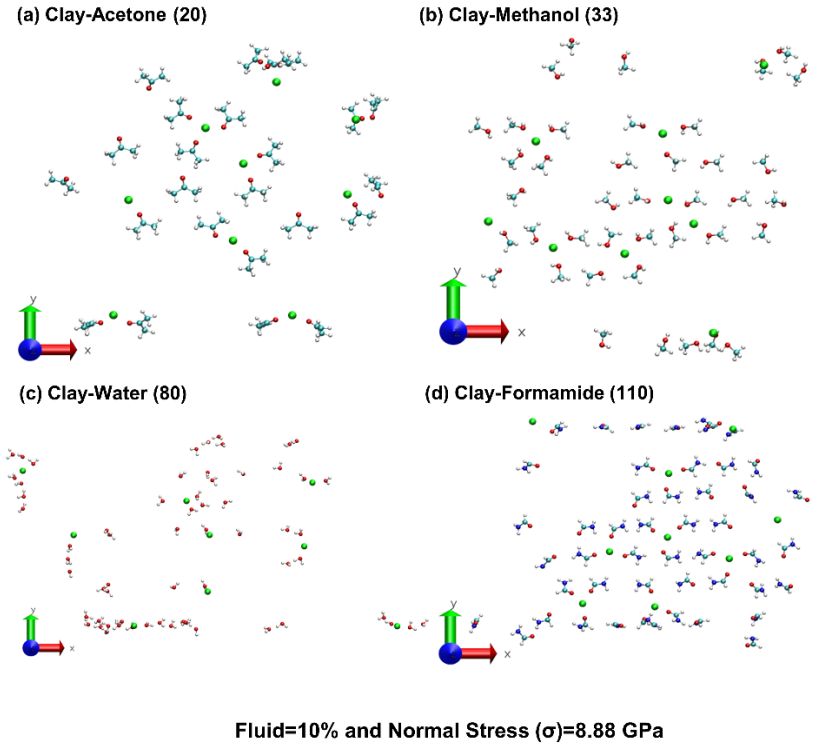

Figure 5.11. Planar view showing the hydration of sodium cations in the interlayer for Na-MMT with 10% acetone, methanol, water, and formamide when shearing (a-d) σ=8.88 GPa.

In addition, the planar view in Figure 5.11 showed that the change in the conformation of the fluid molecules, and the hydration of sodium ions continued when sheared at 8.88 GPa. The oxygen atoms of each of the fluid molecules attracted and oriented towards the sodium ions, and a well-organized shell formation continued and increased with an increase in the polarity of the fluids. Furthermore, the hydration of Na-MMT with 30% methanol, water, and formamide when sheared at normal stress of 0 GPa was showed in Figure 5.12(a-c). Furthermore, the change in the conformation of the interlayer cations and fluid molecules when sheared at normal stress of 8.88 GPa was shown in Figure 5.12(d-f). This planar view showed that the number of fluid molecules to make a well-organized pattern around sodium cations increased with an increase in the polarity of the fluids; at least two oxygen atoms of methanol, four oxygen atoms of water, and three oxygen atoms of formamide molecules were in close proximity to the sodium cations as shown in Figure 5.12(d-f).

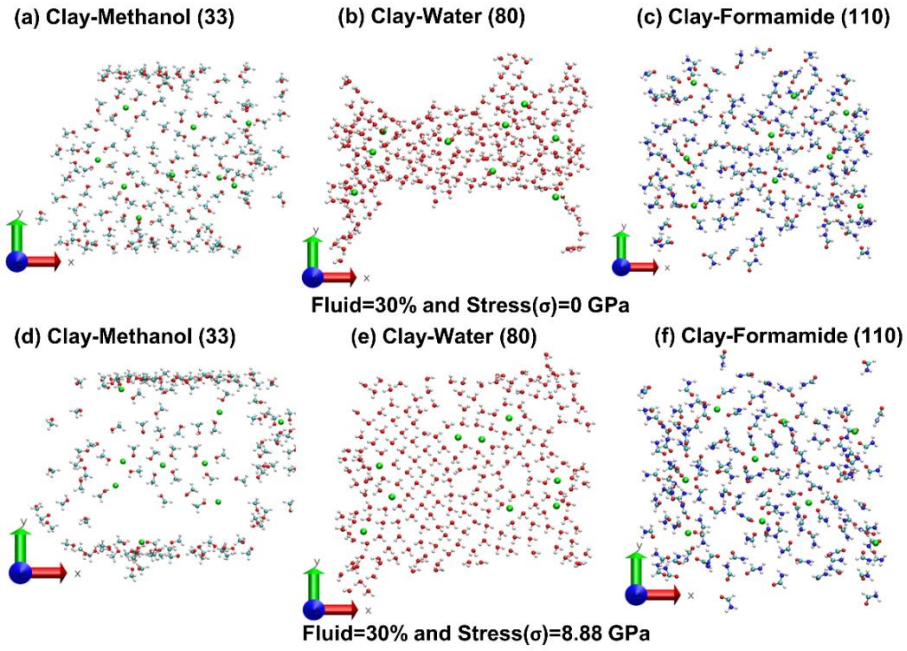

Figure 5.12. Planar view showing the hydration of sodium cations in the interlayer for Na-MMT with 30% methanol, water, and formamide when shearing (a-c) σ=0 GPa and (d-f) σ=8.88 GPa.

5.4.4. Quantitative Nonbonded Interactions of Na-MMT with the Interlayer Fluids

The nonbonded interaction energies—the sum of van der Walls and electrostatic—between the Na-MMT layers, sodium cations, and fluid molecules for dry Na-MMT and Na-MMT with 10% and 30% fluid when sheared at 0 GPa and 8.88 GPa were presented in Table 5.1. These interactions were computed at the frame corresponding to the maximum shear stress. The interactions between layers, sodium cation, and fluid molecules provided an insight about the mechanism that played an important role in the shear strength of dry and hydrated Na-MMT.

The total attractive nonbonded interaction between the layers for dry Na-MMT at 0 GPa was the highest with relative to the hydrated Na-MMT. For dry Na-MMT, the repulsive electrostatic interactions at 0 GPa and 8.88 GPa between the layers were because of the negatively charged layers. As soon as the 10% fluid molecules were allowed to enter into the interlayer and sheared in the absence of externally applied stress (σ=0 GPa), a significant drop in the total attractive layer-layer interactions in comparison to dry Na-MMT was observed. Thus, the fluid molecules played an influencing factor in shear strength of Na-MMT as soon as they entered into the interlayer. Moreover, the repulsive electrostatic interactions between the layers, in case of dry Na-MMT, became less dominating factor for swelling and shear strength with relative to hydrated Na-MMT with 10% fluid content. Increased polarity of the fluids caused increased in the layer-layer interactions at 0 GPa. Furthermore, Na-MMT-water had the highest attractive layer-layer interaction than that of Na-MMT with other fluids, and this highest interaction resulted in the largest cohesion. Also, the total layer-layer interaction when sheared at σ=8.88 GPa for dry Na-MMT was about the same with relative to 0 GPa. However, this interaction at 8.88 GPa for 10% fluid content was increased by 77% for Na-MMT with acetone, 66% for Na-MMT with methanol, 78% for Na-MMT with water, and 52% for Na-MMT with

formamide. The nature of the interaction when sheared at 0 GPa and 8.88 GPa was primarily attractive van der Waals energies.

As the 10% fluid molecules entered into the interlayer, the attractive layers-sodium interactions also decreased when the top layer was pulled in the absence of the normal stress as summarized in Table 5.1. The layers-sodium interactions for dry Na-MMT when sheared at 0 GPa and 8.88 GPa remained the same, whereas these interactions at 8.88 GPa with relative to 0 GPa were increased by increased by 11% for Na-MMT-acetone, 4% for Na-MMT-methanol and Na-MMT-water, and 2% for Na-MMT-formamide. These attractive interactions were primarily electrostatic in nature because of the interactions between the negatively charged layers and positively charged sodium cations. Nevertheless, van der Waals interactions in both conditions were negligible. These interactions further decreased with increase in the polarity of the fluids. Thus, the large magnitude of these attractive interactions brought the Na-MMT layers together and provided the structural stability by holding the layer when sheared in the presence of no and high normal stresses. The attractive interactions between layers and sodium cations at no normal stress delivered cohesion, which was responsible to hold the layers together at no externally applied stress, for dry Na-MMT and Na-MMT with four fluids. Our results also showed a good agreement with the shear failure mechanism of a 2:1 smectite mineral with organic dyes where cohesion between the layers were dominated by the electrostatic interactions between the negatively charged layers and interlayer cations [17]. Furthermore, the interlayer space was small for dry Na-MMT, and thus the layers-sodium interactions for dry Na-MMT at 0 GPa was significantly higher than that of Na-MMT with 10% fluid content.

Another significant observation was that the contribution of attractive layers-fluid and sodium-fluid interactions resulted in the reduction in the attractive layers-sodium interactions at

0 GPa for Na-MMT with all four fluids. Thus, the hydration of the layers and sodium cations also played a significant role in controlling cohesion of Na-MMT with these four organic fluids.

The domination of the repulsive nature of the short-range van der Waals at 0 GPa and 8.88 GPa supported that the fluid molecules were in close proximity of the sodium cations, and thus hydration continued at no normal and high normal stresses. The large magnitude of attractive sodium-fluid interactions and the conformation of the fluid molecules in close proximity of the sodium cations at 8.88 GPa contributed in the reduction of the layer-layer interactions in comparison to 0 GPa. Thus, the large separation between the layers augmented the sliding as well as assisted the layers in slipping past each other, which resulted in increased in the internal angle of friction of hydrated Na-MMT as compared to dry Na-MMT.

The total layers-fluid interactions when the top layer sheared at 0 GPa increased with an increase in the polarity of the fluids. These interactions were predominated by the attractive van der Waals interactions, whilst there were strong attractive electrostatic interactions existed between the layers and fluid molecules. The total layers-fluid interactions were primarily attractive electrostatic in nature for these four fluids when the top layer was sheared at 8.88 GPa normal stress, but the attractive nature of van der Waals interactions between the layers and fluid molecules at 0 GPa changed to the repulsive interactions at 8.88 GPa as presented in Table 5.1. This behavior was explained by the fact the top layer moved in close proximity to the fluid molecules that upon externally applied high stress, and the distance between them decreased. Therefore, the short-range repulsive van der Waals energy became predominant that resulted in repulsion between the layers and fluid molecules. Furthermore, the total attractive nonbonded interaction at 8.88 GPa with respect to 0 GPa was decreased by 98% for Na-MMT with acetone, 52% for Na-MMT with methanol, 38% for Na-MMT with water, and 29% for Na-MMT with

formamide. Thus, a significant rise in the angle of internal friction of wet Na-MMT as comparted to dry Na-MMT was correlated to increase in the interlayer space as well as the hydration of the interlayer sodium cations and layers at separated the Na-MMT layers and resulted in facilitating the sliding phenomenon.

Furthermore, the total nonbonded interactions when the top layer sheared at 0 GPa and 8.88 GPa for Na-MMT with 30% methanol, water, and formamide were presented in Table 5.1. When the amount of the fluid content in the interlayer was increased, the layer-layer interaction energies further decreased. The total layer-layer interactions at 0 GPa for Na-MMT with methanol and Na-MMT with water were about the same, which was correlated with having the same magnitude of cohesion for Na-MMT with these two fluids. However, Na-MMT with formamide had the lowest attractive interaction between the layers. Additionally, layer-layer interactions at 8.88 GPa relative to 0 GPa were increased by 233% for Na-MMT-methanol, 73% for Na-MMT with water, and 37% for Na-MMT with formamide. The previous study showed that the Na-MMT with lower and medium polar fluids compressed significantly higher than that of Na-MMT with high polar fluids. These interactions at 8.88 GPa also decreased with increased in the polarity of the fluids.

Table 5.1 also showed the attractive layers-sodium interactions at 8.88 GPa as compared to 0 GPa increased by 44% for Na-MMT-methanol, 8% for Na-MMT-water, and 18% for Na-MMT-formamide. In both cases, the nature of the interaction was predominated by attractive electrostatic energy, and the interaction decreased with increase in the polarity of fluids. Thus, the interlayer sodium cations tried to hold as the top layer was pulled.

Table 5.1 also showed the total attractive interactions between sodium and 30% methanol, water, and formamide. These sodium-fluid interactions in both cases, O GPa and 8

GPa, were primarily electrostatic in nature. The large magnitude of electrostatic interactions kept the fluid molecules in close proximity to the sodium cations, which was showed in Figure 5.12, which also indicated a well-organized pattern of the fluid molecules around the sodium cations. High attractive electrostatic interactions of fluid molecules with interlayer cations also elucidated that the hydration of the interlayer cations continued when the Na-MMT top layer was sheared in the presence of no and high normal stresses. Furthermore, when the normal stress increased from 0 GPa to 8.88 GPa, the ability of this interaction was decreased due to expelling of the fluid molecules from the interlayer upon compression. Thus, the sodium-fluid interactions at 8.88 GPa as compared to 0 GPa decreased by 36% for Na-MMT-methanol, 19% for Na-MMT-water, and 15% for Na-MMT-formamide. The comparisons between the attractive interactions between layers and fluid molecules for 30% methanol, water, and formamide were also presented in Table 5.1. The layer-fluid interactions at 8.88 GPa relative to 0 GPa decreased by 6% for Na-MMT with methanol, 10% for Na-MMT with water, and 2% for Na-MMT with formamide.

Table 5.1. Nonbonded interactions for dry clay and clay with 10% and 30% fluid upon shearing.

Fluid (%)	Interactions	Molecular Models	Energy (kJ/mol)					
			At 0 GPa			At 8.88 GPa		
			ELE	VDW	Total	ELE	VDW	Total
10	Layer-Layer	Dry Na-MMT	46	-2498	-2452	6	-2484	-2478
		Na-MMT–Acetone (20)	-284	-586	-870	-262	-1274	-1536
		Na-MMT–Methanol (33)	-336	-653	-989	-319	-1323	-1642
		Na-MMT–Water (80)	-447	-741	-1188	-277	-1835	-2112
		Na-MMT–Formamide (110)	-367	-677	-1043	-301	-1286	-1587
	Layers-Sodium	Dry Na-MMT	-4991	265	-4726	-5338	554	-4785
		Na-MMT–Acetone (20)	-4187	66	-4121	-4653	98	-4555
		Na-MMT–Methanol (33)	-2819	-58	-2878	-3175	175	-2999
		Na-MMT–Water (80)	-2721	-40	-2762	-3273	412	-2861
		Na-MMT–Formamide (110)	-3192	-28	-3220	-3370	84	-3286
	Sodium-Fluid	Na-MMT–Acetone (20)	-1974	207	-1767	-1578	126	-1452
		Na-MMT–Methanol (33)	-3360	219	-3140	-3288	204	-3084
		Na-MMT–Water (80)	-3653	255	-3398	-2971	342	-2628
		Na-MMT–Formamide (110)	-2315	121	-2195	-2150	121	-2029
	Layers-Fluid	Na-MMT–Acetone (20)	-158	-575	-733	-74	60	-13
		Na-MMT–Methanol (33)	-630	-747	-1377	-670	13	-657
		Na-MMT–Water (80)	-576	-549	-1125	-1421	724	-696
		Na-MMT–Formamide (110)	-352	-1185	-1536	-1261	167	-1094
30	Layer-Layer	Na-MMT–Methanol (33)	-271	-164	-435	-354	-1094	-1448
		Na-MMT–Water (80)	-317	-136	-453	-281	-502	-783
		Na-MMT–Formamide (110)	-42	-81	-123	-85	-105	-188
	Layers-Sodium	Na-MMT–Methanol (33)	-2441	-54	-2496	-3625	25	-3600
		Na-MMT–Water (80)	-2263	-37	-2299	-2419	-71	-2489
		Na-MMT–Formamide (110)	-1227	-30	-1257	-1441	-36	-1478
	Sodium-Fluid	Na-MMT–Methanol (33)	-6214	251	-5963	-4007	212	-3794
		Na-MMT–Water (80)	-8840	276	-8564	-7125	216	-6909
		Na-MMT–Formamide (110)	-5880	269	-5610	-4952	177	-4775
	Layers-Fluid	Na-MMT–Methanol (33)	-5374	-2052	-7425	-5897	-1087	-6983
		Na-MMT–Water (80)	-1289	-1150	-2440	-588	-1598	-2186
		Na-MMT–Formamide (110)	-1733	-1839	-3572	-1526	-1988	-3514

ELE=Electrostatic; VDW=van der Waals; Total=Nonbonded=ELE+VDW

The magnitude of reduction of the layers-fluid interaction at 8.88 GPa was significantly less than that of sodium-fluid interactions, which also indicated that the fluid molecules were strongly bound to the Na-MMT layers when compressed and sheared at high stresses as showed in Figure 5.12(d-f). These interactions decreased with an increase in the polarity of the fluids with the exception of the lowest interaction for Na-MMT with water in both cases at 0 GPa and 8.88 GPa.

5.5. Conclusions

- SMD simulation were used to evaluate the shear stress and displacement characteristic of dry Na-MMT clay and clay with 10% and 30% fluid content with fluids with a range of polarities that are also indicated by their dielectric constants values: low polar fluids acetone (20), methanol (33), and high polar fluids water (80), and formamide (110). Shear stress of swelling clay versus displacement plots are different for each normal stress. Shear stress required to pull the top clay layer increased with increase in normal stresses that varied from 2.22 to 8.88 GPa.
- Shear stress of swelling clay with polar fluid is significantly higher than that of medium and low polar fluids. It is also observed that more shear stress is required to pull the top clay sheet for clay with polar fluid than clay with medium and low polar fluids. Thus, the shear stress is increased with increased in the polarity of fluids.
- The molecular shear strength parameters, cohesion and angle of internal friction, of dry Na-MMT clay and clay with 10% and 30% fluid content with fluids with a range of polarities were evaluated. The polarity of fluids significantly influenced cohesion and angle of internal friction. At 10% fluid content, the angle of internal friction and cohesion increased with an increase in the polarity of fluids. Upon adding more fluids in the

interlayer, the angle of internal friction for 30% fluid content almost diminished; whereas there was a strong cohesion.

- The nonbonded interactions energies between layer-layer, layer-sodium, sodium-fluid, and layer fluid for 10% and 30% fluid content when the top layer was sheared in absence and presenace of high normal stresses are computed. The attractive layer-layer interactions for dry Na-MMT was the higher than Na-MMT clay with 10% and 30% fluid when the top clay layer is sheared at σ =0 GPa and σ=8.88 GPa, Thus, the value of cohesion for dry Na-MMT clay was higher than that of clay with 10% and 30% fluid content in the clay interlayer. Furthermore, the clay-clay interactions increased with increase in the polarity of fluids when the top clay layer was sheared at σ =0 GPa, and thus the cohesion of Na-MMT with polar fluids was higher than that of low and medium polar fluids. Additionally, the layer-layer interactions when sheared at σ=8.88 GPa were higher than that of σ=0 GPa. The attractive sodium-fluid for Na-MMT with 10% and 30% fluid content when sheared at σ=8.88 GPa indicated that the hydration continued upon shearing. The layers-fluid interactions for Na-MMT with 10% fluid content when shearing in the presence of high compression significantly decreased with relative to normal stress. Furthermore, the attractive nature of van der Waals energies changed from attractive to repulsive when shearing at high stress, which indicated that the hydration of clay sheets continues upon shearing at high normal stress. Although the total layers-fluid interactions for Na-MMT with 30% fluids decreased, the nature of the attractive van der Waals interactions remained the same.
- This study provides an insight into the influence of the polarity of the fluids on the shear strength behavior of swelling clays. Incorporation of clay-fluid interactions with the

molecular shear strength parameters—cohesion and angle of internal friction—is crucial not only for a better understanding of the share failure mechanism but also for effective design and economical construction of the civil infrastructures in the swelling clay regions.

5.6. Acknowledgement

The authors would like to acknowledge the support from the USDoT, Mountain Plains Consortium (MPC) grants MPC-506 (agreement # DTRT13-G-UTC38) and MPC-548 (agreement# 69A3551747108). The authors also acknowledge Computationally Assisted Science and Technology (CCAST) (NSF# 1229316) for providing the computational resources at North Dakota State University. Author K. B. T. acknowledges the support from ND EPSCoR through a doctoral dissertation fellowship.

5.7. References

[1] K. Kayabali, Engineering aspects of a novel landfill liner material: Bentonite-amended natural zeolite, Engineering Geology 46(2) (1997) 105-114.

[2] H.H. Murray, Applied clay mineralogy today and tomorrow, Clay Minerals 34(1) (1999) 39-49.

[3] D. Sikdar, S.M. Pradhan, D.R. Katti, K.S. Katti, B. Mohanty, Altered phase model for polymer clay nanocomposites, Langmuir 24(10) (2008) 5599-5607.

[4] M. Abdelrahman, D.R. Katti, A. Ghavibazoo, H.B. Upadhyay, K.S. Katti, Engineering Physical properties of asphalt binders through nanoclay-asphalt interactions, Journal of Materials in Civil Engineering 26(12) (2014).

[5] D. Katti, V. Shanmugasundaram, Influence of swelling on the microstructure of expansive clays, Canadian Geotechnical Journal 38(1) (2001) 175-182.

[6] P.M. Amarasinghe, K.S. Katti, D.R. Katti, Insight into role of clay-fluid molecular interactions on permeability and consolidation behavior of Na-montmorillonite swelling clay, Journal of Geotechnical and Geoenvironmental Engineering 138(2) (2012) 138-146.

[7] S.M. Pradhan, K.S. Katti, D.R. Katti, Evolution of molecular interactions in the interlayer of na-montmorillonite swelling clay with increasing hydration, International Journal of Geomechanics 15(5) (2015) 1-9.

[8] D.R. Katti, L. Srinivasamurthy, K.S. Katti, Molecular modeling of initiation of interlayer swelling in Na-montmorillonite expansive clay, Canadian Geotechnical Journal 52(9) (2015) 1385-1395.

[9] D.R. Katti, Z.R. Patwary, K.S. Katti, Modelling clay-fluid interactions in montmorillonite clays, Environmental Geotechnics 4(5) (2016) 322-338.

[10] D.R. Katti, K.B. Thapa, K.S. Katti, The role of fluid polarity in the swelling of sodium-montmorillonite clay: A molecular dynamics and Fourier transform infrared spectroscopy study, Journal of Rock Mechanics and Geotechnical Engineering 10(6) (2018) 1133-1144.

[11] B.M. Das, K. Sobhan, Principles of geotechnical engineering, Cengage Learning2013.

[12] F. Barbosa, J. Woetzel, J. Mischke, M.J. Ribeirinho, M. Sridhar, M. Parsons, N. Bertram, S. Brown, Reinventing construction: A route to higher productivity, McKinsey Global Institute, New York: McKinsey & Company (2017).

[13] I.J. Brackley, Swell pressure and free swell in compacted clay, National Building Research Institute, Council for Scientific and Industrial (1973).

[14] G. Sinnathamby, L. Korkiala-Tanttu, L.T. Salvador, Shear resistance of bentonite backfill materials and their interfaces under varying hydraulic conditions in a deep rock nuclear waste repository, Applied Clay Science 104 (2015) 211-220.

[15] C. Dimaio, G.B. Fenelli, Residual strength of kaolin and bentonite - the influence of their constituent pore fluid, Geotechnique 44(2) (1994) 217-226.

[16] J.F. Lupini, A.E. Skinner, P.R. Vaughan, The drained residual strength of cohesive soils, Geotechnique 31(2) (1981) 181-213.

[17] E. Duque-Redondo, H. Manzano, N. Epelde-Elezcano, V. Martinez-Martinez, I. Lopez-Arbeloa, Molecular forces governing shear and tensile failure in clay-dye hybrid materials, Chemistry of Materials 26(15) (2014) 4338-4345.

[18] G. Hantal, L. Brochard, H. Laubie, D. Ebrahimi, R.J.M. Pellenq, F.J. Ulm, B. Coasne, Atomic-scale modelling of elastic and failure properties of clays, Molecular Physics 112(9-10) (2014) 1294-1305.

[19] N.T. Skipper, G. Sposito, F.R.C. Chang, Monte-carlo simulation of interlayer molecular-structure in swelling clay-minerals. 2. monolayer hydrates, Clays and Clay Minerals 43(3) (1995) 294-303.

[20] B.J. Teppen, K. Rasmussen, P.M. Bertsch, D.M. Miller, L. Schafer, Molecular dynamics modeling of clay minerals .1. Gibbsite, kaolinite, pyrophyllite, and beidellite, Journal of Physical Chemistry B 101(9) (1997) 1579-1587.

[21] K.S. Katti, D. Sikdar, D.R. Katti, P. Ghosh, D. Verma, Molecular interactions in intercalated organically modified clay and clay-polycaprolactam nanocomposites: Experiments and modeling, Polymer 47(1) (2006) 403-414.

[22] D.R. Katti, S.R. Schmidt, P. Ghosh, K.S. Katti, Modeling the response of pyrophyllite interlayer to applied stress using steered molecular dynamics, Clays and Clay Minerals 53(2) (2005) 171-178.

[23] D. Sikdar, D.R. Katti, K.S. Katti, A molecular model for epsilon-caprolactam-based intercalated polymer clay nanocomposite: Integrating modeling and experiments, Langmuir 22(18) (2006) 7738-7747.

[24] W. Humphrey, A. Dalke, K. Schulten, VMD: Visual molecular dynamics, Journal of Molecular Graphics 14(1) (1996) 33-.

[25] J.C. Phillips, R. Braun, W. Wang, J. Gumbart, E. Tajkhorshid, E. Villa, C. Chipot, R.D. Skeel, L. Kale, K. Schulten, Scalable molecular dynamics with NAMD, Journal of Computational Chemistry 26(16) (2005) 1781-1802.

[26] A.D. MacKerell, D. Bashford, M. Bellott, R.L. Dunbrack, J.D. Evanseck, M.J. Field, S. Fischer, J. Gao, H. Guo, S. Ha, D. Joseph-McCarthy, L. Kuchnir, K. Kuczera, F.T.K. Lau, C. Mattos, S. Michnick, T. Ngo, D.T. Nguyen, B. Prodhom, W.E. Reiher, B. Roux, M. Schlenkrich, J.C. Smith, R. Stote, J. Straub, M. Watanabe, J. Wiorkiewicz-Kuczera, D. Yin, M. Karplus, All-atom empirical potential for molecular modeling and dynamics studies of proteins, Journal of Physical Chemistry B 102(18) (1998) 3586-3616.

[27] W.L. Jorgensen, J. Chandrasekhar, J.D. Madura, R.W. Impey, M.L. Klein, Comparison of simple potential functions for simulating liquid water, Journal of Chemical Physics 79(2) (1983) 926-935.

[28] L. Kale, R. Skeel, M. Bhandarkar, R. Brunner, A. Gursoy, N. Krawetz, J. Phillips, A. Shinozaki, K. Varadarajan, K. Schulten, NAMD2: Greater scalability for parallel molecular dynamics, Journal of Computational Physics 151(1) (1999) 283-312.

[29] P.M. Amarasinghe, K.S. Katti, D.R. Katti, Nature of organic fluid-montmorillonite interactions: An FTIR spectroscopic study, Journal of Colloid and Interface Science 337(1) (2009) 97-105.

[30] L. Börgesson, L.E. Johannesson, T. Sandén, J. Hernelind, Modelling of the physical behaviour of water saturated clay barriers. Laboratory tests, material models and finite element application, Swedish Nuclear Fuel and Waste Management (1995).

[31] Y.C. Wang, L. Cong, Effects of Water Content and Shearing Rate on Residual Shear Stress, Arabian Journal for Science and Engineering 44(10) (2019) 8915-8929.

[32] K. Bláhová, L. Ševelová, P. Pilařová, Influence of water content on the shear strength parameters of clayey soil in relation to stability analysis of a hillside in Brno region, Acta Universitatis Agriculturae et Silviculturae Mendelianae Brunensis 61(6) (2013) 1583-1588.

6. EXPERIMENTAL EVALUATION OF SHEAR STRENGTH OF SWELLING CLAYS FOR VARIOUS MAGNITUDE OF SWELLING[4]

6.1. Introduction

Swelling clays are found throughout the world and can undergo a significant volume change with relative to original volume when mixed with water. These clays are very active clay minerals. Some unique properties of swelling clays are high specific surface area, low permeability and low compressibility, and high swelling capacity due to which these clays are used in geotechnical engineering, geoenvironmental engineering, and industrial applications. Furthermore, these clays have been used as barrier materials in landfill liners, as drilling mud, to enhance the mechanical properties of clay-polymer-nanocomposities, and as modifiers in pavement construction. On the other hand, the uplift pressure developed upon swelling can damage infrastructures such as buildings, roads, bridges, embankments, and canals. Thus, it is essential to evaluate the compressive strength, undrained cohesion, and probe the evolution of the microstructure of swelling clays to avoid detrimental effects and use these clays in geotechnical engineering and geoenvironmental applications.

Sodium-montmorillonite (Na-MMT), an expansive clay mineral that is commonly found in swelling clays. The structure of Na-MMT clay consists of a tetrahedral-octahedral-tetrahedral (T-O-T) arrangement where an octahedral clay sheet is sandwiched between tetrahedral clay sheets [1]. Due to isomer substitution in the tetrahedral or octahedral sheet, the negative charges are developed in the clay sheets. These negative charges are balanced by introducing sodium

[4] This chapter describes to evaluate the mechanical properties of swelling clays at various level of swelling at the macroscale and nanoscale. Also, the evolution of the microstructures of swelling clays is discusses. The content of this chapter will be submitted for the publication. Keshab B. Thapa had primary responsibility for collecting samples in the field and for interviewing users of the test system. Keshab B. Thapa was the primary developer of the conclusions that are advanced here. Keshab B. Thapa also drafted and revised all versions of this chapter. Dinesh R. Katti and Kalpana S. Katti served as proofreader and checked the math in the statistical analysis conducted by Keshab B. Thapa.

cations in the interlayer for Na-MMT. In our previous experimental work, the swelling pressure of saturated bentonite at a predetermined level of swelling has been evaluated [2]. The swelling pressure decreased with increase in swelling level, resulting in clay particles breakdown into a smaller size. Furthermore, the clay-fluid interactions result in increasing the disorientation of the clays sheets with increase in the levels of swelling [3]. The molecular hydraulic conductivity of Na-MMT clay interlayer has been evaluated using polarized Fourier transform infrared (FTIR) spectroscopy [4, 5]. The interactions of Na-MMT clay with various organic fluids, which are not only commonly found leachates in the landfill but also toxic to human health, have been accomplished [4]. The interactions between Na-MMT clay and organics fluids are nonbonded in nature. Furthermore, the polar fluids such as water and formamide have higher interaction with Na-MMT than with medium polar fluid methanol and low polar fluid acetone [4].

Besides experimental studies, the computational techniques such as Molecular Dynamics (MD) simulations, Steered Molecular Dynamics (SMD), Discrete Element Method (DEM), and Monte Carlo (MC) have been extensively used to study swelling behavior and clay-water interactions at the molecular level [6-11]. In our previous work, the mechanical response of the dry Na-MMT and hydrated with multiple monolayers of water is carried out using SMD simulations [8, 12]. The results have shown that the hydration of interlayer cations, water content in the interlayer, and interactions between clay and water influence the interlayer spacing, stress-strain behavior of the interlayer, and interlayer modulus. Furthermore, the DEM study has shown that the particle breakdown of Na-MMT is responsible for increasing the swelling pressure [9].

Understanding of the fundamental mechanical properties of clay is essential for the design properties of the composite materials [13, 14]. The mechanical behavior of the swelling

clays is also necessary to the barrier liners in landfills as well as to store high-level radioactive waste [15]. The mechanical properties of swelling clays are also essential for the efficient and economic extraction of oil and gas from oil shale—sedimentary rock [16, 17]. The knowledge of elastic properties is used for analyzing the geophysical subsurface exploration and reservoir characterization using seismic waves [18]. The mechanical properties of clays are furthermore required to evaluate the settlement of the laterally loaded foundations [19]. The elastic properties at the macroscale can be easily computed using uniaxial compression or tensile testing method. Nevertheless, the elastic properties at the nanoscale whether thin films on substrate or free standing samples require a sophisticated method. Therefore, nanoindentaion is an experimental technique to measure the nanomechanical properties of the materials at the nanoscale based on the theory of elastic contact. The frequently measured two mechanical properties are the elastic modulus (E) and the hardness (H). The indenter is allowed to press the sample at a specific load and then withdrawn. The load-displacement data are recorded from one complete loading and unloading cycle. The withdrawn of the indenter results in recovering the elastic deformation, and certain displacement remains as the plastic deformation, which is also known as residual indentation depth. The displacement during unloading is typically elastic in nature; the initial portion of the unloading curve is used for the analysis. The indenter tip is made up of diamond that has high resistance to deformation.

The elastic properties of clay minerals have a great importance for the characterization and exploration of the shale formations, as the clay minerals are common in the sedimentary formations and environments. The Elastic modulus and hardness of air dried layered aluminosilicates—muscovite and rectorite clay minerals—have been studied using load-controlled nanoindentation at various loading rates [20]. The variation of the nanomechanical

properties of bentonite and kaolinite clays that are subjected to an elevated temperature from 25^{o}C to 200^{o}C have been studied using nanoindentation. It has been observed that the resistance to penetration and elastic modulus increased with increase in temperature, and bentonite clay has higher elastic modulus than kaolinite clay [21]. The load-controlled nanoindentation of kaolinite clay mineral stabilized with oil-in-water emulsions and dried at room temperature is carried out, and the elastic modulus and hardness are found to be 0.5-3 GPa and hardness of 15-40 MPa, respectively [22]. The mechanical properties of sand grains are examined using nanoindentaiton, and it has been reported that the individual behavior at the nanoscale influences the overall behavior of sand at the macroscale [23]. Previous work on bionanocomposites—seashell and bone—has shown that the nonbonded interactions (electrostatic and van der Waals) between the minerals and organics influence the mechanics of the organic structures [24-26]. Furthermore, similar phenomenon has been found in synthetic nanocomposites in which the mineral-polymer interactions influence the mechanical response of polymers. Thus, the material properties of nanoscale systems are influenced by the interactions at the molecular level. Nanaoindentaion experiments in this study also allow to identify difference in the nanomechanical properties of dry clay as well as clay saturated with one of the organic fluids, water. Additionally, the influence of swelling on the nanomechanial properties is also incorporated in this study.

The unconfined compressive strength of swelling clay mineral such as kaolinite at various moisture content has been examined, and the reported unconfined compressive strength for kaolinite at optimum moisture content is about 300 kPa [27]. Furthermore, the unconfined compressive strength of clays with high plasticity at optimum moisture reported about 226 kPa [28]. Most of the studies have used examined the unconfined compressive strength for the treatment and stabilization of expansive clays using mechanical and chemical technique [29],

using crumb rubber, natural and synthetic fibers [30], fly ash [31], and jute fiber reinforcement [32]. However, compressive strength of saturated Na-MMT at various level of swelling has not been thoroughly evaluated. The changes in unconfined compressive strength and undrained cohesion at no volume change and at various levels of swelling is presented in this study.

Our previous studies have shown that the clay-fluid interactions for saturated swelling clays at the nanoscale control the macroscopic properties of swelling clays such as microstructure, permeability, and consolidation [33, 34]. The measurement of mechanical properties of swelling clays is challenging because of their affinity to water, expansive in nature, and plate like structures [35]. Thus, in most of the reported literatures, the elastic modulus and hardness of clay minerals are measured either in dry in oven at high temperature or very small water content conditions. In this work, we also present our results from displacement-controlled nanoindentation on undisturbed dry and saturated Na-MMT clay samples. Furthermore, this study captures insight into the role of water on the elastic modulus and hardness of the undisturbed clay samples at various level of swelling.

6.1.1. Materials

Sodium (Na)-montmorillonite clay mineral was obtained from the Clay Minerals Society at the Purdue University, West Lafayette, Indiana. The chemical formula of the Na-MMT clay mineral is $NaSi_{16}(Al_6FeMg)O_{20}(OH)_4$, and the clay has a specific gravity of 2.67, the initial void ratio of 2.14, the density of 850 kg/m^3, and a cationic exchange capacity of about 76.4 mequiv/100 g. The deionized water was prepared in our laboratory in Civil and Environmental Engineering Department, North Dakota State University. Prior to each sample preparation, Na-MMT clay mineral was ground finely and passed through a 76 μm mesh (No. 200 sieve). In

order to have a consistent moisture content, the powder specimen was then placed in a drying oven at 105 ^{o}C for 24 hours.

6.1.2. Methods and Sample Setup

The clay samples were saturated using a new controlled uniaxial swelling (CUS) device. Furthermore, this CUS device was allowed to move to a predetermined level for the measurement of swelling level. A detailed design and explanation of the CUS device is explained in our prior work to evaluate the swelling pressure as well as evolution of the microstructures at various levels of swelling [2]. In brief, the CUS device allows the samples to saturate and swelling in uniaxial direction and can be split vertically to remove the sample with minimum disturbance. At the bottom of the CUS device, a porous stone disc was placed followed by a Whatman No. 40 filter paper. About 232 grams of dry NaMMT clay was placed in the controlled uniaxial (CUS) device of 70 mm internal diameter. To be consistent with our previous experiments [2, 34], the clay sample is loosely compacted in four layers by gently tapping a few times to the height of 72 mm in the CUS device where each layer had about 58 grams to maintain the void ratio of 2.14 as shown in Figure 6.1. A filter paper was then placed on top of the clay surface followed by a porous stone disc. Thus, all the samples at this stage were placed between two porous stones.

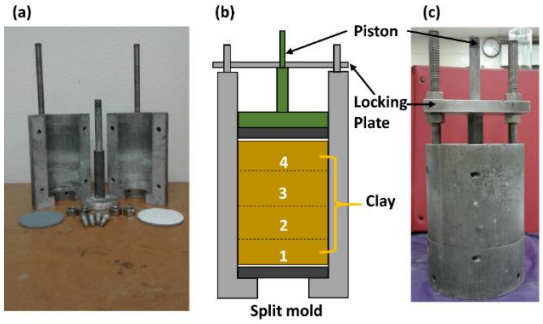

Figure 6.1. (a) The controlled uniaxial device parts with piston, porous stones, filter paper, and hexagonal bolts; (b) schematic showing the dry clay sample compacted in four layers; (c) locking of the CUS device at zero swelling level using the piston and locking plate.

The movable piston that can fit inside the CUS device was used to lock in the position to maintain a zero swelling level during saturation. This piston was made of aluminum that can be easily fit inside the CUS device of internal diameter of 70 mm. This piston was connected to the rod where the diameter of the rod varied from 12.70 mm to 20.30 mm. Furthermore, two fined threaded bolts of internal diameter 22.20 mm were screwed in the CUS device. A flat locking plate of height of 6 mm with three holes—one at the center and two at the sides—was placed at the center of the piston and then locked using four hexagonal stainless steel nuts. Up to this condition, the diameter of the clay sample is 70 mm, and height of the sample is 72 mm, and the sample was locked and maintained at zero level of swelling. Then this CUS device with dry clay was placed inside a diameter of 203 mm cylindrical Plexiglass chamber for the saturation. The clay samples were prepared in the three identical CUS devices A, B, and C as shown in Figure 6.2.

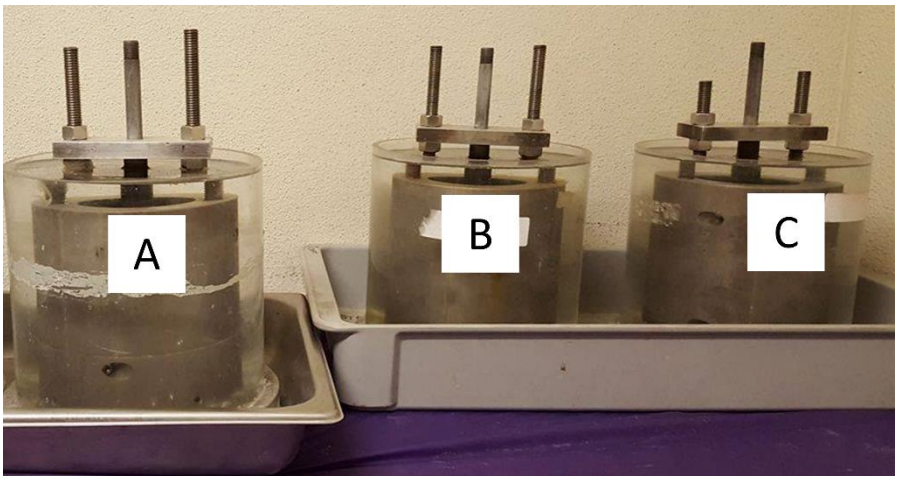

Figure 6.2. The CUS devices A, B, and C placed in the cylindrical Plexiglass chamber to saturate the clay samples at various level of swelling (0%, 10%, and 20%).

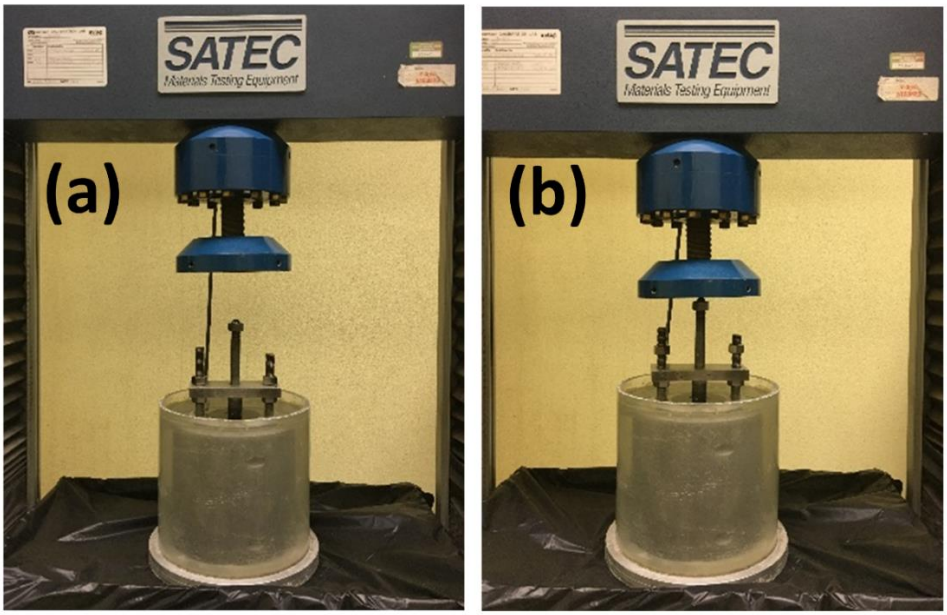

Figure 6.3. The CUS cell with the saturated clay sample placed in a SATEC load frame to measure the predetermined level of swelling (a) before and (b) after the movable load frame contacted the piston and hexagonal nuts released to allow swelling.

Previous extensive experiments for the measurement of the swelling pressure and on swelling clays using the same CUS device showed that it took about 30 days to completely saturate the smectite swelling clay minerals. This was further confirmed by recording swelling pressure developed at zero level of welling over time in which the swelling pressure remained constant after 21 days, and the degree of saturation was 100%. However, in our case, all the samples were kept in the Plexiglass chamber for about 365 days to acquire a complete saturation. The Plexiglass chamber was continually filled with water to provide a sufficient amount of water to saturate the samples.

The Plaxiglass chamber with CUS device was placed in the SATEC 22 EMF Universal testing equipment. The piston of the CUS device was centered with the loading ram of the universal testing equipment, and the load-cell was brought in contact with the piston of the CUS device. The locking of the piston of the CUS device was released by unscrewing the hexagonal nuts. At this condition, the piston was maintained at zero swelling. The CUS device was kept

under the SATEC load-frame at least for 30 days. The loading ram was moved up in order to remove the CUS device, and the sample was furthermore used to evaluate the microstructure, undrained cohesion, and nanomechanical properties, which are discussed in the next sections. Additionally, the loading ram was moved up to the predermined level of 7.20 mm for 10% swelling and 14.40 mm for 20% swelling. To measure the swelling level, the piston locking system was again released. Once the piston moved vertically up and touched the loading arm to attain the predermined level of swelling at least for 30 days, the piston was locked to continue to maintain that level of swelling and saturation. Furthermore, the swelled clay samples were used to perform the microstructure, undrained cohesion, and nanomechanical properties at various level of swelling. A complete experimental plan is shown in Figure 6.1 (a).

6.1.3. Unconfined Compression Test

When the bulk samples were saturated, the next stage of the experiment was to preform unconfined compression (UC) test for the measurement of the undrained cohesion. In order to evaluate the undrained compressive strength of saturated swelling clays at various level of swelling, a series of unconfined compression tests of the various level of swelled samples were accomplished. Firstly, the zero percent swelled sample was removed from the CUD device.

Figure 6.4 (b) showed a cylindrical split mold of internal diameter of 35 mm, height of 70 mm, and thickness of 3 mm, which was used to take the sample from the CUS device. This cylinder was made up of polymethyl methacrylate (PMMA) white, which can be vertically split to two pieces, and they were connected using 160 mm long stainless steel cable tie. Before taking the sample for the compression test, the cylinder was lubricated with silicone high vacuum grease (Dow Corning Corporation, USA) to reduce the adhesion between sample and cylinder. The cylinder was then gently pressed as showed in Figure 6.4 (c) on top of the swelled sample

and removed up gently. A sample of diameter of 35 mm and height of 70 mm was then removed from the cylindrical split mold by releasing stainless steel cable tie for the compression test as shown in Figure 6.4 (d). For the unconfined compressive strength test, the strain rate of 1%/min was used according to the ASTM D 2166-16 by keeping the volume of the sample constant. A Shimadzu loading frame (Shimadzu Scientific Instruments, USA) was used for the compression test for 0%, 10%, and 20% swelling. The load capacity of this Shimadzu loading frame was 2 kN, which was appropriate for the compression of the saturated swelling clays. The moisture content and weight of the sample were measured before and after the compressive strength test as well .The degree of saturation of each sample was found to be 100%.

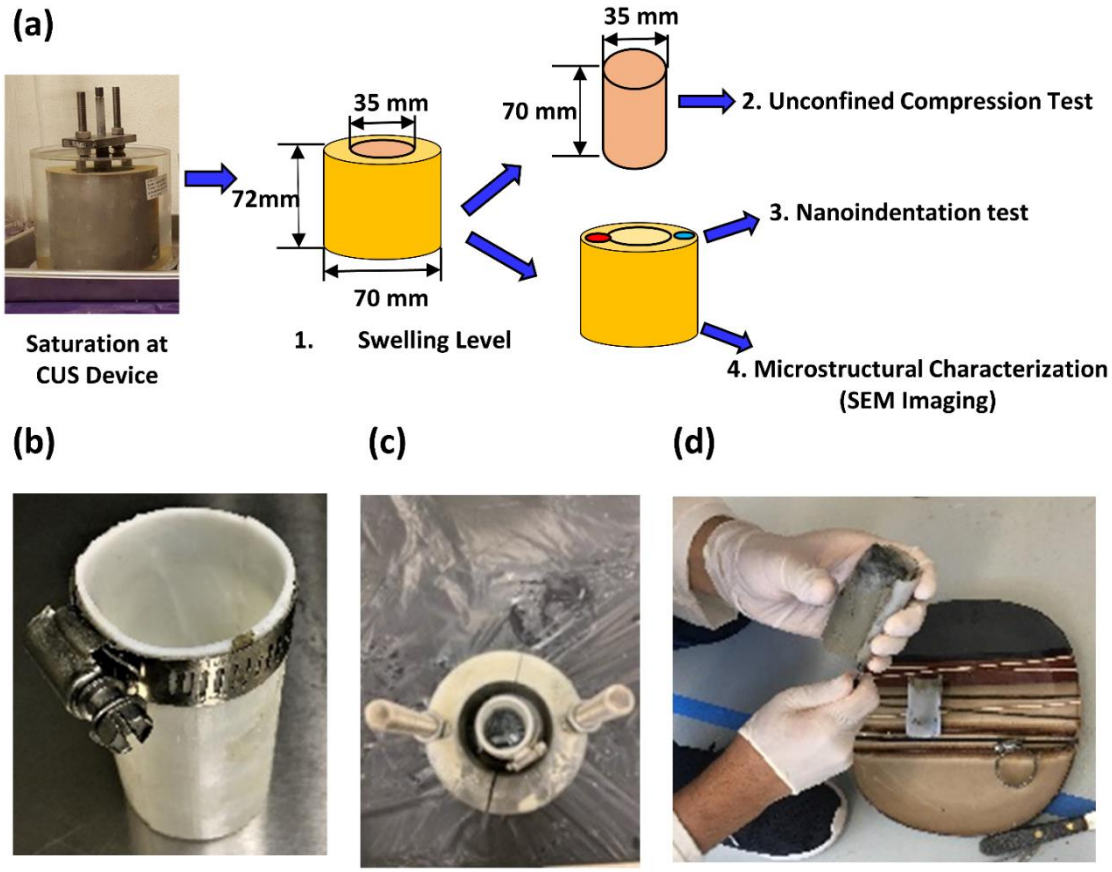

Figure 6.4. (a) Types of experiments (b) a cylindral split mold of height 70 mm and diameter 35 mm, (c) spilt mold pressed in the CUS device, and (d) removavle of undisturbed sample for the compression test.

6.1.4. Nanomechanical Properties

For nanoindentation experiment for dry clay, 0.575 gram of oven dried clay sample was then placed in the disc-cylinder by gently tapping to acquire the initial density of 850 kg/m^3 clay sample. The disc-cylinder had a height of 6 mm, a diameter of 12 mm, and thickness of 1 mm as shown in Figure 6.5; this cylinder was made up of polymethyl methacrylate (PMMA) white. The base of the disc-cylinder was glued with a diameter of 15 mm stainless steel disc to support the sample as shown in Figure 6.5(c). For nanoindentation on statured clay, the undisturbed saturated sample was taken by gently pressing the disc-cylinder from swelled sample in the CUS device.

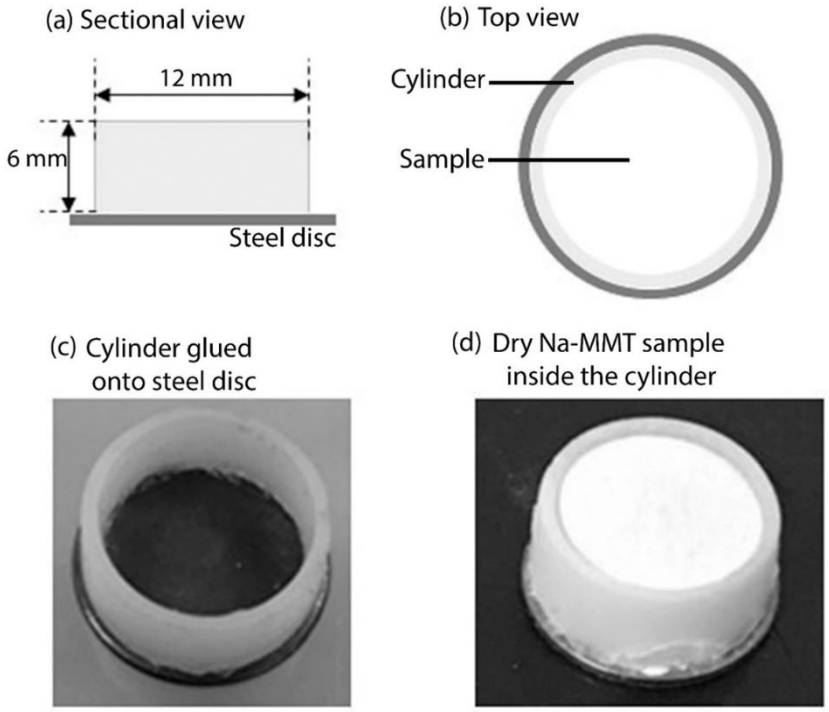

Figure 6.5. Schematic showing the assembly for nanoindentation experiment of dry clay.

Nanoindentation tests were accomplished using contact mode with a Hysitron Triboscope nanomechanical testing instrument (Minneapolis, MN). The load resolution and displacement resolution of this instrument were 1 nN and 1 nm, respectively. A trigonal pyramid Berkovich diamond tip (100-200 nm tip radius) was used to perform the test. To evaluate how the

nanomechanical properties of swelling clay change during saturation at different level of swelling, the displacement-controlled indentation tests at forward displacement of 500 nm were carried to determine the elastic modulus and hardness of dry as well as saturated Na-MMT clay. The dry and saturated samples that are placed in the magnetic stage for the nanoindentation experiments are shown in Figure 6.6. Also, a 4-4 triangular loading function was selected at loading and unloading rate of 125 nm/s. An average of 14 indents were made on each sample, and the distance between the neighboring tests locations are kept at least 5 µm. Furthermore, the indenter tip is cleaned after each indentation using acetone to reduce the interaction between the tip and clay sample.

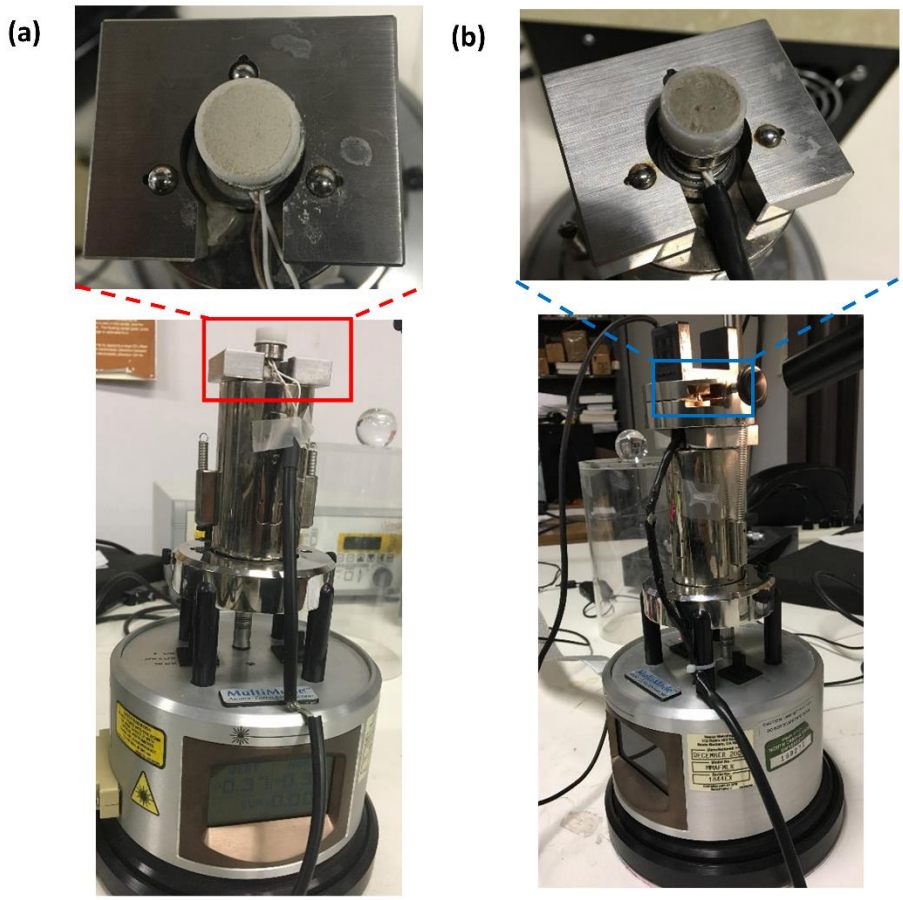

Figure 6.6. The samples placed at the magnetic stage for nanoindentation tests (a) dry clay and (b) saturated clay.

6.1.5. Microstructural Evaluation

The microstructure of the swelling level tested samples is examined using a scanning electron microscope (SEM). After swelling level was measured, the clay sample was removed from the controlled uniaxial swelling (CUS) device. A 5 mm x 10 mm sample was then sliced axially from the circumferential region using a thin ceramic knife. The sample was then placed into an appropriately sized hole drilled into a brass sample-holder cryostub (JEOL USA, Peabody, Massachusetts, USA) with Teflon feet to isolate it thermally from its surroundings and allow it to warm at a slower rate. The material was secured in the hole using Tissue-Tek O. C. T. Compound (Sakura Finetek USA, Inc., Torrance, California). The cryostub with attached sample material was submerged in liquid nitrogen. Once the sample was completely frozen, the clay extending above the surface of the cryostub was fractured by striking it with the edge of a new razor blade that had been previously cooled in liquid nitrogen; excess fractured clay was removed and discarded. The brass holder was inserted promptly into a variable-pressure scanning electron microscope (SEM; JEOL JSM-6490LV, JEOL USA, Peabody, Massachusetts). The sample was allowed to stand in the SEM for 5-10 minutes so that surface moisture/frost could sublimate before the fractured surface was examined. Images then were acquired within a ten-minute window. Backscattered electron images were taken in low-vacuum mode at a pressure of 30 Pa.

6.2. Results and Discussions

6.2.1. Effect of Swelling on Unconfined Compressive Strengths

A plot of unconfined compressive stress versus axial strain for 0%, 10%, and 20% swelling is shown in Figure 6.7. The stress-strain behavior for each level of swelling is different. The initial slope below 2% axial strain of the stress-strain curve for 0% swelling is steeper than

that of 10% and 20% swelling, whereas the slope of the stress-train plot is the same for 10% and 20% swelling. Beyond 2% axial strain, the increase in unconfined strength follows a different path each level of swelling. Also, the stress-strain plot for 10% swelling falls between that of plots of 0% and 20% swelling. The stress-strain plot also shows a continuous deformation, and the pronounced stress-strain peak at strain of 8.00%, 7.30%, and 7.02% for 0% swelling, 10% swelling, and 20% swelling, respectively.

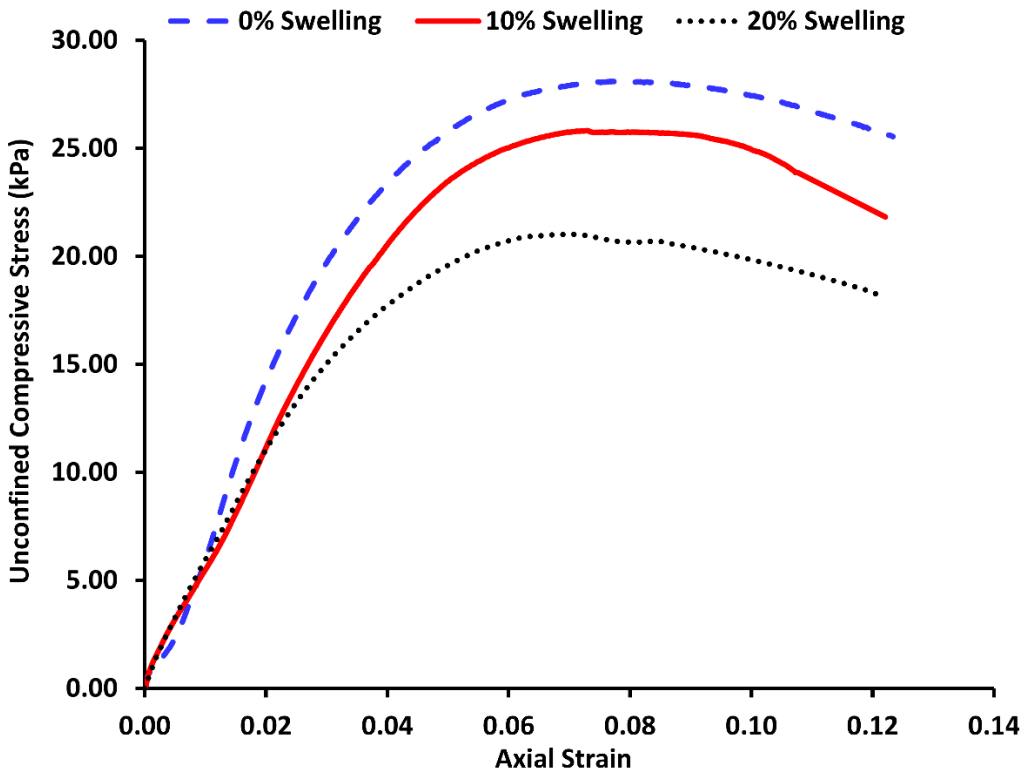

Figure 6.7. Stress-strain from unconfined compressive strength test for 0%, 10%, and 20% swelling.

The unconfined compressive stress after maximum value gradually decreased with increased in axial strain, and the maximum strain is about 12% for all level of swelling. The values of the maximum unconfined compressive strength are 28.10 kPa for no swelling, 25.82 kPa for 10% swelling, and 21.03 kPa for 20% swelling as shown in Figure 6.8. In unconfined compressive strength test, the confining pressure around the circumference of the sample is zero,

which also mimics no radial confining pressure when shearing the clay samples. Thus, the total minor principal stress is zero, as there is no confining pressure, and the major principal stress is the maximum unconfined stress obtained from the stress-strain plot. When the sample is completely saturated and fully undrained upon shearing, undrained cohesion is independent of confining pressure. Thus, the undrained cohesion in this case is half of the unconfined compressive stress. The values of undrained cohesion are 14.05 kPa, 12.91 kPa, and 10.52 kPa for 0%, 10%, and 20% swelling, respectively. These values are within the range for saturated montmorillonite clay minerals as reported in the literatures [19, 36]. Therefore, the undrained cohesion is also decreased with increase in the levels of swelling.

The swelling pressure at no volume change is the highest, and the values of swelling pressure are decreased with increased in the level of swelling [2, 37]. This large swelling pressure at no volume change provides a significant amount of resistance when the external normal stress is applied. Furthermore, the maximum unconfined compressive strength of the clay sample at no volume change is 8% and 25% higher than the unconfined strength of the samples swollen to 10% and 20% swelling, respectively.

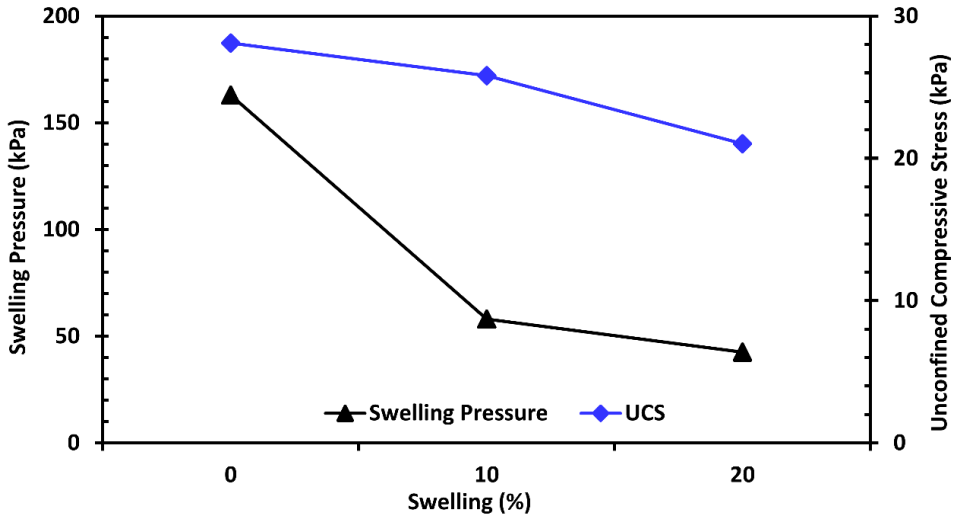

Figure 6.8. The unconfined compressive stress (UCS) versus swelling level. The swelling pressure is adopted from our previous work (Katti, D., & Shanmugasundaram, V. 2001).

6.2.2. Role of Swelling on Naomechanical Properties

In order to assess the influence of swelling on the nanomechanical properties of swelling clays, the displacement-controlled experiments at maximum depth of 500 nm is carried using nanoindentation. The load-displacement (L-D) curves for dry and 0%, 10%, and 20% swelling are shown in Figure 6.9. The L-D curve for 0% swelling is wider than that of dry clay sample. Furthermore, the L-D curves for the clay samples swollen to 10% and 20% are narrower. It is also observed that the L-D curve for 0% swelling is steeper than that of 10% and 20% swelling, which indicates that the stiffness decreases with increased in the level of swelling.

The average maximum forces needed to indent for dry, 0%, 10%, and 20% swelling are presented in Table 6.1. The average maximum forces required for 0% swelling and dry clay are 88.56 μN and 32.04 μN, respectively. The volume of the sample at 0% swelling at CUS device is not allowed to change with respect to the original volume, and thus the void ratio of the clay sample swollen to no volume change does not change. Although the void ratio for the dry sample and no volume change sample is about the same, much larger force is required to indent for the 0% swelling than that of dry for the same indentation depth of 500 nm. Our previous experimental study has shown that the significant amount of swelling pressure is exerted by clay during swelling [2]. To oppose this internal swelling pressure, it can be correlated that the force required to indent the saturated sample is significantly higher than that of dry clay. This can be correlated with the swelling pressure developed when adding water in dry clay because of the clay-water interactions, and large force is required during indentation to overcome the swelling pressure for 0% swelling.

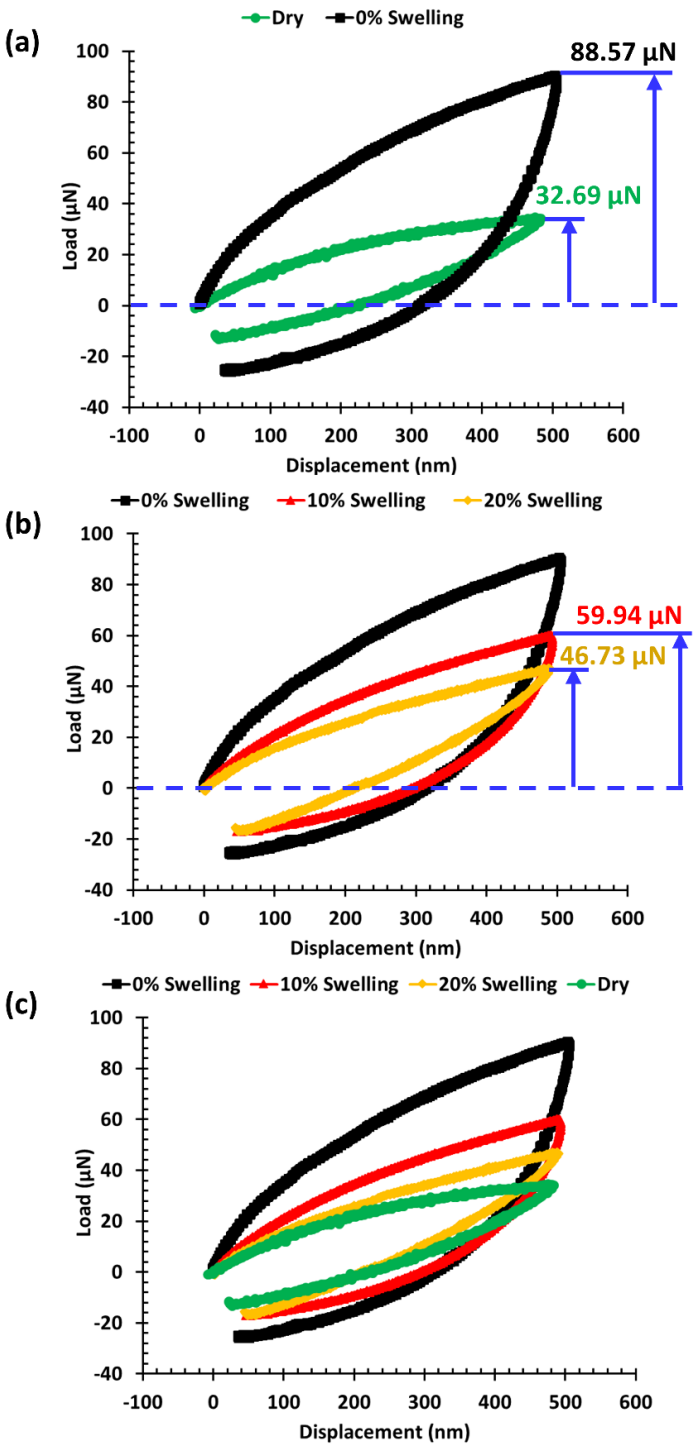

Figure 6.9. The maximum force at indentation depth of 500 nm for (a) dry clay and 0% swelling, (b) 0%, 10%, and 20% , and (c) dry and 0%, 10%, and 20% swelling.

Furthermore, the average maximum forces required to indent at a depth of 500 nm for 10% and 20% swelling are 58.49 µN and 45.44 µN, respectively. The swelling pressure

decreases with an increase in swelling level, and the high swollen samples exhibit lesser resistance to deformation than that of no volume change sample. Thus, the force needed to indent the same displacement is decreased with increased in the levels of swelling.

Table 6.1 also shows the average modulus of elasticity of the dry clay sample as well as the saturated samples swollen to 0%, 10%, and 20% swelling at maximum indentation depth of 500 nm. It is evidently indicates that the elastic modulus at 0% swelling is significantly lower than that of 10% and 20% swelling as shown in Figure 6.10 (a). The modulus of elasticity further decreases with increase in the levels of swelling. The dry clay sample has the lowest modulus of elasticity as shown in Figure 6.10 (a). The modulus of elasticity is 324.75 MPa (Standard Deviation=1.42) for 0% swelling, which is 4.2 times higher than that of dry clay. At no volume change condition (0% swelling), the volume of the clay sample does not alter upon saturation, and thus the void ratio remains the same as that of dry clay. However, it is clearly evident that the saturated samples at no volume change is significantly stiffer than dry clay. The elastic modulus of 0% swelling is in the order of the same magnitude for clayey soils reported in the literature [38]. At the nanoscale level, the clay-water interactions provide the molecular bridge to achieve superior mechanical properties that that of dry clays. Similar results have been observed in where the interactions between clay blocks and polymer significantly enhanced the mechanical properties of polymer-clay-nanocompostities with relative to pristine polymer [76]. Furthermore, the most of the literatures reported that the modulus of elasticity of smectice clay minerals either in dry or low water content condition in Giga Pascal (GPa). The modulus of elasticity of sodium montmorillonite clay ranges from 6-11 GPa at various porosities using uniaxial stress compaction [35]. The average elastic modulus of vermiculite clay mineral is about 32.3 GPa using compression test [39]. Also, the elastic modulus of the compressed and dried

montmorillonite is reported to be about 4.04 GPa using nanoindentation experiments. However, the values of the elastic modulus for NaMMT sample at no volume change in our study is in Mega Pascal, which is much lower than reported values in the literatures; this is due to fact that our sample is completely saturated and much softer than dried and compacted clays reported in the literatures. Additionally, the nanoindentation experiments in this study are carried out on the undisturbed samples.

Table 6.1. The mean values of the elastic modulus, hardness, and maximum force at 500 nm indentation depth.

Sample	Indentation Depth (nm)	Elastic Modulus (MPa)		Hardness (MPa)		Maximum Force (μN)		No. of Exp.
		Avg.	ST. Dev.	Avg.	ST. Dev.	Avg.	ST. Dev.	
0% Swelling	500	324.74	1.42	18.10	0.59	88.56	0.93	15
10 % Swelling		209.01	2.51	11.27	0.50	58.49	1.72	17
20 % Swelling		102.99	1.84	9.43	0.84	45.44	1.44	14
Dry		77.55	1.40	7.16	0.76	32.04	0.67	22

A decreasing elastic modulus with increasing swelling level for the same indentation depth is also observed. It appears that 0% swelling has the highest modulus of elasticity followed by 10% and 20% swelling, which further indicates that the clays become much softer upon swelling. At 500 nm indentation depth, the average elastic modulus for 10% swelling is 209.01 MPa (Standard Deviation=2.51), which is about 1.6 times lower than 0% swelling. Furthermore, the elastic modulus of swelling clay continues to decrease with increase in the level of swelling. The modulus of elasticity for 20% swelling is 102.99 MPa (Standard Deviation=1.84), which is one half of the elastic modulus of 10% swelling. Additionally, the elastic modulus of dry clay is

found to be 77.55 MPa (Standard Deviation=1.84) that is 1.3 times lower than that of 20% swelling, and it further indicates that the dry is much softer than 20% swelling.

The hardness values from displacement-controlled at a maximum depth of 500 nm on dry as well as saturated samples swollen to 0%, 10%, and 20% swelling are evaluated. Table 6.1 also presents the hardness values for dry clay and saturated clays. The average hardness for 0% swelling is 18.10 MPa (Standard Deviation=0.59), which is 2.8 times higher than that of dry clay. Thus, the saturated sample at no volume change condition becomes much harder than dry clay. However, the hardness values decrease with increase in the levels of swelling. Furthermore, the hardness of 10% swelling is 11.27 MPa (Standard Deviation=0.50) that is 1.5 times lower than 0% swelling. The hardness of 20% swelling is 9.43 MPa (Standard Deviation=0.84) that is 1.3 times lower than that of 10% swelling, whereas the hardness of 20% swelling is 1.4 times higher than that of dry clay. Thus, it is evidently clear that the level of swelling not only influences the elastic modulus but also hardness.

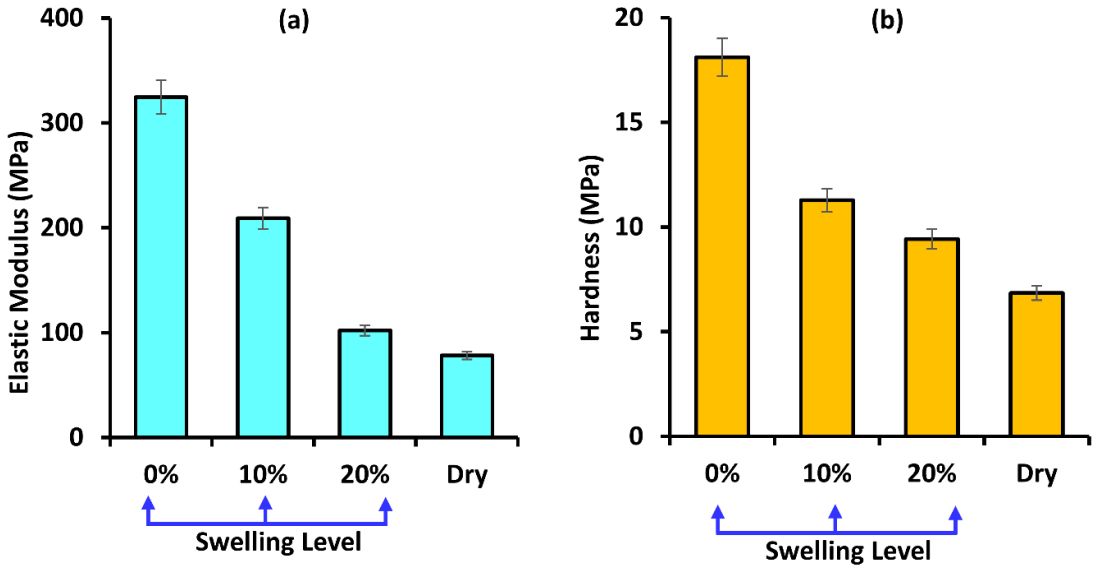

Figure 6.10. The nanomechanical properties for dry clay, and saturated clay at 0%, 10%, and 20% swelling using nanoindentation: (a) modulus of elasticity and (b) hardness.

6.2.3. Evolution of Microstructure

In order to understand the role of swelling on the macro scale and nanoscale mechanical properties of swelling clays, the study of the evolution of the microstructures at various level of swelling is necessary. Figure 6.11 shows the SEM micrographs of dry as well as saturated NaMMT samples at various level of swelling. For the dry case, relatively large particle sizes are observed, and the void spaces between the particles are visible. As soon as water molecules are added to dry clay and allowed to swell to the predermined levels of swelling, the microstructure of clay is altered, leading to particle breakdown into smaller sizes as shown in Figure 6.11 (b-d). This phenomenon can be correlated with the results from the molecular modeling of dry as well as NaMMT hydrated at various level of swelling in which the stability of the structure in dry NaMMT clay is maintained by the attentive interactions between the clay sheets and interlayer cations [65]. However, with increase in water content in the interlayer gallery, the interactions between clay sheets rapidly diminish, causing particle breakdown. Also, the attractive nonbonded interactions between the interlayer sodium cations and water molecules that form a well-organized pattern called hydration shell, which initiates swelling through exfoliation of clay sheets [40].

Figure 6.11 also clearly shows that the breakdown of the clay particles increases with an increase in the levels of swelling, resulting in the filling of void spaces between the clay particles. Furthermore, the void ratio is defined as the ratio of the volume of voids to the volume of solids, and the void ratio does not alter at 0% swelling sample because the volume of solids or change in the total volume with respect to original volume is not allowed during saturation period. However, the values of void ratio for 10% and 20% swelling increase because the

samples are allowed to swell because of change in total volume of the sample during swelling process.

It is clearly observed that the particle sizes decrease significantly with increase in swelling level. The clay-fluid interactions play an important role to alter the microstructure of swelling clay, causing large agglomerations of clay particles breakdown into the smaller sizes. Similar observations have been reported in the literatures to evaluate the effect of swelling pressure not only with water but also with a various organic polar and nonpolar fluids [2, 34]. The change in microstructure influences the macroscale properties—unconfined compressive strength and undrained cohesion—of swelling clays.

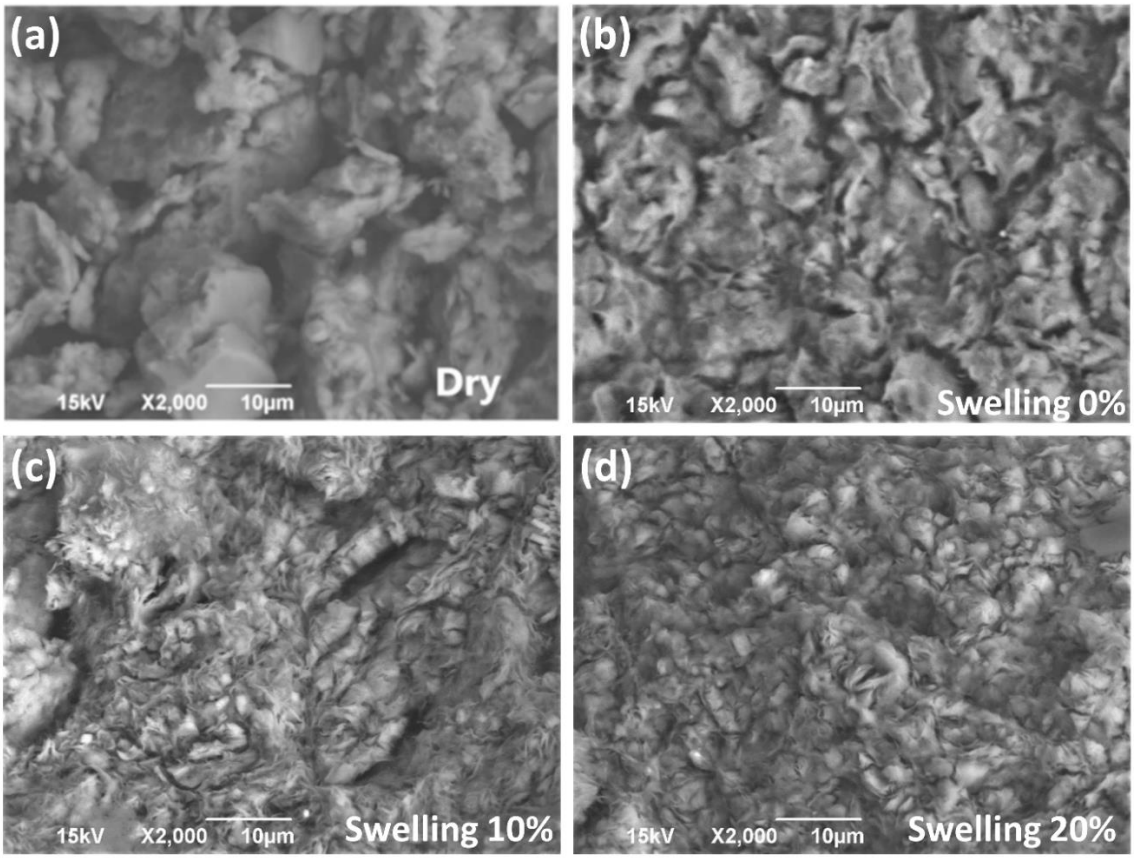

Figure 6.11. SEM micrographs at the same scale showing the evolution of microstructure of dry and saturated NaMMT clay swollen to various swelling level: (a) dry (adopted from our previous work by Amarasinghe et al. 2012), (b) 0%, (c) 10%, and (d) 20%.

6.3. Conclusions

- This work provides an insight into the role of swelling on the macroscale mechanical properties, evolution of microstructures, and nanomechanical properties of NaMMT swelling clays. A controlled uniaxial (CUS) device is used to saturate the samples, and this device further allows to swell in a predermined level of swelling without bulging the swelling clay samples. In this study, we choose three swelling levels: 0%, 10%, and 30%. The unconfined compressive strength and undrained cohesion of these three swollen samples at the macroscale are evaluated. Furthermore, the swelling level tested samples are used to study the microstructures using a scanning electron microscope and nanomechanical properties (elasticity and hardness) at the molecular level using nanoindentation experiments.
- The unconfined compressive strength of the NaMMT sample decreases with increase in the swelling level. The swelling pressure of NaMMT clay under no volume change condition is the highest, and swelling pressure continues to decrease with an increase in swelling level. Thus, large unconfined compressive strength at no volume change is higher than that of the samples swollen to 10% and 20% swelling. This is because the internal swelling forces developed by the clay-water interactions provide more resistance upon compressive and shearing at constant strain rate. Furthermore, the undrained cohesion decreases with increase in the levels of swelling.
- Swelling also controls the evolution of the microstructure of NaMMT clay. As water molecules enter to the NaMMT interlayer gallery, the interactions of water with clay sheets and interlayer cations initiate swelling as well as develop the internal swelling forces, and the microstructure of clay is altered. Furthermore, the particles breakdown

into smaller sizes with an increase in the levels of swelling, and thus the void spaces between the particles are filled. Therefore, the change in the microstructure of the swelling clays significantly alters the unconfined compressive strength at various levels of swelling. The results further demonstrate that swelling influences the mechanism on the evolution of the microstructures and macroscale mechanical properties of swelling clays.

- Nanoindentation experiments in the displacement controlled mode are carried out for dry clay as well as undisturbed saturated clay swollen to 0%, 10, and 20% swelling for the first time. The Berkvich tip is cleaned prior to each indent to reduce the interaction between the tip and samples. In this work, Oliver and Pharr method is used to compute the elastic modulus for all samples. The load-dispalcement curve for no volume change clay sample is much wider than the swollen clay samples. With an increase in the level of swelling, the L-D plots become much narrower. The maximum force needed to indent the same magnitude of displacement for saturated sample at no volume change condition is significantly higher than that of dry clay. Furthermore, the maximum force needed to indent decreases with increase in the levels ofswelling, which be correlated with a much larger force is required to oppose the internal swelling pressure for 0% swelling than that of 10% and 20% swelling. The modulus of elasticity and hardness also decrease with increase in the levels of swelling.
- In summary, the change in the nanomechanical properties of swelling clays at various levels of swelling is linked with the variation of the macroscopic unconfined compressive strength, undrained cohesion, and evolution of the microstructures. In this work, the influence of the nanomechanical properties of swelling clays at various levels of swelling

has been reported for the first time. The results from the experimental techniques at the macroscale, microscale, and nanoscale could be an important factor for the development of the multiscale modeling of swelling clays.

6.4. Acknowledgements

The authors would like to acknowledge the support from the USDoT, Mountain Plains Consortium (MPC) grants MPC-506 (agreement # DTRT13-G-UTC38) and MPC-548 (agreement# 69A3551747108). The authors also acknowledge Dr. Scott Payne from NDSU the electron microscopy center at NDSU for help with scanning electron microscopy imaging. The support from the National Science Foundation under grant no. 0619098 is also acknowledged for the scanning electron microscope. Author K. B. T. acknowledges the support from ND EPSCoR through a doctoral dissertation fellowship.

6.5. References

[1] J.K. Mitchell, K. Soga, Fundamentals of soil behavior, (2005).

[2] D. Katti, V. Shanmugasundaram, Influence of swelling on the microstructure of expansive clays, Canadian Geotechnical Journal 38(1) (2001) 175-182.

[3] K.S. Katti, D.R. Katti, Relationship of swelling and swelling pressure on silica-water interactions in montmorillonite, Langmuir 22(2) (2006) 532-537.

[4] P.M. Amarasinghe, K.S. Katti, D.R. Katti, Nature of organic fluid-montmorillonite interactions: An FTIR spectroscopic study, Journal of Colloid and Interface Science 337(1) (2009) 97-105.

[5] P.M. Amarasinghe, K.S. Katti, D.R. Katti, Molecular hydraulic properties of montmorillonite: a polarized fourier transform infrared spectroscopic study, Applied Spectroscopy 62(12) (2008) 1303-1313.

[6] E.S. Boek, P.V. Coveney, N.T. Skipper, Monte Carlo molecular modeling studies of hydrated li-, na-, and k-smectites: understanding the role of potassium as a clay swelling inhibitor, Journal of the American Chemical Society 117(50) (1995) 12608-12617.

[7] A. Anandarajah, Influence of particle orientation on one-dimensional compression of montmorillonite, Journal of Colloid and Interface Science 194(1) (1997) 44-52.

[8] D.R. Katti, S.R. Schmidt, P. Ghosh, K.S. Katti, Modeling the response of pyrophyllite interlayer to applied stress using steered molecular dynamics, Clays and Clay Minerals 53(2) (2005) 171-178.

[9] D.R. Katti, M.I. Matar, K.S. Katti, P.M. Amarasinghe, Multiscale modeling of swelling clays: A computational and experimental approach, KSCE Journal of Civil Engineering 13(4) (2009) 243-255.

[10] B.J. Teppen, K. Rasmussen, P.M. Bertsch, D.M. Miller, L. Schafer, Molecular dynamics modeling of clay minerals .1. Gibbsite, kaolinite, pyrophyllite, and beidellite, Journal of Physical Chemistry B 101(9) (1997) 1579-1587.

[11] D.E. Smith, Y. Wang, H.D. Whitley, Molecular simulations of hydration and swelling in clay minerals, Fluid Phase Equilibria 222 (2004) 189-194.

[12] D.R. Katti, S.R. Schmidt, P. Ghosh, K.S. Katti, Molecular modeling of the mechanical behavior and interactions in dry and slightly hydrated sodium montmorillonite interlayer, Canadian Geotechnical Journal 44(4) (2007) 425-435.

[13] S. SinhaRay, M. Biswas, Preparation and evaluation of composites from montmorillonite and some heterocyclic polymers: 3. A water dispersible nanocomposite from pyrrole-montmorillonite polymerization system, Materials Research Bulletin 34(8) (1999) 1187-1194.

[14] D. Sikdar, S.M. Pradhan, D.R. Katti, K.S. Katti, B. Mohanty, Altered phase model for polymer clay nanocomposites, Langmuir 24(10) (2008) 5599-5607.

[15] E.E. Alonso, J. Vaunat, A. Gens, Modelling the mechanical behaviour of expansive clays, Engineering Geology 54(1-2) (1999) 173-183.

[16] K.N. Alstadt, K.S. Katti, D.R. Katti, Nanoscale morphology of kerogen and in situ nanomechanical properties of green river oil shale, Journal of Nanomechanics and Micromechanics 6(1) (2015) 1-10.

[17] D.R. Katti, K.B. Thapa, K.S. Katti, Modeling molecular interactions of sodium montmorillonite clay with 3D kerogen models, Fuel 199 (2017) 641-652.

[18] Z.J. Wang, Fundamentals of seismic rock physics, Geophysics 66(2) (2001) 398-412.

[19] B.M. Das, K. Sobhan, Principles of geotechnical engineering, Cengage Learning2013.

[20] G.P. Zhang, Z.X. Wei, R.E. Ferrell, Elastic modulus and hardness of muscovite and rectorite determined by nanoindentation, Applied Clay Science 43(2) (2009) 271-281.

[21] S. Kadali, S. Sharma, D.N. Singh, Application of nanoindentation to establish influence of heat on soils, Engineering Geology 162 (2013) 14-21.

[22] G. Mallikarjunachari, T. Nallamilli, P. Ravindran, M.G. Basavaraj, Nanoindentation of clay colloidosomes, Colloids and Surfaces a-Physicochemical and Engineering Aspects 550 (2018) 167-175.

[23] N.P. Daphalapurkar, F. Wang, B. Fu, H. Lu, R. Komanduri, Determination of mechanical properties of sand grains by nanoindentation, Experimental Mechanics 51(5) (2011) 719-728.

[24] P. Ghosh, D.R. Katti, K.S. Katti, Mineral proximity influences mechanical response of proteins in biological mineral-protein hybrid systems, Biomacromolecules 8(3) (2007) 851-856.

[25] P. Ghosh, D.R. Katti, K.S. Katti, Mineral and protein-bound water and latching action control mechanical behavior at protein-mineral interfaces in biological nanocomposites, Journal of Nanomaterials (2008) 1-8.

[26] R. Bhowmik, K.S. Katti, D.R. Katti, Influence of mineral on the load deformation behavior of polymer in hydroxyapatite-polyacrylic acid nanocomposite biomaterials: A steered molecular dynamics study, Journal of Nanoscience and Nanotechnology 8(4) (2008) 2075-2084.

[27] B. Ajmera, B. Tiwari, J. Koirala, Z. Obaid, Compaction characteristics, unconfined compressive strengths, and coefficients of permeability of fine-grained soils mixed with crumb-rubber tire, Journal of Materials in Civil Engineering 29(9) (2017).

[28] A.J. Puppala, C. Musenda, Trb, Effects of fiber reinforcement on strength and volume change in expansive soils, Soils, Geology and Foundation (1736) (2000) 134-140.

[29] A.R. Estabragh, H. Rafatjo, A.A. Javadi, Treatment of an expansive soil by mechanical and chemical techniques, Geosynthetics International 21(3) (2014) 233-243.

[30] S.M. Hejazi, M. Sheikhzadeh, S.M. Abtahi, A. Zadhoush, A simple review of soil reinforcement by using natural and synthetic fibers, Construction and Building Materials 30 (2012) 100-116.

[31] Y. Yilmaz, Compaction and strength characteristics of fly ash and fiber amended clayey soil, Engineering Geology 188 (2015) 168-177.

[32] Y.X. Wang, P.P. Guo, W.X. Ren, B.X. Yuan, H.P. Yuan, Y.L. Zhao, S.B. Shan, P. Cao, Laboratory Investigation on strength characteristics of expansive soil treated with jute fiber reinforcement, International Journal of Geomechanics 17(11) (2017) 1-12.

[33] D.R. Katti, K.B. Thapa, K.S. Katti, The role of fluid polarity in the swelling of sodium-montmorillonite clay: A molecular dynamics and Fourier transform infrared spectroscopy study, Journal of Rock Mechanics and Geotechnical Engineering 10(6) (2018) 1133-1144.

[34] P.M. Amarasinghe, K.S. Katti, D.R. Katti, Insight into role of clay-fluid molecular interactions on permeability and consolidation behavior of Na-montmorillonite swelling clay, Journal of Geotechnical and Geoenvironmental Engineering 138(2) (2012) 138-146.

[35] T. Vanorio, M. Prasad, A. Nur, Elastic properties of dry clay mineral aggregates, suspensions and sandstones, Geophysical Journal International 155(1) (2003) 319-326.

[36] A. Sridharan, S.N. Rao, G.V. Rao, Shear strength characteristics of saturated montmorillonite and kaolinite clays, Soils and Foundations 11(3) (1971) 1-22.

[37] F.H. Chen, Foundations on expansive soils, Elsevier (2012).

[38] L.E. Bowles, Foundation analysis and design, McGraw-hill (1996).

[39] S. Hedan, F. Hubert, D. Pret, E. Ferrage, V. Valle, P. Cosenza, Measurement of the elastic properties of swelling clay minerals using the digital image correlation method on a single macroscopic crystal, Applied Clay Science 116 (2015) 248-256.

[40] D.R. Katti, L. Srinivasamurthy, K.S. Katti, Molecular modeling of initiation of interlayer swelling in Na-montmorillonite expansive clay, Canadian Geotechnical Journal 52(9) (2015) 1385-1395.

7. MODELING MOLECULAR INTERACTIONS OF SODIUM MONTMORILLONITE CLAY WITH 3D KEROGEN MODELS[5]

7.1. Introduction

Current Energy demands of the world continue to increase and thus increase the oil demand worldwide. Overreliance on conventional sources of energy can cause the instability of supply and demand in the future. The fluctuation of oil price over the years has also led researchers to seek to develop unconventional sources of energy. Thus, oil shale is an integral and alternative source of energy. The Green River Formation is situated in western United States in Colorado, Utah, and Wyoming and it has 70% of the total oil shale reserves in the world [1]. These regions have about 1.5 trillion barrels of oil with estimated recoverable oil of 800 billion barrels [2], which is three times greater than the reserves of oil in Saudi Arabia [3].

Oil shale is a fine-grained sedimentary rock that is formed by the deposition of clay size mineral particles and organic matter. The organic matter in oil shale consists of bitumen and kerogen. Kerogen is the most abundant form of combustible carbonaceous material on earth, which is a precursor of crude oil and insoluble in common organic solvents [4]. Kerogen contains hydrogen, oxygen, carbon, nitrogen, and sulphur. The classification of kerogen as Type I, Type II, and Type III depends on the hydrogen, carbon, and oxygen content [5]. Green River oil shale belongs to Type I kerogen because the hydrogen to carbon ratio is greater than 1.25 and oxygen to carbon ratio is less than 0.15 [6]. Green River oil shale contains 86.2% mineral matter

[5] This chapter describes the development of 3D kerogen, and the nonboned interactions of kerogen with NaMMT clay have been studied at the molecular level. Most of the contents of this chapter has been published in Dinesh R. Katti, Keshab B. Thapa, and Kalpana S. Katti, Modeling molecular interactions of sodium montmorillonite clay with 3D kerogen models, Fuel 199 (2017) 641–652. Keshab B. Thapa had primary responsibility for collecting samples in the field and for interviewing users of the test system. Keshab B. Thapa was the primary developer of the conclusions that are advanced here. Keshab B. Thapa also drafted and revised all versions of this chapter. Dinesh R. Katti and Kalpana S. Katti served as proofreader and checked the math in the statistical analysis conducted by Keshab B. Thapa.

and 13.80% organic matter by weight percentage [7]. The minerals primarily consist of dolomite, calcite, montmorillonite, feldspar, and quartz. Mineral content within kerogen plays a significant role during kerogen formation in oil shale, and clay minerals acts as a catalyst and restrained the organic matter [8, 9]. Oil shale yields a significant amount of oil through pyrolysis or retorting; heating of oil shale under varied temperature produces oil [10, 11]. The pyrolysis of oil shale using a wide range of acids produces a significant amount of oil because self-heating temperature assists to cleave the various hydrocarbon chains [1]. The pyrolysis by MD simulations showed the breakdown of C–C bonds, resulting in formation of small molecules of aliphatic hydrocarbons [12]. However, pyrolysis involves excessive energy to decompose kerogen and mineral matrix to shale oil and produces toxic compounds, and it is commercially uneconomical [13].

Molecular dynamics simulation is an excellent computational tool to understand the behavior of materials at a molecular level. In our previous work, extensive studies have been carried out to investigate the mechanical response of clay as well as interactions between clay and fluids by Fourier transform infrared (FTIR) spectroscopy and molecular dynamics simulations [14-20]. It has been observed that the configuration of fluid molecules in the clay layer during swelling is influenced by non-bonded interactions between them [18]. In the authors' prior work, molecular interaction of the composite system has been studied [21, 22]; the mechanics of organic structures is found to be influenced by the mineral proximity and non-bonded interaction between organics and minerals [23-25]. Furthermore, we studied these phenomena using molecular dynamics simulations in various bio-nanocomposites: seashell [23], bone [26], polymer clay nanocomposites [22], and polymeric hydroxyapatite nanocomposites [27].

Extensive photoacoustic FTIR experiments on insitu Green River oil shale have been performed in our previous work [3]. We have observed significant molecular interaction between kerogen and minerals in oil shale, primarily non-boned interaction. The nanomechanical behavior of oil shale has been studied and the modulus of kerogen is found to be in the range of 5-11 GPa [28, 29]. Kerogen is amorphous and finely dispersed on the minerals mineral with a size in the order of tens of nanometers [29]. Although the structure of kerogen is complex, kerogen moieties in Green River oil shale have been identified [30], and the interactions with minerals have been studied [31]. Montmorillonite, one of the minerals in Green River oil shale, is an expansive clay mineral in swelling clay used as landfill liners, asphalt modifier, drug delivery system, and polymer clay nanocomposites. In addition, the molecular dynamics and FTIR were carried out to investigate the molecular interaction between Na-montmorillonite and three kergoen moiestes: pyridine, heptylamine, and quinidine [32]. It was shown that the strong non-bonded interactions exist between them. The extraction and mechanism of these kerogen moieties from the silica surface have been studied by molecular dynamics simulation [33].

The functional group of kerogen exposed to mineral surface illustrates the binding of kerogen with mineral matrix because of non-bonded interactions [6]. Different methods have been applied to separate unaltered kerogen from mineral matrix in oil shales, but the efficient method of kerogen extraction from oil shale still remains complicated [34]. Thus, molecular modeling analysis of three-dimensional (3D) kerogen and mineral is promising aid to extract kerogen effectively. The representative two-dimensional (2D) kerogen structure of Green River oil shale has been developed by Siskin using mass spectroscopy and NMR analysis [35]. Based on Siskin's 2D structure, 3D Green River kerogen model is developed by ab initio and molecular mechanics computations [36]. Although the fundamental 3D kerogen structure was initially

obtained [37] using a computational tool, simulations have not been carried out on it. The molecular model of 3D of Green River kerogen is developed to mimic the real kerogen structure using 2D Siskin structure, and CHARMM compatible force field parameters in our study. Nevertheless, the non-bonded interactions energy between 3D kerogen and mineral have not been investigated by molecular dynamics simulations. These non-bonded interactions are essential to design the methodologies to extract the oil, efficiently, economically, and environmentally safe from oil shale. In this study, we present our results from molecular dynamics simulation on Green River type I kerogen and Na-montmorillonite clay mineral and insight into conformation and quantitative non-bonded interactions of kerogen in close proximity to the clay mineral at the molecular level.

7.2. Methodology

7.2.1. Model Construction

The Na-montmorillonite is a simplified model of clay sample SWy-2 and was acquired from the Clay Minerals Repository at The University of Missouri, Columbia, Missouri. The chemical formula of the unit cell is $NaSi_{16}(Al_6FeMg)O_{20}(OH)_4$. The coordinates of the unit cell were received from the model proposed by Skipper et al. [38], and the atomic charges were received from Tappen et al. [39]. The 4x2 model was initially constructed for studying the mechanical response of both dry and hydrated sodium montmorillonite clay [40]. The Na-montmorillonite clay layer has a tetrahedral-octahedral-tetrahedral (T-O-T) structure. An octahedral clay sheet is sandwiched between tetrahedral clay sheets. The dimensions of unit cell are 5.28Å x 9.14Å x 6.56Å. However, in our work, each clay model has 6x3 unit cells, and there are 6 unit cells in X-direction and 3 unit cells in Y-direction and overall initial dimensions of 31.68 Å x 27.44 Å x 24.16 Å as shown in Figure 7.1.

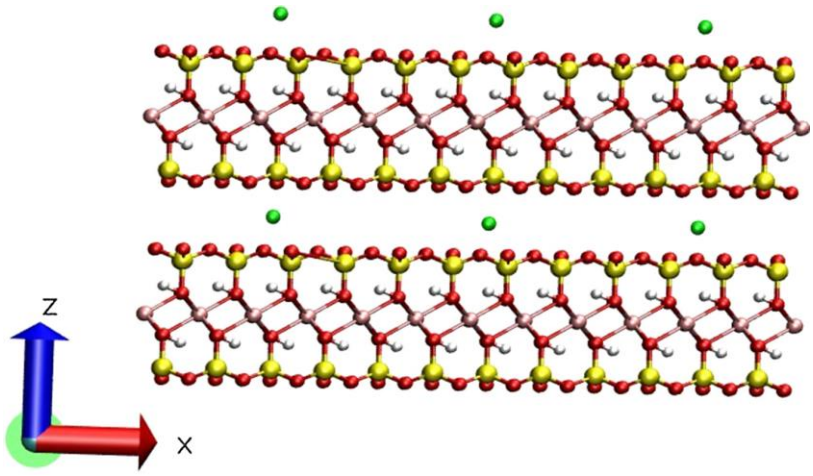

Figure 7.1. Molecular model of Dry Sodium (Na)-Montmorillonite.

The isomer substitution by metal atoms has taken place in the octahedral sheet, resulting in the negative charge on the individual clay sheets. During isomer substitution, nine Aluminum (Al^{+3}) cations are replaced by nine Iron (Fe^{+3}) cations and another nine Aluminum (Al^{+3}) cations by Magnesium (Mg^{+2}) cations. The negative charges of the clay sheets were balanced by adding nine sodium (Na^{+}) cations (naturally found inorganic species in the clays) in the interlayer. The detailed explanation of 6x3 model construction is described in our previous work [41].

The construction of a complete 3D kerogen model is initiated based on the Siskin's 2D kerogen structure. The chemical formula of Green River Type I kerogen is $C_{645}H_{1017}N_{19}O_{17}S_4$ [35]. In this work, the parameter and structure were acquired by dividing kerogen into seven fragments: fragment 1 ($C_{18}H_{38}$), fragment 2 ($C_{18}H_{30}$), fragment 3 ($C_{20}H_{42}$), fragment 4 ($C_{45}H_{60}O$), fragment 5 ($C_{75}H1_{17}N_4O_5$), fragment 6 ($C_{102}H_{167}NOS_2$), and fragment 7 ($C_{367}H_{547}N_{10}O_{10}S_2$). The construction of 3D structure was developed starting from fragment 1 to fragment 7 (Figure 7.2). Materials Studio 6.0 software is used to generate all models. The coordinate file of these models was acquired from Material Studio in protein data bank (pdb) format, and structure file was obtained from Visual Molecular Dynamics (VMD) 1.9.1 plugin in protein structure file (psf) format. These individual fragments were then merged into a single model using Visual

Molecular Dynamics (VMD) Merge Structures plugin. The CHARRM force field parameters for small organic molecules have been developed using CHARMM General Force Field (CGenFF) [42]. CHARMM compatible force field parameters were obtained for the structures using ParamChem – a web based integrated cyber environment developed by multi-disciplinary team collaborating between the members of the research groups from various University Institutions. CHARMM force field parameters were generated by analogy by CHARMM General Force Field (CGenFF) program. The complete fragment 7 (largest) structure was built by splitting the fragment 7 into five smaller parts because a limited number of atoms can be used to generate the force field parameters in a molecule using ParamChem.

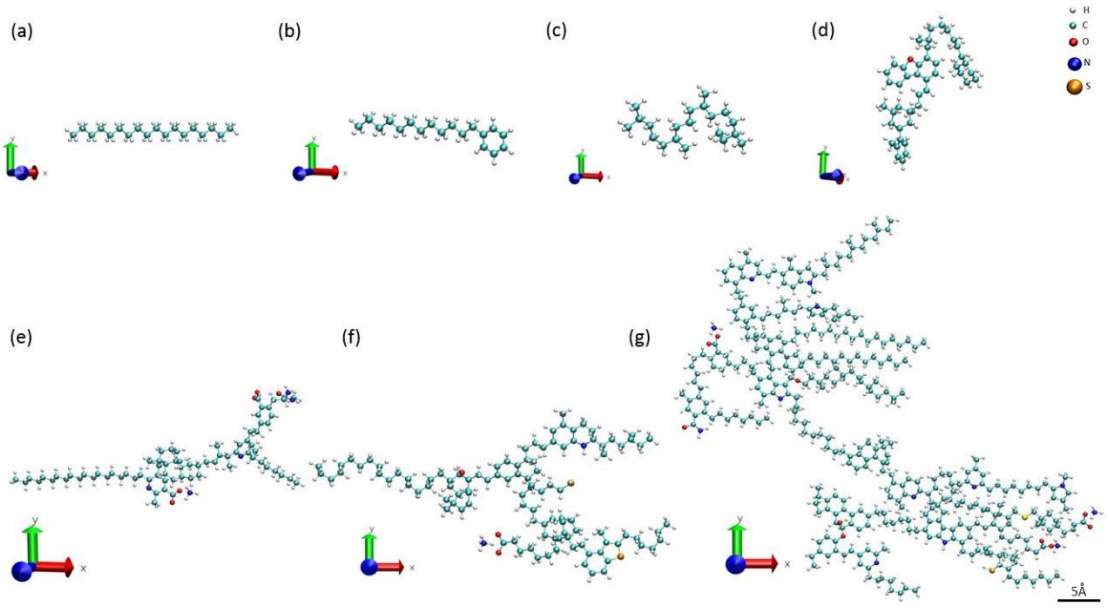

Figure 7.2. Molecular structure of kerogen based on Siskin's structure a) fragment 1, b) fragment 2, c) fragment 3, d) fragment 4, e) fragment 5, f) fragment 6, and g) fragment 7.

These fragments were then merged to construct a single 3D kerogen molecule as shown in Figure 7.3. In order to mimic real condition, the 12-unit 3D kerogen model was constructed by merging twelve single 3D kerogen molecules using VMD Merge Structures plugin. From our previous studies, extensive experimental results have shown that the dimension of kerogen is in

tens of nanometer (Alstadt et al., 2015). Therefore, overall dimensions of the 12-Unit 3D kerogen model are X=71.92 Å, Y=88.98 Å, and Z=63.89 Å which is also consistent with the experimental result (Figure 7.4).

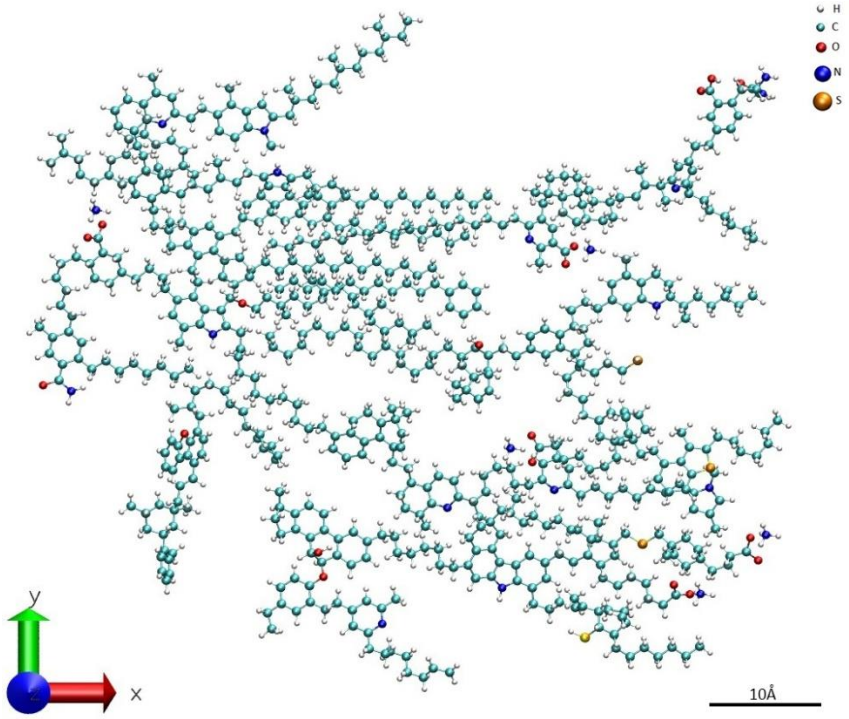

Figure 7.3. Molecular model of three-dimensional Green River Type I kerogen. The chemical formula is C645 H1017N19O17S4. Color coding: C (cyan), H (white), N (blue), O (red), and S (orange).

With the 12-unit 3D kerogen as a verified molecular model, the next step in the modeling work involved subjecting the molecular model to the insitu stresses experienced during the geologic formation of the kerogen to create an insitu kerogen molecular model. The kerogen model was brought in close proximity of one of the major minerals, Na-montmorillonite clay, identified in the Green River oil shale. Therefore, 12-unit 3D kerogen model was inserted between two 6x3 unit Na-montmorillonite clay models using VMD Merge Structures plugin, resulting in representative kerogen-mineral model. Overall dimensions were found to be X=71.92 Å, Y=88.98 Å, and Z=105.89 Å (Figure 7.5).

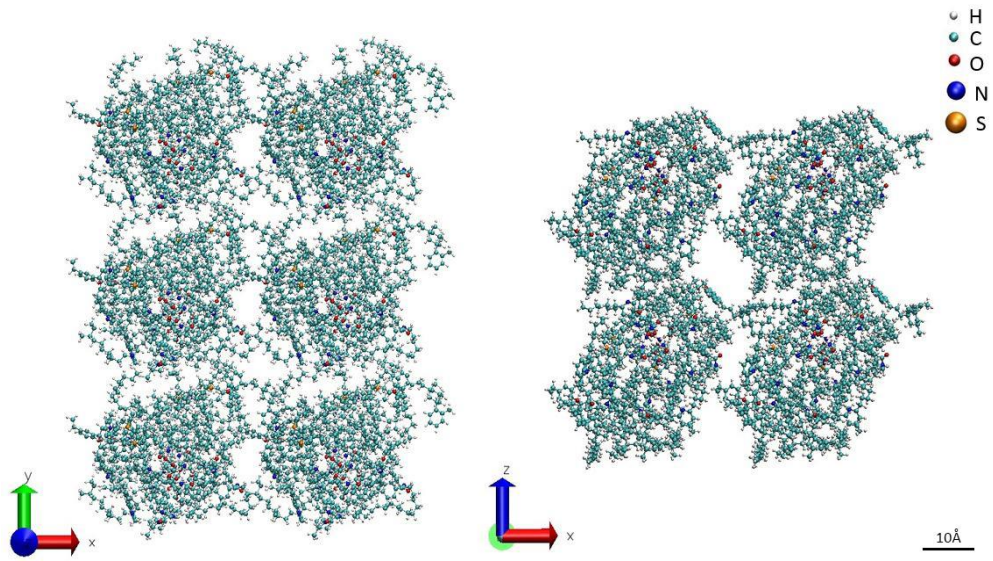

Figure 7.4. 12-unit three-dimensional kerogen model.

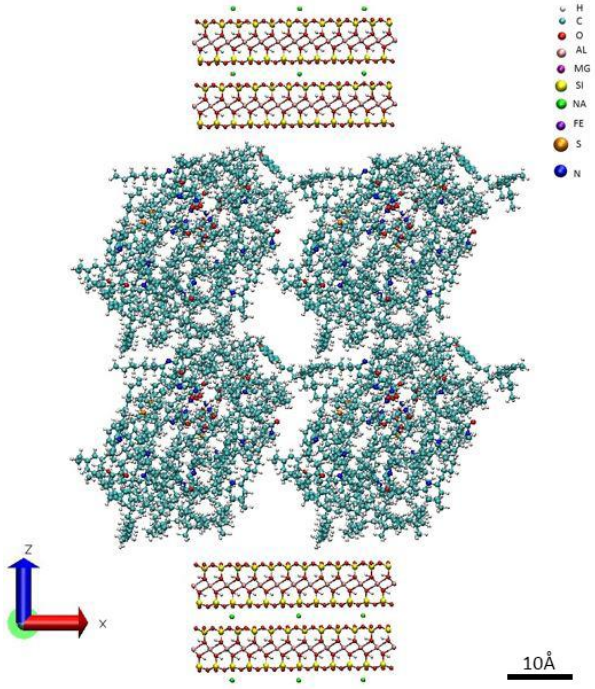

Figure 7.5. Initial 12-unit three-dimensional kerogen and 6x3 unit Na-montmorillonite clay model showing kerogen within clay mineral matrix.

7.2.2. Simulation Details

Molecular dynamics was used for the molecular modeling of 12-unit 3D kerogen model and Na-montmorillonite clay. In molecular dynamics (MD), NAMD 2.9 developed by

Theoretical and Computational Biophysics Group, Beckman Institute, the University of Illinois at Urbana-Champaign, was used. After the construction of a single unit of 3D kerogen molecule model was completed, the next task was to make the molecular cluster of kerogen molecules to mimic real conditions. For this purpose, twelve single 3Dkerogen molecules were combined. The 12-unit 3D model was minimized and run through annealing cycles to assure that the confirmation of molecule was the true confirmation and free from artifacts during molecule building process. In minimization, the temperature was 0 K, and pressure was 0 atmosphere. After minimization, an annealing process was carried out, which involved optimization of the large and complex system [43].

Temperature decreases slowly in annealing process and molecules get sufficient time to redistribute their position [44]. In the first step, the simulations were run at normal room temperature and atmospheric pressure (NTP), resulting in isothermal-isobaric conditions. The temperature was increased from O K to 300 K in three steps with an increment of 100 K. The pressure was increased from O atmosphere to 1 atmosphere (1.013 bars), keeping the constant temperature at 300 K. However, the pressure was raised in four steps with 0.25 bar in each step. The second step of the simulation was to increase the temperature of the 12-unit 3D kerogen model from 300 K to 500 K with increment of 100 K. In the final step, the model was cooled from 500 K to 300 K at same steps as in increment. Final simulation was done for 2,000,000 steps with the time step of 0.5 fs, simulation period of 5 ns. The energy vs time for a typical simulation is shown in Figure 7.6, which validates equilibration of the system. All simulations were run using Thunder Cluster with 2 nodes and 20 processors at the Center for Computationally Assisted Science and Technology (CCAST) at North Dakota State University, Fargo, North Dakota.

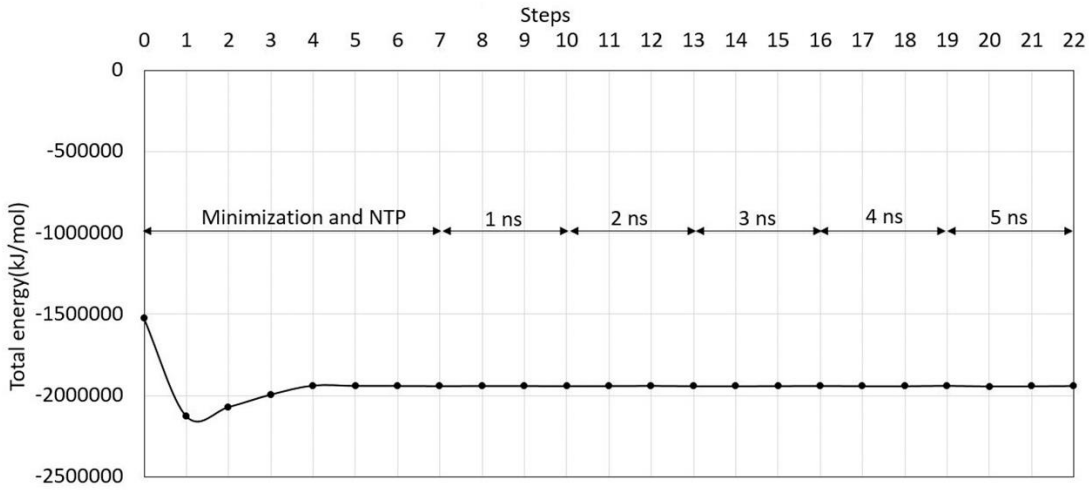

Figure 7.6. Plot of total energy versus time from minimization to 5 ns. Plot shows the equilibration of 12-unit kerogen and Na-montmorillonite clay model in MD simulation.

The representative model of 6x3 Unit Na-montmorillonite was acquired by comparing d-spacing simulation result of the clay sheet with X-Ray diffraction (XRD) result. The simulation was run for 800,000 steps with the time step of 0.5 fs, which is equivalent to 400 ps. The periodic boundary conditions were applied to models to imitate the infinite number of clay sheets separated by interlayer. The clay sheets are constrained in X and Y direction but allowed to move in Z direction. On the other hand, 12-unit 3D kerogen model is allowed to move in all directions. The 12-unit 3D kerogen and Na-montmorillonite model was also run for 400 ps at NTP. Additionally, the model was run for 5 ns in 15 steps after NTP to ensure the simulation was stable for longer duration.

7.3. Results and Discussions

For the representative model of Na-montmorillonite, the d-spacing was measured by computing the vertical distance between the corresponding surface oxygen atoms of the clay sheets molecular model of the Na-montmorillonite after MD simulation is shown in Figure 7.7. The experimentally obtained d-spacing of dry Na-montmorillonite was 9.85 Å [15], and our molecular dynamics simulation resulted in d-spacing value of 10.72 Å. These data agree with the

modeling system for our studies. Although this clay model has a small size, periodic boundary condition was used to replicate the infinite clay sheets parallel to each other.

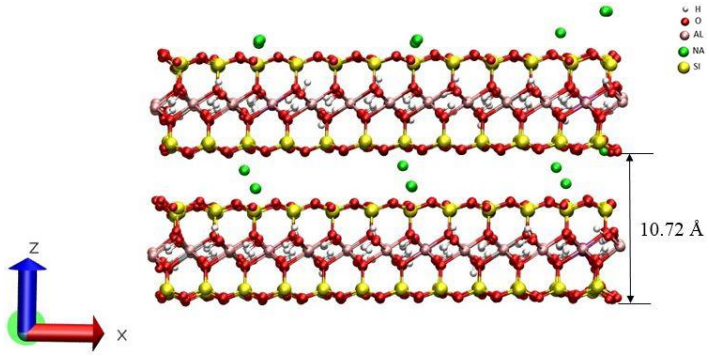

Figure 7.7. Structure of representative model of Na-montmorillonite at 300 K temperature and 1 atmospheric pressure (d-spacing = 10.72 Å).

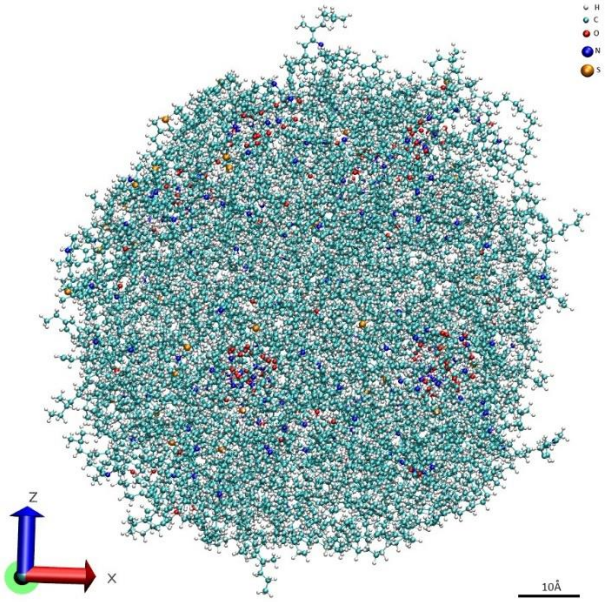

Figure 7.8. 12-unit three dimensional molecular model of kerogen after equilibrium.

Figure 7.8 shows the equilibrated 12-unit 3D kerogen model after annealing process for time period of 1 ns. The atomic pair distribution functions (PDFs) analysis was conducted on the 12-unit 3D kerogen to validate the kerogen modeling system. A PDF plot was developed, as seen in Figure 7.9, using VMD-Radial Pair Distribution Function plugin, and results were compared with the radial distributions from NMR experiment and a computational model from literature

(Orendt et al., 2013) on kerogen from the Green River oil shale. The atom−atom correlations agree with Orendt et al. [36] based on typical carbon bond lengths, C–H (1.15 Å) and C–C (1.55 Å), angles, C–C–H (2.15 Å) and C–C–C (2.55 Å), and dihedrals, C–C–C–C (3.85 Å). The distributions are also consistent with results from NMR data presented by the same authors. These results suggest that the newly constructed 12-unit 3D kerogen model is a viable, representative kerogen model for incorporation into kerogen-mineral interaction studies.

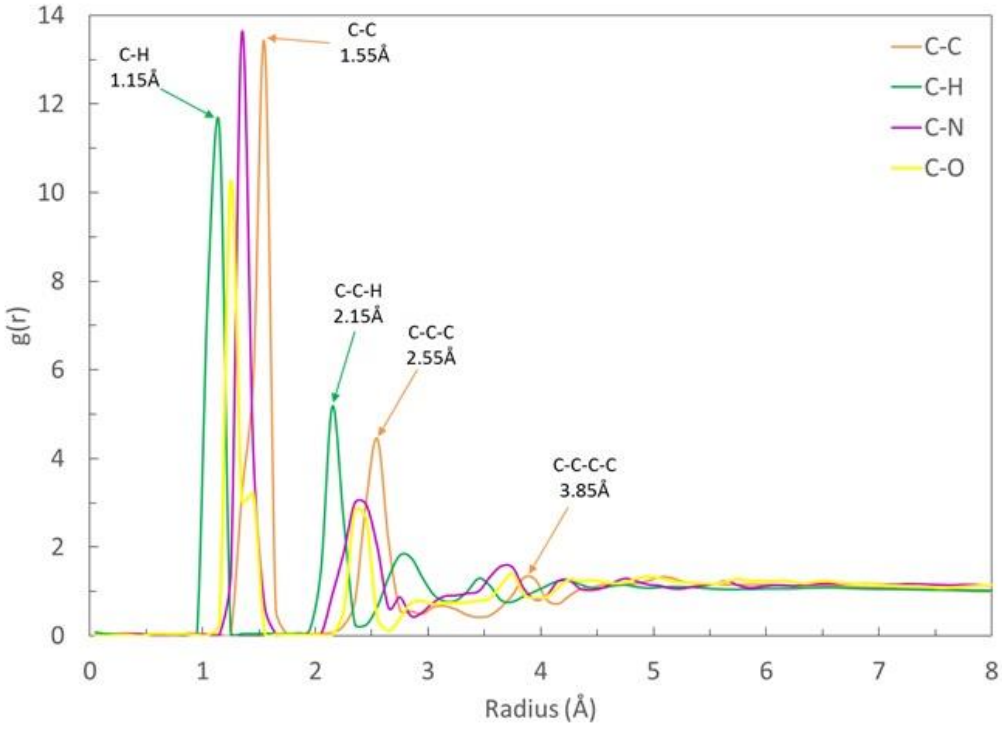

Figure 7.9. A Pairwise Distribution Function (PDF) plot of 12-unit kerogen model at time period of 1 ns.

A snapshot of the 12-unit 3D kerogen and 6x3 unit clay model after the simulation duration of 5 ns is shown in Figure 7.10. The overall dimension of the model is x = 65.42 Å, y = 86.62 Å, and z = 99.70 Å, which is still on the order of tens of nanometer size and smaller than the initial dimension of the model. The conformation of kerogen was observed to be changed in the presence of clay mineral. The kerogen pulled the clay sheet by 11 Å in z-direction which

supports the strong attractive non-bonded interaction between them. The snapshots of kerogen fragment 1 through fragment 7 with clay sheets after the MD simulations are shown in Figure 7.11 and 7.12. The total non-bonded interaction between clay and the individual seven fragments of 12-unit kerogen was computed. Due to isomeric substitution, negative charges were developed in the clay sheets, and the hydrogen atoms of the kerogen that were present in all the fragments were attracted by the clay sheet. The nonbonded interaction becomes weak when the distance between the kerogen and clay sheets exceeds 12 Å, the region within this distance is considered in proximity to clay sheet in this study. Overall the resulting interactions were strong because a large number of atoms have been included in the interaction.

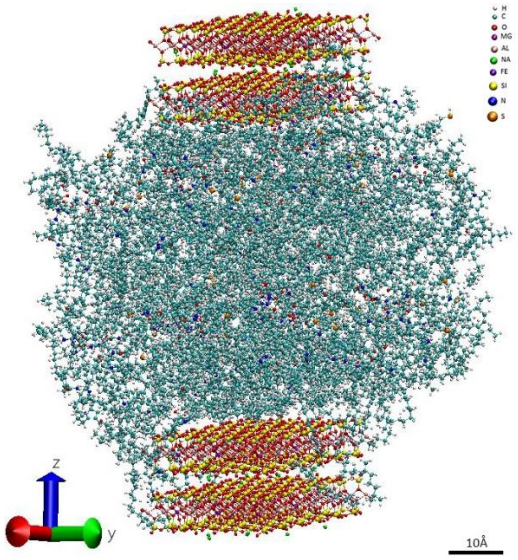

Figure 7.10. Kerogen-clay model after the simulation up to 5 ns.

The conformation of kerogen fragments in clay mineral provides insight about the trapped kerogen within the mineral matrix. In this work, the orientation of individual fragments at the molecular level was studied. There were 12 of each of the seven fragments in the 12-unit 3D kerogen model. However, only certain numbers of each fragment, as seen in Figure 7.11(a-f) and Figure 7.12, were in proximity to clay sheets: fragment 1 had two, fragment 2 had five,

fragment 3 had three, fragment 4 had three, fragment 5 had three, fragment 6 had three, and fragment 7 had four. In the case of fragment 1, which mainly consists of aliphatic hydrocarbons, one of the fragment units was aligned parallel and perpendicular to the clay surface in the XY-plane as shown in Figure 7.11(a). The aromatic hydrocarbons of fragment 2, on the other hand, were more influenced and attracted to the clay sheet than its aliphatic hydrocarbons, as seen in Figure 7.11(b). It was evident that the aliphatic hydrocarbons of fragment 3 and aromatic hydrocarbons of fragment 4 were flat and parallel to the surface of the clay sheet as shown in Figure 7.11(c) and Figure 7.11(d) respectively. Figure 7.11(e and f) shows the aliphatic and aromatic hydrocarbons of the fragments 5 and 6 were shifted toward the clay sheet. Most of the aromatic hydrocarbons were perpendicular, and aliphatic hydrocarbons were parallel to the clay surface in fragment 5. In contrast, the aromatic hydrocarbons of fragment 6 were perpendicular to the clay surface. Fragment 7 was the largest fragment, and it contains a higher number of atoms than other fragments. It was found that the aliphatic hydrocarbons, aromatic hydrocarbons, and aromatic nitrogen were oriented toward clay surface as shown in Figure 7.12. Aliphatic hydrocarbons were flat and randomly oriented, but aromatic hydrocarbons were normal to the clay surface. Aromatic nitrogens were flat, parallel, and inclined to the clay surface. This study shows that the edges of the functional groups of these fragments were pointed towards the clay sheet because the oxygen atoms lying on the surface of clay sheets possess high negative charge.

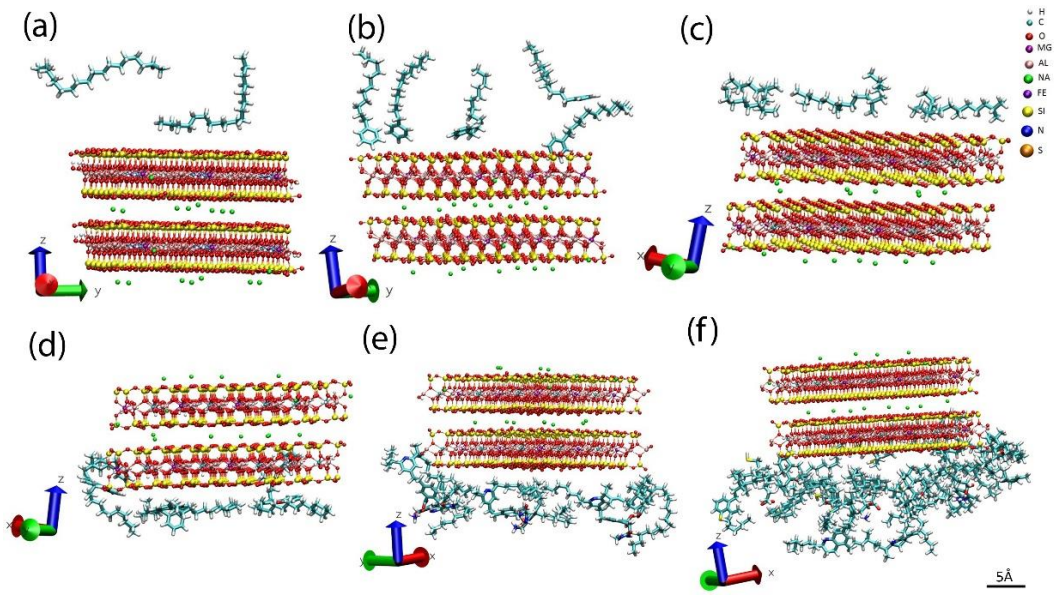

Figure 7.11. Snapshot showing the conformation of different fragments of kerogen in close proximity to clay models a) fragment 1, b) fragment 2, c) fragment 3, d) fragment 4, e) fragment 5, and f) fragment 6. Only certain numbers of individual fragment are close to clay surface represented by Licorice form.

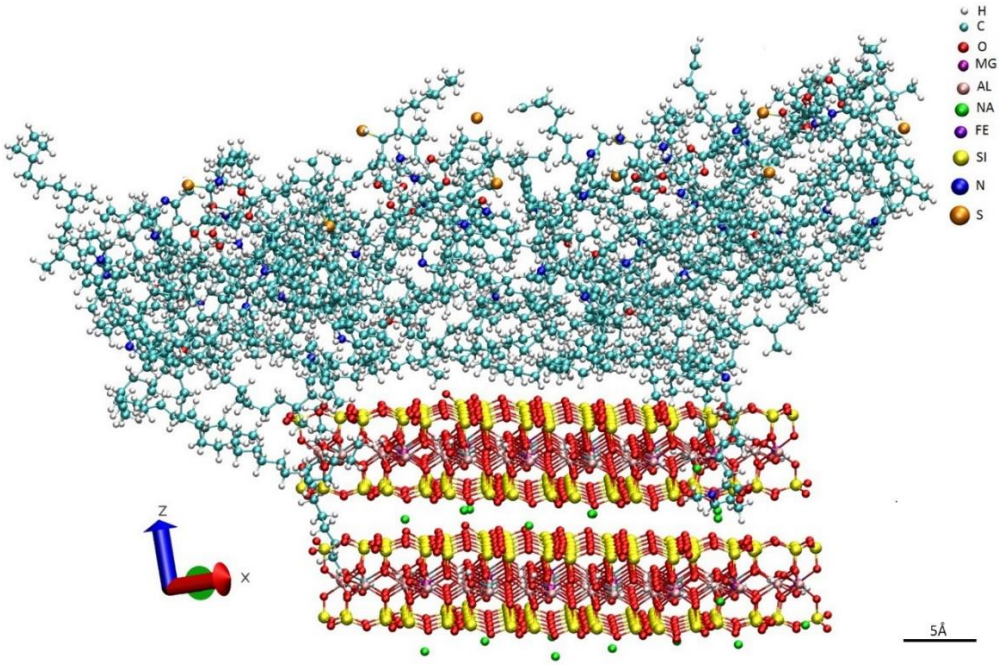

Figure 7.12. The conformation of kerogen fragment 7 in close proximity to clay surface.

Kerogen-mineral interaction was studied in our previous work by photoacoustic FTIR on the Green River Oil shale [3]. The result showed that the kerogen-clay interaction is mainly non-

bonded in nature. Thus, in this work, the non-bonded energies between kerogen and clay and between kerogen fragments have been computed. The non-bonded energy is the summation of electrostatic energy and van der Waals (VDW) energy. The attractive and repulsive energies between the two constituents of the modeling system are represented by the negative and positive energies respectively. Figure 7.13 shows the interaction energy between 12-unti kerogen and clay, which is a strong attractive non-bonded. These results are consistent with our previous studies on the Green River oil shale [3]. The VDW energy between kerogen and clay sheets was very high, and it was 290% higher than electrostatic energy. However, the interaction energy between kerogen and sodium was small compared to kerogen-clay interaction. The nonbonded interactions between sodium (Na) and clay sheets before and after the introduction of kerogen is shown in Figure 7.14.

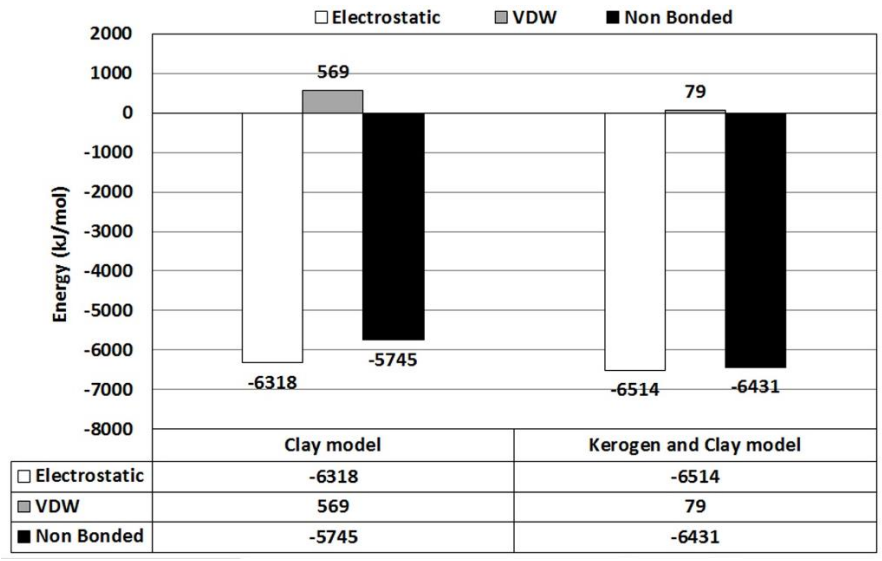

	Clay model	Kerogen and Clay model
Electrostatic	-6318	-6514
VDW	569	79
Non Bonded	-5745	-6431

Figure 7.13. Overall interaction energy of 12-unit 3D kerogen with clay.

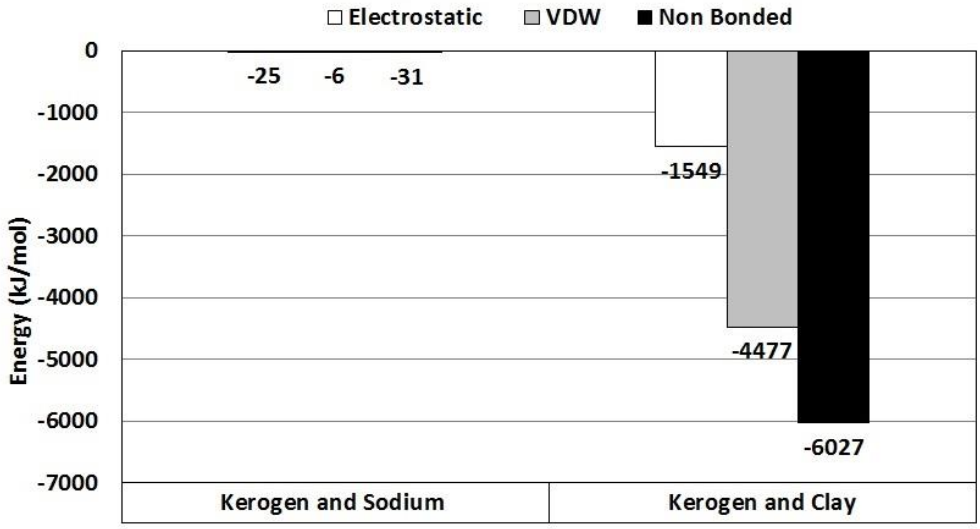

Figure 7.14. The interaction energy between sodium (Na) cations and clay sheets before and after the introduction of kerogen.

The computation of energies was carried out by considering kerogen fragments in proximity to clay surface only. Figure 7.15 shows that fragments 4 through 7 have higher non-bonded interactions with clay than other fragments, and these attractive interactions were predominated by VDW energy. VDW energy was found to be almost the same for fragments 1 and 2, resulting in same total non-bonded energy. However, VDW energy between fragment 3 and clay sheet was 250% greater than fragments 1 and 2 and clay. Similarly, VDW energy of fragment 4 and clay was more than 200% greater than fragment 3 and clay. The total non-bonded energy of fragment 4 with clay was slightly greater than fragment 5 with clay whereas the corresponding electrostatic interaction energy was similar. The non-bonded energy between fragment 7 and clay was observed to be more than 250% greater than that between fragment 6 and clay. Although the VDW energy was 300% greater, in this case, electrostatic energy remained the same. Thus, our molecular dynamics studies show a significant non-bonded interaction between kerogen fragments and clay. Among the seven fragments, fragment 7

exhibited the highest non-bonded interaction with clay. These results also suggest that the VDW interactions play a significant role in kerogen-mineral interfaces.

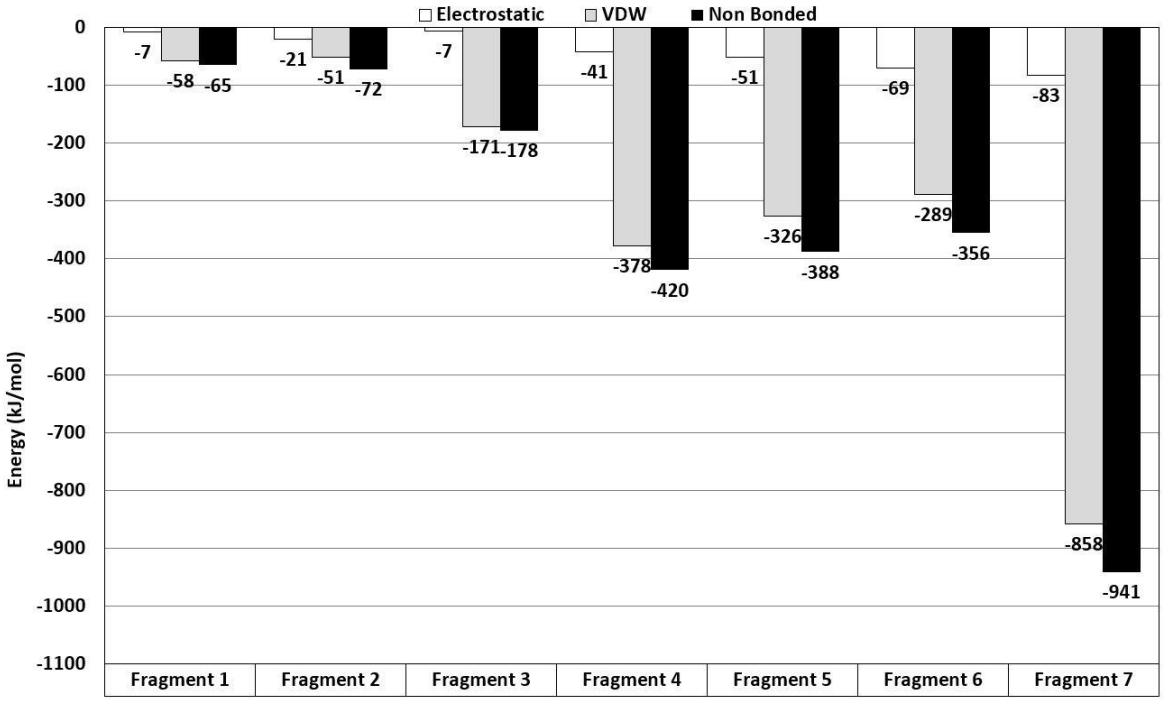

Figure 7.15. Interaction energy of clay with seven fragments of kerogen, fragment 1, fragment 2, fragment 3, fragment 4, fragment 5, fragment 6, and fragment 7, in close proximity to clay surface.

At the same time when kerogen interacted with clay, strong molecular interactions between kerogen fragments were observed. Figure 7.16 shows the variation of interaction energy between kerogen fragments, fragments 4 through fragment 7. These interactions were attractive in nature and increased with increasing fragments from 4 to 7. The interactions within kerogen fragments arose due to both VDW and electrostatic interactions. All the interactions were primarily attractive in nature. Although the total nonbonded interaction between fragments 4 and 5 and fragments 4 and 7 was approximately the same, interaction energy between fragments 4 and 6 was slightly greater than fragments 4 and 7.

On the other hand, the total non-bonded interaction between fragments 5 and 6 was about 350% higher than fragments 4 and 7. These interactions were VDW in nature. The non-bonded interaction between fragments 5 and 7 was more than 150% greater than fragments 5 and 6. Figure 7.16 also shows a plot of total non-bonded interaction between fragments 5 and 7 indicating that it was more than 250% higher than between fragments 6 and 7. These interactions were observed to be attractive and electrostatic in nature, and the magnitude of these interactions was also much higher than individual kerogen fragments and clay interactions. Thus, attractive interactions between kerogen fragments hold the kerogen structure together.

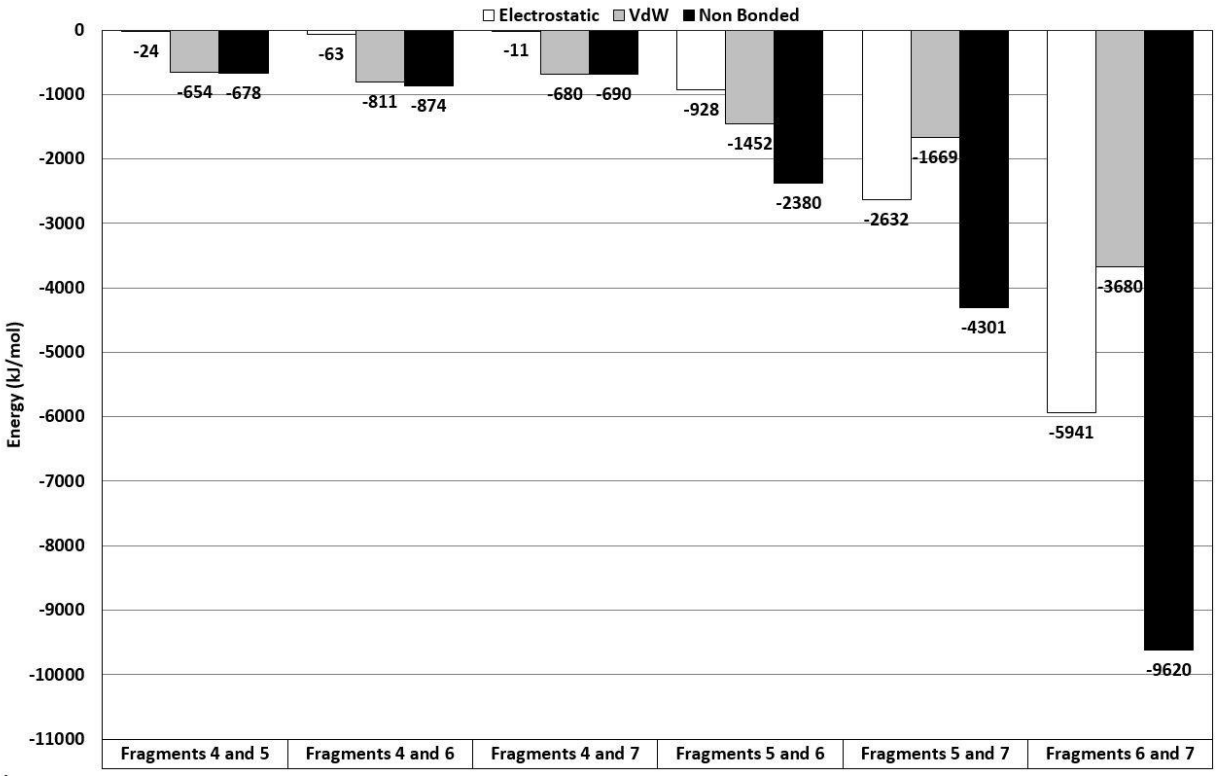

Figure 7.16. Attractive interactions between kerogen fragments: fragments 4 and 5, fragments 4 and 6, fragments 4 and 7, fragments 5 and 6, fragments 5 and 7, and fragments 6 and 7.

7.4. Conclusions

- In this work, the non-bonded interactions between the complete 3D kerogen structure and clay were studied using molecular dynamics simulation. The construction of the

molecular model of 12-unit 3D kerogen was based on Siskin's 2-dimensional structure divided among seven fragments. Fragments 1, 2 and 3 consisted of aliphatic hydrocarbons (carbon-carbon single bond). In addition, fragment 3 consisted of aromatic hydrocarbon (one benzene ring) which was connected with aliphatic hydrocarbons. Fragment 4 consisted of aromatic and olefinic hydrocarbons and one Oxygen atom with high negative charge. Similarly, fragments 5, 6, and 7 comprised of aliphatic, olefinic, and aromatic hydrocarbons, aliphatic nitrogen, ammonical nitrogen, oxygen atoms, and these fragments were larger than other fragments. Additionally, fragments 6 and 7 had sulphur atoms. Oxygen and nitrogen atoms present in these fragments exhibited high negative charge, resulting in high non-bonded interaction energy.

- The representative 3D kerogen model was verified by developing PDFs on the 12-unit 3D kerogen model. On the other hand, the validation of clay model was accomplished by comparing d-spacing of the clay structure from molecular dynamics simulations with the experimental result from XRD. Thus, merging these two models, the complex and robust kerogen-clay model was developed in our study.
- Our simulation results reveal that attractive non-bonded interactions between kerogen and clay were responsible for holding them together. The identification of the seven kerogen fragments and their orientations was studied in proximity to the clay surface. While the aliphatic hydrocarbons of fragment 1 and aromatic hydrocarbons of fragment 2 were attracted toward clay surface, fragments 3 and 4 were observed to be flat and parallel to the clay surface. The aromatic hydrocarbons of fragments 5 and 6 were normal to the clay surface. The aliphatic and aromatic hydrocarbons as well as the aromatic nitrogen atoms were observed to be shifted toward the clay surface, with flat orientations. Furthermore,

the non-bonded energy between each of kerogen fragments and clay was computed. The computations indicate that the clay exhibits strong non-bonded interactions with kerogen fragments 4 through 7. These non-bonded interactions were observed to be comparatively higher than interactions between clay and fragments 1 through 3. Fragment 7 exhibited higher non-bonded interactions with clay than other fragments. These attractive interactions were found to be predominated by VDW energy. Similarly, the nonbonded interactions within kerogen fragments 4 through 7 have been studied. Fragments 5 and 6, fragments 5 and 7, and fragments 6 and 7 have strong attractive non-bonded interactions that were predominantly electrostatic in nature.

- These non-bonded interactions between specific kerogen fragments and between clay and kerogen fragments play an important role in understanding the existence and mechanisms of the kerogen-clay interlocking in the oil shale at the molecular level. The extent of the energy differences and also locations of the preferential and higher interactions is important for evaluation of kerogen extraction in future studies. This work provides insight for future research to develop new methods of extraction of the kerogen economically, efficiently, and environmental friendly from the oil shale.

7.5. Acknowledgements

The authors wish to acknowledge the support of Department of Energy National Nuclear Security Administration under grant # DE-FG52-08NA28921. We would also acknowledge Computationally Assisted Science and Technology (CCAST) for providing computational resources at North Dakota State University. We also acknowledge support from Mountain Plains Consortium (MPC) Grant #: DTRT13-G-UTC38.

7.6. References

[1] H. Guo, J. Lin, Y. Yang, Y. Liu, Effect of minerals on the self-heating retorting of oil shale: Self-heating effect and shale-oil production, Fuel 118 (2014) 186-193.

[2] E. Fletcher, Development of America's strategic unconventional fuels resources, by Task Force on Strategic Unconventional Fuels, Resource Specific (2007).

[3] K.N. Alstadt, D.R. Katti, K.S. Katti, An in situ FTIR step-scan photoacoustic investigation of kerogen and minerals in oil shale, Spectrochimica Acta Part a-Molecular and Biomolecular Spectroscopy 89 (2012) 105-113.

[4] F.P. Miknis, Solid-state 13C NMR in oil shale research: an introduction with selected applications, composition, geochemistry and conversion of oil shales, Springer (1995).

[5] M. Razvigorova, T. Budinova, B. Tsyntsarski, B. Petrova, E. Ekinci, H. Atakul, The composition of acids in bitumen and in products from saponification of kerogen: Investigation of their role as connecting kerogen and mineral matrix, International Journal of Coal Geology 76(3) (2008) 243-249.

[6] G. Brons, M. Siskin, R.I. Botto, N. Guven, Quantitative mineral distribution in green river and rundle oil shales, Energy & Fuels 3(1) (1989) 85-88.

[7] T.F. Yen, G.V. Chilingarian, Oil shale, (1976).

[8] W.D. Johns, Clay mineral catalysis and petroleum generation, Annual Review of Earth and Planetary Sciences 7 (1979) 183-198.

[9] L.M. Wu, C.H. Zhou, J. Keeling, D.S. Tong, W.H. Yu, Towards an understanding of the role of clay minerals in crude oil formation, migration and accumulation, Earth-Science Reviews 115(4) (2012) 373-386.

[10] P. Tiwari, M. Deo, C.L. Lin, J.D. Miller, Characterization of oil shale pore structure before and after pyrolysis by using X-ray micro ct, Fuel 107 (2013) 547-554.

[11] J.G. Na, C.H. Im, S.H. Chung, K.B. Lee, Effect of oil shale retorting temperature on shale oil yield and properties, Fuel 95(1) (2012) 131-135.

[12] X. Liu, J.-H. Zhan, D. Lai, X. Liu, Z. Zhang, G. Xu, Initial pyrolysis mechanism of oil shale kerogen with reactive molecular dynamics simulation, Energy & Fuels 29(5) (2015) 2987-2997.

[13] J.H. Bauman, M. Deo, Simulation of a conceptualized combined pyrolysis, in situ combustion, and CO_2 storage strategy for fuel production from green river oil shale, Energy & Fuels 26(3) (2012) 1731-1739.

[14] D.R. Katti, S.R. Schmidt, P. Ghosh, K.S. Katti, Modeling the response of pyrophyllite interlayer to applied stress using steered molecular dynamics, Clays and Clay Minerals 53(2) (2005) 171-178.

[14] D.R. Katti, S.R. Schmidt, P. Ghosh, K.S. Katti, Modeling the response of pyrophyllite interlayer to applied stress using steered molecular dynamics, Clays and Clay Minerals 53(2) (2005) 171-178.

[15] P.M. Amarasinghe, K.S. Katti, D.R. Katti, Nature of organic fluid-montmorillonite interactions: An FTIR spectroscopic study, Journal of Colloid and Interface Science 337(1) (2009) 97-105.

[16] P.M. Amarasinghe, K.S. Katti, D.R. Katti, Insight into role of clay-fluid molecular interactions on permeability and consolidation behavior of na-montmorillonite swelling clay, Journal of Geotechnical and Geoenvironmental Engineering 138(2) (2012) 138-146.

[17] D.R. Katti, Z.R. Patwary, K.S. Katti, Modelling clay-fluid interactions in montmorillonite clays, Environmental Geotechnics 4(5) (2016) 322-338.

[18] S.M. Pradhan, K.S. Katti, D.R. Katti, Evolution of molecular interactions in the interlayer of na-montmorillonite swelling clay with increasing hydration, International Journal of Geomechanics 15(5) (2015) 1-9.

[19] D.R. Katti, L. Srinivasamurthy, K.S. Katti, Molecular modeling of initiation of interlayer swelling in Na-montmorillonite expansive clay, Canadian Geotechnical Journal 52(9) (2015) 1385-1395.

[20] D.R. Katti, K.B. Thapa, K.S. Katti, The role of fluid polarity in the swelling of sodium-montmorillonite clay: A molecular dynamics and Fourier transform infrared spectroscopy study, Journal of Rock Mechanics and Geotechnical Engineering 10(6) (2018) 1133-1144.

[21] S.M. Pradhan, D.R. Katti, K.S. Katti, Steered molecular dynamics study of mechanical response of full length and short collagen molecules, Journal of Nanomechanics and Micromechanics 1(3) (2011) 104-110.

[22] D. Sikdar, S.M. Pradhan, D.R. Katti, K.S. Katti, B. Mohanty, Altered phase model for polymer clay nanocomposites, Langmuir 24(10) (2008) 5599-5607.

[23] P. Ghosh, D.R. Katti, K.S. Katti, Mineral proximity influences mechanical response of proteins in biological mineral-protein hybrid systems, Biomacromolecules 8(3) (2007) 851-856.

[24] P. Ghosh, D.R. Katti, K.S. Katti, Mineral and protein-bound water and latching action control mechanical behavior at protein-mineral interfaces in biological nanocomposites, Journal of Nanomaterials (2008) 1-8.

[25] D.R. Katti, S.M. Pradhan, K.S. Katti, Directional dependence of hydroxyapatite-collagen interactions on mechanics of collagen, Journal of Biomechanics 43(9) (2010) 1723-1730.

[26] S.M. Pradhan, K.S. Katti, D.R. Katti, Multiscale Model of Collagen Fibril in Bone: Elastic Response, Journal of Engineering Mechanics 140(3) (2014) 454-461.

[27] A. Sharma, S. Payne, K.S. Katti, D.R. Katti, Evaluating Molecular Interactions in Polycaprolactone-Biomineralized Hydroxyapatite Nanocomposites using Steered Molecular Dynamics, Jom 67(4) (2015) 733-743.

[28] R. Ahmadov, T. Vanorio, G. Mavko, Confocal laser scanning and atomic-force microscopy in estimation of elastic properties of the organic-rich Bazhenov Formation, The Leading Edge 28(1) (2009) 18-23.

[29] K.N. Alstadt, K.S. Katti, D.R. Katti, Nanoscale morphology of kerogen and in situ nanomechanical properties of green river oil shale, Journal of Nanomechanics and Micromechanics 6(1) (2015) 1-10.

[30] S. R. Kelemen, M. Afeworki, M. L. Gorbaty, M. Sansone, P. J. Kwiatek, C. C. Walters, H. Freund, M. Siskin, A. E. Bence, D. J. Curry, M. Solum, R. J. Pugmire, M. Vandenbroucke, M. Leblond, F. Behar, Direct characterization of kerogen by X-ray and solid-state 13C nuclear magnetic resonance methods, Energy & Fuels 21(3) (2007) 1548-1561).

[31] M. Siskin, G. Brons, J.F. Payack, Disruption of kerogen-mineral interactions in oil shales, Energy & Fuels 1(3) (1987) 248-252.

[32] D.R. Katti, H.B. Upadhyay, K.S. Katti, Molecular interactions of kerogen moieties with Na-montmorillonite: An experimental and modeling study, Fuel 130 (2014) 34-45.

[33] Wu, Q. Xue, X. Li, Y. Tao, Y. Jin, C. Ling, S. Lu, Extraction of kerogen from oil shale with supercritical carbon dioxide: Molecular dynamics simulations, The Journal of Supercritical Fluids, 107 (2015) 499-506.

[34] R.A. Ibrahimov, K.K. Bissada, Comparative analysis and geological significance of kerogen isolated using open-system (palynological) versus chemically and volumetrically conservative closed-system methods, Organic Geochemistry 41(8) (2010) 800-811.

[35] M. Siskin, C.G. Scouten, K.D. Rose, T. Aczel, S.G. Colgrove, R.E. Pabst Jr, Detailed structural characterization of the organic material in rundle ramsay crossing and green river oil shales, composition, geochemistry and conversion of oil shales, Springer (1995).

[36] A.M. Orendt, I.S.O. Pimienta, S.R. Badu, M.S. Solum, R.J. Pugmire, J.C. Facelli, D.R. Locke, K.W. Chapman, P.J. Chupas, R.E. Winans, Three-dimensional structure of the siskin green river oil shale kerogen model: A comparison between calculated and observed properties, Energy & Fuels 27(2) (2013) 702-710.

[37] J.L. Faulon, M. Vandenbroucke, J.M. Drappier, F. Behar, M. Romero, 3D chemical model for geological macromolecules, Organic Geochemistry 16(4-6) (1990) 981-993.

[38] N.T. Skipper, G. Sposito, F.R.C. Chang, monte-carlo simulation of interlayer molecular-structure in swelling clay-minerals. 2. Monolayer hydrates, Clays and Clay Minerals 43(3) (1995) 294-303.

[39] B.J. Teppen, K. Rasmussen, P.M. Bertsch, D.M. Miller, L. Schafer, Molecular dynamics modeling of clay minerals. 1. Gibbsite, kaolinite, pyrophyllite, and beidellite, Journal of Physical Chemistry B 101(9) (1997) 1579-1587.

[40] S.R. Schmidt, D.R. Katti, P. Ghosh, K.S. Katti, Evolution of mechanical response of sodium montmorillonite interlayer with increasing hydration by molecular dynamics, Langmuir 21(17) (2005) 8069-8076.

[41] D. Sikdar, D.R. Katti, K.S. Katti, A molecular model for epsilon-caprolactam-based intercalated polymer clay nanocomposite: Integrating modeling and experiments, Langmuir 22(18) (2006) 7738-7747.

[42] K. Vanommeslaeghe, E. Hatcher, C. Acharya, S. Kundu, S. Zhong, J. Shim, E. Darian, O. Guvench, P. Lopes, I. Vorobyov, A.D. MacKerell, Jr., CHARMM general force field: a force field for drug-like molecules compatible with the charmm all-atom additive biological force fields, Journal of Computational Chemistry 31(4) (2010) 671-690.

[43] S. Kirkpatrick, C.D. Gelatt, M.P. Vecchi, Optimization by simulated annealing, Science 220(4598) (1983) 671-680.

8. SUMMARY AND CONCLUSIONS

In this chapter, we summarize the systematic experimental and modeling work from the macroscale to the molecular level to evaluate the behavior of two materials—swelling clay and oil shale. The focus of this work is to investigate how the material properties at the molecular scale are influenced by the nonboned interactions. The research findings and methods developed in this work provide insight into the development of robust multiscale models of swelling clays. The conclusions of the research work are as follows:

1. The role of fluid polarity in the swelling of Na-MMT clay: a molecular dynamics and Fourier transform infrared spectroscopy study.
    - In this study, FTIR and MD simulations are carried out to investigate the swelling behavior of Na-MMT with a formamide, water, methanol, and acetone. The shifts of bands in the Si-O stretching band and Fe-OH deformation band are observed only on the FTIR spectra of Na-MMT with formamide and water. This indicates that there are significant nonbonded interactions of clay with polar fluids, causing the disorientation of tetrahedral and octahedral clay sheets.
    - The results from the molecular dynamic simulations have indicated that the attractive nonbonded clay-formamide and clay-water interactions are significantly higher than clay-methanol and clay-acetone interactions. These results correlated well and are consistent with the shifts of bands in FTIR studies. The MD simulations are able to accurately model the experimental observations.
    - It is also observed that the patterns of the fluid molecules around the interlayer cations are well organized observed when the amount and polarity of the interlayer fluids increase.

- The molecular dynamics study with 10% fluid content for four fluids revealed that the molecular interactions between clay sheets, sodium ions and fluid molecules are significantly different for each of the four fluids. The clay-clay interactions have decreased with increased in the polarity of fluids. On the other hand, the sodium-fluid and clay-fluid interactions appear to relate to the size, number of amount of fluid molecules in the interlayer, and the physical distribution of the fluid molecules in the interlayer.

2. Compression of Na-MMT swelling clay interlayer.
    - In this work, SMD simulations are used to assess the mechanical response of the interlayer of dry Na-MMT clay as well as clay with 10% and 30% fluid content with low polar fluid acetone (20), medium polar fluid methanol (33), and high polar fluids water (80) and formamide (110). Upon compression from 0 GPa to 1.48 GPa, the interlayer spacing for dry Na-MMT clay decreased rapidly but linearly; whereas the interlayer spacing decreased gradually when compressed from 2.22 GPa to 8.88 GPa. For all clay-fluid models, it is found that the stress-deformation response of the clay interlayer is linear from 0-1.48 GPa, but it is nonlinear from 2.22 to 8.88 GPa.
    - A much softer clay interlayer response is found for clay with fluids than that of dry clay interlayer. Moreover, the clay interlayer with polar fluids is less compressible but much stiffer than that of low and medium polar fluids. It is observed that the polarity of the fluid influenced the compressibility of clay interlayer.
    - The compressibility of the clay interlayer is due to combined compression of the clay-fluid interaction zone, exiting of the fluid molecules from the interlayer, and the compression of the fluid molecules in the interlayer. The compression of the

thickness of the fluid layers is observed for clay with 30% fluid, but the thickness of 10% fluid content remained unchanged.

- The nonbonded interactions between clay-clay, clay-sodium, sodium-fluid, and clay-fluid molecules before and after compression for 10% and 30% fluid content are evaluated. The attractive clay-fluid interactions for Na-MMT clay with 30% water (80) and formamide (110) remain attractive upon compression, which indicates that the hydration of the clay sheets continues upon compression; whereas the nature of interactions for 30% methanol changed from attractive to repulsive upon compression because of higher compressibility of the interlayer.

3. Influence of the molecular interactions on shear strength of Na-MMT with organic fluids
    - SMD simulations are used to evaluate the molecular shear strength parameters for dry Na-MMT clay interlayer and clay with 10% and 30% fluid content with fluids with a range of polarities. Shear stress versus displacement plots are different for each of the four organic fluids. Upon increasing the normal stress, shear stress required to shear the top clay layer is increased. Shear strength of swelling clay upon shearing is significantly higher for clay with polar fluids than that of medium and low polar fluids.
    - The molecular shear strength parameters, cohesion and angle of internal friction, of dry Na-MMT clay and clay with 10% and 30% fluid content with fluids with a range of polarities are computed. These parameters for Na-MMT with 10% fluids are higher than Na-MMT with 30% fluid content in the interlayer.
    - The layer-layer interactions, which are attractive in nature, for dry Na-MMT are higher than Na-MMT clay with 10% and 30% fluid when the top clay layer is sheared

at σ =0 GPa and σ=8.88 GPa, The attractive sodium-fluid interactions for Na-MMT with 10% and 30% fluid content when sheared at σ=8.88 GPa are strong, which indicated that the hydration continues upon shearing. Also, the clay-fluid interactions for Na-MMT with 10% fluid content when shearing under high compression significantly decreased relative to no normal stress; the nature of van der Waals energies changed from attractive to repulsive when shearing at high stress.

4. Experimental evaluation of shear strength of swelling clays at various level of swelling
    - In this work, a controlled uniaxial (CUS) device is used to saturate the samples and allow them to swell to various levels of swelling. The unconfined compressive strength and undrained cohesion at 0%, 10%, and 30% swelling are investigated.
    - The values of unconfined compressive strength of the Na-MMT samples decrease with an increase in swelling. Furthermore, the unconfined compressive strength at no volume change is significantly higher than the samples with 10% and 20% swelling. Additionally, the undrained cohesion that is the half of the maximum unconfined compressive strength is evaluated. Thus, undrained cohesion also decreased with an increase in the level of swelling.
    - The clay particles breakdown into smaller size with an increase in swelling. Thus, the level of swelling controls the evolution of the microstructures of swelling clays, resulting in change of the unconfined compressive strength at various levels of swelling.
    - The nanomechanical properties, the modulus of elasticity and hardness, for undisturbed dry and saturated clay at three levels (0%, 10%, and 20%) of swelling are

accomplished using nanoindentation experiments in the displacement controlled mode for the first time.

- The load-displacement curves show that the maximum force needed to indent for the same magnitude of displacement for 0% swelling is significantly higher than dry clay. The magnitude of maximum force needed to indent further decreases with increase in swelling. Also, the modulus of elasticity and hardness decrease with the increase in the level of swelling, as result of molecular scale interaction between the clay and fluid.
- In summary, the above findings demonstrate that swelling influences the macroscale mechanical properties, nanomechanical properties, and change in the microstructures of swelling clays.

5. Modeling molecular interactions of Na-MMT clay with 3d kerogen models
    - In this study, a three-dimensional (3D) molecular model of kerogen has been developed based on Siskin's 2-dimensional structure. A kerogen molecule has seven fragments; the fragments 1, 2 and 3 are aliphatic hydrocarbons, fragment 4 has aromatic and olefinic hydrocarbons, and fragments 5, 6, and 7 have aliphatic, olefinic, and aromatic hydrocarbons, aliphatic nitrogen, ammonical nitrogen, oxygen atoms. The representative 3D kerogen model has been verified by developing atomic pair distribution functions (PDFs) on the 12-unit 3D kerogen model. Also, the clay model was validated by comparing d-spacing of the clay structure from molecular dynamics simulations with the results from XRD experiments.
    - It has been observed that attractive nonbonded kerogen-clay interactions are significantly higher than kerogen-sodium interactions, resulting in binding them

together. Seven fragments of kerogen interacted and oriented differently with clay surface, resulting in certain parts of the kerogen molecules have high interactions with clay.

- The strong attractive non-bonded interactions between the kerogen fragments are primarily electrostatic in nature. The nonbonded interactions between the fragments of kerogen and between clay and kerogen fragments at the molecular level play a critical role in understanding the mechanisms of the kerogen-clay binding in the oil shale.

The major contributions from the studies are as follows:

1. The quantitative nonbonded interactions of swelling clays with organic fluids with various dielectric constant have been investigated using molecular dynamics simulations.
2. Correlations have been developed for identifying the effect of the polarity of fluids on swelling clays by bridging the results from molecular modeling with the results from experiments.
3. Steered molecular dynamics simulations of swelling clays with a wide range of polar fluids have been conducted. The polarity of the fluids and the fluid content in the interlayer plays a vital role in the interlayer spacing, interlayer volume, interlayer compressive strain, interlayer modulus, nonbonded interactions, and conformation of the fluid molecules upon compression.
4. The compressibility of the clay interlayer is due to the compression of the clay-fluid interaction zone, exiting of the volume of fluids from the interlayer, and the compression of the fluid molecules in the interlayer, and these are influenced by the clay-fluid molecular interactions and the amount of the fluid in the interlayer.

5. It has been demonstrated that the magnitude of shear stress required to pull the clay sheet for polar fluids is significantly higher than that of medium and low polar fluids. The shear strength parameters, the angle of internal friction and cohesion, are also influenced by the polarity of fluids and the amount of the fluid content in the clay interlayer.
6. It has been found that swelling controls the macroscale mechanical properties, nanomechanical properties, and evolution of the microstructure of swelling clay. The unconfined compressive strength and undrained cohesion decrease with an increase in swelling level.
7. Nanoindentation experiments on the undisturbed dry and saturated swelling clays have been conducted for the first time. The effect of swelling on the modulus of elasticity and hardness is investigated. The results show that the modulus of elasticity and hardness reduce with increase in the levels of swelling.
8. 3D molecular model of kerogen has been developed. This work further shows a comprehensive analysis of the nonbonded interactions of kerogen with sodium montmorillonite clay.
9. It has been found that there are strong attractive nonbonded interactions between kerogen and clay, and only certain portions of the kerogen molecules have high interactions with clay. The attractive interactions within the kerogen molecule are also strong.

9. FUTURE WORK

The studies presented in this dissertation provide insight into the role of clay-fluids interactions for complete understanding of swelling mechanism as well as the influence of swelling on the mechanical properties of swelling clays at the macroscale and nanoscale. Also, the interactions between organic matter and mineral matrix in oil shale are investigated in this work. The following suggestions are recommended for the future research avenues:

1. The compressibility and shear strength parameters with increased amount of initial fluid content in the clay interlayer are needed to better understand the influence of the polarity on mechanical properties at the molecular level.
2. The development of solvation model with a wide range of organic fluids—high polar, medium polar, and low polar—is needed to study the molecular flow rate in the clay interlayer.
3. The unconfined compressive strength of swelling clays is influenced by predermined level of swelling. Therefore, it is recommended to evaluate the compressive strength and undrained cohesion at higher swelling level.
4. The compressive strength of swelling clays with various organic fluids such as formamide, methanol, and acetone is recommended to completely uncover the role of clay-fluid interactions on the compressive strength of swelling clays.
5. The shear strength behavior of swelling clays at various level of swelling under different drainage conditions are recommended using triaxial experiments. This will answer a number questions about influence of swelling on the long-term and short-term behavior of swelling clays.

6. The modulus of elastic of the 12-unit 3D kerogen model in the presence and absence of the mineral matrix using constant-force steered molecular dynamics simulations and compare the results from nanoindentation experiments.
7. The load-displacement and shear characteristics of kerogen in proximity and non-proximity of minerals are also suggested using constant-velocity steered molecular dynamics simulations. The results from this study may provide the fundamental mechanism behind unfolding and extracting of kerogen at mineral proximity.